The Effect of Corrosion Damage Morphology on Fatigue Crack Initiation and Small Crack Propagation Behavior of AA 7050-T7451

A Dissertation

Presented to

the faculty of the School of Engineering and Applied Science

University of Virginia

in partial fulfillment

of the requirements for the degree

Doctor of Philosophy

by

Noelle Easter Co

May

2018

APPROVAL SHEET

The dissertation

is submitted in partial fulfillment of the requirements

for the degree of

Doctor of Philosophy

AUTHOR

The dissertation has been read and approved by the examining committee:

James T. Burns

Advisor

Michael D. Sangid

Devin K. Harris

Sean R. Agnew

John R. Scully

Robert G. Kelly

Accepted for the School of Engineering and Applied Science:

Craig H. Benson, Dean, School of Engineering and Applied Science

This dissertation is dedicated to Jeff, to my parents, to my brother, and most especially to my grandmother, Mary R. Cruz†

Abstract

Corrosion nucleated fatigue is a primary failure mode in aerospace structures. Built up aerospace aluminum assemblies are commonly joined by stainless steel fasteners. The complex geometries and high stress levels often lead to coating breakdown at these locations. Such coating failure can give rise to electrolyte ingress, setting up a galvanic couple between aluminum structure and the stainless steel fastener. Several corrosion morphologies in aluminum substructure can form due to the galvanic coupling of aluminum and stainless steel. Corrosion morphologies depend on the alloy microstructure, potential distribution, pH distribution and local chemistry within the fastener-hole geometry. The presence of corrosion on the aluminum substructure affects the structural integrity of the airframe and complicates the prognosis of the remaining life as fatigue cracks can initiate at the corrosion damage during in-flight cyclic loading. Detailed investigation of the fatigue crack formation process in pitted AA 7075-T651 specimens established the primary role of micro-topography along the broad pit surface. However, similar studies in high strength steels that exhibit smoother pit morphology demonstrated a primary role of macro-topography. This discrepancy motivates the current study to investigate the fatigue initiation, propagation and crack growth behavior of AA 7050-T7451 with various corrosion morphologies produced using conditions typical of a galvanic couple. Furthermore, this study seeks to determine the contribution of corrosion geometry, constituent particle distribution, and grain orientation to the local plasticity that dictates fatigue crack formation location.

It is hypothesized that the fatigue crack initiation can be found on the location with most severe corrosion damage shape. In order to test this hypothesis, vastly different corrosion damage morphologies (discrete pits, general corrosion with surface recession, fissures, cigar-shaped pit, and intergranular corrosion) are artificially formed on the surface of the AA 7050-T7451 using electrochemical techniques. The corrosion morphologies are characterized using optical microscopy, white light interferometry, X-ray computed tomography, and scanning electron microcopy. Specimens are cyclically loaded in a longitudinal direction at a relative humidity of > 90% maintained within a sealed acrylic chamber. A programmed fatigue loading sequence with σ_{max} of 200 MPa, R of 0.5 and 20

Hz frequency is used to create marker bands on the fracture surface. The microstructurally small crack growth rates and the fatigue initiation life to create a 10 µm crack are determined using these marker bands. A combination of 2D and 3D images enables the determination of the fatigue initiation sites. These fatigue formation sites are correlated to the macro-scale (> 250 µm) corrosion damage features. The different metrics analyzed for discrete pits are the pit depth, pit density, pit volume, surface area of pit mouth, pit diameter, number of pits per plane, average pit depth per plane, and total pit depth per plane. On the other hand, the macro-scale metrics analyzed for fissure and IGC morphologies are fissure depth, number of fissures per plane, average fissure depth per plane and total fissure depth per plane. Roughness metrics such as average roughness or root mean square (RMS), peak density, maximum valley depth, maximum height, texture aspect ratio, auto correlation length, kurtosis, and arithmetic mean height are analyzed for general corrosion with surface recession. Results show that individual contribution of the macro-scale features does not independently dictate the location of fatigue crack formation location. The fatigue initiation life of specimens with different corrosion morphologies is very low and has near constant values. The crack growth rates of the specimens with different corrosion morphologies converge to similar values. However, the increased initial size for large corrosion damage can lead to mildly lower total life.

The analysis of the contribution of individual macro-scale corrosion metrics is extended to discrete pit specimens tested at low relative humidity (< 5% RH) and high σ_{max} (300 MPa). Results show that despite changes in the fatigue testing environment or the σ_{max}, the individual contribution of the macro-scale corrosion features still does not solely influence the location of the fatigue crack formation. Initiation life of specimens tested at < 5% RH is still very low. The crack growth rate of these specimens is lower, compared to the specimens tested at > 90% RH, leading to higher total fatigue life. The increase of σ_{max} results in a decreased total fatigue life and increased crack growth rates.

This study also looks at the effect of micro-scale (< 250 µm) corrosion damage features. It is hypothesized that fatigue crack initiation can be found on areas with distinct micro-scale corrosion damage feature. The fatigue crack initiation features are classified according to the micro-features such as jut-ins, micro-pits, ligament with high aspect ratio and ligament with low aspect ratio. Most of the fatigue crack initiation occurs at jut-in features along the corroded surface however not all jut-ins initiate fatigue cracks. The underlying alloy microstructure features are also considered; specifically, the constituent particle distribution, grain orientation with respect to the loading direction, grain orientation spread, grain size and misorientation angles. It is also hypothesized that the fatigue initiation site occurs at the area with high density of constituent particles, or at grains with large amount of deformation, or at larger grains, or at grains with high misorientation angles. Results show that individual contribution of the micro-features and underlying microstructure do not independently identify the location of fatigue crack initiation.

Since individually the macro-scale, micro-scale corrosion features and alloy microstructure are shown to not solely prescribe the location of fatigue crack initiation, the combined effects of these parameters are considered via (1) data science approaches, and (2) analytical calculation of microstructure scale driving force. Data science is employed to understand the combined effects of the macro-scale corrosion features. Logistic regression and random forests modeling are used to predict the probability of fatigue crack initiation using the macro-scale metrics as predictor variables. Crystal plasticity modeling is used to analytically evaluate the combined effects of corrosion morphology and alloy microstructure. Crystal plasticity computed local stress/strain state is established for specific corrosion morphology, grain structure, and constituent particle distribution in order to calculate different fatigue indicator parameters (FIP) within the perimeter of the corrosion damage. Results of this study will help inform and validate current micro-mechanical models of initiation and MSC taking into account pertinent FIPs to properly predict crack formation location, fatigue initiation life and total fatigue life of aerospace structures with corrosion damage.

The results and conclusion of this effort will quantitatively characterize the crack formation behavior of a relevant aerospace Al alloy in realistic conditions and leverage this data to further mechanistic understanding of the factors governing the corrosion to fatigue crack transition. This understanding is critical to inform engineering scale prognosis strategies and provide guidance on the critical criteria for designing corrosion mitigation strategies in the context of fatigue damage.

Acknowledgement

I would like to express my sincere gratitude to my advisor, Prof. James Burns for the guidance and support in various undertakings I had during my PhD.

I also would like to extend my gratitude to my committee members, Dr. Sean Agnew, Dr. Devin Harris, Dr. Michael Sangid, Dr. John Scully and Dr. Robert Kelly, for their time, effort, for their insightful review and constructive comments.

Thanks to Dr. Donald Brown of UVa Systems and Information Engineering for the help in data science analysis.

A special thanks to our collaborators in Purdue University, Andrea Nicolas and Dr. Michael Sangid for the fatigue indicator parameter calculations.

This research is funded by Office of Naval Research with Mr. William Nickerson as the Scientific Officer.

I appreciate the help and encouragement of all my colleagues in the Center for Electrochemical Science and Engineering. I would like to particularly mention the old and new members of the Burns Research Group, Ryan Donahue, Jenny Jones, Justin Dolph, Amber Lass, Thaddeus Watterman, Dr. Michael McMurtrey, Zach Harris, Allison Popernack, Matt McMahon, Patrick Steiner, Adam Thompson, Andrew Jamieson, Luke Brown and Keiko Amino. I also appreciate the friendship and meaningful conversations with the other graduate students I had a chance to work with. Special mention goes to Dr. Mary Lyn Lim for influencing me to go to UVA and pursue graduate school. I also want to thank Dr. Jayendreyan Srinivasan, Dr. Balaji Kannan, Dr. Piyush Khullar, Dr. Marybeth Parker, Dr. Begum Unveroglu, Dr. Eaman Abdul Karim, Dr. Bonnie McFarland, Dr. Fulin Wang, Dr. Jishnu Battacharrya, and Dr. Shamsujoha for the conversations about graduate school struggles and for the continuous encouragement. I want to acknowledge Chao (Gilbert) Liu and Veronica Rafla for being good research collaborators for the AA 7050-T7451 project in UVa. I want to thank Barry Baber, Tanner Fitzgerald, Kim Fitzhugh-

Higgins, Sherri Sullivan, Karri Wares, Ashley Duke and most especially Richard White for helping me in any capacity.

I greatly appreciate my friends who became my family here in Charlottesville, Aileen Kim, Pastor IJ Kim, Sally Niesly, Sherry Felker, Nancy Ryalls, Betsy Noble, Ed Yu, Julie Lee, my Women's small group and my Chi Alpha grad core group, for constantly praying for me, for the spiritual guidance and for the words of encouragement. I also want to acknowledge Prof. Hui Ma for being a good friend and companion in Charlottesville. Special shout outs go to my friends from the other side of the world for being my person whenever I need someone to talk to. I gratefully appreciate Katrina Clemente, Jomar Flores, Mariville Cuasay, Kathy Maniquiz, Crispinne Patiño, Don Albao for their time, prayers and moral support. I also want to express my gratitude to my past teachers and mentors at the Jesus Is Lord Colleges Foundation and professors at the University of the Philippines. A special mention goes to Dr. Manolo Mena for his constant encouragement and for introducing me electrochemistry.

I sincerely express my gratitude to my family, most especially to my parents, to my brother, to my Aunt Raquel and Aunt Essa, and to my in-laws for the love and support. Thank you for being my inspiration. Last, but not the least, I want to thank my husband, Jeff, for the sacrifices especially during our long distance relationship, for the prayers, moral support, words of encouragement, and above all, for letting me feel that I am always truly loved.

All praises and glory to Jesus Christ!

Bibliography and Awards

The works included in this dissertation resulted to the following publications:

- Co NEC, Brown DB, Burns JT. Data-Science Analysis of the Macro-scale Features Governing the Corrosion to Crack Transition in AA 7050-T7451 *Accepted for publication in Journal of Minerals, Metals and Materials, April 2018.*
- Co NEC, Burns JT, Nicolas A, Sangid MD. Effect of corrosion micro-scale features and alloy microstructure on the fatigue initiation and crack growth of AA 7050-T7451. Paper No. 2017-845990. 2017 Dep. Def. Allied Nations Tech. Conf., 2017.
- Co NEC, Burns JT. Effects of Macro-scale Corrosion Damage Feature on Fatigue Crack Initiation and Fatigue Behavior. Int J Fatigue 2017;103:234–47. doi:10.1016/j.ijfatigue.2017.05.028.
- Co NEC, Burns JT. Galvanic Corrosion Induced Fatigue Crack Initiation and Propagation Behavior in AA 7050-T7451. CORROSION 2016;72:1215–9. doi:10.5006/2132.

The works included in this dissertation received the following awards:

- Honorable Mention, UVa Engineering Research Symposium Poster (Best in Materials Science and Engineering Department), March 2018
- Honorable Mention, UVa Engineering Research Symposium Podium Presentation (Best in Materials Science and Engineering Department), March 2017
- 1st Place Poster Award, TMS Annual Meeting: Fatigue in Materials Session Division, February 2017
- Best Poster in Environmental Cracking, International Conference on Fatigue Damage of Structural Materials, September 2016
- Honorable Mention, UVa Engineering Research Symposium (Best in Materials Science and Engineering Department), April 2016
- 1st Place Poster NACE Marcel Pourbaix Award for Corrosion Science, March 2016
- 2nd Place Poster Department of Defense Milton Levy Award for Corrosion Science, November 2015

Table of Contents

Abstract i

Acknowledgement v

Bibliography and Awards vii

Table of Contents viii

List of Tables xii

List of Figures xiv

1. Introduction 1

1.1 Background 1

1.1.1 AA 7xxx- Series Alloys 1

1.1.2 Galvanic Coupling of AA 7050-T7451 and Stainless Steel 7

1.1.3. Corrosion Fatigue in Aerospace Aluminum Alloys 10

1.2 Knowledge Gaps 13

1.3 Objective Statements 13

1.4 Thesis Organization 14

1.5 References 14

2. Effect of Macro-Scale Corrosion Features 20

2.1 Overview 20

2.2. Effects of Macro-scale Corrosion Damage Feature on Fatigue Crack Initiation and Fatigue Behavior 22

2.2.1 Introduction 22

2.2.2 Materials and Methods 26

2.2.3 Results 30

2.2.4 Discussion 52

2.2.5 Conclusion 58

2.2.6 References 59

2.3 Effects of Relevant Corrosion Morphology, Relative Humidity, and σ_{max} on Fatigue Crack Initiation and Fatigue Behavior 67

2.3.1 Introduction 67

2.3.2 Methodology 68

2.3.3 Results 74

2.3.4 Discussion 87

2.3.5 Conclusions 97

2.3.6 References 98

3. Effect of Micro-scale Corrosion Feature and Alloy Microstructure 102

3.1 Introduction 102

3.2 Methodology 103

3.2.1 Materials 103

3.2.2 2D and 3D Characterization of Corrosion Micro-features 103

3.2.3 Determination of 2D and 3D Constituent Particle Distribution 104

3.2.4 Determination of Grain Character through EBSD 105

3.3 Results 106

3.3.1 Corrosion Micro-feature 106

3.3.2 Constituent Particles in the alloy matrix 123

3.3.3 Grain Character 134

3.4 Discussion 142

3.4.1 Effects of Corrosion Microfeatures 142

3.4.2 Effects of Microstructure 143
3.5 Conclusions 147
3.6 References 148
4. Combined Effects 152
4.1 Overview 152
4.2 Data Science Analysis of the Macro-scale Features Governing the Corrosion to Crack Transition in AA7050-T7451 154
4.2.1 Introduction 154
4.2.2 Methodology 155
4.2.3 Results 160
4.2.4 Discussion 163
4.2.5. Conclusion 165
4.2.6 References 166
4.3 Fatigue Indicator Parameters 168
4.3.1 Introduction 168
4.3.2 Methodology 171
4.3.3 Results 180
4.3.4 Discussion 184
4.3.5 Future Work and Analysis 185
4.3.6 Conclusions 186
4.3.7 References 187
5. Conclusions 190
5.1 Macro-scale Corrosion Features 190
5.2 Micro-scale Corrosion Features and Alloy Microstructure 191

5.3 Combined Effects 192
6. Future Works 195
6.1 References 196

List of Tables

Chapter 1

Table 1.1 Nominal Compisition of AA 7050 in wieght %[1] 2

Chapter 2 Section 2

Table 2.2.1 Number of fatigue cycles for each sample, location of first marker band, location of primary fatigue crack initiation point and the number of initiation points on the main fracture plane 53

Chapter 2 Section 3

Table 2.3.1 Parameters for fatigue test... 71

Table 2.3.2 Summary of fatigue specimens and the corresponding depth of primary initiation point and the number of initiation points observed in the main fracture plane. 78

Table 2.3.3 Summary of initiation life and total fatigue life for each specimen.............. 87

Table 2.3.4 Summary of average values of fatigue initiation life, total fatigue life, number of initiation points and depth of corrosion feature that initiate the crack for DP2, FIS, DP3 and IGC specimens. Fatigue tests are done at room temperature with RH > 90%, and σ_{max} of 200 MPa, R of 0.5 and a frequency of 20 Hz. 90

Table 2.3.5 Summary of fatigue initiation life, total fatigue life, number of initiation points on the main fracture plane and depth of corrosion feature that initiate the crack for DP1 specimens tested at low RH (< 5%) and high RH (> 90%). Fatigue tests are done with σ_{max} of 200 MPa, R of 0.5 and a frequency of 20 Hz. 91

Table 2.3.6 Summary of fatigue initiation life, total fatigue life, number of initiation points on the main fracture plane and depth of corrosion feature that initiate the crack for DP1 specimens tested at low σ_{max} (200 MPa) and high σ_{max} (300 MPa). Fatigue tests are done in moist air (> 90% RH) , R of 0.5 and frequency of 20 Hz. 95

Chapter 4 Section 2

Table 4.2.1 Hypothesis test thresholds ($p < 0.05$) for each morphology, each test replicate, and each model, and model predicted probabilities for the presence of an initiation point. Parenthetical predictions show minimum and maximum predicted probabilities for multiple initiation points in a morphology for logistic regression and for the 10 separate runs of random forest for each initiation point in the morphology. Highlighted predicted values show significance ($p < 0.05$). 161

List of Figures

Chapter 1

Figure 1.1 EBSD image representing microstructure of AA 7050-T7451 along different surfaces (TS, TL, LS). L is the rolling direction, S is the short transverse direction while T is the transverse direction. 3

Figure 1.2 Average size of constituent particles along different surfaces (TS, TL, LS) at varying locations with respect to the thickness of the plate (t/0=surface of plate or point 0 in the graph, t/8= 1/8 of the plate or 0.11 in the graph, t/4= ¼ of the plate or 0.25 on the graph, t/2=1/2 of the plate or 0.5 on the graph). A 50-mm thick plate of AA 7050-T7451 is used in this constituent particles distribution analysis. 5

Figure 1.3 Density of constituent particles along different surfaces (TS, TL, LS) of AA 7050-T7451 at different locations with respect to the thickness of the plate (t/0=surface of plate or point 0 in the graph, t/8= 1/8 of the plate or 0.11 in the graph, t/4= ¼ of the plate or 0.25 on the graph, t/2=1/2 of the plate or 0.5 on the graph). A 50-mm thick plate of AA 7050-T7451 is used in this constituent particles distribution analysis. 6

Figure 1.4 Cumulative distribution plot for the constituent particle size of AA 7050-T7451 LS surface at different locations with respect to the thickness of the plate (t/0=surface of plate, t/8= 1/8 of the plate, t/4= ¼ of the plate, t/2=1/2 of the plate). A 50-mm thick plate of AA 7050-T7451 is used in this constituent particles distribution analysis. 7

Figure 1.5 Schematic representation of fastener-hole configuration in AA 7050-T7451 substructure. The second phase particles present in AA 7050-T7451 are identified in the diagram. 8

Figure 1.6 Polarization scans of SS316 and AA 7050 under aerated and deaerated conditions using 4M NaCl with pH of 9 (Plot obtained from unpublished works of V. Rafla) 10

Chapter 2 Section 2

Figure 2.2.1 Corrosion morphologies (a) and (e) shallow discrete pit (DP1) (b) and (f) deep discrete pit (DP2) (c) and (g) fissures (FIS) (d) and (h) general corrosion with surface recession (GCSR); top view of corrosion damage (a, b, c, d); corrosion morphologies traced on fracture surface (e, f, g, h). Figure 2.2.1 (a, b, c, e, f, g) are taken at the same magnification (100×), but note the different scale in (d) and (h)..................................... 28

Figure 2.2.2 Marker bands are traced on the fracture surface. Multiple fatigue cracks at the fracture surface of GCSR specimen converge to form a larger crack. Crack grows from bottom to top along the T-direction of the specimen. Fatigue testing of AA 7050-T7451 is performed in moist air environment at 23°C with σ_{max}= 200 MPa, R=0.5 at 20 Hz frequency.. 30

Figure 2.2.3 Plot of total fatigue life, N_{total}, (filled markers) and initiation life, N_i, to create a 10 μm crack (open markers) with respect to the depth of fatigue crack formation site (depth of initiating feature) measured from the non-corroded surface for each specimen. Measurements are taken from the SEM images of the fracture surface. Fatigue testing of AA 7050-T7451 performed in moist air environment at 23^{o}C with σ_{max}= 200 MPa, R=0.5 at 20 Hz frequency. Arrow on top of the pristine data point indicate that pristine specimen did not fail after 1.4×10^6 cycles and testing is halted at 3×10^6 cycles............................. 32

Figure 2.2.4 Crack growth rate for AA 7050-T7451 specimens with different corrosion morphologies cyclically loaded along L-direction with σ_{max}= 200 MPa, R=0.5 at 20 Hz frequency with moist air environment at 23^{o}C; crack length (a) is measured from non-corroded surface growing along the T-direction of the specimen. Indicated numerical values above the arrows represent the average depth at which the primary fatigue crack forms. R1, R2, R3 correspond to the three test replicates done for each corrosion morphologies.. 33

Figure 2.2.5 (a) Top view of corroded surface (LS) imaged using SEM (b) top view of corroded surface (LS) imaged using optical microscope (c) top view of the fracture surface (TS) imaged using SEM (d) white light interferometry 3D image. Combination of the 2D images and the 3D image allows the determination of the fracture initiation locations.

Fatigue testing of AA 7050-T7451 performed in moist air environment at 23^{o}C with σ_{max}= 200 MPa, R=0.5 at 20 Hz frequency. 35

Figure 2.2.6 Histogram of pit depths for (a) DP1 specimens and (b) DP2 specimens. Location of the primary fatigue crack initiation points are marked using filled markers, while location of secondary crack initiation points are marked with open markers. Actual value of the pit depth for R1, R2, R3 is centered on the red bar of the histogram. Fatigue testing of AA 7050-T7451 is performed in moist air environment at 23^{o}C with σ_{max}= 200 MPa, R=0.5 at 20 Hz frequency. R1, R2, R3 correspond to the three test replicates. 37

Figure 2.2.7 Histogram of pit density for (a) DP1 specimens and (b) DP2 specimens. Location of the primary fatigue crack initiation points are marked using filled markers, while location of secondary crack initiation points are marked with open markers. Actual value of the pit density for R1, R2 and R3 is centered on the red bar of the histogram. Fatigue testing of AA 7050-T7451 is performed in moist air environment at 23^{o}C with σ_{max}= 200 MPa, R=0.5 at 20 Hz frequency. R1, R2, R3 correspond to the three test replicates. 39

Figure 2.2.8 Plot of average depth (filled markers) and maximum depth (open markers) versus pit density of DP1. ΔD = maximum depth - average depth where fatigue crack initiated. Values for the primary initiation points are indicated by the green markers. Fatigue testing of AA 7050-T7451 is performed in moist air environment at 23^{o}C with σ_{max}= 200 MPa, R=0.5 at 20 Hz frequency. R1, R2, R3 correspond to the three test replicates. 40

Figure 2.2.9 Results of line profile measurements for DP1 indicating (a) total pit depth, (b) number of pits per line and (c) average depth of pits per line, filled markers indicate location of the fracture plane where primary fatigue crack initiate. Actual values of total pit depth per line, number of pits per line, average depth of pits per line for R1, R2, R3 are centered on the red bar of the histogram. Fatigue testing of AA 7050-T7451 is performed in moist air environment at 23^{o}C with σ_{max}= 200 MPa, R=0.5 at 20 Hz frequency. R1, R2, R3 correspond to the three test replicates. 42

Figure 2.2.10 Histogram of individual fissure depths measured for FIS specimens. Location of the primary fatigue crack initiation points are marked using filled markers, while location of secondary crack initiation points are marked with open markers. Actual values of the fissure depths for R1, R2, R3 are centered on the red bar of the histogram. Fatigue testing of AA 7050-T7451 is performed in moist air environment at 23^{o}C with σ_{max}= 200 MPa, R=0.5 at 20 Hz frequency. R1, R2, R3 correspond to the three test replicates. 44

Figure 2.2.11 Histogram of the total (cumulative) fissure depth per plane of FIS specimens. Location of the primary fatigue crack initiation points are marked using filled markers, while location of secondary crack initiation points are marked with open markers. Actual values of the total fissure depth for R1, R2, R3 are centered on the red bar of the histogram. Fatigue testing of AA 7050-T7451 is performed in moist air environment at 23^{o}C with σ_{max}= 200 MPa, R=0.5 at 20 Hz frequency. R1, R2, R3 correspond to the three test replicates. 45

Figure 2.2.12 Histogram of the number of fissures per plane for FIS specimens. Location of the primary fatigue crack initiation points are marked using filled markers, while location of secondary crack initiation points are marked with open markers. Actual values of the number of fissures per plane for R1, R2, R3 is centered on the red bar of the histogram. Fatigue testing of AA 7050-T7451 is performed in moist air environment at 23^{o}C with σ_{max}= 200 MPa, R=0.5 at 20 Hz frequency. R1, R2, R3 correspond to the three test replicates.. 46

Figure 2.2.13 Plot of total fissure depth versus the number of fissures per plane for FIS specimens. The locations of fatigue crack formation are by the red markers on the plot. Fatigue testing of AA 7050-T7451 is performed in moist air environment at 23^{o}C σ_{max}= 200 MPa, R=0.5 at 20 Hz frequency. R1, R2, R3 correspond to the three test replicates. Reproduced with permission from NACE International, Houston, TX. All rights reserved. Co, NEC. Burns, JT. Galvanic Corrosion-Induced Fatigue Crack Initiation and Propagation in AA 7050-T7451, CORROSION, 72, 10, 2016. ©NACE International 2016 47

Figure 2.2.14 Histograms of (a) GCSR root mean square, (b) peak density, (c) maximum valley depth, filled markers indicate location of primary crack initiation that caused failure, while open markers indicate secondary initiation sites. Actual values of root mean square, peak density, maximum valley depth for R1, R2, R3 are centered on the red bar of the histogram. Fatigue testing of AA 7050-T7451 is performed in moist air environment at 23^{o}C with σ_{max}= 200 MPa, R=0.5 at 20 Hz frequency. R1, R2, R3 correspond to the three test replicates. 50

Figure 2.2.15 (a) Plot of peak density and root mean square for GCSR specimens. (b) Plot of the combination effects of maximum valley depth and root mean square. Location of fatigue crack formation are indicated by the red markers. Fatigue testing of AA 7050-T7451 is performed in moist air environment at 23^{o}C with σ_{max}= 200 MPa, R=0.5 at 20 Hz frequency. R1, R2, R3 correspond to the three test replicates. 51

Chapter 2 Section 3

Figure 2.3.1 Fatigue specimen machined from AA 7050-T7451 plate 69

Figure 2.3.2 Fatigue test set-up for AA 7050-T7451 specimen contained in sealed acrylic chamber to control the test environment 72

Figure 2.3.3 Traced marker bands on the fracture surface. Crack grows from bottom to top of the fractograph. Crack length, a, is measured (along the red line) from the non-corroded surface of the specimen. 73

Figure 2.3.4 Fracture surface (TS surface) with corrosion damage that grew towards T-direction**.** (a) cigar-shaped corrosion damage (DP3); (b**)** intergranular corrosion damage (IGC) ; (c) discrete pit (DP1) 75

Figure 2.3.5 Cross section of specimens with relevant corrosion morphology (a) cigar-shaped pit (b) inter-granular corrosion from unpublished works of V. Rafla [2] 76

Figure 2.3.6 White light interferometry (WLI) image reconstruction using Mountains Map for (a) cigar- shaped corrosion (DP3), (b) intergranular corrosion (IGC) and (c) discrete pit (DP1) specimens. Spectrum on the right of each image shows depth of pits. 77

Figure 2.3.7 Histogram of corrosion feature metrics for the cigar-shaped corrosion specimens (DP3) (a) pit depth (b) area of the pit mouth, (c) pit density. The markers on the histograms indicate the location of the fatigue crack initiation. 80

Figure 2.3.8 Histogram of corrosion metrics (a) pit depth, (b) pit density for DP1 specimens subjected to fatigue loading with high σ_{max} (300 MPa). Markers indicate the location of fatigue crack initiation. 81

Figure 2.3.9 Histogram of corrosion metrics (a**)** pit depth, (b**)** pit density for DP1 specimens subjected to fatigue loading with low relative humidity (< 5%). Markers indicate the location of fatigue crack initiation. 82

Figure 2.3.10 Intergranular corrosion damage (IGC) specimen (a) 3D reconstruction of images from X-ray computed tomography (b) 2D orthogonal views of images processed using Avizo 84

Figure 2.3.11 Histogram of (a) fissure depths (b) total depth of fissures per plane **c.** number of fissures per plane for IGC specimens measured using XCT. Markers on the histogram indicate where the primary fatigue crack initiate for each specimen. The values of the histogram are centered at the red bar 86

Figure 2.3.12 Crack growth rates (da/dN) for DP3, IGC specimens plotted against the distance measured from the non-corroded edge of the specimen. Plot includes values for DP2 and FIS specimens as reported in Chapter 2 Section 2. Specimens are tested at 23°C in moist air environment (> 90% RH) with σ_{max} of 200 MPa, R of 0.5 and frequency of 20 Hz. 90

Figure 2.3.13 Crack growth rates (da/dN) for DP1 specimens tested at low RH (< 5%) plotted against the distance measured from the non-corroded edge of the specimen. Plot includes values for DP1 specimens tested at high RH (> 90%) as reported in Chapter 2 Section 2. Specimens are tested with σ_{max} of 200 MPa, R of 0.5 and frequency of 20 Hz. 93

Figure 2.3.14 Crack growth rates (da/dN) for DP1 specimens tested at high σ_{max} (300 MPa) plotted against the distance measured from the non-corroded edge of the specimen. Plot includes values for DP1 specimens tested at low σ_{max} (200 MPa) as reported in Chapter 2 Section 2. Specimens are tested at room temperature with moist air (> 90% RH). 96

Chapter 3

Figure 3.1 Fractographs of fatigue specimens showing (a) micro-features (< 50 μm) such as jut-ins and micro-pit enclosed on the boxes, (b) ligament (> 50 μm) with low aspect ratio (low AR) and high aspect ratio (high AR)... 109

Figure 3.2 Histogram of the micro-scale corrosion features (binned based on the types such as jut-in, micro-pit, ligament with high aspect ratio, ligament with low aspect ratio) within the vicinity of the fatigue initiation site. Micro-scale features on the corrosion surface that do not fit in the classification are binned as others. Different colors in the histogram represent the corrosion morphology of the specimens. 110

Figure 3.3 SEM image of fatigue initiation point at the grain or phase boundary that is intersected by the corrosion damage. The arrow points to the fatigue initiation location. 111

Figure 3.4 Histogram of corrosion surface roughness metrics for DP1 with a defined area size of 250 μm x 250 μm (a) Root Mean Square, (b) Maximum Valley Depth, (c) Arithmetic Mean Height, (d) Arithmetic Mean Curvature (e) Peak Density. Filled markers indicate location of primary fatigue crack initiation, while hollow markers indicate secondary fatigue crack initiation. The color of the markers correspond to the replicate number. 113

Figure 3.5 Histogram of corrosion surface roughness metrics for DP2 with a defined area size of 250 μm x 250 μm (a) Root Mean Square, (b) Maximum Valley Depth, (c) Arithmetic Mean Height, (d) Arithmetic Mean Curvature (e) Peak Density. Filled markers indicate location of primary fatigue crack initiation, while hollow markers indicate secondary fatigue crack initiation. The color of the markers correspond to the replicate number. 115

Figure 3.6 Histogram of corrosion surface roughness metrics for GCSR with a defined area size of 250 μm x 250 μm (a) Root Mean Square, (b) Maximum Valley Depth, (c) Arithmetic Mean Height, (d) Arithmetic Mean Curvature (e) Peak Density. Filled markers indicate location of primary fatigue crack initiation, while hollow markers indicate secondary fatigue crack initiation. The color of the markers correspond to the replicate number. 117

Figure 3.7 Histogram of corrosion surface roughness metrics for DP1 with a defined area size of 100 μm x 100 μm (a) Root Mean Square, (b) Maximum Valley Depth, (c) Arithmetic Mean Height, (d) Arithmetic Mean Curvature (e) Peak Density. Filled markers indicate location of primary fatigue crack initiation, while hollow markers indicate secondary fatigue crack initiation. The color of the markers correspond to the replicate number. 119

Figure 3.8 Histogram of corrosion surface roughness metrics for DP2 with a defined area size of 100 μm x 100 μm (a) Root Mean Square, (b) Maximum Valley Depth, (c) Arithmetic Mean Height, (d) Arithmetic Mean Curvature (e) Peak Density. Filled markers indicate location of primary fatigue crack initiation, while hollow markers indicate secondary fatigue crack initiation. The color of the markers correspond to the replicate number. 121

Figure 3.9 Histogram of corrosion surface roughness metrics for GCSR with a defined area size of 100 μm x 100 μm (a) Root Mean Square, (b) Maximum Valley Depth, (c) Arithmetic Mean Height, (d) Arithmetic Mean Curvature (e) Peak Density. Filled markers indicate location of primary fatigue crack initiation, while hollow markers indicate secondary fatigue crack initiation. The color of the markers correspond to the replicate number. 123

Figure 3.10 Plot of the constituent particle size per area division of 250 μm x 250 μm of the fracture surface. Each dot on the graph corresponds to a value that represents the individual area division of 250 μm x 250 μm. The red marks on the plot represent the area division that has the primary fatigue crack initiation site. 124

Figure 3.11 Plot of constituent particle number density vs the normalized size of constituent particles per area division. Each dot on the graph corresponds to a value that represents the individual area division of 250 μm x 250 μm. The red marks on the plot represent the area division that has the primary fatigue crack initiation site. 126

Figure 3.12 Mean spacing between constituent particles within the defined area of analysis plotted against the average nearest neighbor (ANN) ratio. Each dot on the graph corresponds to a value that represents the individual area division of 250 μm x 250 μm. The red marks on the plot represent the area division that has the primary fatigue crack initiation site........ 127

Figure 3.13 Plot of ANN Ratio vs (a) normalized size of constituent particles and (b) number density of constituent particles measured per area division. Each dot on the graph corresponds to a value that represents the individual area division of 250 µm x 250 µm. The red marks on the plot represent the area division that has the primary fatigue crack initiation site.......... 129

Figure 3.14 (a) Histogram of average size of large constituent particles near the fatigue crack initiation site, and (b) nearest distance between the large constituent particle and the primary fatigue initiation site.......... 131

Figure 3.15 Histogram of constituent particles number density within the 250 µm × 250 µm × 500 µm defined cube from XCT analysis. Markers indicate the number density of the cube that enclosed the fatigue crack initiation. Hollow markers indicate specimens with low fatigue life, filled markers indicate specimens with high fatigue life.......... 133

Figure 3.16 Histogram of constituent particles number density within the 100 µm × 100 µm × 100 µm defined cube from XCT analysis. Markers indicate the number density of the cube that enclosed the fatigue crack initiation. Hollow markers indicate specimens with low fatigue life, filled markers indicate specimens with high fatigue life.......... 134

Figure 3.17 Graph of grain size per specimen. Stars indicate the size of the grain that corresponds to the location of fatigue crack initiation. Maximum values of grain size for each specimen are noted on the top of the graph.......... 137

Figure 3.18 Graph of grain orientation spread per specimen. Stars indicate the size of the grain that corresponds to the location of fatigue crack initiation. Maximum values of grain size for each specimen are noted on the top of the graph.......... 138

Figure 3.19 Boxplots of misorientation angles of grains near the location of fatigue crack initiation. Stars indicate the size of the grain that corresponds to the location of fatigue crack initiation. Maximum values of grain size for each specimen are noted on the top of the graph.......... 139

Figure 3.20 (a) Fractograph of the fatigue specimen with initiation point identified (b) EBSD image overlaid on the fracture surface (c) inverse pole figure of AA 7050-T7451 with respect to the loading direction (L-direction), black markers on IPF corresponds to orientation of the primary fatigue crack initiating grain. 141

Chapter 4 Section 2

Figure 4.2.1 (a.) Image representation of white light interferometry data obtained for DP1 specimen with corrosion pits on the surface. (b.) 3D rendering of pits within the 500 μm x 500 μm area. The depth of pits corresponds to the value denoted by the color map...... 157

Figure 4.2.2 Example of random forest single tree partitioning of two variables X_1 and X_2 in order to classify green crosses and blue triangles... 159

Figure 4.2.3 t-SNE plots of DP1 line profile predictors with color coding for pit depth. The locations of initiation points are marked (circle, square) on the graph. Bin sizes determined by the statistics in a box plot.. 164

Chapter 4 Section 3

Figure 4.3.1 Topography of the fracture surface after fatigue testing obtained using white light interferometry prior to EBSD sample preparation. 173

Figure 4.3.2 Schematic of specimen preparation for EBSD. TS surface represents the fracture surface polished down for EBSD characterization. T is the transverse direction, S is the short-transverse direction while L corresponds the longitudinal (rolling) direction. 174

Figure 4.3.3 EBSD cube for AA 7050-T7451. The EBSD cube shows the grains on the LS plane, TS plane and LT planes.. 174

Figure 4.3.4 a. Fractograph of FIS specimen where the yellow lines indicate the location of the marker bands produced by the loading protocol and the primary fatigue crack is indicated by the red cross mark on the image b. EBSD image overlaid on the fracture surface, the white lines indicate the marker bands transposed on the EBSD image, while the primary fatigue crack is indicated by the red cross mark. The boxes on the images correspond to the 500 μm x 500 μm area.. 176

Figure 4.3.5 3D volume rendering of (a) bottom and (b) top portion of the fracture specimens using Avizo software. The boxes indicate the location of 500 μm x 500 μm x 500 μm subvolume. The bottom and top portion are carefully aligned to obtain a bigger volume surrounding the fatigue crack initiation site.. 178

Figure 4.3.6 (a) Volume rendering of the aluminum matrix showing the fracture surface and the corroded surface; (b) volume rendering of the constituent particles for the 500 μm x 500 μm x 500 μm subvolume of the bottom portion of the fractured specimen.......... 182

Figure 4.3.7 Combined spatial representation of the aluminum matrix, constituent particles from the top and bottom portions and the grainIDs of FIS specimen. Final volume rendering and GrainID matching are obtained by Purdue. 183

Figure 4.3.8 Calculated FIP for FIS specimen. The secondary phase particles are shown in green. The arrow indicates the location of the primary fatigue crack formation site. The color shows the level of FIP values calculated for the fracture surface. FIP calculation and image rendering are done by Purdue. 184

1. Introduction

1.1 Background

Aluminum alloys, such as AA 7xxx, are commonly used in airframe applications due to their high strength-to-weight ratio and good fracture toughness [1–3]. These complex aerospace structures necessitate the use of fasteners and joints. Stainless steel fasteners are often used in these built-up components. These high stress fastener locations are prone to coating failure, thereby enabling the wicking of electrolyte into the crevice formed between the aluminum substructure and stainless fastener steel, resulting in the formation of a local electrochemical cell. This galvanic coupling of aluminum and stainless steel can lead to corrosion damage that will deleteriously influence the structural integrity of the aluminum and complicate prognosis of the structural integrity of airframe components. In particular, nucleation of fatigue cracking during in-service cyclic loading is promoted by the presence of corrosion damage [4–8]. Several corrosion morphologies can form on the aluminum substructure based on the local chemistry, potential distribution and pH distribution along the geometry of the fastener hole [9]. The effect of these corrosion morphologies on the fatigue crack initiation location/life as well as their influence on the behavior of the fatigue crack growth is not fully understood [4,10].

1.1.1 AA 7xxx- Series Alloys

AA 7xxx series alloys (Al-Zn-Mg-Cu) are heat-treatable high strength aluminum alloys commonly used in aircraft components where strength and fatigue resistance are of primary importance [1,11]. AA 7075-T6 is a legacy alloy extensively used in aerospace application due to its high strength-to-weight-ratio, good machinability, and low cost, but suffers from intergranular stress corrosion cracking susceptibility [1,11]. AA 7050 was developed to address the required balance between strength and stress corrosion cracking resistance by increasing copper content and modifying the Zn/Mg ratio [1,11,12]. These changes in the composition affect the distribution and size of grain boundary precipitates and the width of the precipitate free zones in AA 7xxx [12,13]. AA 7050 has improved fracture toughness due to the substitution of 0.1%Zr for 0.2%Cr in AA 7075 [1,14]. Zr effectively prevents recrystallization and grain growth during subsequent thermomechanical processing leading to improved fracture toughness [1,12,14]. The nominal composition of AA 7050 is given in **Table 1.1** [1]. There are several secondary phase particles in AA 7050-T7451 including strengthening precipitates (5-10 nm), constituent particles (5-30 μm) and dispersoids (20-50 nm) [12,15]. The primary age hardening precipitate of AA 7050-T7451 is η-$MgZn_2$ with some η', while Al_2CuMg, Mg_2Si, Al_7Cu_2Fe are the common constituent particles in this alloy system, and dispersoids are mostly Al_3Zr [12,15].

Aside from compositional adjustments, alloy developers also improve the properties of AA 7xxx series alloys by heat treatment temper processes. T7451 is one of the common variants of AA 7050 temper treatment that improves the stress corrosion cracking resistance. T74 in the alloy designation represents overaging heat treatment, and the T-51 designation indicates that the alloy is stress relieved by stretching to ~2.3% during the temper process [16]. Pre-stretching in the temper process is done to relieve quench-induced internal stress that can result in the formation of coarse strengthening $MgZn_2$ (η) precipitates [16]. Thus, pre-stretching leads to slightly lower strength but an increase in fracture toughness [16]. **Figure 1.1** shows electron backscatter diffraction (EBSD) scans taken along different orientations in the current lot of material for AA 7050-T7451. Analysis of the grain size in accordance with ASTM E112 and E1382 reveals that grains in the L (rolling) direction ranges from 22 to 1230 μm, while the grains in the S (short transverse) direction and T (transverse) direction range from 12 to 112 μm, and from 14 to 264 μm respectively [17,18].

Table 1.1 Nominal Compisition of AA 7050 in wieght %[1]

Zn	**Mg**	**Cu**	**Zr**	**Fe**	**Si**	**Al**
6.2	2.25	2.3	0.1	0.15	0.12	Balance

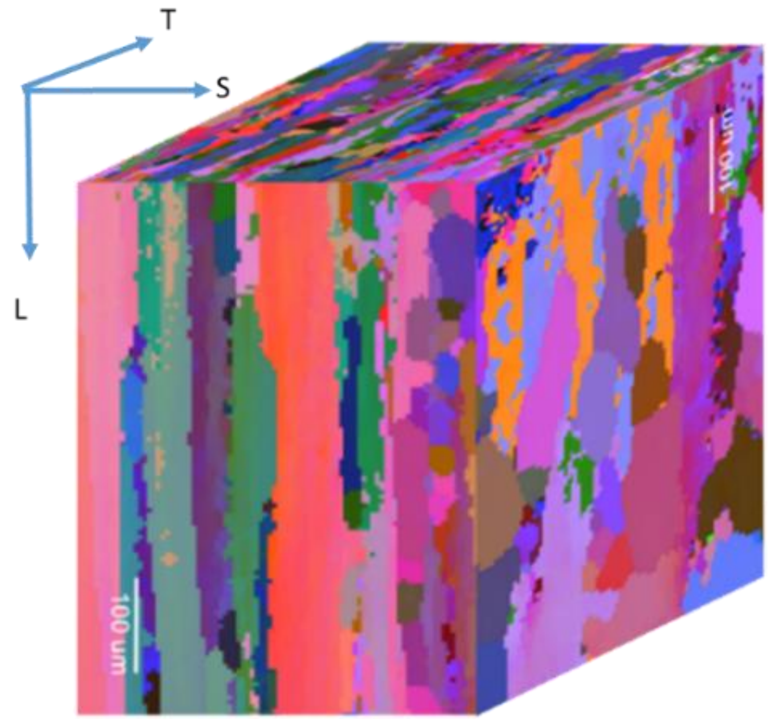

Figure 1.1 EBSD image representing microstructure of AA 7050-T7451 along different surfaces (TS, TL, LS). L is the rolling direction, S is the short transverse direction while T is the transverse direction.

Several studies have shown that the microstructure of aluminum alloys affect its fatigue crack initiation and fatigue crack growth behavior [15,19]. Fatigue cracks can form at regions where strain has become localized, this often occurs at heterogeneities in the alloy system, such as notches (e.g. mechanical flaw or corrosion pit), persistent slip bands (PSB), precipitate free zones, and/or constituent particles [15]. For specimens without corrosion damage, the most common fatigue crack initiating features are cracked coarse, brittle constituent particles, or the voids that nucleated because of the separation of these intermetallic particles with the aluminum matrix [15,20–23]. However, with the presence of corrosion damage on the surface of the alloy, reports show that fatigue crack tend to initiate at the corrosion damage [5,6,8,24–27].

The development of corrosion damage on the surface of aluminum is believed to initiate due to the breakdown of the passive film on the metal surface [28]. In AA 7050-T7451, this breakdown is greatly influenced by the heterogeneity of the alloy microstructure [29]. Some of the secondary particles (Al_7Cu_2Fe) are cathodic (noble) with respect to the Al-matrix [29–31], while others ($MgZn_2$) are anodic (active) with respect to the Al-matrix [29–31]. Two possible corrosion mechanisms, depending on the exposure environment, are discussed by Birbilis et al. for AA 7xxx, (1) the development of circumferential pits where attack mainly occurs on the matrix of aluminum in which secondary phase particles are more noble than the matrix; and (2) selective dissolution of the constituent particles where the secondary phase particles are more electrochemically active than the matrix [29]. According to Song et al, pitting and intergranular corrosion (IGC) are commonly seen on AA 7050-T7451 [13]. The formation of IGC is attributed to the $MgZn_2$ precipitates at the grain boundary resulting in preferential dissolution of the grain boundary [13]. AA 7xxx series alloy are also prone to exfoliation corrosion which is a type of corrosion that is relevant to the grains with large aspect ratio and subjected to environmental exposure [32,33]. This exfoliation corrosion results from subsurface (inter-granular) corrosion followed by grain lift out [32,33]. Subsequent heat treatment (e.g. T74) tends to increase the resistance of AA 7xxx series alloys to exfoliation corrosion [34].

In rolled AA 7xxx plates, secondary phase constituent particle stringers aligned in the L-direction are normally the preferred sites for localized corrosion due to galvanic coupling as previously discussed [22,29]. **Figure 1.2** and **Figure 1.3** show respectively the constituent particle size and density obtained for different polished surfaces of 50-mm thick AA 7050-T7451 sample at different location with respect to the plate thickness (t/0-surface of plate, t/8- 1/8 of thickness location, t/4- ¼ of thickness location and t/2- ½ of thickness location). These figures confirm the well-known metallurgical finding that the size and distribution of secondary phase varies along the thickness of the plate as well as at different faces/planes. **Figure 1.4** on the other hand represents the cumulative particle size for the LS surface of the AA 7050-T7451. These graphs show the heterogeneity of microstructure of AA 7050-T7451 with respect to the secondary phase particle size distribution and density. These data agree with previous findings for AA 7xxx. Zhang characterized the constituent particle populations in AA 7050-T7451 and generalized that the spatial distributions can be categorized as random [35] while Harlow reported the number of secondary phase particle density for AA 7075 greater than 1 μm^2 in size to be about 2000 per mm^2 [20,22]. Heterogeneity of secondary phase particle sizes and spatial distribution, coupled by environmental conditions within the fastener hole geometry can affect the corrosion morphology of AA 7050-T7451. A separate study, outside of the scope of this dissertation, is done to investigate the effects of the alloy microstructure and pH of electrolyte on the corrosion morphologies of AA 7050-T7451 [36]. However, the information about the secondary phase particle sizes and distribution are important and used to determine the fatigue specimen area for corrosion exposure.

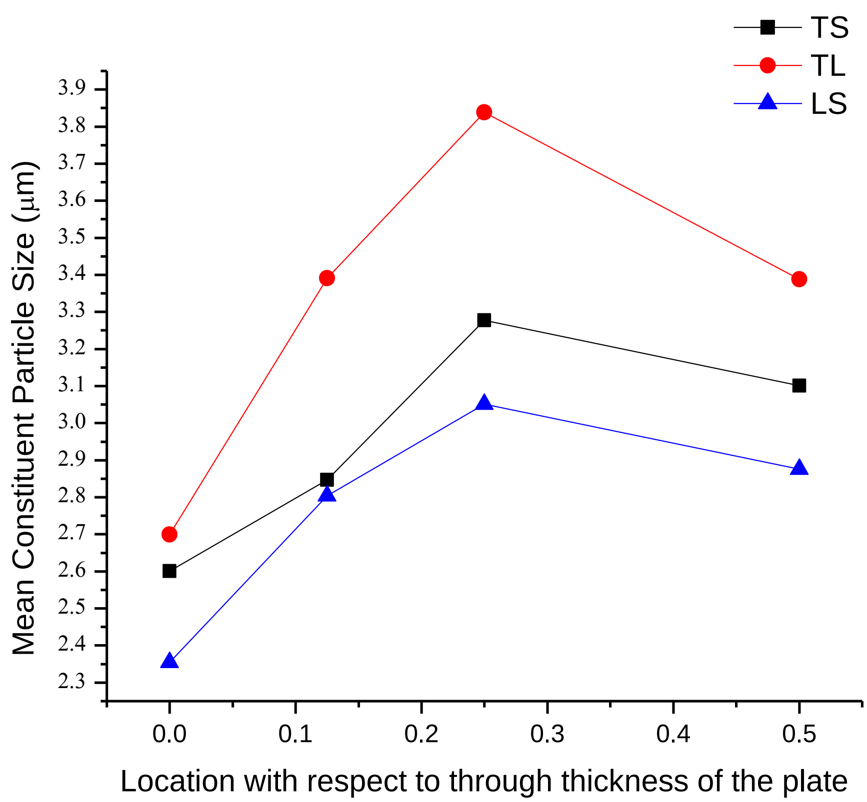

Figure 1.2 Average size of constituent particles along different surfaces (TS, TL, LS) at varying locations with respect to the thickness of the plate (t/0=surface of plate or point 0 in the graph, t/8= 1/8 of the plate or 0.11 in the graph, t/4= ¼ of the plate or 0.25 on the graph, t/2=1/2 of the plate or 0.5 on the graph). A 50-mm thick plate of AA 7050-T7451 is used in this constituent particles distribution analysis.

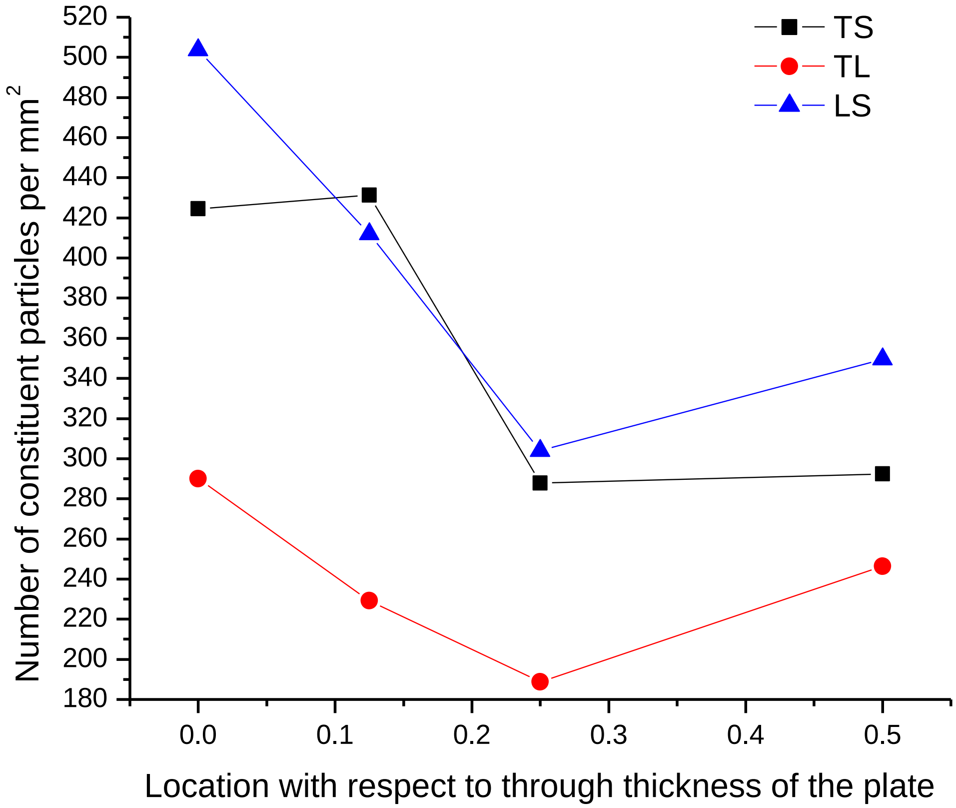

Figure 1.3 Density of constituent particles along different surfaces (TS, TL, LS) of AA 7050-T7451 at different locations with respect to the thickness of the plate (t/0=surface of plate or point 0 in the graph, t/8= 1/8 of the plate or 0.11 in the graph, t/4= ¼ of the plate or 0.25 on the graph, t/2=1/2 of the plate or 0.5 on the graph). A 50-mm thick plate of AA 7050-T7451 is used in this constituent particles distribution analysis.

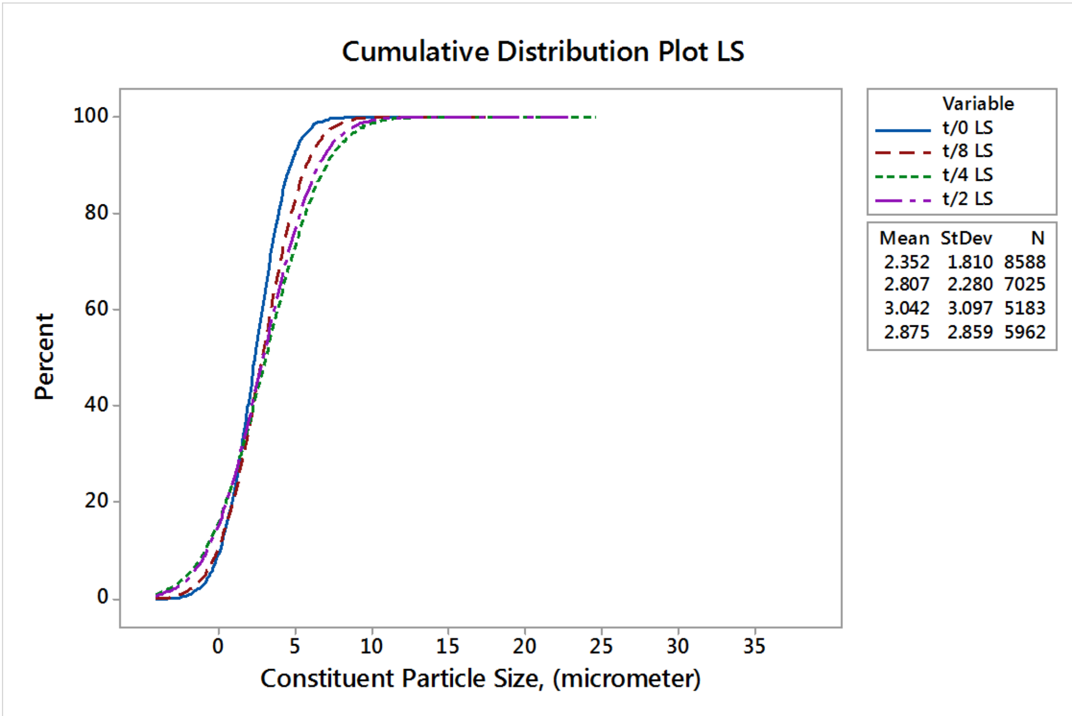

Figure 1.4 Cumulative distribution plot for the constituent particle size of AA 7050-T7451 LS surface at different locations with respect to the thickness of the plate (t/0=surface of plate, t/8= 1/8 of the plate, t/4= ¼ of the plate, t/2=1/2 of the plate). A 50-mm thick plate of AA 7050-T7451 is used in this constituent particles distribution analysis.

1.1.2 Galvanic Coupling of AA 7050-T7451 and Stainless Steel

It has been established that corrosion damage on the surface greatly affects the response of the aluminum substructure to cyclic loading and that microstructural heterogeneity of the aluminum alloy is responsible for the development of corrosion damage in the alloy matrix. However, the susceptibility of aluminum alloys to corrosion will critically depend on the external electrochemical conditions to which the system is exposed. Stainless steel fasteners are commonly used in complex aluminum aerospace structures which can lead to formation of galvanic couple. Furthermore, due to the higher local stress concentration at the fastener-hole, breakdown of barrier/coating system can be enhanced at these locations. During ground basing, aerospace structures can be subject to aggressive environment (e.g. salt aerosol deposition, thin film deliquescence, rain, salt water splashes, etc.) enabling the development of corrosion damage on the aluminum substructure (though growth of corrosion damage is often assumed to be minimal during in flight [37]). Therefore, when the protective coating system is compromised, chloride-containing electrolyte can get trapped in between the aluminum substructure and the stainless steel fastener leading to the setup of a galvanic couple. An electrochemical cell is complete when there is (1) an anode where the oxidation reaction occurs, (2) a cathode where the reduction reaction occurs, (3) an ionic path (such as an electrolyte), and (4) an electrical path in the system. According to the galvanic series in salt water, aluminum alloys have a more negative electrochemical potential (-1.0 to -0.6 V_{SCE}) than the stainless steel 316 (-0.5 to -0.3 V_{SCE}) [38]. As such the more active aluminum is the anode in the galvanic cell set-up, causing the formation of corrosion damage at the aluminum substructure. **Figure 1.5** provides a schematic representation of the typical fastener-hole configuration in aluminum substructure where electrolyte is present at the crevice.

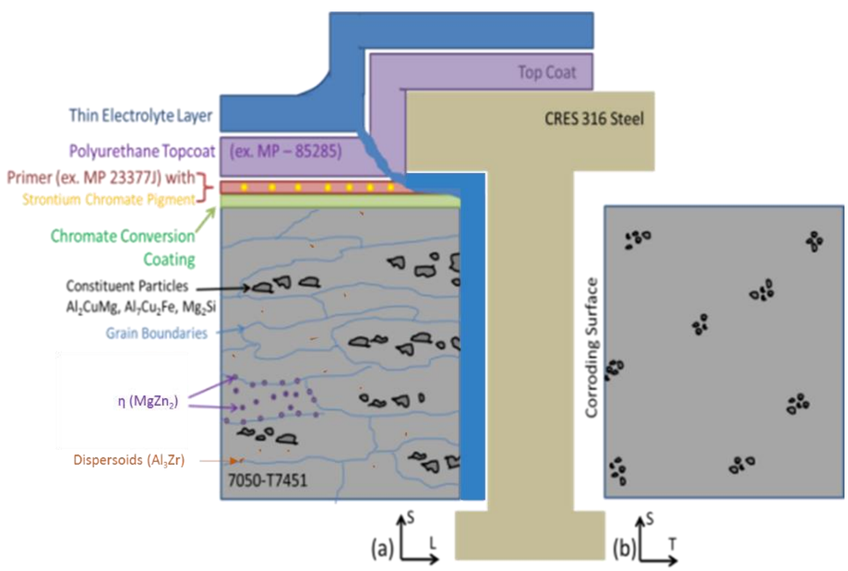

Figure 1.5 Schematic representation of fastener-hole configuration in AA 7050-T7451 substructure. The second phase particles present in AA 7050-T7451 are identified in the diagram.

The complexity of the fastener hole also affects the local electrochemical condition along the geometry of the fastener hole [9]. Locations at the mouth of the crevice will have a higher oxygen concentration while the portion of the crevice at the base of the fastener hole will have depleted oxygen concentration; these oxygen levels influence the electrochemical conditions. **Figure 1.6** shows the effect of varying oxygen concentration on the polarization scans of SS316 and AA 7050, the values of open circuit potentials (E_{OCP}) and corrosion current densities (i_{corr}) change for each individual alloy. This difference in oxygen concentration can then affect the corrosion mechanisms and ultimately the morphology of corrosion formed at different locations along the geometry of the fastener hole. Aside from these factors, the underlying heterogeneity (e.g. the through thickness variability of the particle distribution, **Figure 1.2-1.3**) of the AA 7050-T7451 microstructure can also affect the morphology of the damage on the surface of the aluminum substructure as it can interact with the local electrochemical conditions. Companion modeling [9] and experimental [30,31] studies look at the changes in the local chemistry along the geometry of the fastener hole and the corresponding corrosion morphology that develops based on the local environment. While these studies are outside the scope of the current effort, they clearly establish that geometry and microstructure induced changes in the electrochemical conditions can lead to variation in the morphology of the corrosion damage. It is the goal of the current work to determine how such variations impact the fatigue behavior which is a design/structure management critical property for these applications.

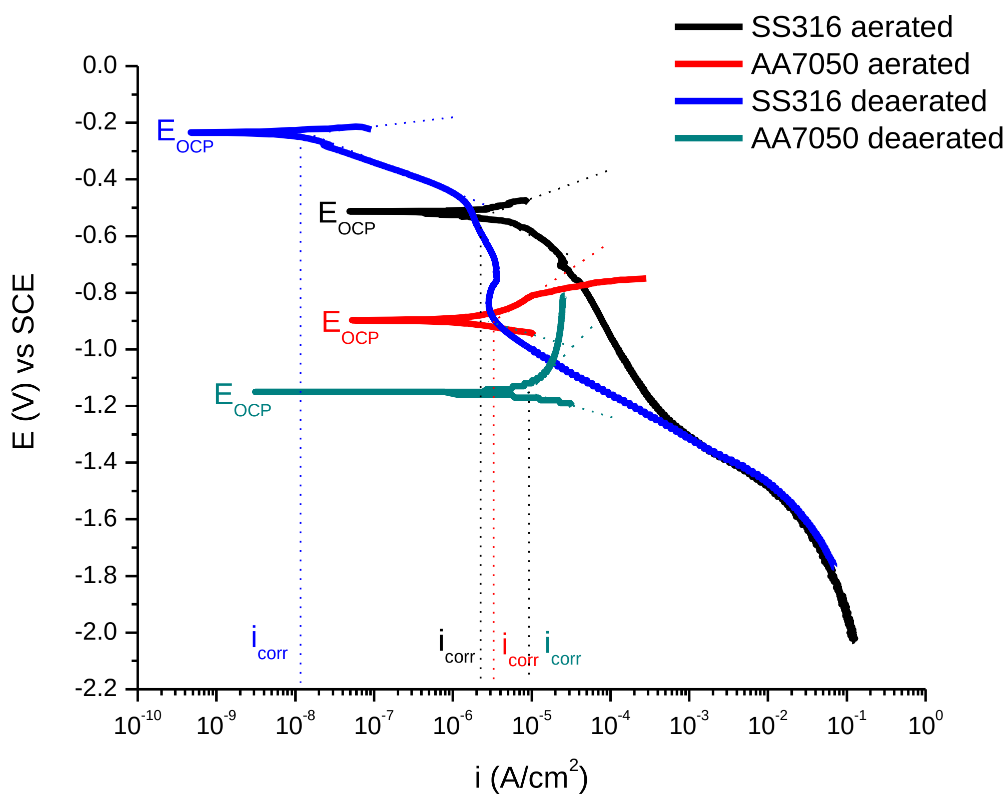

Figure 1.6 Polarization scans of SS316 and AA 7050 under aerated and deaerated conditions using 4M NaCl with pH of 9 (Plot obtained from unpublished works of V. Rafla)

1.1.3. Corrosion Fatigue in Aerospace Aluminum Alloys

The interaction of corrosion damage and cyclic loading is a critical issue in the context of aerospace structural integrity [26]. In a recent teardown reported by the US Air Force Academy (USAFA), 80% of fatigue cracks formed at regions of corrosion damage and only 20% formed at regions of mechanical damage [8]. In a laboratory setting, several authors report that corrosion damage reduces the total fatigue life of aluminum alloys [5,26,39–41]. One important finding on the effect of corrosion on total fatigue life was described by Burns et al. which indicated that following a sharp initial degradation, the reduction in the total fatigue life becomes nearly independent of the corrosion exposure time (e.g. extent of corrosion damage) [40].

Researchers have proposed a variety of different linear elastic fracture mechanics (LEFM) techniques to predict total fatigue life of specimens with corrosion damage on the surface of aluminum alloys [5,40–43]. However, such LEFM modeling only predicts the long crack propagation regime, whereas the corrosion nucleated fatigue cracking consists of four broad stages. Specifically, (1) corrosion damage formation, (2) nucleation (initiation) of cracks from the corrosion damage (i.e. pit-to-crack or corrosion-to-crack transition), (3) small fatigue crack growth that is influenced by the local corrosion and microstructure, and (4) long crack growth that is well described by continuum LEFM approaches [26,44,45]. Corrosion damage formation and long fatigue crack growth in different alloys have been widely investigated in conjunction with the corresponding alloy development [14,46–49]. While other complicating phenomenon are possible (corrosion induced blunting during ground basing, corrosion product in the crack wake, etc), initial attempts at modeling service life of aerospace structures typically assume that corrosion develops between flights and cyclic loading happens during flights [50]. As such, the current effort will focus on the effect of corrosion that is induced prior to fatigue loading [6].

Despite the extensive research on corrosion fatigue, a systematic, high-fidelity study of the transition from corrosion to an active crack has not been performed for a wide range of relevant corrosion morphologies [51]. Generally, researchers have attempted to correlate macro-scale corrosion features (corrosion damage depth, pit density, pit surface area, etc.) with fatigue crack formation site [4,5,39–41,52–54]. However, the interaction of these corrosion damage features and high fidelity validation of these parameters via comparison to actual crack formation locations and fatigue lives have not been studied in detail [39]. Burns et al. demonstrated that the total fatigue life becomes independent on the corrosion exposure time (depth of corrosion damage) after a sharp initial degradation, however this study did not provide a detailed characterization of the features governing crack formation [40]. Conversely, more recent studies have performed high fidelity characterization of the corrosion to crack transition, but these studies were narrowly focused on isolated laboratory [5,10,40,41,51,55] or field [50] corrosion morphologies. Specifically, Turnbull studied pit-to-crack (corrosion-to-crack) transition involving smooth pits in turbine steel and reported that macro-scale stress/strain states governed the location of fatigue initiation [56]. On the other hand, Burns et al. showed that micro-topographical features associated with the pit in aluminum alloys tend to dominate the location of fatigue initiation sites [4,40]. *In toto*, the literature demonstrates that the morphology of the corrosion damage can potentially lead to changes in the mechanisms that govern crack formation. As such, in order to develop models that accurately capture the remaining life of a component exposed to a galvanic couple, it is necessary to understand the factors that govern the corrosion to crack transition for relevant corrosion morphologies.

Aside from the effects of alloy microstructure and corrosion damage feature/morphology on the fatigue initiation, their influence on microstructurally small crack (MSC) growth rates have also been reported. Burns et al. reported that high initial fatigue crack growth rate (low initiation life) in AA 7075-T651 is due to the zone of influence of the pit precursor having locally high plastic strains coupled with subsurface constituent interaction [4,5,21,57,58]. The MSC growth rate fluctuates as it moves away from the corrosion damage and encounters microstructural barriers which can impact crack propagation such as grain boundaries and secondary phase particles [4,19,45,58–60]. MSC growth rate is typically faster than long crack data and the concept of LEFM, particularly the Paris law (Equation 1.1 where da/dN represents crack growth, C and m are material properties, ΔK is the stress intensity range) fails to correlate with MSC growth rate [57,58,61,62]. While such small crack complexities have been recognized for a long time [58], the magnitude of the relative effect of the local stress gradient proximate to varying corrosion damage features on the overall life has not been systematically investigated.

$$\frac{da}{dN} = C\Delta K^{m} \qquad \textit{Equation 1.1}$$

1.2 Knowledge Gaps

A literature review of corrosion nucleated fatigue in aerospace aluminum structures has identified the following knowledge gaps:

- A systematic and quantitative investigation of the effect of realistic corrosion morphologies (resulting from an aluminum-stainless steel galvanic couple) on the fatigue crack initiation and fatigue crack growth behavior is lacking

- A high fidelity analysis of the macro- and micro-scale corrosion and/or microstructural features that govern/correlate to the location of fatigue crack initiation and small crack growth behavior from such galvanically-induced corrosion is lacking

1.3 Objective Statements

The main goal of this dissertation is to investigate the fatigue crack formation and fatigue crack behavior of pre-corroded AA 7050-T7451 having vastly different corrosion morphologies representative of fastener-hole configuration wherein aluminum is galvanically coupled with stainless steel. The objectives of the dissertation are systematically addressed in the following tasks which will be described in the corresponding chapters:

- Determine the effects of corrosion morphology on fatigue behavior by (1) quantification of initiation, propagation, total life and MSC growth rates, (2) correlation of macro-scale corrosion metrics and crack formation location; Understand the influence of relative humidity and applied σ_{max} on observed trends in macro-scale corrosion effects on fatigue initiation and fatigue behavior

- Correlate the crack formation with the micro-scale corrosion morphology and microstructure (location/size of constituent particles and grain size/orientation) of the alloy

- Evaluate the combined effects of corrosion morphology and alloy microstructure on the location of fatigue crack formation

1.4 Thesis Organization

This dissertation is divided into 6 chapters (Chapter 1: Introduction; Chapter 2: Macro-Scale Feature Analysis; Chapter 3: Micro-Scale Feature Analysis; Chapter 4: Feature Interaction Analysis; Chapter 5: Summary/Conclusions; Chapter 6: Future Works).

- Chapter 2 Section 1 provides a summary of findings from the published works on the macro-scale (> 250 μm) corrosion feature effects on fatigue initiation and fatigue behavior of AA 7050-T7451. This section presents the important methods, results and take-aways; a published literature paper is provided in Section 2 for more details. Section 3 deals with the effect of relative humidity, high σ_{max} and severe corrosion morphologies on fatigue initiation and fatigue behavior of AA 7050-T7451.
- Chapter 3 presents the effects of micro-scale (< 250 μm) corrosion feature and alloy microstructure on fatigue initiation of AA 7050-T7451.
- Chapter 4 Section 1 provides an overview of findings for the interaction analysis of the macro-scale features using data science methods. A literature paper that is published is provided in Section 2 to give further details of this work. Section 3 presents the results of the analysis of corrosion morphologies and alloy microstructure interaction measured in terms of Fatigue Indicator Parameters determined by crystal plasticity modeling. This analysis was performed in collaboration with Purdue University.
- Chapter 5 provides the summary of conclusions from the main chapters.
- Chapter 6 enumerates the future works for this study

1.5 References

[1] Starke EA, Staley JT. Application of modern aluminum alloys to aircraft. Progr Aerosp Sci 1996;32:131–72.

[2] Campbell F. Manufacturing Technology for Aerospace Structural Materials.

Manuf. Technol. Aerosp. Struct. Mater., Elsevier; 2006, p. 15–92. doi:10.1016/B978-185617495-4/50002-0.

[3] Peters M, Leyens C. Aerospace and Space Materials. Mater Sci Eng n.d.;III:1–11.

[4] Burns JT, Larsen JM, Gangloff RP. Effect of initiation feature on microstructure-scale fatigue crack propagation in Al-Zn-Mg-Cu. Int J Fatigue 2012;42:104–21. doi:10.1016/j.ijfatigue.2011.08.001.

[5] Burns JT, Larsen JM, Gangloff RP. Driving forces for localized corrosion-to-fatigue crack transition in Al-Zn-Mg-Cu. Fatigue Fract Eng Mater Struct 2011;34:745–73. doi:10.1111/j.1460-2695.2011.01568.x.

[6] Sankaran KK, Perez R, Jata KV. Effects of pitting corrosion on the fatigue behavior of aluminum alloy 7075-T6: modeling and experimental studies. Mater Sci Eng A 2001;297:223–9. doi:10.1016/S0921-5093(00)01216-8.

[7] Gruenberg KM, Craig BA, Hillberry BM, Bucci RJ, Hinkle AJ. Predicting fatigue life of pre-corroded 2024-T3 aluminum. Int J Fatigue 2004;26:629–40. doi:10.1016/j.ijfatigue.2003.10.011.

[8] Shoales GA, Fawaz SA, Walters MR. Compilation of damage findings from multiple recent teardown analysis programs. Bridg. Gap between Theory Oper. Pract. 25th ICAF Symp., Rotterdam, The Netherlands: Springer; 2009, p. 187–207. doi:10.1007/978-90-481-2746-7_11.

[9] Liu C, Rafla VN, Scully JR, Kelly RG. Mathematical modeling of potential and current distributions for atmospheric corrosion of galvanic coupling in airframe components. Corros. 2015, Dallas, Texas: NACE International; 2015.

[10] Turnbull A, McCartney LN, Zhou S. A model to predict the evolution of pitting corrosion and the pit-to-crack transition incorporating statistically distributed input parameters. Corros Sci 2006;48:2084–105. doi:10.1016/j.corsci.2005.08.010.

[11] Dursun T, Soutis C. Recent developments in advanced aircraft aluminium alloys. Mater Des 2014;56:862–71. doi:10.1016/j.matdes.2013.12.002.

[12] Dixit M, Mishra RS, Sankaran KK. Structure–property correlations in Al 7050 and Al 7055 high-strength aluminum alloys. Mater Sci Eng A 2008;478:163–72. doi:10.1016/j.msea.2007.05.116.

[13] Song FX, Zhang XM, Liu SD, Han NM, Li DF. Anisotropy of localized corrosion in 7050-T7451 Al alloy thick plate. Trans Nonferrous Met Soc China (English Ed 2013;23:2483–90. doi:10.1016/S1003-6326(13)62758-2.

[14] Sanders RE, Starke EA. The effect of intermediate thermomechanical treatments

on the fatigue properties of a 7050 aluminum alloy. Metall Trans A 1978;9:1087–100. doi:10.1007/BF02652213.

[15] Telesman J. Review of the Effects of Micro structure on Fatigue in Aluminum Alloys. 1984.

[16] Han N, Zhang X, Liu S, Ke B, Xin X. Effects of pre-stretching and ageing on the strength and fracture toughness of aluminum alloy 7050. Mater Sci Eng A 2011;528:3714–21. doi:10.1016/j.msea.2011.01.068.

[17] ASTM International. ASTM E112 Standard Test Methods for Determining Average Grain Size. 2013.

[18] ASTM International. ASTM E1382 Standard Test Methods for Determining Average Grain Size Using Semiautomatic and Automatic Image Analysis. 2010.

[19] Davidson DL, Lankford J. The Effects of Aluminum Alloy Microstructure on Fatigue Crack Growth. Mater Sci Eng 1985;74:189–99.

[20] Harlow DG, Nardiello J, Payne J. The effect of constituent particles in aluminum alloys on fatigue damage evolution: Statistical observations. Int J Fatigue 2010;32:505–11. doi:10.1016/j.ijfatigue.2009.02.036.

[21] Bozek JE, Hochhalter JD, Veilleux MG, Liu M, Heber G, Sintay SD, et al. A geometric approach to modeling microstructurally small fatigue crack formation: I. Probabilistic simulation of constituent particle cracking in AA 7075-T651. Model Simul Mater Sci Eng 2008;16:65007. doi:10.1088/0965-0393/16/6/065007.

[22] Harlow DG, Wei RP. Probability modeling and material microstructure applied to corrosion and fatigue of aluminum and steel alloys. Eng Fract Mech 2009;76:695–708. doi:10.1016/j.engfracmech.2008.01.010.

[23] Weiland H, Nardiello J, Zaefferer S, Cheong S, Papazian J, Raabe D. Microstructural aspects of crack nucleation during cyclic loading of AA7075-T651. Eng Fract Mech 2009;76:709–14. doi:10.1016/j.engfracmech.2008.11.012.

[24] Mcintyre P, Trant PJ. Fatigue-crack initiation at corrosion pits. Met Technol 1982;9:135–42.

[25] Barter SA, Molent L. Fatigue cracking from a corrosion pit in an aircraft bulkhead. Eng Fail Anal 2014;39:155–63. doi:10.1016/j.engfailanal.2014.01.020.

[26] Sabelkin V, Perel VY, Misak HE, Hunt EM, Mall S. Investigation into crack initiation from corrosion pit in 7075-T6 under ambient laboratory and saltwater environments. Eng Fract Mech 2015;134:111–23. doi:10.1016/j.engfracmech.2014.12.016.

[27] Hoeppner DW, Taylor AMH. Chapter 13 –Modeling pitting corrosion fatigue: pit growth and pit/crack transition issues. RTO-AG-AVT-140 Corros. Fatigue Environ. Assist. Crack. Aging Mil. Veh., 2011, p. 1–20.

[28] Liao CM, Olive JM, Gao M, Wei RP. In-Situ Monitoring of Pitting Corrosion in Aluminum Alloy 2024. CORROSION 1998;54:451–8. doi:10.5006/1.3284873.

[29] Birbilis N, Buchheit RG. Electrochemical characteristics of intermetallic phases in aluminum alloys. J Electrochem Soc 2005;152:B140–51. doi:10.1149/1.1869984.

[30] Rafla VN, Davenport A, Scully JR. Determination of Cathodic and Anodic Charge from Operando X-Ray Tomography Observation of Galvanic Corrosion of Aluminum Alloy 7050-T7451 and 304 Stainless Steel in a Simulated Fastener. CORROSION 2015;71:1300–3. doi:10.5006/1871.

[31] Rafla VN, King AD, Glanvill S, Parsons A, Davenport A, Scully JR. Operando Observation of Galvanic Corrosion Between Aluminum Alloy 7050-T7451 and 304 Stainless Steel in a Simulated Fastener Arrangement Using X-Ray Tomography. CORROSION 2015;71:1171–6. doi:10.5006/1813.

[32] Marlaud T, Malki B, Deschamps A, Reboul M, Baroux B. Electrochemical testing of exfoliation corrosion sensitivity of aluminium alloys 2006;3 (31):285–93. doi:10.1149/1.2789235.

[33] Davis JR. Corrosion of Aluminum and Aluminum Alloys (#06787G). ASM Int 1999:1–10.

[34] Lee S, Lifka BW. Modification of the EXCO test method for exfoliation susceptibility in 7xxx, 2xxx and aluminium-lithium alloys 1992:1–19.

[35] Zhang J, Przystupa MA, Luévano AJ. Characterizations of pore and constituent particle populations in 7050-T7451 aluminum plate alloys. Metall Mater Trans A 1998;29:727–37. doi:10.1007/s11661-998-0263-2.

[36] Rafla VN. Unpublished Works. University of Virginia, 2018.

[37] Medved JJ, Breton M, Irving PE. Corrosion pit size distributions and fatigue lives - A study of the EIFS technique for fatigue design in the presence of corrosion. Int J Fatigue 2004;26:71–80. doi:10.1016/S0142-1123(03)00069-0.

[38] Jones DA. Principles and Prevention of Corrosion. Prentice Hall; 1996.

[39] Jones K, Hoeppner DW. Pit-to-crack transition in pre-corroded 7075-T6 aluminum alloy under cyclic loading. Corros Sci 2005;47:2185–98. doi:10.1016/j.corsci.2004.10.004.

[40] Burns JT, Kim S, Gangloff RP. Effect of corrosion severity on fatigue evolution in

Al-Zn-Mg-Cu. Corros Sci 2010;52:498–508. doi:10.1016/j.corsci.2009.10.006.

[41] Kim S, Burns JT, Gangloff RP. Fatigue crack formation and growth from localized corrosion in Al-Zn-Mg-Cu. Eng Fract Mech 2009;76:651–67. doi:10.1016/j.engfracmech.2008.11.005.

[42] Burns JT, Gangloff RP. Scientific advances enabling next generation management of corrosion induced fatigue. Procedia Eng 2011;10:362–9. doi:10.1016/j.proeng.2011.04.062.

[43] Gangloff RP, Burns JT, Kim S. Laboratory characterization and fracture mechanics modeling of corrosion-fatigue interaction for aluminum alloy substitution. Final Report, Contract F09650-03-D-0001, WPAFB. OH: 2005.

[44] Donahue JR, Burns JT. Effect of chloride concentration on the corrosion–fatigue crack behavior of an age-hardenable martensitic stainless steel. Int J Fatigue 2016;91:79–99. doi:10.1016/j.ijfatigue.2016.05.022.

[45] Turnbull A. The environmentally small/short crack growth effect: current understanding. Corros Rev 2012;30:1–17. doi:10.1515/corrrev-2012-0003.

[46] Schubbe JJ. Fatigue crack propagation in 7050-T7451 plate alloy. Eng Fract Mech 2009;76:1037–48. doi:10.1016/j.engfracmech.2009.01.006.

[47] Wang YL, Pan QL, Wei LL, Li B, Wang Y. Effect of retrogression and reaging treatment on the microstructure and fatigue crack growth behavior of 7050 aluminum alloy thick plate. Mater Des 2014;55:857–63. doi:10.1016/j.matdes.2013.09.063.

[48] Hou W, Ji W, Zhang Z, Xie J, Cheng X. The effect of homogenization temperature on the corrosion resistance of extruded 7050 Al-alloy bars. J Mater Process Technol 2014;214:635–40. doi:10.1016/j.jmatprotec.2013.11.009.

[49] Ou BL, Yang JG, Wei MY. Effect of homogenization and aging treatment on mechanical properties and stress-corrosion cracking of 7050 alloys. Metall Mater Trans A Phys Metall Mater Sci 2007;38:1760–73. doi:10.1007/s11661-007-9200-z.

[50] McMurtrey MD, Bae D, Burns JT. Fracture mechanics modelling of constant and variable amplitude fatigue behaviour of field corroded 7075-T6511 aluminium. Fatigue Fract Eng Mater Struct 2017;40:605–22. doi:10.1111/ffe.12536.

[51] Turnbull A. Corrosion pitting and environmentally assisted small crack growth. Proc R Soc A Math Phys Eng Sci 2014;470:20140254. doi:10.1098/rspa.2014.0254.

[52] van der Walde K, Hillberry BM. Initiation and shape development of corrosion-nucleated fatigue cracking. Int J Fatigue 2007;29:1269–81. doi:10.1016/j.ijfatigue.2006.10.010.

[53] van der Walde K, Hillberry BM. Characterization of pitting damage and prediction of remaining fatigue life. Int J Fatigue 2008;30:106–18. doi:10.1016/j.ijfatigue.2007.02.020.

[54] van der Walde K, Brockenbrough JR, Craig BA, Hillberry BM. Multiple fatigue crack growth in pre-corroded 2024-T3 aluminum. Int J Fatigue 2005;27:1509–18. doi:10.1016/j.ijfatigue.2005.06.026.

[55] Zhou, Turnbull. Influence of pitting on the fatigue life of a turbine blade steel. Fatigue Fract Eng Mater Struct 1999;22:1083–93. doi:10.1046/j.1460-2695.1999.00226.x.

[56] Turnbull A. Characterising the pit to crack transition. Annu. Conf. Australas. Corros. Assoc. 2012, Melbourne, Victoria, Australia: 2012, p. 139–45.

[57] Rios ERDL, Xin XJ, Navarro a. Modelling Microstructurally Sensitive Fatigue Short Crack Growth. Proc R Soc A Math Phys Eng Sci 1994;447:111–34. doi:10.1098/rspa.1994.0131.

[58] Ritchie RO, Lankford J. Small fatigue cracks: A statement of the problem and potential solutions. Mater Sci Eng 1986;84:11–6. doi:10.1016/0025-5416(86)90217-X.

[59] Spear AD, Li SF, Lind JF, Suter RM, Ingraffea AR. Three-dimensional characterization of microstructurally small fatigue-crack evolution using quantitative fractography combined with post-mortem X-ray tomography and high-energy X-ray diffraction microscopy. Acta Mater 2014;76:413–24. doi:10.1016/j.actamat.2014.05.021.

[60] Lankford J. The growth of small fatigue cracks in 7075-T6 Aluminum. Fatigue Eng Mater Struct 1982;5:233–48.

[61] Pearson S. Initiation of fatigue cracks in commercial aluminium alloys and the subsequent propagation of very short cracks. Eng Fract Mech 1975;7:235–47. doi:10.1016/0013-7944(75)90004-1.

[62] Suresh S, Ritchie RO. Propagation of short fatigue cracks. Int Met Rev 1984;29:445–76. doi:10.1179/imtr.1984.29.1.445.

2. Effect of Macro-Scale Corrosion Features

2.1 Overview

In order to understand the effects of macro-scale (> 250 μm) corrosion feature parameters to the fatigue behavior and systematically correlate these parameters to the fatigue formation location, four different corrosion morphologies are considered in this study such as discrete pit (shallow DP1 and deep DP2), general corrosion with surface recession (GCSR) and fissures (FIS). These morphologies represent the damage relevant to galvanic coupling of aerospace aluminum with stainless steel fastener. It is hypothesized that the fatigue crack initiation can be found at the location with the most severe corrosion damage feature. The severity of corrosion damage feature is represented by the level of pit/fissure depth/size for DP and FIS specimens, or by the level of roughness metrics for GCSR specimens.

The specimens are exposed to different electrochemical environment to artificially create corrosion damage of different shapes on the LS surface of the fatigue samples. The corrosion products are removed from the specimen using HNO_3. The specimens are cleaned by sonication in DI water and in acetone and then in methanol. Prior to fatigue testing, images of the corrosion damage are taken using white light interferometry (WLI) and optical microscope. The specimens are loaded along the L-direction with σ_{max} of 200 MPa, R of 0.5 and frequency of 20 Hz. The relative humidity (> 90%) is controlled using a Plexiglass chamber during the entire fatigue test. A special loading protocol is used to create the marker bands on the fracture surface. These marker bands are used to determine the fatigue initiation location, the fatigue initiation life to create a 10 μm crack from the formation site, and the crack growth rates. X-ray computed tomography (XCT) and scanning electron microscope (SEM) are used for post-test characterization.

Different corrosion metrics are evaluated for different corrosion morphologies. For DP1 and DP2, the following metrics are analyzed: pit depth, pit volume, surface area of the pit mouth, pit diameter and pit density. Additional metrics are analyzed for DP1 and DP2 for the line profile analysis in order to understand the effects of coplanar pits on fatigue initiation. The line profile analysis is done to correspond to the planes perpendicular to the loading direction. The metrics considered are namely the number of pits per line, the total depth of pits per line, average depth of pits per line. The metrics analyzed for FIS specimens are fissure depth, total fissure depth per plane, number of fissures per plane, average fissure depth per plane. On the other hand, the roughness metrics are considered for GCSR specimens. The corroded area for GCSR is divided in to smaller regions of 500 μm × 500 μm. The metrics considered are the root mean square (RMS), peak density, maximum valley depth, maximum peak height, average roughness, and texture aspect ratio. Results show that amongst all the macro-scale corrosion metrics analyzed for fissure morphology, the planes with high total fissure depth and high number of fissures tend to preferentially form fatigue crack. The other individual macro-scale corrosion metrics for DP1, DP2, GCSR and FIS do not strongly correlate to fatigue crack formation location.

The presence of corrosion damage on the AA 7050-T7451 greatly reduced the total fatigue life. Results also show that the initiation life for different corrosion morphologies are almost negligible and relatively constant. Furthermore the crack growth rates of the specimens with different corrosion morphologies converge to similar values as the crack extends away from the initiation point. The slight decrease in the total life as the damage size increases are attributed to the increase in the number of crack formation sites and the larger crack initiation feature which decrease the crack propagation length necessary to reach the critical crack size. The overarching finding from this aspect of the work is that the macro-features are not sufficient to uniquely identify the crack formation location; full details of this analysis are reported in a literature paper that is presented in Chapter 2 Section 2.

Section 3 of this chapter extends the analysis to different relevant corrosion morphologies, stress levels, and loading environments to test the extent to which these conclusions can be generalized. It is hypothesized that for the additional corrosion morphologies, the macro-scale corrosion damage features do not dictate the location of the fatigue initiation. The additional morphologies considered are the cigar-shaped pit and the intergranular corrosion (IGC) damage. These additional morphologies are classified as corrosion damage representative of the results when AA 7050-T7451 is coupled with stainless steel 316. The corrosion metrics considered for cigar-shaped pits are similar to those that are considered for DP specimens, while the corrosion metrics used for IGC are similar to those that are used for FIS specimens. The two stress (σ_{max}) levels considered in this section are 200 MPa and 300 MPa. The environment is also varied in terms of the % relative humidity, one exposure is at < 5% RH while the other exposure is at > 90% RH. The number of initiation points, the initiation life and total fatigue life, as well as the crack growth rates are compared for the specimens tested. Results show that conclusions drawn from the initial macro-scale feature analysis can be extended to other corrosion morphologies. Results also show that the change in stress levels and environment mainly affects the crack growth rate of the specimens.

Further analysis of the contribution of the corrosion damage micro-scale features and underlying microstructure are presented in Chapter 3 to comprehend the effects of these factors to the fatigue crack formation location. Rigorous analysis of the combined effects of the macro-scale corrosion metrics is also necessary since these metrics are considered individually and only a crude determination of combined effects is done in Chapter 2. The more rigorous approach for the combined effects analysis is described in Chapter 4.

2.2. Effects of Macro-scale Corrosion Damage Feature on Fatigue Crack Initiation and Fatigue Behavior

2.2.1 Introduction

Aluminum alloys are widely used in the aerospace industry due their high strength-to-weight ratio [1,2]. However high strength aerospace alloys are prone to localized corrosion and a recent US Air Force airframe teardown analysis shows 80% of fatigue cracks formed at such corrosion damage [3]. This interaction of corrosion damage developed during ground-basing with aircraft operational loading has a deleterious effect on fatigue life and has been extensively documented in failure analyses of airframe components [3–7]. Substantial research has been performed on corrosion development in aerospace components [8–11], empirical characterization of the detrimental influence on fatigue behavior [6,7,12–19], engineering scale modeling of the pit-to-crack transition [20–23], and incorporating corrosion damage into a life prediction framework [12,14,17,24–

28]. Furthermore, recent micro-scale characterization provided insight into the corrosion features that govern crack formation [18]. However, significant mechanistic and logistical challenges remain concerning the linkage of micro-scale damage mechanisms to enable next generation prognosis techniques to predict the remaining useful life of a corroded component.

Aggressive basing environments enhance the development of corrosion, making the corrosion-fatigue interaction acutely pertinent to the structural integrity of airframes based in sea-coast or marine environments [4,5,25,29,30]. During basing in marine environments, splash, rain water or salt enabled deliquescence can establish a local chloride-containing electrolyte [4,5,25,29,30]. Defects in the corrosion protection system are common and inevitable due to the intense operating/maintenance conditions and are likely enhanced at complex component joining/fastener locations. Furthermore, the geometry of faying surface and fastener holes inherently aids trapping/wicking of the electrolyte into tight crevices typical of these component joining locations. This leads to a severe occluded local environment where a galvanic cell can be established between the aerospace aluminum component and a high strength fasteners (typically stainless steels) causing localized corrosion of the Al component. In the context of structural integrity, such galvanically induced localized corrosion damage enhances the already high inherent stress concentration associated with a fastener hole. The geometry of fastener hole will also result in variation of the local electrochemical condition of along the depth of the hole [31]. Locations at the mouth of the crevice will have a higher oxygen concentration while the portion of the crevice at the base of the fastener hole will have depleted oxygen concentration. This gradient of electrochemical conditions along the geometry of the fastener hole can alter the corrosion mechanisms and ultimately result in variations of the corrosion morphology along the depth of the fastener hole. The current effort will leverage companion modeling and experimental studies that are probing the variation in corrosion morphology associated with such geometry induced electrochemical variations for AA 7050-T7451 [31–33].

The development of corrosion damage on the surface of aluminum is believed to initiate due to the breakdown of the passive film which is greatly influenced by the heterogeneity of the alloy microstructure [8–10,34]. The common aerospace alloy AA 7050-T7451 (Al-Zn-Mg-Cu; used in upper wing skins, fuselage stiffeners, bulkheads, floor beams, etc.) is considered in the current study. AA 7xxx-series alloys contain three broad types of second phase particles; strengthening precipitates ($MgZn_2$ 5-10 nm; semi-coherent η' and incoherent η), dispersoids (e.g. Al_3Zr; 20-50 nm) to control grain size and recrystallization, and coarse (5-30 µm) constituent particles (e.g. Al_2CuMg – *s*, Al_7Cu_2Fe – β, and Mg_2Si) which become aligned in stringers parallel to the rolling axis [35–42]. It is well documented that constituent particles are dominant sites for local corrosion due to their size and local electrochemical characteristics [10,35,43]. As such, the constituent size and spacing are of critical importance and have been extensively characterized [44]. Some constituent particles (Al_7Cu_2Fe) are cathodic (noble) with respect to the Al-matrix [10,32], while others ($MgZn_2$) are anodic (active) with respect to the Al-matrix [10,32]. Two possible corrosion mechanisms, depending on the exposure environment are discussed by Birbilis et al. for AA 7xxx, (1) the development of circumferential pits where attack mainly occurs on the matrix of aluminum in which secondary phase particles are more noble than the matrix; and (2) selective dissolution of the constituent particles where the secondary phase particles are more electrochemically active than the matrix [10]. In rolled AA 7xxx plates, secondary phase constituent particle stringers aligned in the L-direction and can be preferentially located at various through thickness locations of a plate [44]. The progression and morphology of the corrosion damage, and thus the impact on structural integrity, will be governed by the local galvanic coupling between the steel and Al components and the interaction with the local microstructure features.

While other complicating phenomenon are possible (corrosion induced blunting during ground basing, corrosion product in the crack wake, etc.), initial attempts at modeling service life of corroded aerospace structures typically assume that corrosion develops between flights and cyclic loading happens during flights [16,45,46]. As such, the current effort will focus on the effect of corrosion that is induced prior to fatigue loading. Corrosion nucleated fatigue cracking consists of four broad stages. Specifically, (1) corrosion damage formation, (2) nucleation (initiation) of cracks from the corrosion damage (i.e. pit-to-crack or corrosion-to-crack transition), (3) small fatigue crack growth that is influenced by the local corrosion and microstructure, and (4) long crack growth that is well described by continuum approaches [47–49]. Despite the extensive research on corrosion fatigue, a systematic, high-fidelity study of the transition from corrosion to an active crack has not been performed for a wide range of corrosion morphologies [50]. Generally, researchers have attempted to correlate macro-scale (> 250μm) corrosion features (corrosion damage depth, pit density, pit surface area, etc.) with fatigue crack formation sites [17–20,28,48,50–55]. However, the interaction of these corrosion damage features and validation of these parameters via comparison to actual crack formation locations, fatigue initiation lives, and total lives have not been performed. For example, Burns et al. demonstrated that the total fatigue life becomes independent on the corrosion exposure time (depth of corrosion damage) after a sharp initial degradation, however this study did not provide a detailed coupled characterization of the features governing crack formation [17].

More recent studies have performed the needed high fidelity characterization (e.g. quantifying crack formation to < 10 μm) of the corrosion-to-crack transition, but these studies were narrowly focused on isolated laboratory [17–20,28,48,50–55] or field [45] corrosion morphologies. These studies however suggest a strong potential role of corrosion morphology on the factors that govern the corrosion-to-crack transition. Specifically, Turnbull et al. studied the corrosion-to-crack transition involving smooth pits in turbine steel and reported that macro-scale stress/strain states governed the location of fatigue initiation [55–57]. Conversely, Burns et al. showed that micro-topographical features associated with pitting in aluminum alloys tend to dominate the location of fatigue initiation sites [17–19]. *In toto,* the literature demonstrates that the morphology of the corrosion damage can potentially lead to changes in the mechanisms that govern crack formation [17–19,55–57]. These results warrant a systematic evaluation of the fatigue detriment due to varying of corrosion morphologies relevant to galvanic couples in for AA 7xxx-series alloys. Such understanding is necessary to develop prognosis modeling tools that accurately capture the remaining life of a component corroded via a galvanic coupling.

The objectives of this study are to (1) quantify the fatigue behavior (crack initiation life, small crack propagation life, and total life) associated with different corrosion morphologies relevant to an Al-stainless steel galvanic couple, (2) characterize relevant macro-scale geometric features/metrics of the fatigue crack initiation locations, (3) analyze these metrics in the context of other locations on the broadly corroded surface that did not initiate cracking, and (4) couple these correlations with the detailed crack initiation and small crack growth data to inform mechanistic interpretation. Of note, while the interaction of underlying microstructure with corrosion damage features are critical to the crack formation behavior, this analysis is outside of the scope of this effort and will be reported in a companion study.

2.2.2 Materials and Methods

2.2.2.1 Materials

Fatigue specimens with 7.60 mm thickness, uniform gage length of 20.96 mm and a reduced gage width of 7.60mm were machined from a 50-mm thick rolled AA 7050-T7451 plate centered at a through-thickness (t) location of t/8. The plate is a precipitation hardened (primarily $MgZn_2$) [35–42] aluminum alloy with the following composition, 6.1 Zn- 2.2 Cu- 2.2 Mg- 0.11 Zr-0.08 Fe- 0.04 Si- 0.02 Ti- 0.01 Mn- balance Al; wt.%. The primary constituent particles are Al_2CuMg, Mg_2Si, and Al_7Cu_2Fe [35–42]. The average grain sizes of this partially recrystallized material were determined using linear intercept method based on ASTM E112 and E1382 [58,59]. The values obtained are as follows: 20.38 μm in the short-transverse or thickness (S) direction, 46.30 μm in the transverse (T) direction. Most of the grains along the longitudinal (L) direction exceeded the horizontal field view of 100× magnification image (1.27 mm) due to grain elongation in the rolling direction, thus the grain size along L-direction was estimated to be 1.5-2 mm long using 70× magnification [60]. The tensile yield strength is 471 MPa (L-oriented), ultimate tensile strength was 510 MPa (L-oriented) and fracture toughness is 43 MPa$\sqrt{m}$ for the L-T orientation (as reported by the manufacturer).

2.2.2.2 Corrosion Protocols

To investigate the effect of corrosion morphology on the fatigue behavior, four different pre-test protocols were applied to an exposed area (~4-7mm^2) of the LS surface within the specimen gauge section polished using 600 grit SiC papers. The details of the morphologies and electrochemical protocols were developed in a companion study that aims to mimic realistic bounds of the electrochemical conditions caused by the galvanic coupling of stainless steel and aluminum in a crevice-like fastener-hole configuration. These protocols aimed to achieve: two levels of discrete pitting morphologies consisting of a distribution of isolated pits in the exposed area (DP1 and DP2), general corrosion where there was broad surface recession in the entire exposed area (GCSR), and corrosion consisting of vertical fissures into the material (FIS). DP1 specimens were held at -700 mV_{SCE} for 1.5 h in 0.5 M NaCl electrolyte adjusted to pH 8 by adding $NaAlO_2$. On the other hand, DP2 specimens were held at -700 mV_{SCE} for 5 h in 0.5 M NaCl electrolyte adjusted to pH 8 by adding $NaAlO_2$. GCSR specimens were held at -700 mV_{SCE} for 72 h using the same electrolyte (0.5 M NaCl pH 8). FIS specimens were prepared by exposing a 3mm-diameter area of the LS surface to a thin film electrolyte with the composition of 1M NaCl + 0.022 M $AlCl_3$ + 0.05M $K_2S_2O_8$ [61]; a thermodynamically stable electrolyte thickness was achieved for the 7 day duration of the test (168 h) by holding the specimen in a relative humidity (RH) chamber set at 96% RH and 30^oC. The thin layer of electrolyte on the specimen surface was replaced every 24 hours for the entire duration of the experiment. The general shape of the corrosion morphologies are shown in **Figure 2.2.1** (a-d) for the corroded LS surface and **Figure 2.2.1** (e-h) showing the cross-sectional TS surface (e-h). All parts of the specimens besides the purposefully exposed areas were masked using a solvent-resistant vinyl electroplating tape (3M) and a peelable butyl rubber lacquer (Miccro Super XP2000). After the exposure, corrosion products were removed by using HNO_3, followed by 15 min ultrasonic baths in de-ionized water then methanol. Samples were stored in a desiccator until fatigue testing.

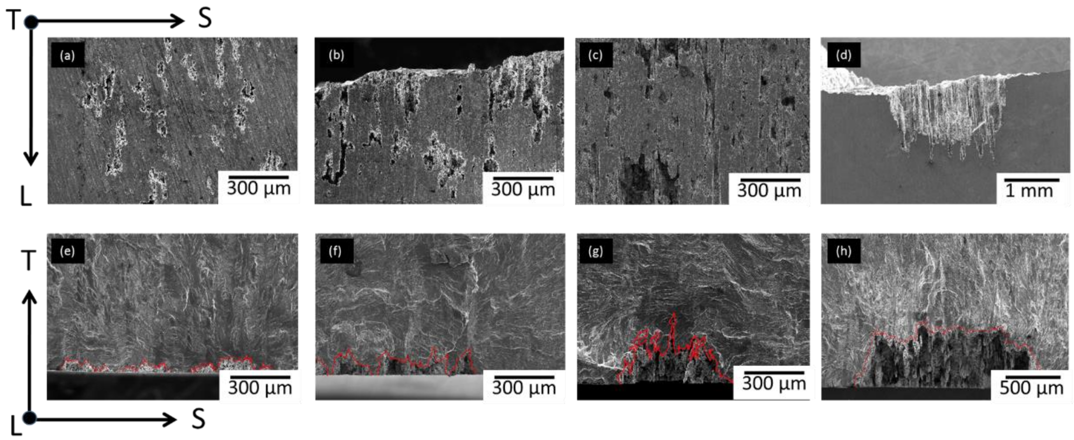

Figure 2.2.1 Corrosion morphologies (a) and (e) shallow discrete pit (DP1) (b) and (f) deep discrete pit (DP2) (c) and (g) fissures (FIS) (d) and (h) general corrosion with surface recession (GCSR); top view of corrosion damage (a, b, c, d); corrosion morphologies traced on fracture surface (e, f, g, h). Figure 2.2.1 (a, b, c, e, f, g) are taken at the same magnification (100×), but note the different scale in (d) and (h).

Prior to fatigue testing, the corrosion damage for each exposure was extensively characterized. Micrographs of the corroded surface were taken using optical and/or Scanning Electron Microscope (SEM). Additionally, white light interferometry (WLI; via a Zygo 7300) was used to obtain a 3D representation of the corrosion damage morphology [62–64], and the broad characterization of damage feature on the exposed area. WLI is a line-of-sight technique that worked well for discrete pits and general corrosion with surface recession; the fidelity of this technique was established by isolated validations against cross-sectional SEM analysis. However, depth measurements obtained from WLI are dependent on the amount of reflected light captured back by the detector, thus this technique is not rigorous for deep and narrow fissures. Instead, post-test X-ray computed tomography (XCT, via Xradia MicroXCT-200) was used [33,65] to fully characterize the deep/narrow fissures and any secondary cracks [66–68] common to the FIS samples [33]. Samples were imaged via XCT using 2× magnification with 2 μm pixel size and 10× magnification with a 0.7 μm pixel resolution.

2.2.2.3 Fatigue Testing

Fatigue cycling at a maximum stress (σ_{max}) of 200 MPa, with a frequency (f) of 20 Hz, and fatigue loading ratio ($R=\sigma_{min}/\sigma_{max}$) of 0.5 was performed on both pristine and pre-corroded specimens; three test replicates were done for each corrosion condition. A high relative humidity (RH > 90%) was achieved/maintained by bubbling N_2 through distilled water then into a sealed Plexiglas chamber fastened about the test specimen. Critically, a programmable loading sequence was used to impart resolvable fatigue markings (highlighted in yellow in **Figure 2.2.2**) on the fracture surface of the specimens thus enabling quantitative characterization of the crack formation lives and microstructure scale crack progression via post-test SEM fractography (FEI Quanta 650) [17–19,28,48,69–72]. The current protocol typically produced the first marker band within ~10 μm of the crack formation feature, and the number of cycles associated with markings sequences is < 5% of the total life. Prior work demonstrated that the marker banding technique does not induce significant transients or influence the overall fatigue life of the material [17,18,28]. While the exact loading protocol was optimized during the course of this study, typically there were 5000 baseline constant amplitude R=0.5 cycles, with σ_{max} of 200 MPa and f of 20 Hz applied at the beginning of each test. The σ_{max} for the marker cycle was maintained at 200 MPa but R alternated between 0.5 and 0.1. Specifically, the marker sequence consisted of 4 to 8 segments of 20-35 cycles at R=0.1 and f=10 Hz then 40-70 cycles at R=0.5 and f=20 Hz. Baseline loading of 20,000 cycles were alternated with the marker sequences. Coupling the fracture surface observations (number of observed marker-bands and spacing between markers) and the known loading protocol enables calculation of the crack formation life to the first marker band (typically < 10μm from the corroded surface). Specifically, the distance between marker bands can be measured and used to calculate crack growth rate (da/dN) since the number of baseline loading cycles between marker sequences is known. Furthermore, the known number of applied marker sequences can be compared to the number of observed fracture surface marks to calculate the number of cycles necessary to for the crack to grow to the marker closest to the crack formation location. The marker band analysis process was previously reported in detail [17–19,28,48,69–72].

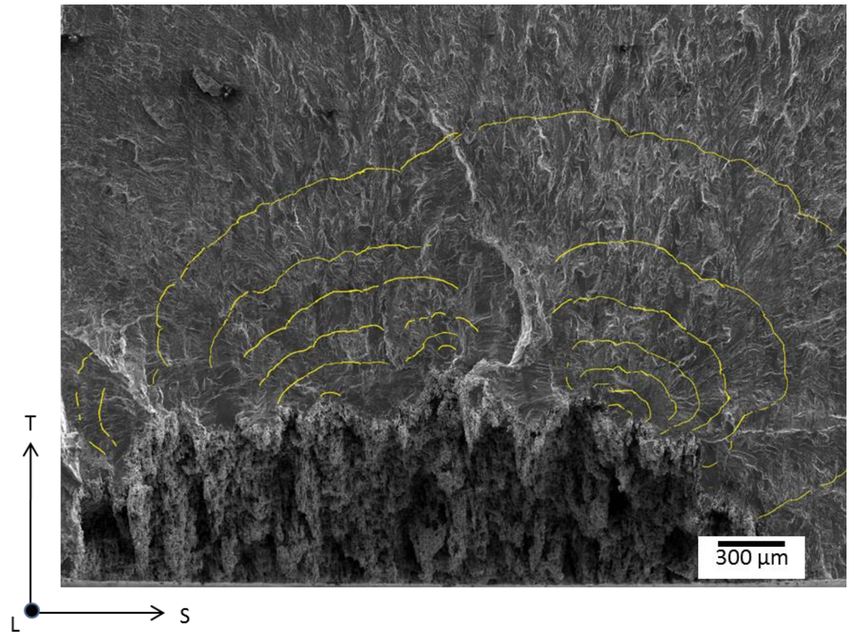

Figure 2.2.2 Marker bands are traced on the fracture surface. Multiple fatigue cracks at the fracture surface of GCSR specimen converge to form a larger crack. Crack grows from bottom to top along the T-direction of the specimen. Fatigue testing of AA 7050-T7451 is performed in moist air environment at 23°C with σ_{max}= 200 MPa, R=0.5 at 20 Hz frequency.

2.2.3 Results

2.2.3.1 Corrosion characterization

Exposure of AA 7050-T7451 to different corrosion protocols produced various corrosion morphologies with diverse average damage depths, D. Data from WLI are post processed using Mountains Map software to obtain measurements of corrosion damage for DP1, DP2, and GCSR samples on the LS surface of the fatigue specimen. The WLI measurements are leveled through average plane orientation to remove tilting effects and the non-measured points are automatically filled by taking the average peripheral measurements. The WLI measurements are then inverted symmetrically along the Z-axis. These measurements are uniformly corrected to a threshold of 5 µm in order to remove the contribution of surface scratches or polishing marks. The individual fissure depths for FIS specimens are obtained from the XCT data. 2D XCT images (taken every 50 µm along the

L-direction of the specimen are stacked to form the 3D representation then are analyzed in order to obtain individual fissure depths and number of fissures per plane. The average corrosion damage of DP1 (D_{DP1}) is generally shallower compared to the corrosion damage of DP2, FIS and GCSR ($D_{DP1} < D_{DP2} < D_{FIS} < D_{GCSR}$). The value of D_{FIS} is similar to D_{DP2}.

In order to evaluate the aspect ratio of the corrosion feature for each morphology, the individual depths and corresponding width of the corrosion damage on the main fracture surface are measured. The aspect ratio of the pits are calculated based on the ratio of the pit depth to half of pit width [17,24,28]. The average aspect ratio for DP1 and DP2 are 2.32 and 3.0 respectively. The average aspect ratio for FIS is 12.54 and average aspect ratio for GCSR is 0.58. This variation in the aspect ratio for different corrosion morphologies are evident in **Figure 2.2.1**.

2.2.3.2 Fatigue Behavior

Figure 2.2.3 shows the plot of the total fatigue life for each specimen tested (both pristine and pre-corroded). The total life of AA 7050-T7451 is greatly reduced by the presence of corrosion damage on the surface of the specimen. The pristine tests are halted after 3×10^6 cycles, then broken via a tensile overload; examination of the fracture surface did not reveal any indication of fatigue crack nucleation/progression. The total life of the pre-corroded specimens are in all cases $< 10^6$ cycles. The average total life of the DP1 (N_{DP1}) is higher than the average total life of other pre-corroded specimens ($N_{DP1} > N_{DP2} > N_{FIS} > N_{GCSR}$), with N_{DP2} having a comparable value to N_{FIS}. The total life for each specimen is plotted against the depth of the features that initiated the dominant fatigue cracks as measured from the fracture surface using SEM (**Figure 2.2.3**); as the initiation depth increases, the total life of the specimen decreases. After a severe initial reduction in life from pristine to DP1 there is only a marginal further reduction in fatigue life with increasing initiation damage size. Similar trends have been previously reported by several authors [17,26,28].

By comparing the number of applied marker sequences and observed fracture surface marks the exact initiation life to the first observed marker band (typically within 5-15 μm from the initiation location) can be determined (full details of this process are presented elsewhere [17–19,28,48,69–72]). For consistency, initiation lives to create a 10 μm crack are plotted in **Figure 2.2.3** for the pre-corroded specimens. Results of the initiation life calculation show that there is a sharp decrease of initiation life for DP1, but further increases in depth of damage for the DP2, FIS and GCSR do not result in a further reduction in crack initiation life as shown in **Figure 2.2.3**. This outcome is consistent with prior findings that suggest near immediate crack formation in corroded samples at relatively high fatigue stress levels [18].

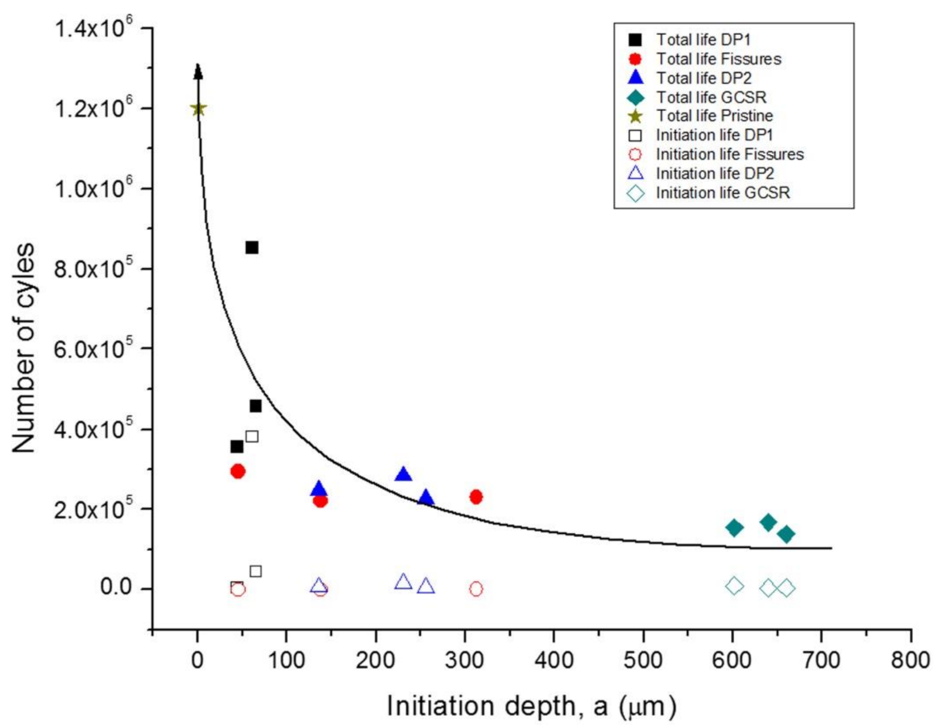

Figure 2.2.3 Plot of total fatigue life, N_{total}, (filled markers) and initiation life, N_i, to create a 10 μm crack (open markers) with respect to the depth of fatigue crack formation site (depth of initiating feature) measured from the non-corroded surface for each specimen. Measurements are taken from the SEM images of the fracture surface. Fatigue testing of AA 7050-T7451 performed in moist air environment at 23°C with σ_{max}= 200 MPa, R=0.5 at 20 Hz frequency. Arrow on top of the pristine data point indicate that pristine specimen did not fail after 1.4×10^6 cycles and testing is halted at 3×10^6 cycles.

The marker band approach also enables characterization of the small crack growth kinetics using SEM images of the fracture surface; specifically, the distance between the marker bands (Δa) are coupled with the known number of applied cycles between marker sequences (ΔN) to a crack growth rate (da/dN) [17,19,28,70]. **Figure 2.2.4** shows a plot of da/dN vs the crack (a) growing along the T-direction perpendicular to the (non-corroded) surface of the specimen. Also shown on the plot are the average initiation depths (ID[1]) for each corrosion damage morphologies. Of note, the small crack growth rates of all the specimens converge to comparable values when the crack front is about ~50-100 μm away from the initiation point; this is despite the expected differences in local stress gradients proximate to the different initiating features.

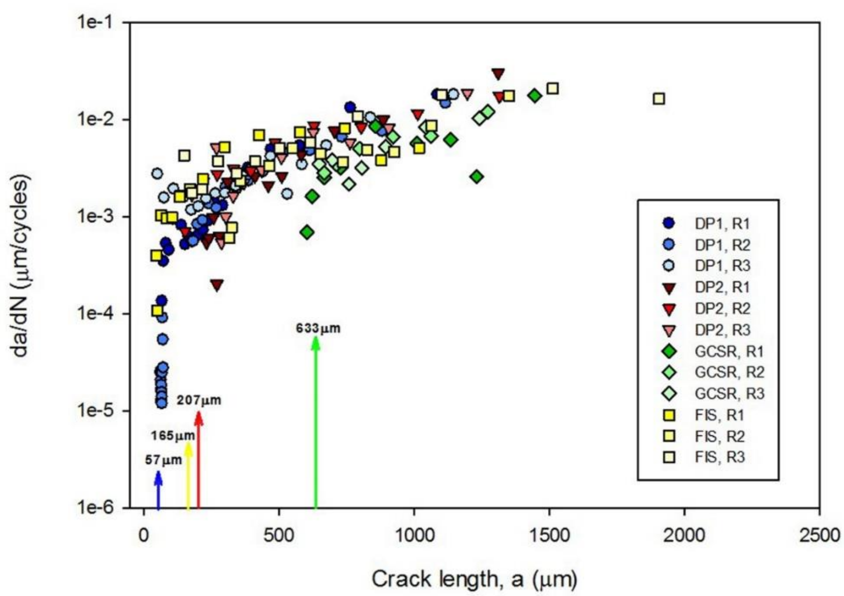

Figure 2.2.4 Crack growth rate for AA 7050-T7451 specimens with different corrosion morphologies cyclically loaded along L-direction with σ_{max}= 200 MPa, R=0.5 at 20 Hz frequency with moist air environment at 23°C; crack length (a) is measured from non-corroded surface growing along the T-direction of the specimen. Indicated numerical values above the arrows represent the average depth at which the primary fatigue crack forms. R1, R2, R3 correspond to the three test replicates done for each corrosion morphologies.

[1] This initiation depth is the average distance from the non-corroded surface to the precise crack formation location on the corrosion feature. This value is the average of the depth of initiation values reported in Figure 2.2.4.

2.2.3.3 Crack Initiation Location

Fatigue cracking initiates at the corrosion damage for all the fracture surface analyzed in this study. The precise location of crack formation is determined by coupling the 2D images of the corroded surface and fracture surface (taken before and after fatigue testing, respectively), and 3D images from WLI technique. The traditional river patterns and marker bands enable precise identification of the crack formation location on the fracture surface. The features of the fracture surface image is then aligned with images of the corroded surface to map the longitudinal location of crack formation. This location is then transferred to images (2D and 3D) of the corroded surface taken prior to testing to identify the latitudinal location of crack formation. This location can then be directly mapped to the 3D representation of the corrosion damage (WLI data); this process has been successfully applied in prior efforts [18,48]. This process is shown for the surface GCSR condition in **Figure 2.2.5**, where boxes represent the location of the initiation sites on the fracture surface (**Figure 2.2.5** (c)), top views of corrosion damage (**Figure 2.2.5** (a),(b)) as well as the 3D image from WLI (**Figure 2.2.5** (d)). Knowledge of the exact location of fatigue crack initiation is critical for the characterization of the initiating feature.

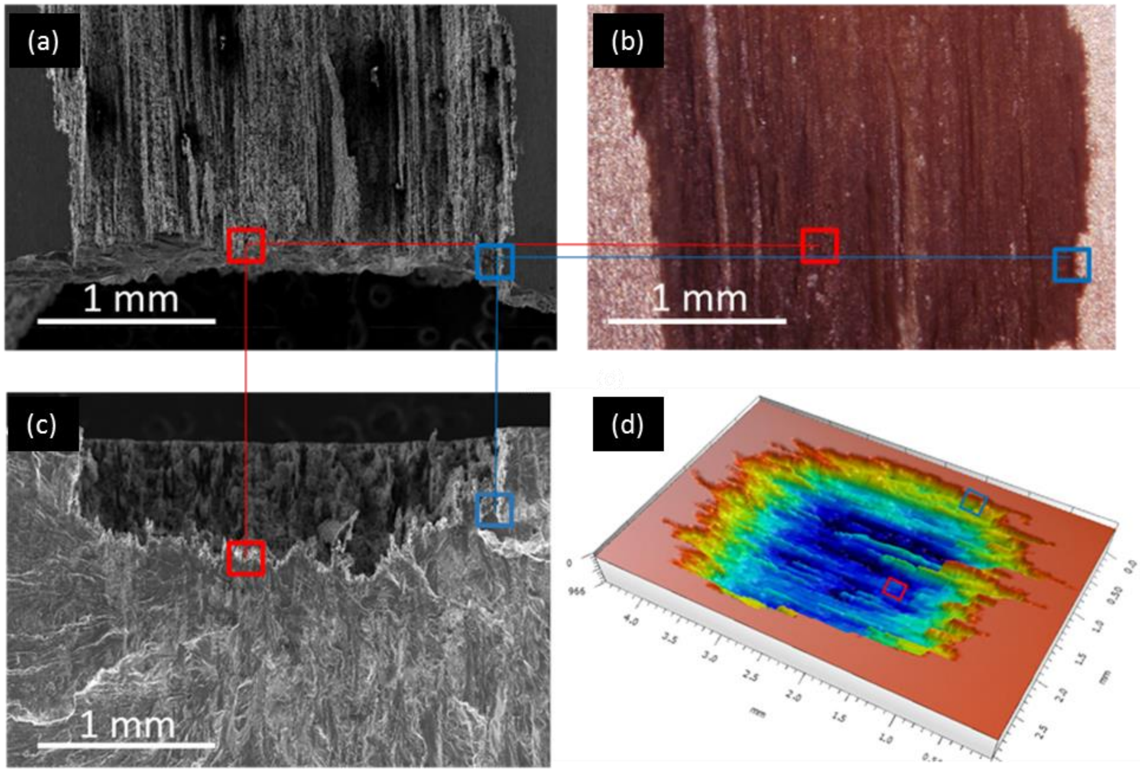

Figure 2.2.5 (a) Top view of corroded surface (LS) imaged using SEM (b) top view of corroded surface (LS) imaged using optical microscope (c) top view of the fracture surface (TS) imaged using SEM (d) white light interferometry 3D image. Combination of the 2D images and the 3D image allows the determination of the fracture initiation locations. Fatigue testing of AA 7050-T7451 performed in moist air environment at 23^{o}C with σ_{max}= 200 MPa, R=0.5 at 20 Hz frequency

2.2.3.4 Corrosion Feature Metrics

Broad characterization of the entire corroded region and precise identification of the initiation feature enable quantitative evaluation of various corrosion metrics to determine if there is a correlation with the crack formation location. Analyzing such correlations (or lack thereof) will identify relative influence of such features in the context of fatigue crack formation. This information is critical to further inform the mechanistic understanding of the governing factors for crack formation as well as identify important metrics when evaluating the structural integrity of a corroded component. These macro-scale metrics are obtained from WLI measurements for DP1, DP2, and GCSR, and from XCT imaging for FIS specimens.

2.2.3.4.1 Discrete Pit Metrics

WLI measurements for DP are post-processed using the Mountains Map software to enable quantitative analysis of the crack formation location relative to the overall distribution of the corrosion features. Pit depths, pit areas, pit volumes are obtained using the volume of islands function on the Mountains Map software which automatically calculates the depth, area, volume, diameter of the individual pit that represents individual island on the exposed surface; individual pit depths of DP1 and DP2 are reported and plotted as histogram in **Figure 2.2.6**. The primary initiation sites are indicated by filled and the secondary initiation sites are indicated by open markers on the histogram plots of data obtained from Mountains Map. The secondary fatigue cracks are observed either (1) growing on the main fracture plane, or (2) on a plane not coincident with the fracture plane (via examination of the corroded surface; typically surface breaking cracks > 15 μm can be observed). The data clearly demonstrate that the cracks do not initiate at the deepest pits, this is contrary to the common use of pit depth as the governing severity metric [52]. Similarly, cracks do not nucleate at the damage site with the highest individual pit area or pit volume (not shown). Critically, these data suggest that damage depth, area, volume do not govern the location of the fatigue initiation.

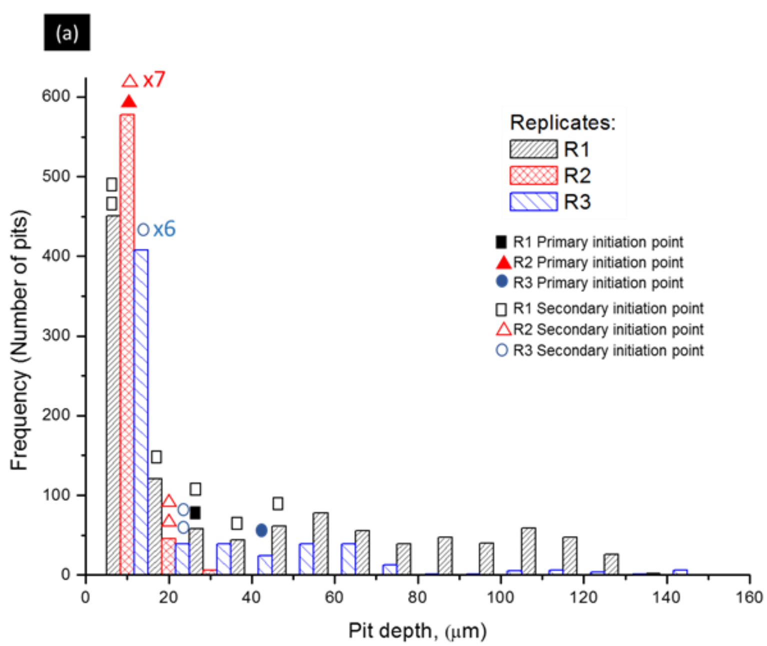

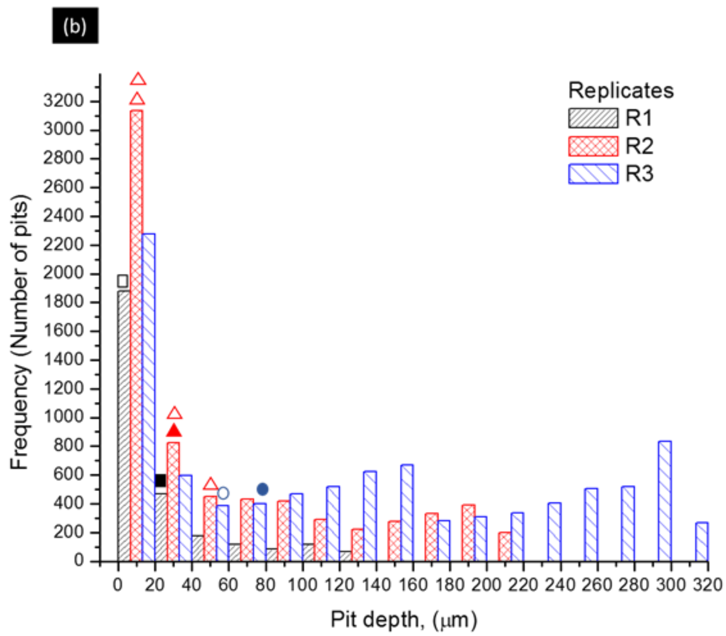

Figure 2.2.6 Histogram of pit depths for (a) DP1 specimens and (b) DP2 specimens. Location of the primary fatigue crack initiation points are marked using filled markers, while location of secondary crack initiation points are marked with open markers. Actual value of the pit depth for R1, R2, R3 is centered on the red bar of the histogram. Fatigue testing of AA 7050-T7451 is performed in moist air environment at 23°C with σ_{max}= 200 MPa, R=0.5 at 20 Hz frequency. R1, R2, R3 correspond to the three test replicates.

The interaction of neighboring pits may also play a critical role in the crack formation process due local stress/strain intensification (or shielding) that differs from that of an isolated damage location. Modeling of such intensification and shielding of proximate cracks reported that such effects are most potent over an area that is roughly 4-5 times the size of the crack [73,74]. The largest pit size on the LS surface for the DP1 specimens is ~100 µm. As such, the exposed LS surface is divided into a grid of 500 µm × 500 µm sections and the pit density (the number of pits per 0.25 mm^2 area) within each grid-section is established. **Figure 2.2.7** plots a histogram of the pit density of DP1 and DP2 in each grid-section; the open and closed symbols identify the density in the region proximate to the primary and secondary crack formation locations, respectively. These data demonstrate that there is not a strong correlation between the areas having the highest pit density and the crack formation location. However, the potency of the interaction between pits is potentially dependent on the size distribution of pits within each grid. As such, **Figure 2.2.8** plots the pit density versus the average pit depth (filled symbols) and maximum depth (open symbols) in each grid-section with the metrics of the initiation site are plotted in green. These data show two important trends. First, features with high density and high depths (either average or maximum) do not correlate with the crack formation feature. Second, for a constant pit density, the difference between the maximum depth and the average depth provides a metric of the homogeneity of the size distribution within each grid; comparing these data for the initiation sites (green symbols) show that in some instances there is a large differences (R1) and in some instances there is a small difference (R2), suggesting no strong correlation between the degree of pit homogeneity and the crack formation location.

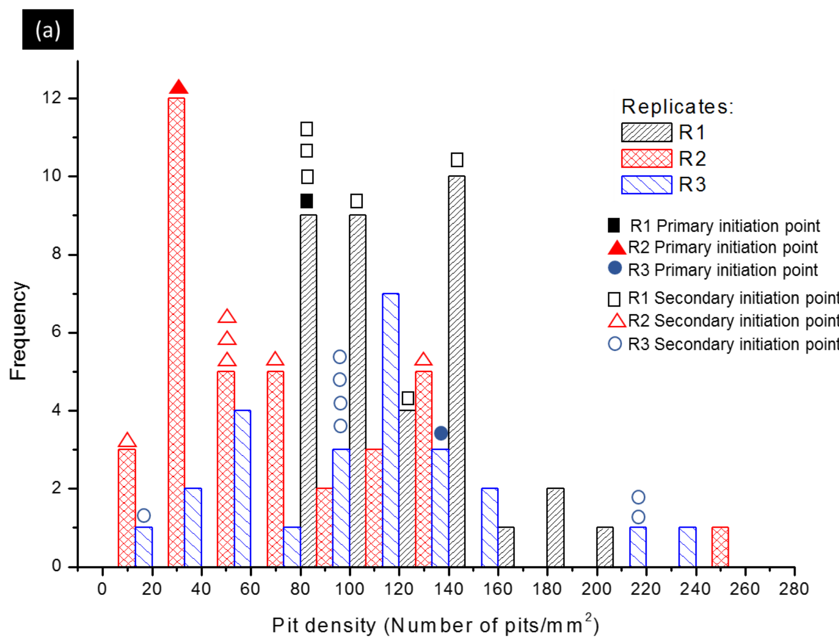

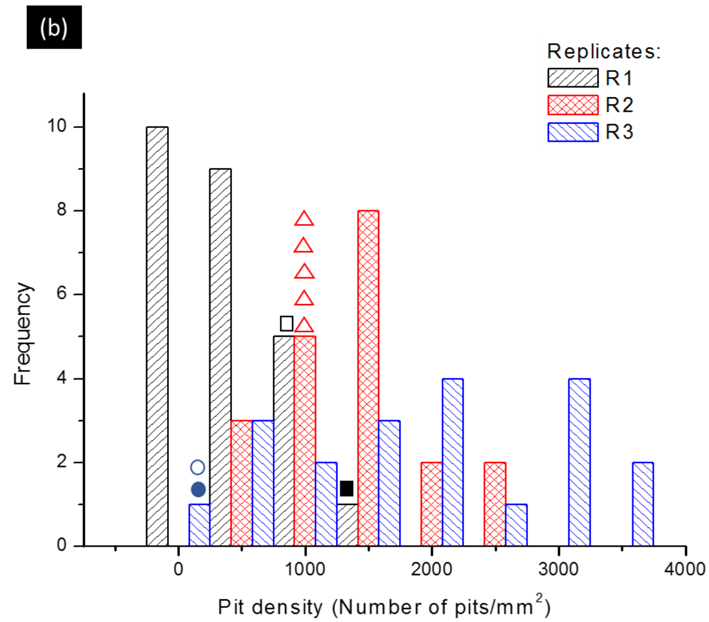

Figure 2.2.7 Histogram of pit density for (a) DP1 specimens and (b) DP2 specimens. Location of the primary fatigue crack initiation points are marked using filled markers, while location of secondary crack initiation points are marked with open markers. Actual value of the pit density for R1, R2 and R3 is centered on the red bar of the histogram. Fatigue testing of AA 7050-T7451 is performed in moist air environment at 23^{o}C with σ_{max}= 200 MPa, R=0.5 at 20 Hz frequency. R1, R2, R3 correspond to the three test replicates.

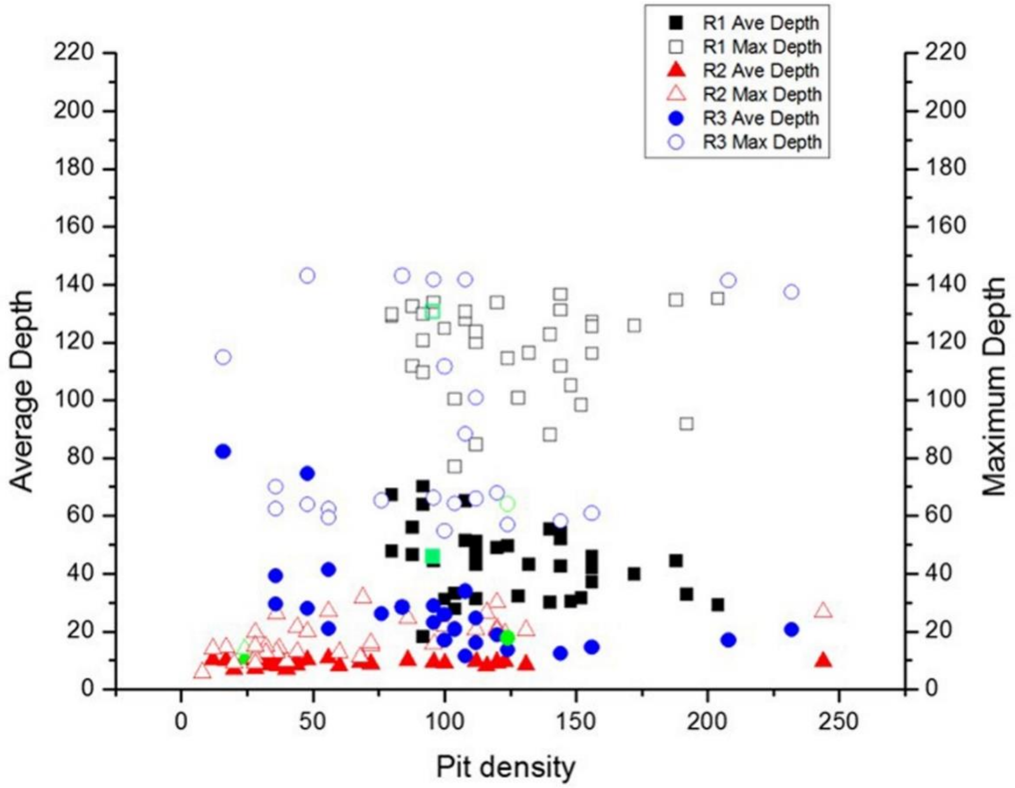

Figure 2.2.8 Plot of average depth (filled markers) and maximum depth (open markers) versus pit density of DP1. ΔD = maximum depth - average depth where fatigue crack initiated. Values for the primary initiation points are indicated by the green markers. Fatigue testing of AA 7050-T7451 is performed in moist air environment at 23°C with σ_{max}= 200 MPa, R=0.5 at 20 Hz frequency. R1, R2, R3 correspond to the three test replicates.

It is also useful to examine cross-sectional profiles that are perpendicular to the loading axis due to the potential influences of co-planar damage sites on the fatigue crack formation, small crack link-up, and growth behavior. As such, individual line scan evaluation, which correspond to a specific plane perpendicular to the loading axis, is performed along the exposed areas at 50 μm intervals, and the pits along the line profile are considered for this analysis. The specific metrics gathered are: the cumulative damage depth along the entire line length, the average damage depth along line length, and number of pits per line length. Results of analysis are shown in **Figure 2.2.9** and this demonstrates that crack formation location tend to be at the lower end of the histogram for the total pit depth per line (**Figure 2.2.9** a), towards the lower end of the histogram for the number of pits per line (**Figure 2.2.9** b), and at mid-value for the average depth of pits per line (**Figure 2.2.9** c). These results demonstrate that these metrics do not strongly correlate with the crack initiation location.

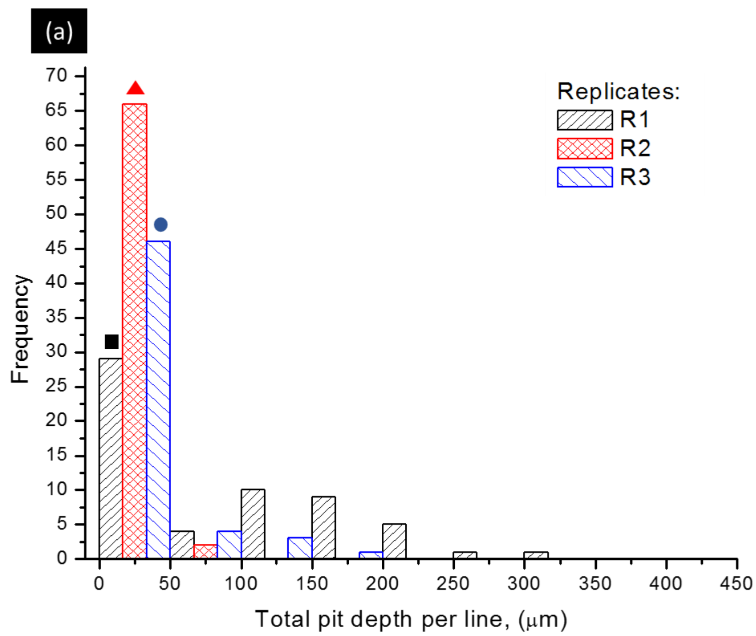

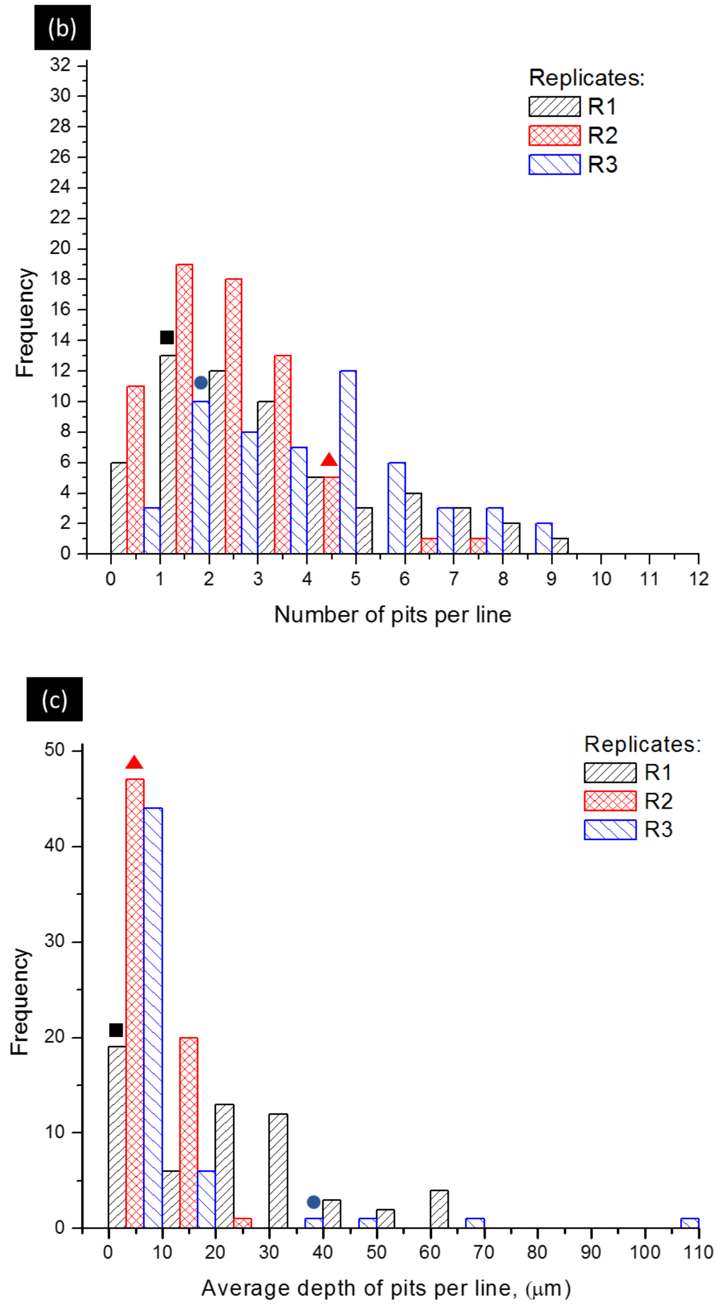

Figure 2.2.9 Results of line profile measurements for DP1 indicating (a) total pit depth, (b) number of pits per line and (c) average depth of pits per line, filled markers indicate location of the fracture plane where primary fatigue crack initiate. Actual values of total pit depth per line, number of pits per line, average depth of pits per line for R1, R2, R3 are centered on the red bar of the histogram. Fatigue testing of AA 7050-T7451 is performed in moist air environment at 23°C with σ_{max}= 200 MPa, R=0.5 at 20 Hz frequency. R1, R2, R3 correspond to the three test replicates.

2.2.3.4.2 Fissure Metrics

For the FIS damage a sub-set of the characterization reported for DP are evaluated; specifically, analysis of the pit depth and the cross-sectional profiles. A histogram of the depth of all fissures on the sample with location of crack initiation is shown in **Figure 2.2.10**; while crack at the R2-sample is at one of the deeper pits, there is no systematic correlation between fissure depth and crack formation location. The results of the individual line scan analysis are reported in **Figure 2.2.11** and demonstrate that the initiation feature does not occur on the cross-sectional planes with the highest cumulative damage depth, or average damage depth (not shown). However, crack formation generally occurs on damage planes where the cumulative damage is high, and in 2 of the 3 tests, crack formation occurred in the plane with the highest number of fissures present (**Figure 2.2.12**). These data suggest a potentially important correlation between the number of fissures per plane and the cumulative damage depth per plane and the crack formation location. This is further supported by data in **Figure 2.2.13** [75] that plots the total fissure depth and number of fissure per plane, and suggests that planes with high total fissure depth and number of fissures preferentially form cracking. This is a distinct behavior in FIS specimens; DP1 and DP2 specimens did not show such trend when identical analysis was performed (**Figure 2.2.9**).

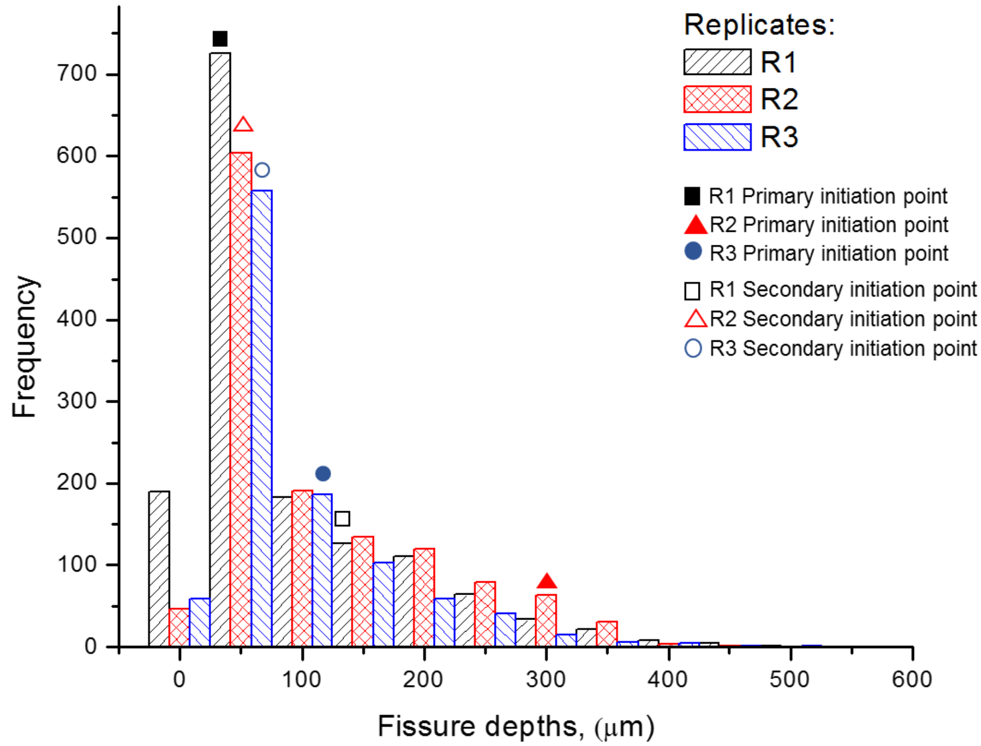

Figure 2.2.10 Histogram of individual fissure depths measured for FIS specimens. Location of the primary fatigue crack initiation points are marked using filled markers, while location of secondary crack initiation points are marked with open markers. Actual values of the fissure depths for R1, R2, R3 are centered on the red bar of the histogram. Fatigue testing of AA 7050-T7451 is performed in moist air environment at 23°C with σ_{max}= 200 MPa, R=0.5 at 20 Hz frequency. R1, R2, R3 correspond to the three test replicates.

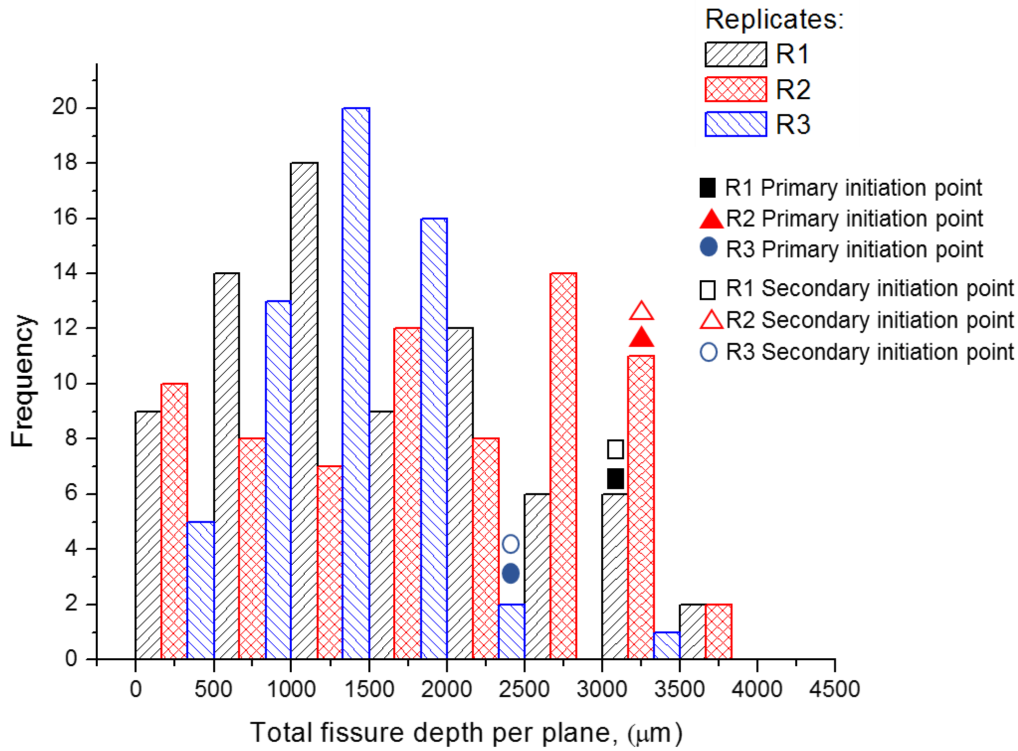

Figure 2.2.11 Histogram of the total (cumulative) fissure depth per plane of FIS specimens. Location of the primary fatigue crack initiation points are marked using filled markers, while location of secondary crack initiation points are marked with open markers. Actual values of the total fissure depth for R1, R2, R3 are centered on the red bar of the histogram. Fatigue testing of AA 7050-T7451 is performed in moist air environment at 23°C with σ_{max}= 200 MPa, R=0.5 at 20 Hz frequency. R1, R2, R3 correspond to the three test replicates.

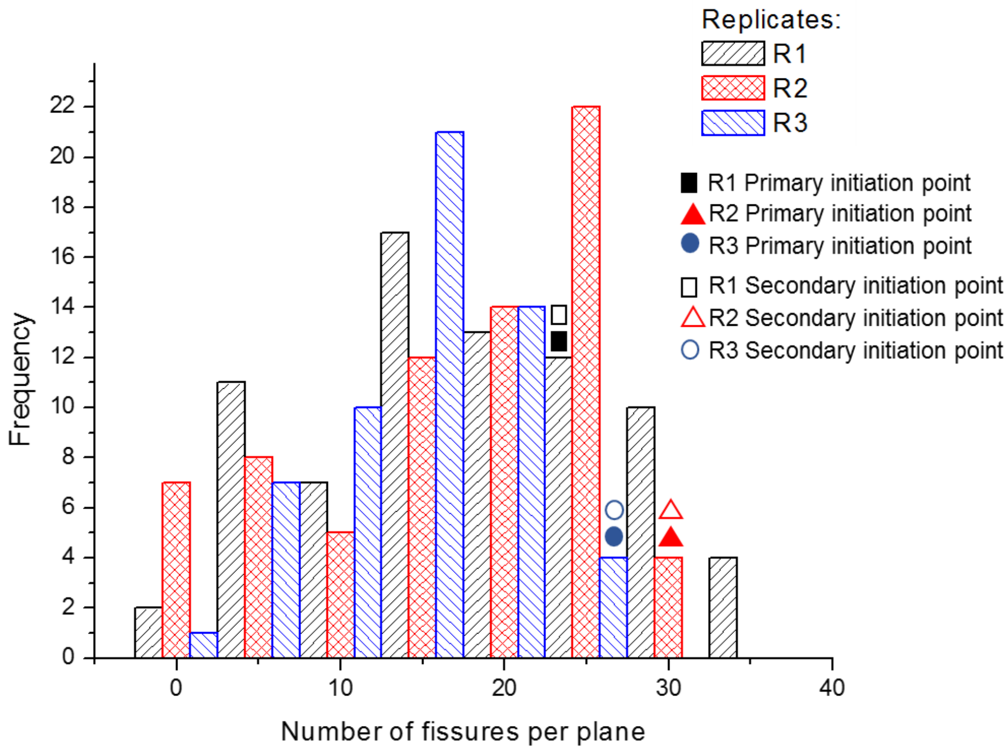

Figure 2.2.12 Histogram of the number of fissures per plane for FIS specimens. Location of the primary fatigue crack initiation points are marked using filled markers, while location of secondary crack initiation points are marked with open markers. Actual values of the number of fissures per plane for R1, R2, R3 is centered on the red bar of the histogram. Fatigue testing of AA 7050-T7451 is performed in moist air environment at 23ºC with σ_{max}= 200 MPa, R=0.5 at 20 Hz frequency. R1, R2, R3 correspond to the three test replicates.

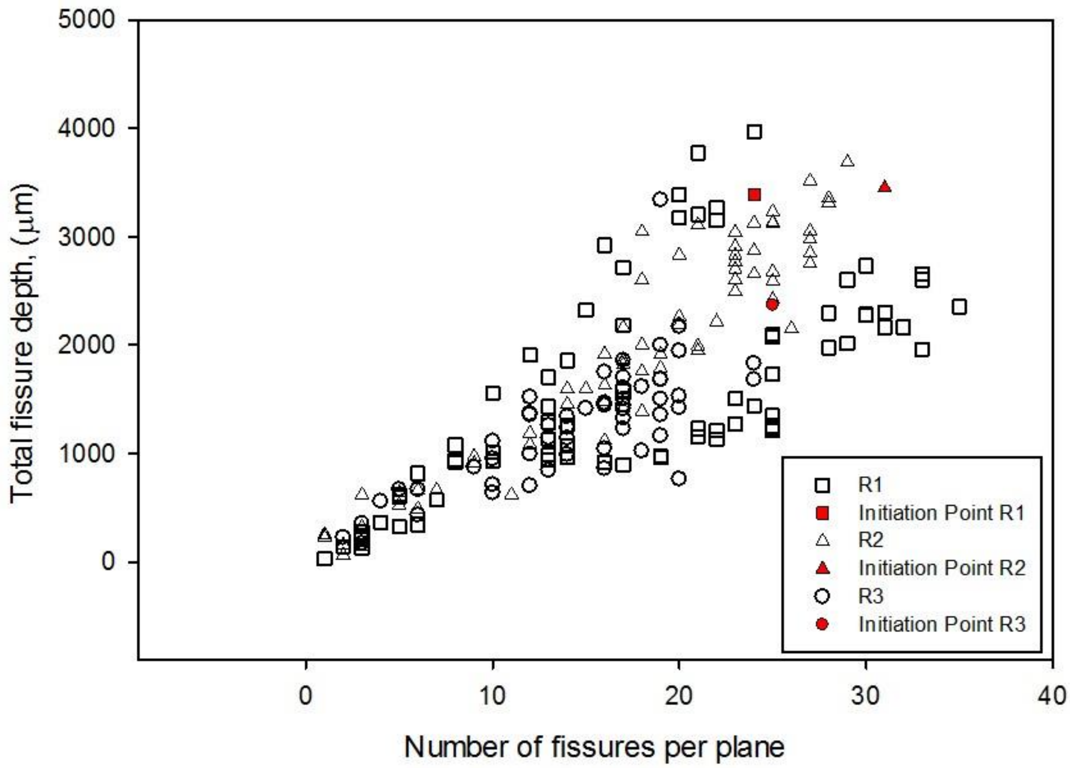

Figure 2.2.13 Plot of total fissure depth versus the number of fissures per plane for FIS specimens. The locations of fatigue crack formation are by the red markers on the plot. Fatigue testing of AA 7050-T7451 is performed in moist air environment at 23°C σ_{max}= 200 MPa, R=0.5 at 20 Hz frequency. R1, R2, R3 correspond to the three test replicates. Reproduced with permission from NACE International, Houston, TX. All rights reserved. Co, NEC. Burns, JT. Galvanic Corrosion-Induced Fatigue Crack Initiation and Propagation in AA 7050-T7451, CORROSION, 72, 10, 2016. ©NACE International 2016

2.2.3.4.3 Surface Recession Metrics

The broad based surface recession morphology is inherently different than the isolated damage in the DP and FIS conditions, as such different metrics are analyzed. Specifically, the GCSR area is divided into a grid of 500 μm × 500 μm sections and various surface roughness metrics are determined using Mountains Map for each grid-sectioning. The following metrics are considered: root mean square (RMS), peak density, maximum valley depth, maximum peak height, average roughness, and texture aspect ratio representative of roughness measurements [76–80]. No correlation was observed between these metrics and the conditions at the crack formation site, as is shown in the histograms of root mean square, peak density and maximum valley depth measurements in **Figure 2.2.14**. Additionally, **Figure 2.2.15** (a) and (b) plots the RMS against peak density (inverse relationship) and maximum valley depth (direct relationship), respectively, for each grid-section. However, there is no direct relationship observed between these combination of metrics and the crack initiation location.

Aside from the corrosion metrics analyzed for GCSR specimens, the location of some of fatigue initiation sites on the main fracture surface are mapped on the 3D image as shown in **Figure 2.2.5**. The primary initiation site for this specimen is indicated by the red box, while the blue box indicate a secondary fatigue crack initiation site. (Of note, other initiation sites are present but not indicated on this diagram.) Critically, the aim of the GCSR damage was not to evaluate the shape of the corroded region rather to investigate the influence of the features of the recessed surface. However, analysis of the crack initiation sites in the context of the macro-shape of the corroded region is informative. Crack initiation sites can either occur at the bottom or on the sidewall of the GCSR corrosion damage. This suggests that the macro-scale stress distribution are not primarily controlling the crack formation location, contrary to prior findings for more smooth corrosion morphologies [20,50,55].

(a)

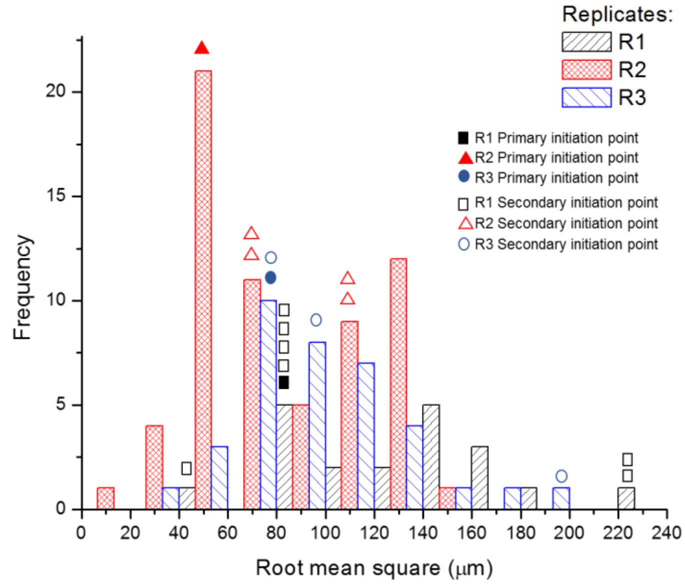
Replicates:
R1
R2
R3
R1 Primary initiation point
R2 Primary initiation point
R3 Primary initiation point
R1 Secondary initiation point
R2 Secondary initiation point
R3 Secondary initiation point
Frequency
0
5
10
15
20
0
20
40
60
80
100
120
140
160
180
200
220
240
Root mean square (μm)

(b)

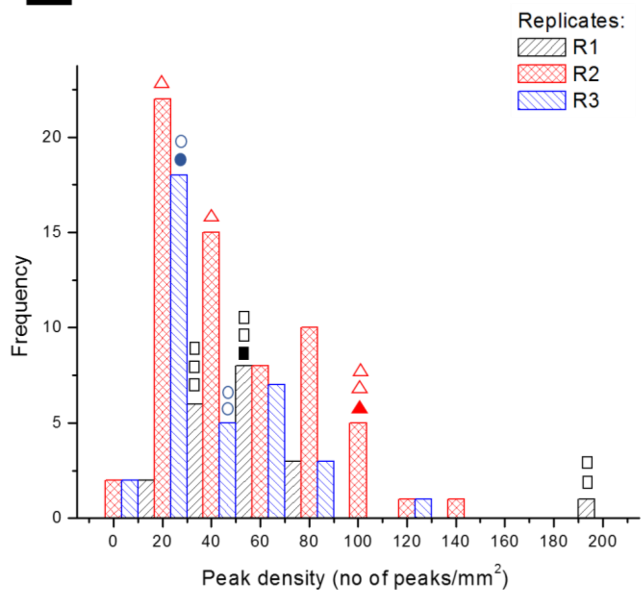
Replicates:
R1
R2
R3
Frequency
0
5
10
15
20
0
20
40
60
80
100
120
140
160
180
200
Peak density (no of peaks/mm2)

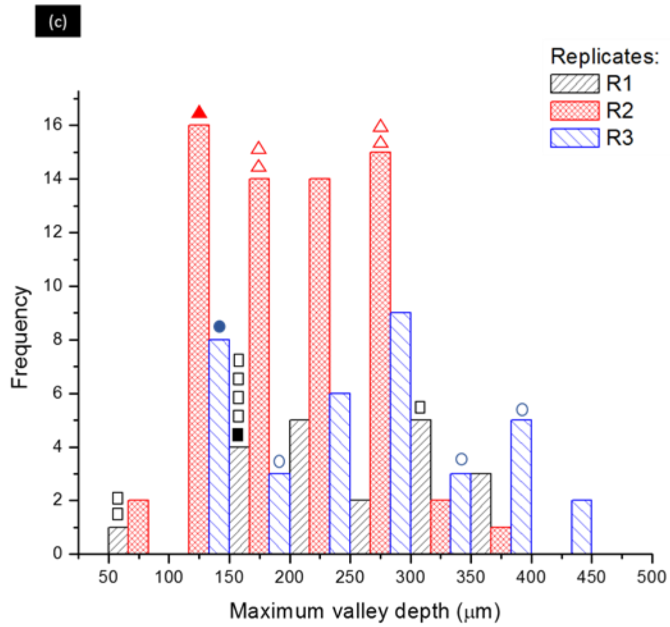

Figure 2.2.14 Histograms of (a) GCSR root mean square, (b) peak density, (c) maximum valley depth, filled markers indicate location of primary crack initiation that caused failure, while open markers indicate secondary initiation sites. Actual values of root mean square, peak density, maximum valley depth for R1, R2, R3 are centered on the red bar of the histogram. Fatigue testing of AA 7050-T7451 is performed in moist air environment at 23^{o}C with σ_{max}= 200 MPa, R=0.5 at 20 Hz frequency. R1, R2, R3 correspond to the three test replicates.

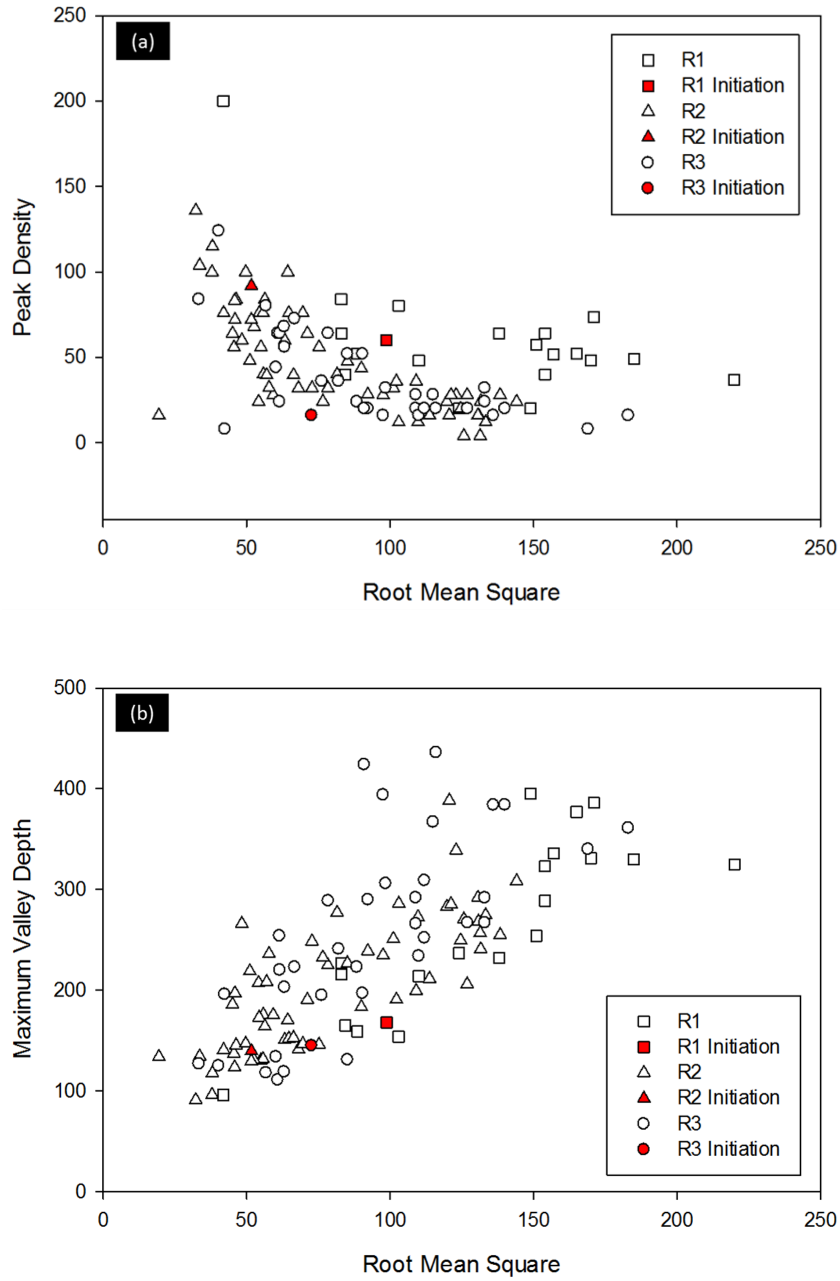

Figure 2.2.15 (a) Plot of peak density and root mean square for GCSR specimens. (b) Plot of the combination effects of maximum valley depth and root mean square. Location of fatigue crack formation are indicated by the red markers. Fatigue testing of AA 7050-T7451 is performed in moist air environment at 23°C with σ_{max}= 200 MPa, R=0.5 at 20 Hz frequency. R1, R2, R3 correspond to the three test replicates.

2.2.4 Discussion

Figure 2.2.3 shows that the initiation life for different corrosion morphologies are almost constant however there is a decrease in the overall total life for different corrosion morphologies. **Figure 2.2.3** also shows that initiation life is low for vastly different corrosion morphologies. Furthermore, histograms of macro-scale features show that, in general, the most severe macro-corrosion metrics do not correlate to the location of the initiation point. These observations motivate two main questions to be probed in the discussion: (1.) Why is the initiation life constant and low despite vastly different macro-scale morphologies? (2.) Why is there a decrease in the overall fatigue life for different corrosion morphologies if the initiation life is constant? The stages of the fatigue crack growth will be quantified to explain trends seen on fatigue life.

For the sake of the subsequent discussion, a functional definition of the regimes contributing to the total number of cycles, N_{total}, to propagate a crack to failure is given in Equation 1. N_i is the initiation life to create a ~10 μm crack from the initiation point. N_i is quantified based on the location of marker bands resolved in the fracture surface. (Of note, the number of baseline cycles to the first marker band (5000 cycles) is considered as N_i if the first marker band is seen beyond 10 μm from the initiation point.) N_{short} is the number of cycles to propagate a crack from 10 μm to a certain crack length. For the purpose of analysis, the crack length is assigned a value of 900 ± 60 μm measured from the non-corroded surface. This value is set based on the deepest corrosion morphology (i.e. GCSR specimens). Specifically, this corresponds to the crack length sufficiently far away from the GCSR corrosion feature (average initiation feature depth of 633 μm) where the da/dN values aligned with those from all other samples. N_{long} is the number of cycles from 900 μm ± 60 μm crack to failure. The values for N_{total}, N_i, N_{short}, and N_{long} are reported in **Table 2.2.1.**

$$N_{total} = N_i + N_{short} + N_{long}$$

Table 2.2.1 Number of fatigue cycles for each sample, location of first marker band, location of primary fatigue crack initiation point and the number of initiation points on the main fracture plane

	N_i to 10 microns from the corroded surface	N_{short} (from 10 microns to 900 microns from the non-corroded surface)	N_{long} Cycles from 900 microns from surface to failure	N_{total}	N_i/N_{total} × 100	Depth of first observed MB, µm	Corrosion feature depth of primary fatigue initiation point, µm	Number of initiation points on the main fracture plane
DP1								
R1	45000	360000	52328	457328	9.84	3	66	2
R2	381076	363924	107103	852103	44.72	1.6	61	1
R3	5000	300000	50268	355268	01.41	13	44	1
Average	**143692**	**341308**	**69900**	**554900**	**25.90**	**5.87**	**57**	**1**
DP2								
R1	16955	228045	38926	283926	5.97	2.7	230	2
R2	6908	178092	62601	247601	2.79	8.6	136	5
R3	5000	180000	42066	227066	2.20	25	256	2
Average	**9621**	**195379**	**47864**	**252864**	**3.80**	**12.10**	**207**	**3**
FIS								
R1	30621	214379	48462	293462	10.43	2	45	2
R2	13941	151059	65013	230013	6.06	3	313	2
R3	5000	160000	55752	220752	2.26	21	138.	2
Average	**16521**	**175146**	**56409**	**248076**	**6.66**	**8.67**	**165**	**2**
GCSR								
R1	9043	75957	69694	154694	5.85	3.5	601	8
R2	5000	60000	74234	139234	3.59	14	660	5
R3	5000	80000	84253	169253	2.95	17	639	4
Average	**6348**	**71986**	**76060**	**154394**	**4.11**	**11.50**	**633**	**6**

2.2.4.1 Fatigue Crack Initiation Life and Features

The total fatigue life, N_{total}, of AA 7050-T7451 is greatly affected by the presence of corrosion damage on the surface of the material. **Figure 2.2.3** shows a very steep change of N_{total} from pristine sample to specimens with shallow discrete pits (DP1). The exact reduction of the N_{total} measurements from pristine specimens to different corrosion morphologies cannot be determined since the pristine samples did not fail during the cyclic test. The difference between the N_{total} of DP1 to other specimens having different corrosion damage on the surface is small compared to the difference between the N_{total} of pristine sample and the DP1 specimen. The N_{total} of DP2 represents 46% of the total life of DP1, while FIS and GCSR represent 44% and 28% of the N_{total} of DP1 respectively. Previous authors reported that the fatigue life of corroded specimens sharply decreases as the damage depth increases and then generally plateaus to constant values [17,28]. While there are subtle decreases in N_{total} with increasing corrosion depth, **Figure 2.2.3** demonstrates that at an engineering scale this trend is upheld for the different corrosion morphologies investigated in this study.

The observed plateau N_{total} can be largely explained by the corresponding trends in N_i, as shown in **Figure 2.2.3**. Specifically, high number of cycles to initiate a 10 µm crack for DP1 specimen leads to high number of cycles accumulated to failure and low N_i results in low N_{total}. The values of N_i for DP2, FIS, and GCSR converge to near constant values (below 20,000 cycles) which is < 7% of N_{total} for each corrosion morphology as reported in **Table 2.2.1**. Prior work reported that small N_i (near zero) values from isolated corrosion features are caused by the micro-scale plastic strain concentration at the vicinity of corrosion feature [18]. These enhanced corrosion induced stress/strains interact with susceptible microstructural features local to the perimeter of the corrosion damage to promote near immediate crack formation [18]. Critically, current results suggests that this paradigm is likely applicable for vastly varying corrosion morphologies at this relatively high loading level (σ_{max} =200 MPa).

Despite the governing role of such local features, prior engineering scale models correlate macro-scale damage features such as corrosion depth, pit density, pit surface area, etc. with fatigue crack formation sites [17–19,25,51–53,81,82]. The high fidelity and systematic data presented in **Figure 2.2.6-15** demonstrate that for DP1, DP2 and GCSR the location of fatigue crack formation does not generally correlate to the most severe macro-features. The only macro-feature metrics that tend to moderately correlate with the location of the fatigue crack initiation location is the combination of large total fissure depth and higher number of fissures per plane for FIS (note that, individually, the total fissure depth and number of fissures per plane do not correlate with fatigue crack initiation). Large number of fissures per plane indicates that individual fissures are possibly interacting with each other due to proximity effects, while higher total depth indicates a higher frequency of severe features. A possible explanation of this behavior is that the higher frequency of severe fissures enables multi-site crack damage that combine to progress quickly to failure. However, this hypothesis is not consistent with the observation that there are typically two crack formation sites observed, which is not significantly higher than the average number of sites observed in other corrosion morphologies. Furthermore, the trend of having larger number of corrosion features (fissures or pits) per plane does not hold true for DP specimens where a similar correspondence between the pit frequency and the crack formation plane was not observed. These data suggest that there is a unique aspect of the FIS damage morphology that leads to this observed correlation. As such a more detailed investigation of the local micro-features (< 50 μm) of the corrosion damage and its interaction with the local microstructure is needed, but outside of the scope of the current paper.

The lack of a unique correlation of the macro-features of corrosion damage to fatigue initiation site supports a strong role of the local micro-scale feature of the corrosion damage and its interaction with the underlying microstructure (e.g. presence of nearby constituent particles) of the aluminum alloy [19]. In one view, the primary role of the macro-feature will be to set up regions of macro-stress concentration within which the governing micro-scale corrosion feature and microstructure interaction will occur [19,83]. As such, as frequency and/or depth of the macro-scale corrosion damage increases so will the regions of macro-stress concentration, thus increasing the probability of having a severe micro-feature align with a susceptible microstructure location. Such a hypothesis is aligned with the sharp initial decrease in N_{total} with low levels of corrosion then a plateau. Specifically, this would suggest that even at low levels of corrosion sufficient macro-stress concentrated regions exist to enable exceedance of the failure criteria for crack formation, thus further increases in the global corrosion morphology does not significantly influence this initiation life. Validation of this hypothesis requires detailed characterization of the local microstructure, local micro-scale feature, local geometry and small crack propagation about the corrosion damage. A full grain specific crystal plasticity analysis of these real features that incorporates the true corrosion morphology, local grain orientation, and underlying constituent particles is needed to establish the local stress/strain states. Such crystal plasticity outputs would enable calculation of hypothesized parameters for crack initiation (e.g. fatigue indicator parameters [84–91]) that can be compared/validated against the qualitative crack formation and small crack growth data reported in **Figure 2.2.4** and **Table 2.2.1**. Such work is ongoing but outside of the scope of the current study.

2.2.4.2 Total Fatigue Life Trends

The quantitative marker band data in **Figure 2.2.4** and **Table 2.2.1** provide the means by which to evaluate why there is a decrease in the overall fatigue life despite the plateau in the observed initiation life. Specifically, despite the similarities in N_i for between GCSR, DP2 and FIS, there is still a slight decrease in the N_{total} as the average initiation feature size increases. This decrease in the total fatigue life of GCSR could potentially be due to (1) the presence of multiple initiation sites that converge to form a larger crack, (2) changes in the small crack growth rates due to a stress gradient that extends deeper into the material for larger corrosion features, and/or (3) to the size of the initiating macro-feature of the corrosion damage itself [52,53,92,93].

First, going from DP1, to DP2, to FIS, to GCSR both the depths and frequencies of the corrosion damage increases, as such, it could be reasonably postulated that there may be an increase in the number of crack initiation sites for the GCSR. GCSR specimens have large number of initiation sites on the main fracture plane as reported in **Table 2.2.1**. The crack from each initiation site can grow larger and converge to a bigger crack as shown in **Figure 2.2.2**, such multi-crack interactions have been correlated to a decrease fatigue life

[52,53,92,93]. However, modeling studies of the predicted life of a corroded component using multiple crack and single crack simulations demonstrated only a modest decrease in fatigue life due to the crack interactions [52,53]. This hypothesis is reasonably consistent with the fact that the GCSR exhibits the most initiation sites on the main fracture plane (**Table 2.2.1**) but comparison of the DP2 and FIS does not support this trend.

Second, while the stress concentration factor is solely dependent on the shape of a feature, the depth of the penetration of the concentrated stress gradient will scale with the size corrosion damage feature. Specifically, the degree of stress concentration about a notch is generally thought to sharply decrease at one radius away from the notch surface and to be trivial at a 2 radii distance [94]. The relative size of the stress gradient relative to the underlying microstructure feature is often considered to be critical in determining the microstructure dependence of the notch sensitivity factor [95]. Similarly, it is reasonable to postulate that the extended stress gradient proximate to the larger corrosion damage would lead to enhanced small crack growth rates deeper into the material which could result in the observed decrease in N_{total}. While reasonable, this hypothesis is not consistent with data in **Figure 2.2.4** that shows the convergence of the da/dN data for FIS, DP1, DP2, and GCSR after the crack extends ~100 μm away from the corrosion feature. Critically, these quantitative data do not support the hypothesis that the decrease in N_{total} for deeper corrosion damage is due to enhanced growth rates associated with faster small crack growth kinetics due to an extended stress gradient.

The third hypothesis contends that slight decrease in N_{total} for deeper corrosion damage is simply due to the larger initial flaw size, as such, once initiated the crack will be closer to the critical crack size for failure (i.e. the crack size at which K_{max} exceeds the fracture toughness). Considering Eqn. 1, the data in **Table 2.2.1** demonstrates that for DP2, FIS, and GCSR that the N_i values are reasonably constant and low. Furthermore, as expected the N_{long} (which is the number of cycles to failure from a crack length of 900 μm from the corroded surface to failure) shows only a modest variation between DP2, FIS and GCSR; with the cycles to failure actually be on-average longer for the GCSR. The observed decrease in N_{total} going from DP2 and FIS (which are nearly identical) to GCSR must be due to an increase in N_{short}, which is the cycles to propagate from 10 μm beyond the initiation feature on the corrosion damage to 900 μm from the original corroded surface. Critically, due to the different initial damage depths, the amount of distance of crack advance in this N_{short} regime varies between DP2 (on average 693 μm), FIS (735 μm), and GCSR (267 μm). **Figure 2.2.4** demonstrates that the small crack growth rates are nearly identical for each corrosion conditions in this size range, as such it is expected that the GCSR samples will have lower N_{short} and thus lower N_{total} values. This expectation is quantitatively validated through marker band analysis that shows that the average N_{short} for GCSR (71,986 cycles) is well below that of DP2 (195,379 cycles) and FIS (175,146 cycles).

2.2.5 Conclusion

The fatigue behavior and crack growth rates of specimens with different damage morphologies representative of Al-stainless steel galvanic coupling are evaluated in moist air at 23^{o}C. Different stages of fatigue life are quantified for each specimen. Several corrosion macro-scale metrics are correlated to the location of the fatigue initiation sites. This systematic investigation of the effects of macro-scale corrosion feature on the fatigue initiation and fatigue behavior of AA 7050-T7451 established the following conclusions:

- Presence of corrosion damage on the surface of the aluminum greatly reduced the total fatigue life of AA 7050-T7451. The fatigue crack initiation life for vastly different corrosion morphologies is relatively constant and can be assumed negligible at this relatively high maximum stress level (200 MPa).
- The metrics analyzed for the macro-scale corrosion damage feature and the combination effects of these metrics do not fully dictate the location of fatigue crack formation sites. The complex interaction of corrosion micro-scale features as well as the presence of nearby constituent particles needs to be further investigated.
- The crack growth rates for specimens having different corrosion damage morphologies converge to comparable values as the crack extends away from the corrosion damage feature.

- The slight decrease in total fatigue life as the corrosion damage increases in severity (despite constant initiation lives) is attributed to an increase in the number of crack formation sites and larger crack formation features that decrease the crack propagation length necessary to reach the critical crack size for failure.

2.2.6 References

[1] Starke EA, Staley JT. Application of modern aluminum alloys to aircraft. Progr Aerosp Sci 1996;32:131–72.

[2] Campbell F. Manufacturing Technology for Aerospace Structural Materials. Manuf. Technol. Aerosp. Struct. Mater., Elsevier; 2006, p. 15–92. doi:10.1016/B978-185617495-4/50002-0.

[3] Shoales GA, Fawaz SA, Walters MR. Compilation of damage findings from multiple recent teardown analysis programs. Bridg. Gap between Theory Oper. Pract. 25th ICAF Symp., Rotterdam, The Netherlands: Springer; 2009, p. 187–207. doi:10.1007/978-90-481-2746-7_11.

[4] Cole G, Clark G, Sharp P. The implication of corrosion with respect to aircraft structural integrity. Report No: DSTO-RR-0102. Commonwealth of Australia: DSTO Aeronautical and Maritime Research Laboratory Melbourne; 1997.

[5] Wanhill RJH, De Luccia JJ. An AGARD-coordinated corrosion fatigue cooperative testing programme. AGARD Report No. 695. 1982.

[6] Barter SA, Molent L, Wanhill RJH. Typical fatigue-initiating discontinuities in metallic aircraft structures. Int J Fatigue 2012;41:11–22. doi:10.1016/j.ijfatigue.2011.10.017.

[7] Barter SA, Molent L. Fatigue cracking from a corrosion pit in an aircraft bulkhead. Eng Fail Anal 2014;39:155–63. doi:10.1016/j.engfailanal.2014.01.020.

[8] Murer N, Buchheit RG. Stochastic modeling of pitting corrosion in aluminum alloys. Corros Sci 2013;69:139–48. doi:10.1016/j.corsci.2012.11.034.

[9] Buchheit RG, Birbilis N, Gambina F. Characterization and modeling of localized corrosion damage accumulation for aircraft structural integrity. Int. Conf. Fract. 11, Turin, Italy: 2005.

[10] Birbilis N, Buchheit RG. Electrochemical characteristics of intermetallic phases in aluminum alloys. J Electrochem Soc 2005;152:B140–51. doi:10.1149/1.1869984.

[11] Frantziskonis GN, Simon LB, Woo J, Matikas TE. Multiscale characterization of pitting corrosion and application to an aluminum alloy. Eur J Mech A/Solids 2000;19:309–18. doi:10.1016/S0997-7538(00)00162-5.

[12] Rusk DT, Hoppe W. Fatigue life prediction of corrosion-damaged high-strength steel using an equivalent stress riser (ESR) model Part I: Test development and results. Int J Fatigue 2009;31:1454–63. doi:10.1016/j.ijfatigue.2009.05.006.

[13] Jones K, Hoeppner DW. The interaction between pitting corrosion, grain boundaries, and constituent particles during corrosion fatigue of 7075-T6 aluminum alloy. Int J Fatigue 2009;31:686–92. doi:10.1016/j.ijfatigue.2008.03.016.

[14] Newman JC, Abbott W. Fatigue-life calculations on pristine and corroded open-hole specimens using small-crack theory. Int J Fatigue 2009;31:1246–53. doi:10.1016/j.ijfatigue.2009.01.007.

[15] Jones K, Hoeppner DW. Prior corrosion and fatigue of 2024-T3 aluminum alloy. Corros Sci 2006;48:3109–22. doi:10.1016/j.corsci.2005.11.008.

[16] Sankaran KK, Perez R, Jata KV. Effects of pitting corrosion on the fatigue behavior of aluminum alloy 7075-T6: modeling and experimental studies. Mater Sci Eng A 2001;297:223–9. doi:10.1016/S0921-5093(00)01216-8.

[17] Burns JT, Kim S, Gangloff RP. Effect of corrosion severity on fatigue evolution in Al-Zn-Mg-Cu. Corros Sci 2010;52:498–508. doi:10.1016/j.corsci.2009.10.006.

[18] Burns JT, Larsen JM, Gangloff RP. Driving forces for localized corrosion-to-fatigue crack transition in Al-Zn-Mg-Cu. Fatigue Fract Eng Mater Struct 2011;34:745–73. doi:10.1111/j.1460-2695.2011.01568.x.

[19] Burns JT, Larsen JM, Gangloff RP. Effect of initiation feature on microstructure-scale fatigue crack propagation in Al-Zn-Mg-Cu. Int J Fatigue 2012;42:104–21. doi:10.1016/j.ijfatigue.2011.08.001.

[20] Turnbull A, McCartney LN, Zhou S. A model to predict the evolution of pitting corrosion and the pit-to-crack transition incorporating statistically distributed input parameters. Corros Sci 2006;48:2084–105. doi:10.1016/j.corsci.2005.08.010.

[21] Rajasankar J, Iyer NR, Gopinath S. Probabilistic modelling of fatigue crack initiation from pits and pit clusters in aluminium alloys. Corros Eng Sci Technol 2007;42:260–5. doi:10.1179/174327807X214626.

[22] Hoeppner DW, Taylor AMH. Chapter 13 –Modeling pitting corrosion fatigue: pit growth and pit/crack transition issues. RTO-AG-AVT-140 Corros. Fatigue Environ. Assist. Crack. Aging Mil. Veh., 2011, p. 1–20.

[23] Smith SW, Newman JA, Piascik RS. Simulation of fatigue crack initiation at corrosion pits with EDM notches. Report No. L-18262. Hampton, Virginia: 2003.

[24] DuQuesnay DL, Underhill PR, Britt HJ. Fatigue crack growth from corrosion damage in 7075-T6511 aluminium alloy under aircraft loading. Int J Fatigue

2003;25:371–7. doi:10.1016/S0142-1123(02)00168-8.

[25] Medved JJ, Breton M, Irving PE. Corrosion pit size distributions and fatigue lives - A study of the EIFS technique for fatigue design in the presence of corrosion. Int J Fatigue 2004;26:71–80. doi:10.1016/S0142-1123(03)00069-0.

[26] Gangloff RP, Burns JT, Kim S. Laboratory characterization and fracture mechanics modeling of corrosion-fatigue interaction for aluminum alloy substitution. Final Report, Contract F09650-03-D-0001, WPAFB. OH: 2005.

[27] Burns JT, Gangloff RP. Scientific advances enabling next generation management of corrosion induced fatigue. Procedia Eng 2011;10:362–9. doi:10.1016/j.proeng.2011.04.062.

[28] Kim S, Burns JT, Gangloff RP. Fatigue crack formation and growth from localized corrosion in Al-Zn-Mg-Cu. Eng Fract Mech 2009;76:651–67. doi:10.1016/j.engfracmech.2008.11.005.

[29] Hoffman ME, Hoffman PC. Corrosion and fatigue research — structural issues and relevance to naval aviation. Int J Fatigue 2001;23:1–10. doi:10.1016/S0142-1123(01)00115-3.

[30] Hoffman PC. Fleet management issues and technology needs. Int J Fatigue 2009;31:1631–7. doi:10.1016/j.ijfatigue.2008.11.016.

[31] Liu C, Rafla V, Scully JR, Kelly RG. Mathematical modeling of potential and current distributions for atmospheric corrosion of galvanic coupling in airframe components. Corros. 2015, Dallas, Texas: NACE International; 2015.

[32] Rafla V, Davenport A, Scully JR. Determination of Cathodic and Anodic Charge from Operando X-Ray Tomography Observation of Galvanic Corrosion of Aluminum Alloy 7050-T7451 and 304 Stainless Steel in a Simulated Fastener. CORROSION 2015;71:1300–3. doi:10.5006/1871.

[33] Rafla V, King AD, Glanvill S, Parsons A, Davenport A, Scully JR. Operando Observation of Galvanic Corrosion Between Aluminum Alloy 7050-T7451 and 304 Stainless Steel in a Simulated Fastener Arrangement Using X-Ray Tomography. CORROSION 2015;71:1171–6. doi:10.5006/1813.

[34] Liao CM, Olive JM, Gao M, Wei RP. In-Situ Monitoring of Pitting Corrosion in Aluminum Alloy 2024. CORROSION 1998;54:451–8. doi:10.5006/1.3284873.

[35] Dixit M, Mishra RS, Sankaran KK. Structure–property correlations in Al 7050 and Al 7055 high-strength aluminum alloys. Mater Sci Eng A 2008;478:163–72. doi:10.1016/j.msea.2007.05.116.

[36] Chen JF, Zhen L, Jiang JT, Yang L, Shao WZ, Zhang BY. Microstructures and mechanical properties of age-formed 7050 aluminum alloy. Mater Sci Eng A

2012;539:115–23. doi:10.1016/j.msea.2012.01.067.

[37] Deshpande NU, Gokhale AM, Denzer DK, Liu J. Relationship between fracture toughness, fracture path, and microstructure of 7050 aluminum alloy: Part I. Quantitative characterization. Metall Mater Trans A 1998;29A:1191–201. doi:10.1007/s11661-998-0246-3.

[38] Deng Y, Yin Z, Cong F. Intermetallic phase evolution of 7050 aluminum alloy during homogenization. Intermetallics 2012;26:114–21. doi:10.1016/j.intermet.2012.03.006.

[39] Dumont D, Deschamps A, Bréchet Y, Sigli C, Ehrström JC. Characterisation of precipitation microstructures in aluminium alloys 7040 and 7050 and their relationship to mechanical behaviour. Mater Sci Technol 2004;20:567–76. doi:10.1179/026708304225016662.

[40] Dumont D, Deschamps A, Brechet Y. On the relationship between microstructure, strength and toughness in AA7050 aluminum alloy. Mater Sci Eng A 2003;356:326–36. doi:10.1016/S0921-5093(03)00145-X.

[41] Robson JD. Microstructural evolution in aluminium alloy 7050 during processing. Mater Sci Eng A 2004;382:112–21. doi:10.1016/j.msea.2004.05.006.

[42] Zhang JB, Zhang YA, Zhu BH, Liu RQ, Wang F, Liang QM. Characterization of microstructure and mechanical properties of Al–Cu–Mg–Ag–(Mn/Zr) alloy with high Cu:Mg. Mater Des 2013;49:311–7. doi:10.1016/j.matdes.2013.01.044.

[43] Pao PS, Feng CR, Gill SJ. Corrosion Fatigue Crack Initiation in Aluminum Alloys 7075 and 7050. CORROSION 2000;56:1022–31. doi:10.5006/1.3294379.

[44] Zhang J, Przystupa MA, Luévano AJ. Characterizations of pore and constituent particle populations in 7050-T7451 aluminum plate alloys. Metall Mater Trans A 1998;29:727–37. doi:10.1007/s11661-998-0263-2.

[45] McMurtrey MD, Bae D, Burns JT. Fracture mechanics modelling of constant and variable amplitude fatigue behaviour of field corroded 7075-T6511 aluminium. Fatigue Fract Eng Mater Struct 2017;40:605–22. doi:10.1111/ffe.12536.

[46] Molent L. Managing airframe fatigue from corrosion pits – A proposal. Eng Fract Mech 2015;137:12–25. doi:10.1016/j.engfracmech.2014.09.001.

[47] Sabelkin V, Perel VY, Misak HE, Hunt EM, Mall S. Investigation into crack initiation from corrosion pit in 7075-T6 under ambient laboratory and saltwater environments. Eng Fract Mech 2015;134:111–23. doi:10.1016/j.engfracmech.2014.12.016.

[48] Donahue JR, Burns JT. Effect of chloride concentration on the corrosion–fatigue crack behavior of an age-hardenable martensitic stainless steel. Int J Fatigue

2016;91:79–99. doi:10.1016/j.ijfatigue.2016.05.022.

[49] Turnbull A. The environmentally small/short crack growth effect: current understanding. Corros Rev 2012;30:1–17. doi:10.1515/corrrev-2012-0003.

[50] Turnbull A. Corrosion pitting and environmentally assisted small crack growth. Proc R Soc A Math Phys Eng Sci 2014;470:20140254. doi:10.1098/rspa.2014.0254.

[51] van der Walde K, Hillberry BM. Initiation and shape development of corrosion-nucleated fatigue cracking. Int J Fatigue 2007;29:1269–81. doi:10.1016/j.ijfatigue.2006.10.010.

[52] Walde K Van Der, Hillberry BMM, van der Walde K, Hillberry BMM, Walde K Van Der, Hillberry BMM, et al. Characterization of pitting damage and prediction of remaining fatigue life. Int J Fatigue 2008;30:106–18. doi:10.1016/j.ijfatigue.2007.02.020.

[53] van der Walde K, Brockenbrough JR, Craig BA, Hillberry BM. Multiple fatigue crack growth in pre-corroded 2024-T3 aluminum. Int J Fatigue 2005;27:1509–18. doi:10.1016/j.ijfatigue.2005.06.026.

[54] Jones K, Hoeppner DW. Pit-to-crack transition in pre-corroded 7075-T6 aluminum alloy under cyclic loading. Corros Sci 2005;47:2185–98. doi:10.1016/j.corsci.2004.10.004.

[55] Zhou, Turnbull. Influence of pitting on the fatigue life of a turbine blade steel. Fatigue Fract Eng Mater Struct 1999;22:1083–93. doi:10.1046/j.1460-2695.1999.00226.x.

[56] Turnbull A. Characterising the pit to crack transition. Annu. Conf. Australas. Corros. Assoc. 2012, Melbourne, Victoria, Australia: 2012, p. 139–45.

[57] Turnbull A, Horner DA, Connolly BJ. Challenges in modelling the evolution of stress corrosion cracks from pits. Eng Fract Mech 2009;76:633–40. doi:10.1016/j.engfracmech.2008.09.004.

[58] ASTM International. ASTM E112 Standard Test Methods for Determining Average Grain Size. 2013.

[59] ASTM International. ASTM E1382 Standard Test Methods for Determining Average Grain Size Using Semiautomatic and Automatic Image Analysis. 2010.

[60] Papazian JM, Anagnostou EL, Engel SJ, Hoitsma D, Madsen J, Silberstein RP, et al. A structural integrity prognosis system. Eng Fract Mech 2009;76:620–32. doi:10.1016/j.engfracmech.2008.09.007.

[61] Khullar P, Badilla JV, Lim MLC, Hahn SC, Ellis DW, Kelly RG. Critical factors

affecting intergranular corrosion of AA5083 under atmospheric axposures. ECS Meet. Abstr., vol. MA2015-02, 2015, p. 689.

[62] O Mahony C, Hill M, Brunet M, Duane R, Mathewson A. Characterization of micromechanical structures using white-light interferometry. Meas Sci Technol 2003;14:1807–14. doi:10.1088/0957-0233/14/10/310.

[63] Holme B, Lunder O. Characterisation of pitting corrosion by white light interferometry. Corros Sci 2007;49:391–401. doi:10.1016/j.corsci.2006.04.022.

[64] Rusk DT, Hoppe W, Braisted W, Powar N. Corrosion fatigue life prediction using an equivalent stress riser model. 11th Jt. NASA/FAA/DoD Conf. Aging Aircr., Phoenix, AZ: 2008.

[65] Salvo L, Cloetens P, Maire E, Zabler S, Blandin J., Buffière J., et al. X-ray micro-tomography an attractive characterisation technique in materials science. Nucl Instruments Methods Phys Res Sect B Beam Interact with Mater Atoms 2003;200:273–86. doi:10.1016/S0168-583X(02)01689-0.

[66] Marrow J, Reinhard C, Vertyagina Y, Saucedo-Mora L, Collins D, Mostafavi M. 3D Studies of Damage by Combined X-ray Tomography and Digital Volume Correlation. Procedia Mater Sci 2014;3:1554–9. doi:10.1016/j.mspro.2014.06.251.

[67] King A, Ludwig W, Herbig M, Buffière J-Y, Khan AA, Stevens N, et al. Three-dimensional in situ observations of short fatigue crack growth in magnesium. Acta Mater 2011;59:6761–71. doi:10.1016/j.actamat.2011.07.034.

[68] Khor KH, Buffiére J-Y, Ludwig W, Toda H, Ubhi HS, Gregson PJ, et al. In situ high resolution synchrotron x-ray tomography of fatigue crack closure micromechanisms. J Phys Condens Matter 2004;16:S3511–5. doi:10.1088/0953-8984/16/33/012.

[69] Barter SA, Molent L, Goldsmith N, Jones R. An experimental evaluation of fatigue crack growth. Eng Fail Anal 2005;12:99–128. doi:10.1016/j.engfailanal.2004.04.002.

[70] Barter SA, Molent L, Wanhill RJH. Marker loads for quantitative fractography of fatigue cracks in aerospace alloys. Bridg. Gap between Theory Oper. Pract. 25th ICAF Symp., Rotterdam, The Netherlands: 2009, p. 14–54.

[71] Spear AD, Li SF, Lind JF, Suter RM, Ingraffea AR. Three-dimensional characterization of microstructurally small fatigue-crack evolution using quantitative fractography combined with post-mortem X-ray tomography and high-energy X-ray diffraction microscopy. Acta Mater 2014;76:413–24. doi:10.1016/j.actamat.2014.05.021.

[72] Barter SA. Fatigue crack growth in 7050T7451 aluminium alloy thick section plate

with a surface condition simulating some regions of the F / A-18 structure. Report No. DSTO-TR-1458. Fishermans Bend, Victoria, Australia: 2003.

[73] Lam KY, Phua SP. Multiple crack interaction and its effect on stress intensity factor. Eng Fract Mech 1991;40:585–92. doi:10.1016/0013-7944(91)90152-Q.

[74] Loehnert S, Belytschko T. Crack shielding and amplification due to multiple microcracks interacting with a macrocrack. Int J Fract 2007;145:1–8. doi:10.1007/s10704-007-9094-1.

[75] Co NEC, Burns JT. Galvanic corrosion-induced fatigue crack initiation and propagation behavior in AA7050-T7451. CORROSION 2016;72:1215–9. doi:10.5006/2132.

[76] Mordo S, Popravko V, Barari A. Study of the effect of coating parameters and substrates on 3D surface roughness in diamond-like-carbon coating process. IFAC Proc Vol 2013;46:1861–6. doi:10.3182/20130619-3-RU-3018.00585.

[77] Pohl M, Stella J. Quantitative CLSM roughness study on early cavitation-erosion damage. Wear 2002;252:501–11. doi:10.1016/S0043-1648(02)00003-0.

[78] Kumar RK, Seetharamu S, Kamaraj M. Quantitative evaluation of 3D surface roughness parameters during cavitation exposure of 16Cr–5Ni hydro turbine steel. Wear 2014;320:16–24. doi:10.1016/j.wear.2014.07.015.

[79] Shivanna DM, Kiran MB, Kavitha SD. Evaluation of 3D surface roughness parameters of EDM components using vision system. Procedia Mater Sci 2014;5:2132–41. doi:10.1016/j.mspro.2014.07.416.

[80] Franco LA, Sinatora A. 3D surface parameters (ISO 25178-2): Actual meaning of Spk and its relationship to Vmp. Precis Eng 2015;40:106–11. doi:10.1016/j.precisioneng.2014.10.011.

[81] Horner DA, Connolly BJ, Zhou S, Crocker L, Turnbull A. Novel images of the evolution of stress corrosion cracks from corrosion pits. Corros Sci 2011;53:3466–85. doi:10.1016/j.corsci.2011.05.050.

[82] Harlow DG, Wei RP. Probability modeling and material microstructure applied to corrosion and fatigue of aluminum and steel alloys. Eng Fract Mech 2009;76:695–708. doi:10.1016/j.engfracmech.2008.01.010.

[83] Cerit M, Genel K, Eksi S. Numerical investigation on stress concentration of corrosion pit. Eng Fail Anal 2009;16:2467–72. doi:10.1016/j.engfailanal.2009.04.004.

[84] Przybyla C, Prasannavenkatesan R, Salajegheh N, McDowell DL. Microstructure-sensitive modeling of high cycle fatigue. Int J Fatigue 2010;32:512–25. doi:10.1016/j.ijfatigue.2009.03.021.

[85] Sangid MD. The physics of fatigue crack initiation. Int J Fatigue 2013;57:58–72. doi:10.1016/j.ijfatigue.2012.10.009.

[86] McDowell DL, Dunne FPE. Microstructure-sensitive computational modeling of fatigue crack formation. Int J Fatigue 2010;32:1521–42. doi:10.1016/j.ijfatigue.2010.01.003.

[87] Bennett V, McDowell DL. Polycrystal orientation distribution effects on microslip in high cycle fatigue. Int J Fatigue 2003;25:27–39. doi:10.1016/S0142-1123(02)00057-9.

[88] Rovinelli A, Lebensohn RA, Sangid MD. Influence of microstructure variability on short crack behavior through postulated micromechanical short crack driving force metrics. Eng Fract Mech 2015;138:265–88. doi:10.1016/j.engfracmech.2015.03.001.

[89] Chan KS. Roles of microstructure in fatigue crack initiation. Int J Fatigue 2010;32:1428–47. doi:10.1016/j.ijfatigue.2009.10.005.

[90] Hochhalter JD, Littlewood DJ, Christ RJ, Veilleux MG, Bozek JE, Ingraffea AR, et al. A geometric approach to modeling microstructurally small fatigue crack formation: II. Physically based modeling of microstructure-dependent slip localization and actuation of the crack nucleation mechanism in AA 7075-T651. Model Simul Mater Sci Eng 2010;18:45004. doi:10.1088/0965-0393/18/4/045004.

[91] Hochhalter JD, Littlewood DJ, Veilleux MG, Bozek JE, Maniatty AM, Rollett AD, et al. A geometric approach to modeling microstructurally small fatigue crack formation: III. Development of a semi-empirical model for nucleation. Model Simul Mater Sci Eng 2011;19:35008. doi:10.1088/0965-0393/19/3/035008.

[92] Barter SA, Sharp PK, Holden G, Clark G. Initiation and early growth of fatigue cracks in an aerospace aluminium alloy. Fatigue Fract Eng Mater Struct 2002;25:111–25. doi:10.1046/j.1460-2695.2002.00482.x.

[93] Hu W, Liu Q, Barter SA. A study of interaction and coalescence of microsurface fatigue cracks in aluminium 7050. 25th ICAF Symp., 2009, p. 643–59.

[94] Pilkey WD, Pilkey DF. Notches and Grooves. Peterson's Stress Conc. Factors, Hoboken, NJ, USA: John Wiley & Sons, Inc.; 2008, p. 57–134. doi:10.1002/9780470211106.ch2.

[95] Schijve J, editor. Stress Concentration at Notches. Fatigue Struct. Mater., Dordrecht: Springer Netherlands; 2009, p. 59–88. doi:10.1007/978-1-4020-6808-9_3.

2.3 Effects of Relevant Corrosion Morphology, Relative Humidity, and σ_{max} on Fatigue Crack Initiation and Fatigue Behavior

2.3.1 Introduction

Previous work described in Chapter 2 Section 1 and detailed in Section 2 considered macro-scale corrosion feature effects in the fatigue behavior of AA 7050-T7451 with various corrosion morphologies (discrete pits, general corrosion with surface recession, and fissure morphologies) but at a fixed stress level, and loading environment [1]. This section will expand this effort to additional morphologies, an additional stress level, and alternate loading environments to determine if the conclusions established in Chapter 2 Section 2 can be more broadly extended.

First, during ongoing study of galvanically induced corrosion due to aluminum coupling with stainless steel, collaborators have observed potentially more "relevant" corrosion morphologies can develop [2]. Most of the corrosion damage considered in the prior works on fatigue of corroded aluminum alloys are artificially created using electrochemical techniques producing discrete pits or clustered pits [3,4]. It is useful to consider the effect of more "relevant" corrosion morphologies on fatigue life and fatigue initiation of aluminum alloys. Based on the results in Chapter 2 Section 2, it is postulated that the fatigue initiation location is not dictated by the macro-scale corrosion damage feature for the additional morphologies tested in this section.

Second, many researchers have reported that a change in the relative humidity can cause change on the fatigue crack growth rate causing a decrease on total fatigue life when the relative humidity is increased [5–15]. However, this previous study did not mention the effects of relative humidity on fatigue crack initiation in terms of the number of fatigue initiation sites and the number of cycles to initiate a fatigue crack. Limited work has been done on the effects of relative humidity on fatigue crack initiation of corroded specimens. Most of the published fatigue crack initiation studies on corroded aluminum specimens are fatigue tested under uncontrolled laboratory air condition [4,16,17]. Some published studies that perform fatigue testing on controlled relative humidity did not look at the particular effect of relative humidity on fatigue initiation [3,10,12,18]. For this study, it is hypothesized that the increase in the level of relative humidity affects the small scale crack growth rate and decrease the fatigue crack initiation life. It is also posited that the amount/level of relative humidity affects the location of the fatigue crack initiation.

Third, an increase in the maximum load generally decreases the total fatigue life. Prior work looked at the effect of maximum load on a controlled corrosion pit that represents a broadly corroded surface with various pit depths [12]. Burns et al. reported that an increase in the maximum load caused fatigue cracks to form quickly at various crack formation sites, and the fatigue initiation life decreases toward zero [12]. However, there is no reported literature investigating how the maximum load impacts the fatigue crack initiation from various corrosion morphologies in aerospace aluminum alloys. Thus, it is theorized that the increase in the maximum load resulting to the decrease in total fatigue life is due to the decrease in fatigue initiation life related to the increase in crack growth rates. It is also hypothesized that the increase in the maximum load affects the location of fatigue crack initiation.

This section will address each of the knowledge gaps detailed above. Specifically, the objective of this study is to determine the effects of more "relevant" corrosion damage on the fatigue initiation location, fatigue initiation life and total fatigue life. Two additional corrosion morphologies are considered: cigar-shaped pits and intergranular corrosion (IGC). Additionally, this study aims to understand the effects of relative humidity and σ_{max} on fatigue initiation location, number of cycles to initiate a crack, total fatigue life and crack growth rates of AA 7050-T7451 with randomly distributed discrete pits.

2.3.2 Methodology

The AA 7050-T7451 fatigue specimens used in all the experiments were machined to have a thickness of 7.60mm, reduced gage width of 7.60 and uniform gage length of 20.96 mm as shown in **Figure 2.3.1** . Details of the material composition and grain sizes are reported in Chapter 2 Section 2. Based on the manufacturer's certificate, the representative tensile strength of the specimens is 471 MPa (L orientation), the ultimate tensile strength is 510 MPa (L orientation), and the fracture toughness is 43 MPa√m (L-T orientation).

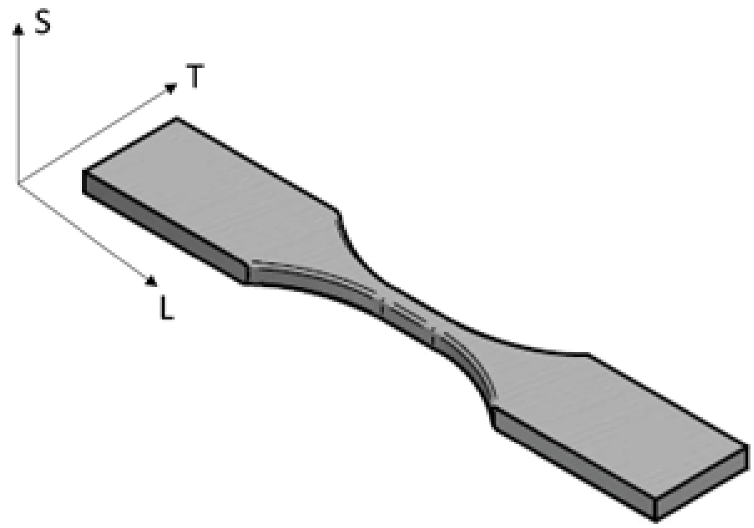

Figure 2.3.1 Fatigue specimen machined from AA 7050-T7451 plate

The surface of the AA 7050-T7451 specimens were prepared by polishing using 600 grit SiC paper. Several corrosion protocols were considered for the experiments. These corrosion protocols were developed in a companion study [2]. A small area (~4-7 mm^2) of the polished LS surface were exposed to each corresponding electrochemical or corrosion protocol to create the desired corrosion damage. A solvent resistant electroplating tape and a peelable rubber butyl (Miccro Super XP2000) were used to mask the specimen exposing only the desired area on the LS surface. In order to create the cigar-shaped corrosion damage, the AA 7050-T7451 specimens were held at a constant potential of -730 mV_{SCE} for 72 h with 0.M NaCl (pH = 5.5) as the electrolyte. The specimens with cigar-shaped corrosion damage are labeled DP3. In order to artificially create the IGC on the AA 7050-T7451 specimens, a zero resistance ammeter (ZRA) protocol was used. The exposed area of the anode (AA 7050-T7451) and the cathode (SS316) were the same. Strips of electroplating tape with a 3 mm punched hole were used to control the exposed area of the anode and the cathode. The ZRA tests were performed using 0.5 M NaCl electrolyte with pH adjusted to 3 using HCl. The ZRA test lasted for 504 h. The specimens subjected to ZRA test were labeled as IGC specimens.

The specimens used for the low relative humidity (< 5%) tests and high σ_{max} (300 MPa) tests were potentiostatically held at -700 mV_{SCE} for 1.5 h in order to create discrete pits. The electrolyte used for these specimen was 0.5 M NaCl with pH adjusted to 8 by adding $NaAlO_2$. These specimens were labeled DP1 since the electrochemical parameter used to artificially create the pits were identical to the protocol [1] detailed in Chapter 2 Section 2. After the electrochemical exposure, the specimens were cleaned using HNO_3 to remove the corrosion product on the surface of AA 7050-T7451 based on ASTM G1[19]. After which, the specimens were subjected to ultrasonic cleaning with DI water, then with acetone, then with methanol for 15 minutes each. The specimens were kept in a desiccator to prevent further corrosion.

The specimens were characterized using the optical microscope and the white light interferometer (WLI) before fatigue testing. These images coupled with the SEM images of the corroded surface and fracture surface (post-fatigue test) were used to locate the fatigue initiation site. X-ray computed tomography (XCT) imaging was also performed post-fatigue test in order to capture deep narrow fissures in the IGC specimens.

Table 2.3.1 provides details of the fatigue testing. The IGC and DP3 specimens were tested using test setting 1. Three replicates of fatigue testing were performed. On the other hand, 2 of the DP1 specimens were tested using setting 2 and the other 2 DP1 specimens were tested using setting 3. The specimens were cyclically loaded along the L direction. The fatigue testing protocol for all settings used baseline loading with R ratio ($\sigma_{min}/\sigma_{max}$) of 0.5 run at 20 Hz frequency, while the marker loading cycles had an R ratio of 0.1 at a frequency of 10 Hz. The marker sequence included 4-8 segments of 35 cycles. The marker loading was alternated with varying number of baseline loading cycles (as reported in **Table 2.3.1**). Previous studies used marker band technique to determine the microstructurally small crack growth [1,3,10,12,20–23] and this technique does not induce loading transient and does not affect the total fatigue life of the material [3,10,12]. The fatigue loading protocol was programmed and automatically controlled using the Multi-Purpose Test program in the MTS software for the hydraulic frame.

Table 2.3.1 Parameters for fatigue test

	Relative Humidity	σ_{Max}	Baseline Loading Cycles
Test Setting 1	> 90 %	200 MPa	20,000
Test Setting 2	> 90%	300 MPa	1,000
Test Setting 3	< 5%	200 MPa	20,000

The relative humidity for test settings 1 and 2 were controlled using an acrylic chamber fastened to the specimen during the fatigue testing duration. Nitrogen gas (N_2) was bubbled through two containers of DI water. The DI water container was connected to the sealed acrylic chamber. The relative humidity for test setting 3 was controlled by blowing purified N_2 into the acrylic chamber. The relative humidity for the entire duration of test was kept at < 5 % for test setting 3 and an RH meter was used to monitor the actual relative humidity inside the acrylic chamber. **Figure 2.3.2** shows the experimental set up.

Figure 2.3.2 Fatigue test set-up for AA 7050-T7451 specimen contained in sealed acrylic chamber to control the test environment

The fracture surfaces were investigated using the SEM (FEI Quanta 650) with a working distance of 10-15 mm, accelerating voltage of 10 kV and spot size of 4. Fractographs were captured using 25×, 100×, 250× magnifications. Initiation point micrographs were taken at 500×, 1000× or 2000× magnification. The post-fatigue test analysis of the fracture surface enabled precise identification of the crack formation location and the fracture surface marks (called marker bands) created by the loading protocol. Crack growth rates (da/dN) were calculated from the difference in the distances (Δa) between two succeeding marker bands and the known number of baseline cycles (ΔN) pre-programmed during the cyclic loading. The initiation point that leads to final fracture was labeled as the primary fatigue crack. The initiation depth was referenced from the edge of the LS surface. Marker band distances were determined based on to the crack growth perpendicular from the non-corroded edge of the LS surface, see **Figure 2.3.3**. The first marker band typically observed on a fracture surface of AA 7xxx lie within 5-15 μm from the fatigue formation site [12]. The initiation life (N_i) to create a 10 μm crack from the initiation point was estimated using the calculated crack growth rates.

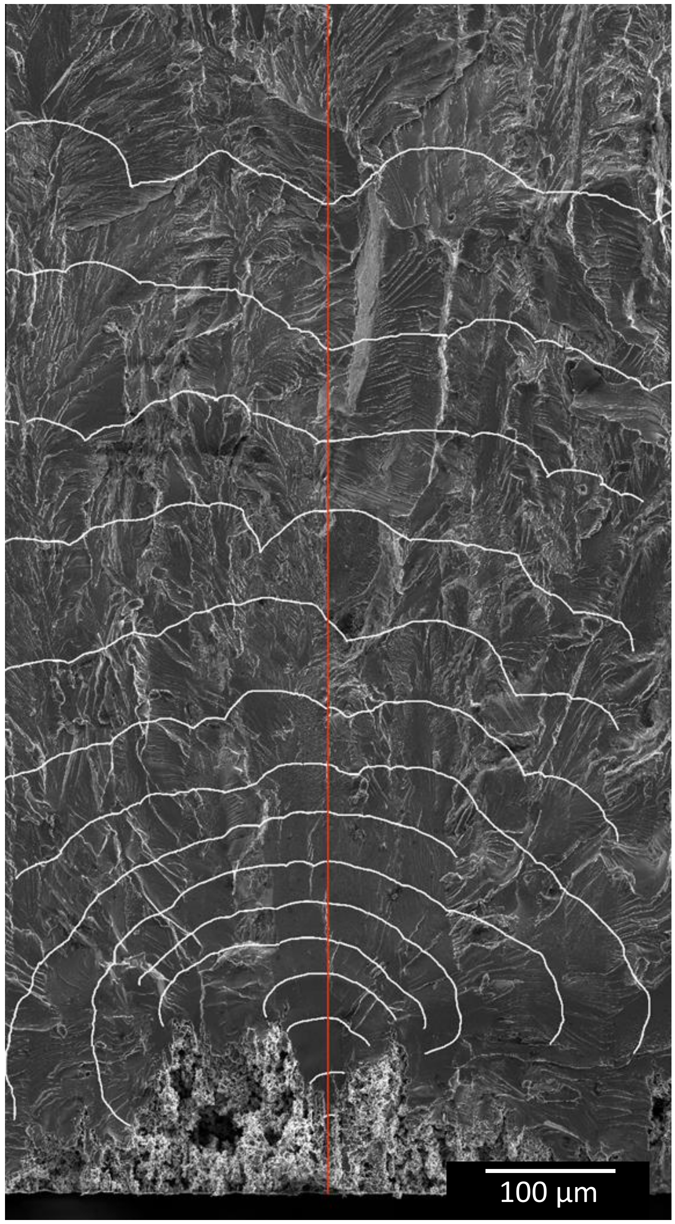

Figure 2.3.3 Traced marker bands on the fracture surface. Crack grows from bottom to top of the fractograph. Crack length, a, is measured (along the red line) from the non-corroded surface of the specimen.

2.3.3 Results

2.3.3.1 Corrosion Morphologies

Different corrosion morphologies are produced by exposing the small area of LS surface to different electrochemical environment. **Figure 2.3.4** shows the different corrosion damage shapes that formed on AA 7050-T7451. The difference in shape is revealed by examining the fracture surface (TS surface). DP3 specimens generally have elongated corrosion damage towards T direction (bottom to top of the fractograph). The IGC specimens show preferential attack on the grain boundaries of the AA 7050-T7451. Of note, while the IG character of the damage is not clearly evidenced in this figure, prior studies by collaborators have shown that IG fissuring will result from the applied exposure protocol [2]. **Figure 2.3.5** shows the cross section of relevant corrosion morphology obtained by the collaborators [2]. DP1 specimens show rough pits that form on the surface of the alloy, see **Figure 2.3.4** (c). The average aspect ratio (pit depth to half of pit width) obtained from the main fracture surface of DP3, IGC, DP1 specimens are 3.35, 7.67, 2.18 respectively.

The representative image in **Figure 2.3.6** provide illustrations of the distribution of pits on the LS surface of the AA 7050-T7451 for DP3, IGC and DP1 specimens. These images are captured using the WLI. These image provide information about the depth and general shape of the corrosion damage in DP3 and DP1 specimens but not for IGC. Based on the WLI readings the average pit depth for DP3 is 85.96, while 26.09 is the average depth for DP1 specimens. Note that the depth obtained from WLI may vary from the depth measured on the fracture surface using SEM. This can be due to the poor signal detected by the white light detector since it is a line of sight technique or due to non-structural (rough) corroded metal along the surface of the pit, see **Figure 2.3.4** (c). The narrow fissures of IGC are measured using XCT. The average fissure depth for the IGC specimens is 172.94 μm.

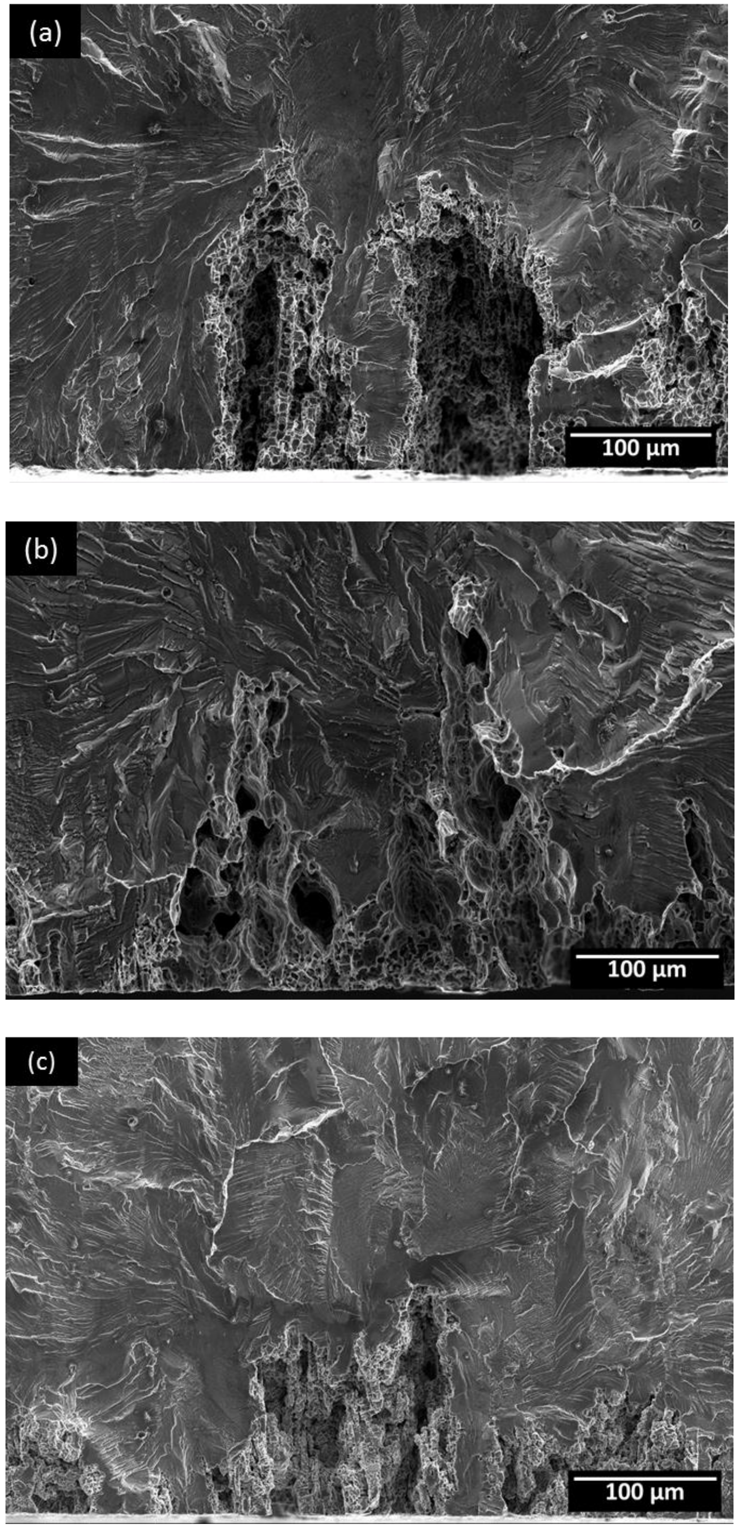

Figure 2.3.4 Fracture surface (TS surface) with corrosion damage that grew towards T-direction**.** (a) cigar-shaped corrosion damage (DP3); (b**)** intergranular corrosion damage (IGC) ; (c) discrete pit (DP1)

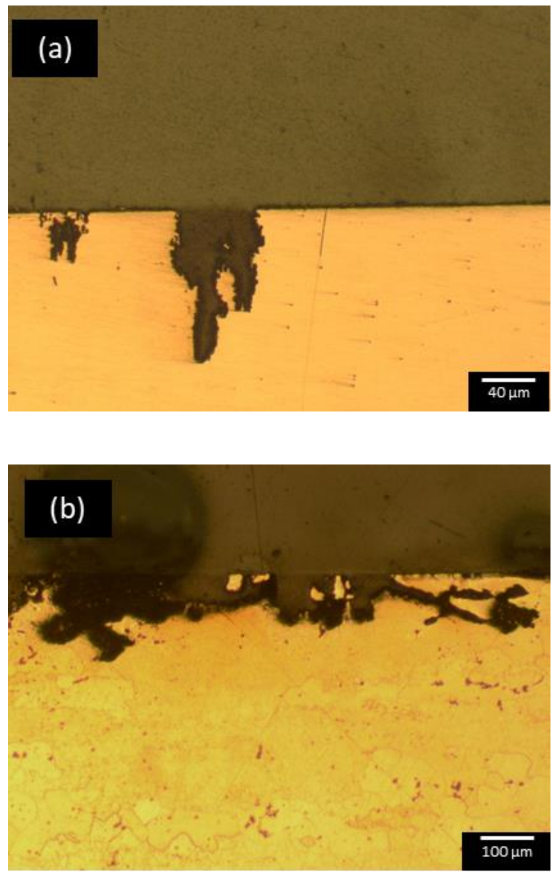

Figure 2.3.5 Cross section of specimens with relevant corrosion morphology (a) cigar-shaped pit (b) inter-granular corrosion from unpublished works of V. Rafla [2]

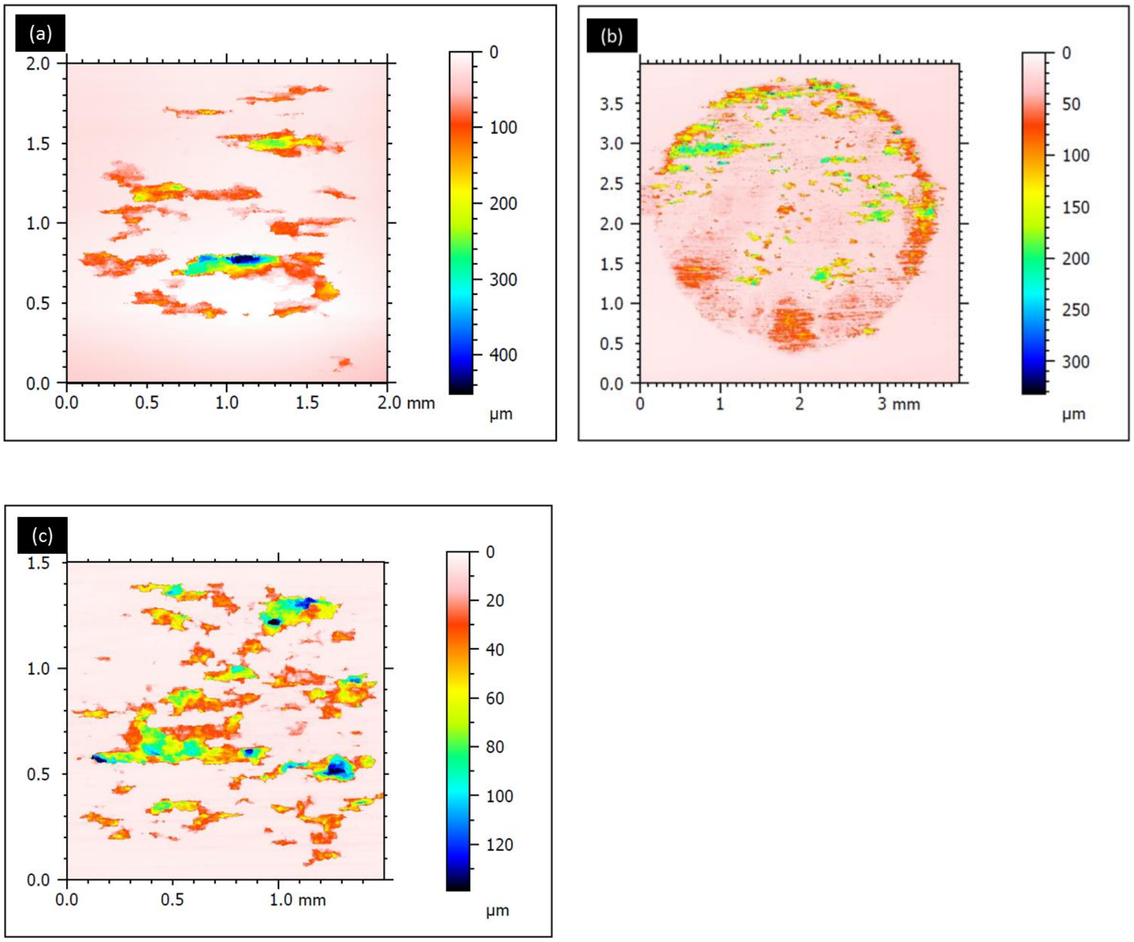

Figure 2.3.6 White light interferometry (WLI) image reconstruction using Mountains Map for (a) cigar- shaped corrosion (DP3), (b) intergranular corrosion (IGC) and (c) discrete pit (DP1) specimens. Spectrum on the right of each image shows depth of pits.

2.3.3.2 Crack formation location

The fatigue crack initiation sites are obtained by coupling the fractographs, optical images of the corrosion damage and the image obtained using WLI. Details of the determination of fatigue crack formation location is described in Chapter 2 Section 2. The marker bands and the river band patterns captured on the fractographs are helpful in identifying the crack formation location. All the fatigue cracks evaluated in this study initiates from the corrosion damage. All specimens tested have more than 1 fatigue crack formation site. These fatigue cracks initiating from different locations tend to grow and coalesce as the crack front advances. The coalescence of cracks starting from different initiation sites has been observed and previously studied [1,11,12,24–28]. The primary fatigue initiation site is the damage site that leads to final failure of the specimen. The depth of the corrosion feature that initiate the primary fatigue crack is measured using SEM. **Table 2.3.2** provides a summary of the number of fatigue crack formation sites seen on the main fracture plane, as well as the depth of the corrosion feature that initiates the primary fatigue crack.

Table 2.3.2 Summary of fatigue specimens and the corresponding depth of primary initiation point and the number of initiation points observed in the main fracture plane.

Specimen	Relative Humidity	σ_{max}	Depth of Initiation Point	Number of initiation points in the main fracture plane
		DP3		
R1	> 90%	200	78	2
R2	> 90%	200	174	3
R3	> 90%	200	99	2
		IGC		
R1	> 90%	200	229	2
R2	> 90%	200	150	5
R3	> 90%	200	69	5
		DP1		
R1	< 5%	200	112	3
R2	< 5%	200	45	5
		DP1		
R1	> 90%	300	45	4
R2	> 90%	300	103	4

2.3.3.3 Corrosion feature metrics

The corrosion metrics considered for DP3 and DP1 are pit depth, surface area of the pit mouth, volume, mean diameter of the pit mouth, and pit density. These metrics have been previously analyzed for other corrosion morphologies (shallow and deep discrete pits) and the details are reported in Chapter 2 Section 2. The images captured using the WLI are post processed using MountainsMap software in order to obtain the values for pit depth, area of the pit mouth, pit volume, mean diameter of the pit mouth and the number of pits. Pit density are calculated based on the number of pits for every 500 μm x 500 μm grid. The data obtained for DP3 are plotted as histograms in **Figure 2.3.7**. Only the data for pit depth, surface area of the pit mouth and pit density are plotted for DP3. The markers on the histograms indicate the corresponding value of the corrosion feature metrics for the primary initiation point. Fatigue crack formation location is generally not on the deepest pit nor on the pit having the largest surface area of the pit mouth. These fatigue crack initiation sites occur at areas not corresponding to the highest pit density. Pit volume and the diameter of the pit mouth metrics are also analyzed and the results (not shown) indicate that fatigue formation location does not correspond to the pit having the largest pit volume nor at the pit having the largest pit mouth diameter.

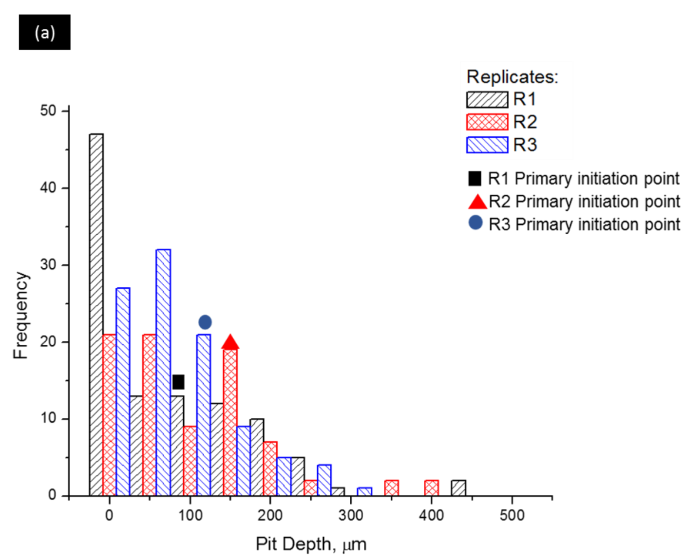

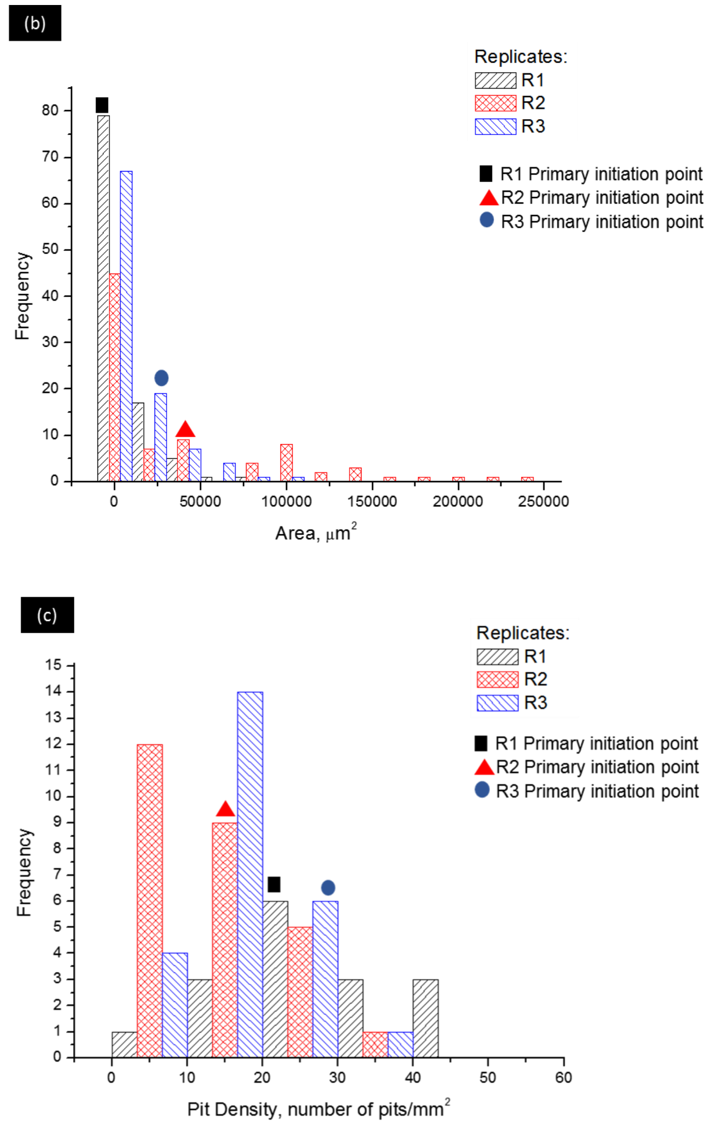

Figure 2.3.7 Histogram of corrosion feature metrics for the cigar-shaped corrosion specimens (DP3) (a) pit depth (b) area of the pit mouth, (c) pit density. The markers on the histograms indicate the location of the fatigue crack initiation.

The histograms in **Figure 2.3.8** are plotted using the pit depth and pit density data for DP1 specimens that are tested using high σ_{max} (test setting 2). The pit depth and pit density data for DP1 specimens used in the low relative humidity testing (test setting 3) are plotted as histograms in **Figure 2.3.9**. Markers on the figure represent the value of the corrosion metrics corresponding to the location of the fatigue crack that caused the final failure of the specimens. Both **Figure 2.3.8** and **Figure 2.3.9** show that fatigue crack formation sites do not correspond to the deepest corrosion pit, and they are not found on areas having the highest pit density.

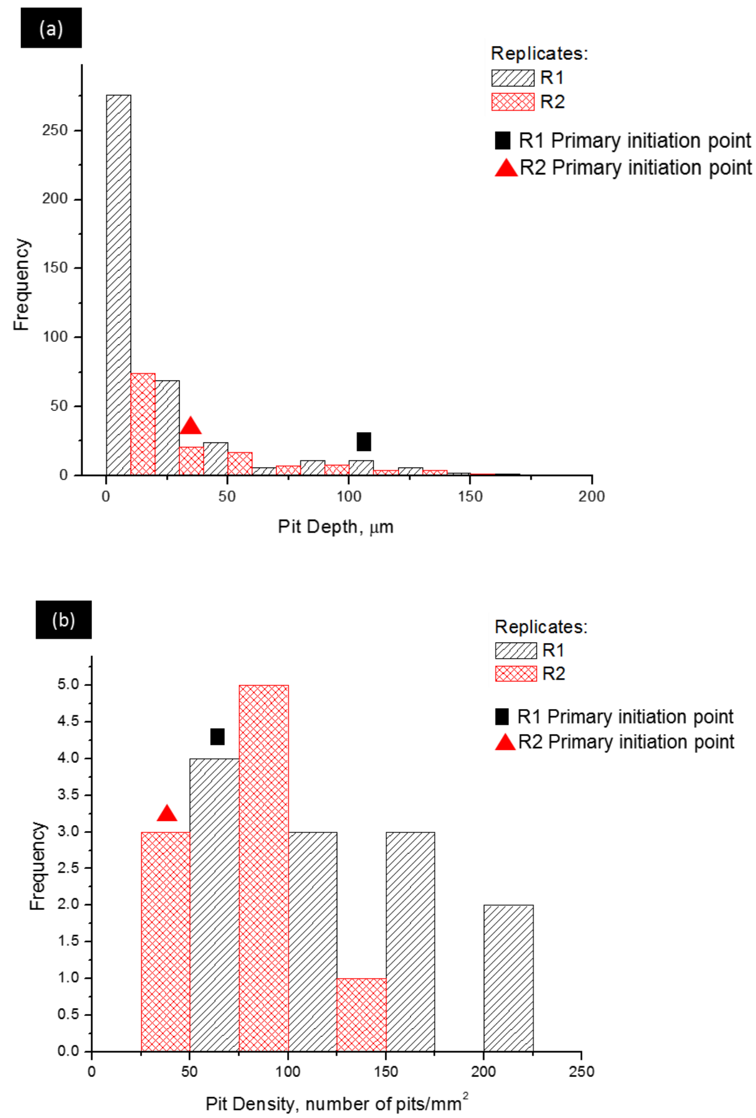

Figure 2.3.8 Histogram of corrosion metrics (a) pit depth, (b) pit density for DP1 specimens subjected to fatigue loading with high σ_{max} (300 MPa). Markers indicate the location of fatigue crack initiation.

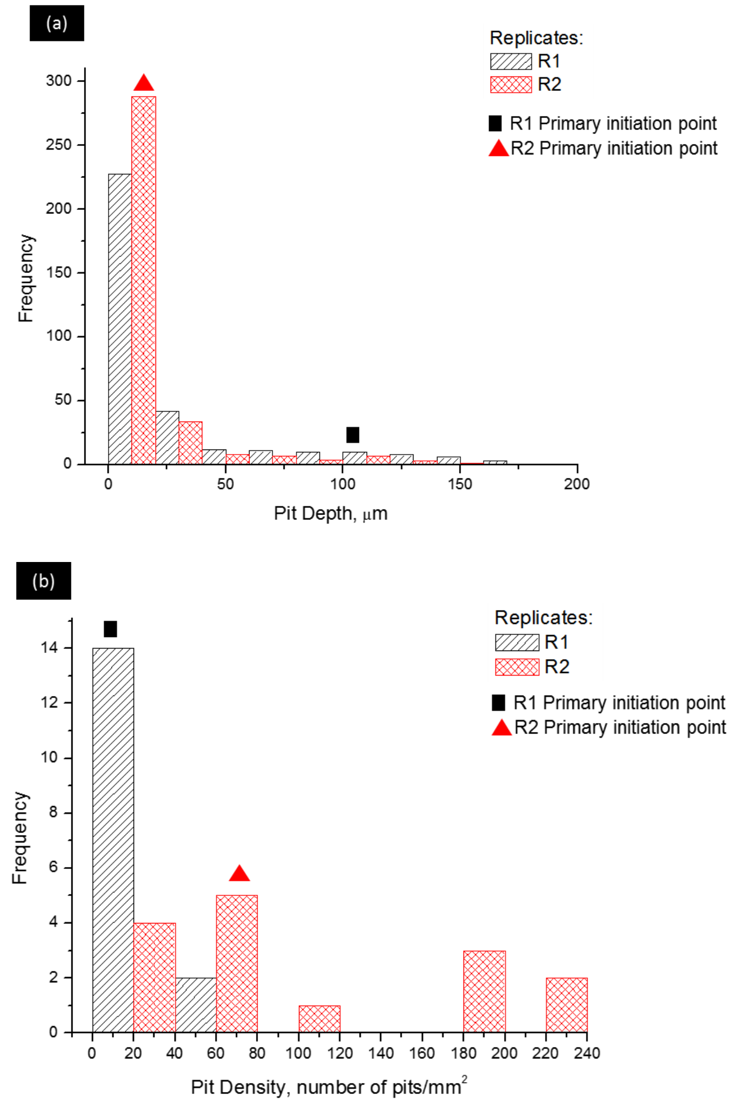

Figure 2.3.9 Histogram of corrosion metrics (a**)** pit depth, (b**)** pit density for DP1 specimens subjected to fatigue loading with low relative humidity (< 5%). Markers indicate the location of fatigue crack initiation.

The 2D images/slices are captured using XCT and these are reconstructed using Avizo software to form the 3D image. The fissure depths are measured every 50 μm along the L-direction. **Figure 2.3.10** shows a 3D reconstruction of the XCT images and the orthogonal views of the 2D slices. The data from the fissure measurements are plotted as histograms as shown in **Figure 2.3.11**. Markers on the histograms indicate the corrosion feature metrics corresponding to the primary fatigue initiation site. The corrosion metrics considered for IGC specimens are fissure depth, number of fissures per plane and the total depth of fissures per plane. These are the metrics used in analyzing the corrosion fissures as reported in Chapter 2 Section 2. The number of fissures per plane represent a density metrics, while a large value for the total depth of fissure per plane can indicate the number of deep fissures on the fracture plane. **Figure 2.3.11** shows that the fatigue crack formation location falls within the mid values for the fissure depth, total depth of fissures and number of fissures per plane. The fatigue crack did not initiate at the deepest fissure, at a plane with the deepest fissures, nor at the plane where there is a high number density of fissures.

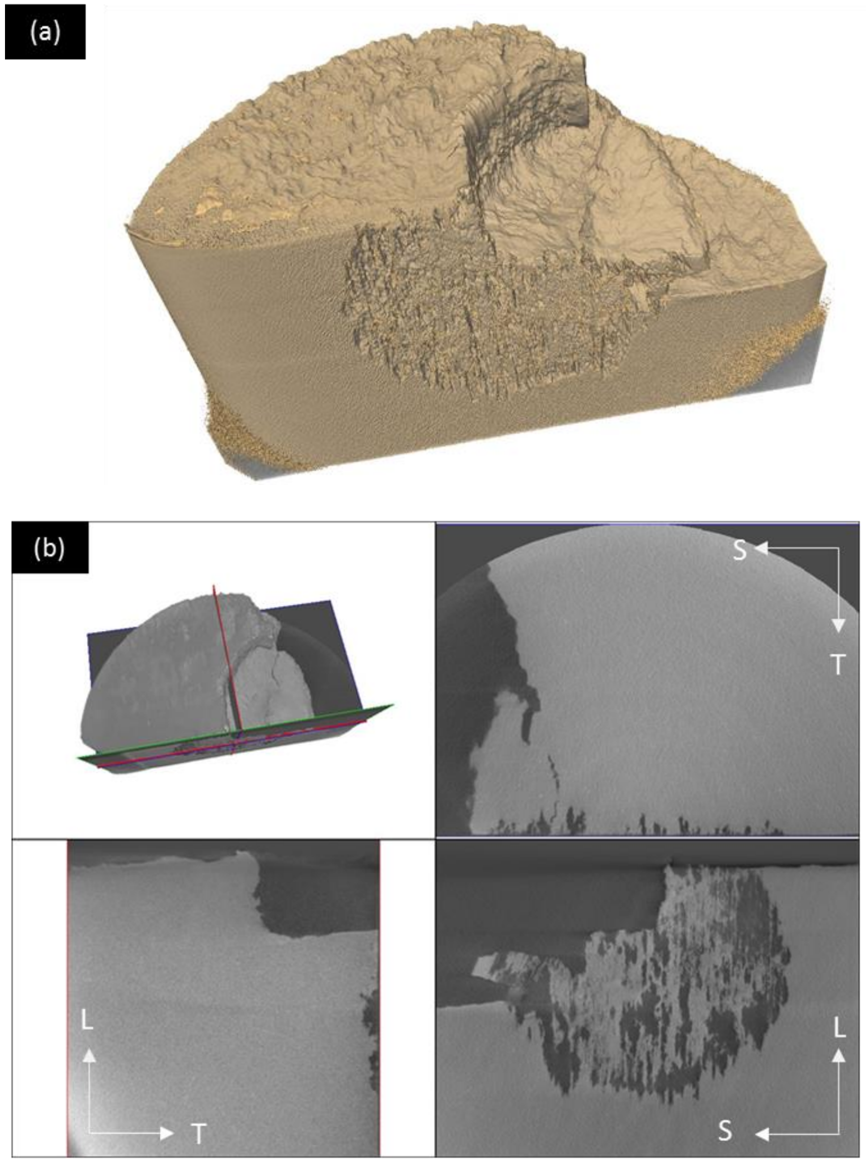

Figure 2.3.10 Intergranular corrosion damage (IGC) specimen (a) 3D reconstruction of images from X-ray computed tomography (b) 2D orthogonal views of images processed using Avizo

(a)

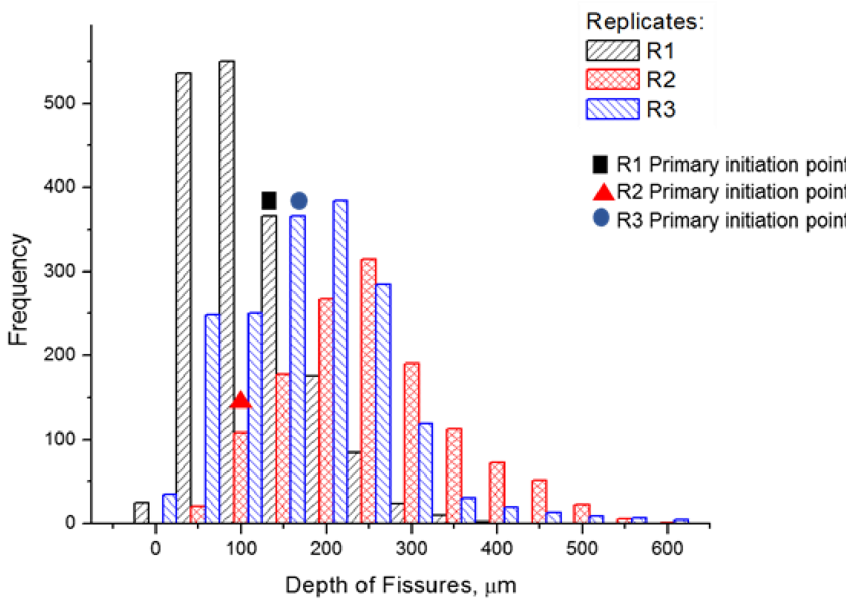
Replicates:
R1
R2
R3
R1 Primary initiation point
R2 Primary initiation point
R3 Primary initiation point
Frequency
0
100
200
300
400
500
0
100
200
300
400
500
600
Depth of Fissures, µm

(b)

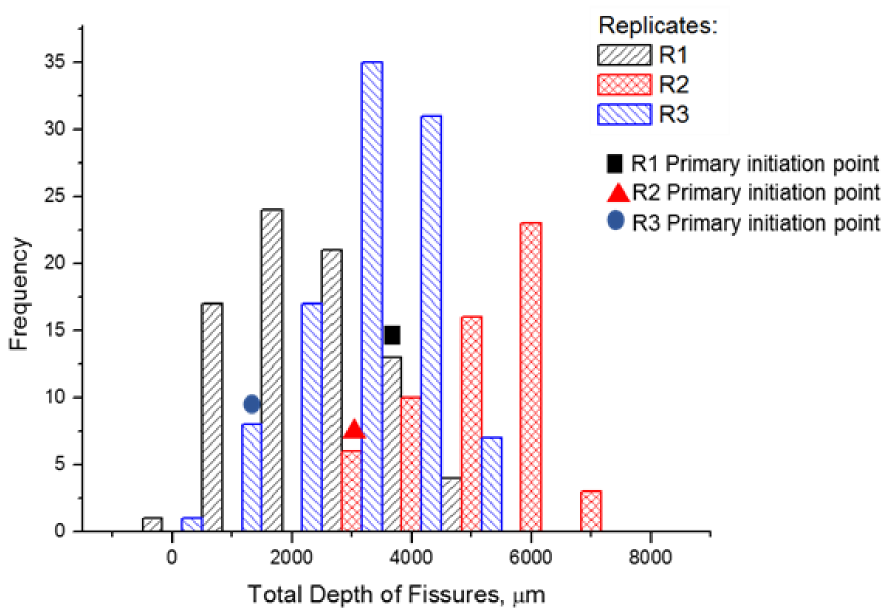
Replicates:
R1
R2
R3
R1 Primary initiation point
R2 Primary initiation point
R3 Primary initiation point
Frequency
0
5
10
15
20
25
30
35
0
2000
4000
6000
8000
Total Depth of Fissures, µm

(c)

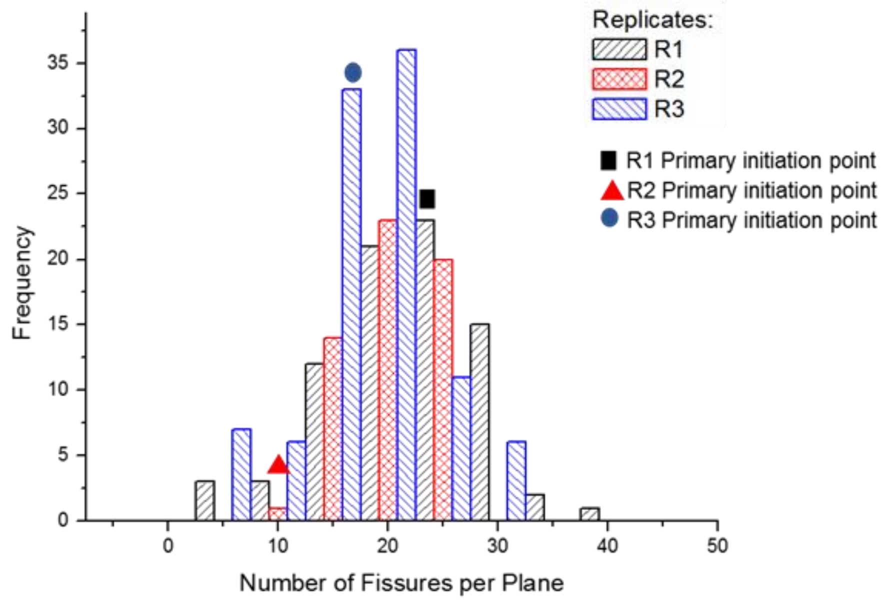

Figure 2.3.11 Histogram of (a) fissure depths (b) total depth of fissures per plane **c.** number of fissures per plane for IGC specimens measured using XCT. Markers on the histogram indicate where the primary fatigue crack initiate for each specimen. The values of the histogram are centered at the red bar

2.2.3.4 Fatigue Behavior

Table 2.3.3 provides a summary of the number of cycles to create a 10 µm crack from the fatigue formation site, the total number of cycles until failure and the ratio of the fatigue initiation life to the total fatigue life. It can be seen that both IGC and DP3 specimens that are tested at > 90% RH with a σ_{max} of 200 MPa have comparable total fatigue life. The DP1 specimens that are cyclically loaded at < 5 % RH with σ_{max} of 200 MPa have the highest total fatigue life, while the DP1 specimens that are fatigue tested at > 90% RH with σ_{max} of 300 MPa have the least total number of cycles. The initiation life, N_i, for each specimen is less than 10% of the total fatigue life.

Table 2.3.3 Summary of initiation life and total fatigue life for each specimen

Specimen	Relative Humidity	σ_{max}	N_i, Initiation life to 10μm from the crack formation site	N_{total}, Total number of cycles	$N_i/N_{total} \times 100$
DP3					
R1	> 90%	200	27784	352863	7.87
R2	> 90%	200	31395	320257	9.80
R3	> 90%	200	18511	334213	5.54
Average			**25896**	**335778**	**7.74**
IGC					
R1	> 90%	200	10253	323234	3.17
R2	> 90%	200	5000	300508	1.66
R3	> 90%	200	5000	291174	1.72
Average			**6751**	**304972**	**2.18**
DP1					
R1	< 5%	200	25250	1019960	2.48
R2	< 5%	200	51382	866753	5.93
Average			**38316**	**943356**	**4.20**
DP1					
R1	> 90%	300	5000	101881	4.91
R2	> 90%	300	4328	104966	4.12
Average			**4664**	**103423**	**4.52**

2.3.4 Discussion

2.3.4.1 Effect of Relevant Corrosion Morphologies

A comparison of the experimental results from this chapter with those in Chapter 2 Section 2 will provide insights as to the extent to which the conclusions can be extended to the similar but potentially more severe DP3 and IGC morphologies. Specifically, the macro-scale damage metrics of the crack formation site will be compared to the full distribution of these metrics across the entire sample to see if there is correlation between extreme values and the crack formation site. Furthermore a quantitative analysis of the total life, the initiation life, and the crack growth behavior will be performed.

Similar to the findings reported in Chapter 2 Section 2 for DP1 and DP2, analysis (**Figure 2.3.7-2.3.9**shows that the fatigue initiation location for DP3 specimens are not dictated by the pit depth, surface area of the pit mouth, pit volume, or the pit density. Additionally, the analysis of the IGC crack formation site relative to the overall distribution of damage (**Figure 2.3.11**) shows that initiation points at the mid values of the total fissures per plane and number of fissure per plane metrics. This is contrary to the results of the FIS specimens, where fatigue crack initiation occurred at the planes having the highest number of fissures and where the cumulative damage is high. This lack of consistency between the trends observed in the FIS and IGC specimens, where corrosion damage shapes are comparable (with the presence of deep fissures), indicate that the macro-scale corrosion feature metrics considered both for FIS and IGC are not fully dictating the location of the fatigue crack formation.

In summary, the analysis of these relevant/more severe corrosion morphologies further suggests that the macro-scale feature metrics (e.g. pit depth or fissure depth, pit density or fissure density, total depth of fissures, surface area of the pit mouth, diameter of the pit mouth, and the volume of the pit) do not fully correlate to the location of the fatigue initiation site.

It is also useful to analyze the crack initiation life, $N_{i,}$ (to create a crack that extends 10 µm beyond the initiation location), **Table 2.3.4** provides average values for DP3 and IGC for the replicate tests. The table also includes N_{short} which is the propagation life from 10 µm (away from the initiation point) to 900 µm measured from the original non-corroded surface, N_{long} which is the propagation life from 900 µm (from the original non-corroded surface) to failure, total fatigue life, number of initiation points on the main fracture plane and the depth of corrosion feature that initiate the fatigue crack. The table also includes the values for DP2 and FIS specimens previously reported in Chapter 2 Section 2. There are several relevant trends. First, the DP2, FIS, DP3 and IGC morphologies at high RH (> 90%) and σ_{max} of 200 MPa all result in fatigue initiation lives that are less than 10% of the total fatigue life although there are subtle differences in the actual cycle-based initiation lives. Second, the total fatigue life of DP3 and IGC specimens are generally higher than the DP2 and FIS specimens. Third, the initiating feature of DP3 and IGC are generally smaller than DP2 and FIS specimens. The N_{short} average values for different corrosion morphologies are slightly different while N_{long} are comparable. **Figure 2.3.12** shows that when the crack growth rates of the specimens are compared, they are fairly the same. The N_{short} values contributes to the changes in the total fatigue life for different specimens with different corrosion morphologies. This subtle differences in the total fatigue life for the specimens with different corrosion morphologies can be understood based on the damage depth. It takes longer for the specimens with shallower damage depth to propagate to the critical crack length resulting to final failure.

Note that even though DP2 and DP3 have comparable aspect ratio, 3.0 and 3.35 respectively, there is still a difference on their total fatigue lives. Some authors indicate that the aspect ratio of the pits affects the stress concentration factor in the corroded specimen, they also indicated that higher aspect ratio results to higher stress concentration factor which can affect the fatigue life of corroded specimens [29–31]. However, when the aspect ratio of DP2 and DP3 are compared, it can be seen that even though DP3 has slightly higher aspect ratio, the total fatigue life and even the initiation life of DP3 is higher than DP2. The stress concentration effects due to higher aspect ratio for DP3 does not result to a lower initiation or lower total fatigue life. Thus, the aspect ratio is not contributing to the difference in the total fatigue life of the specimens.

Table 2.3.4 Summary of average values of fatigue initiation life, total fatigue life, number of initiation points and depth of corrosion feature that initiate the crack for DP2, FIS, DP3 and IGC specimens. Fatigue tests are done at room temperature with RH > 90%, and σ_{max} of 200 MPa, R of 0.5 and a frequency of 20 Hz.

Specimen	Average fatigue initiation life (N_i) to create a 10 µm crack	Average N_{short} (up to 900 µm from non corroded edge)	Average N_{long} (900 µm to failure)	Average total fatigue life	Average N_i/N_{total} × 100	Average Number of initiation points	Average corrosion feature depth that initiate the crack, µm
DP2	9621±66%	195379±14%	47864±26%	252864±11%	3.80±2.03	3±1.73	207±63
FIS	16521±78%	175146±19%	56409±14%	248076±15%	6.66±4.08	2±0	165±135
DP3	25896±26%	252436±13%	57444±27%	335778±4%	7.74±2.13	2±0.58	117±51
IGC	6751±45%	218429±17%	79972±38%	304972±5%	2.18±0.86	4±1.73	149±80

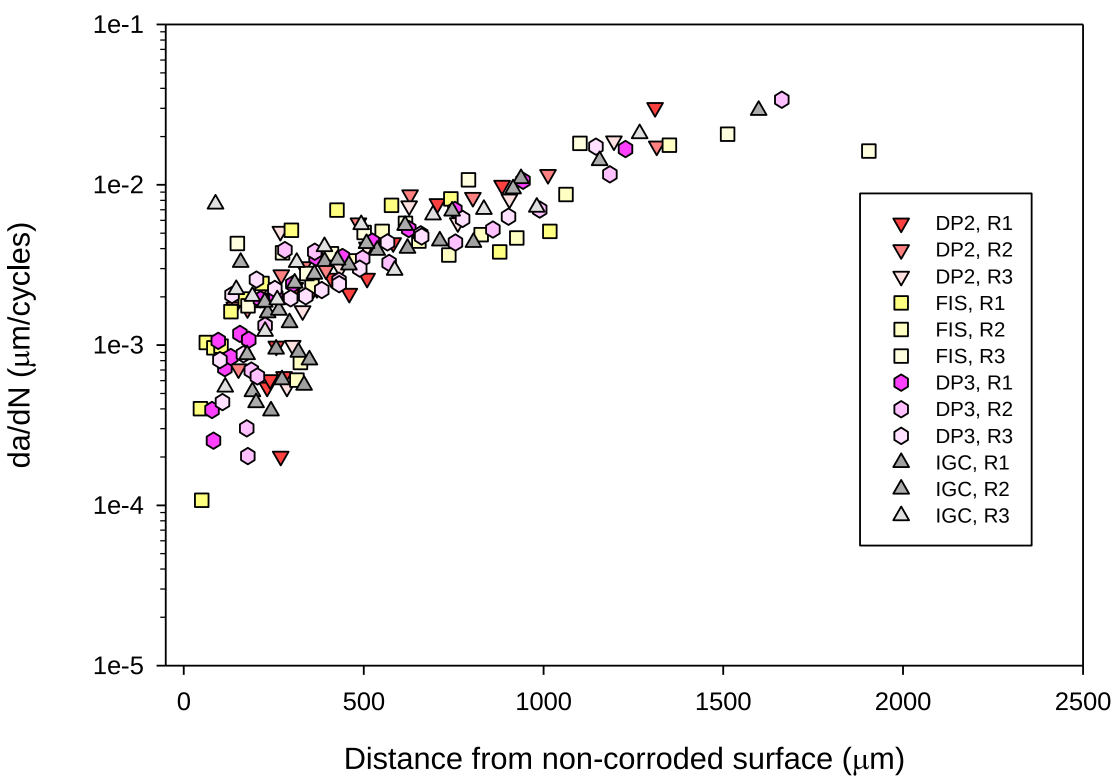

Figure 2.3.12 Crack growth rates (da/dN) for DP3, IGC specimens plotted against the distance measured from the non-corroded edge of the specimen. Plot includes values for DP2 and FIS specimens as reported in Chapter 2 Section 2. Specimens are tested at 23°C in moist air environment (> 90% RH) with σ_{max} of 200 MPa, R of 0.5 and frequency of 20 Hz.

2.3.4.2 Effects of Relative Humidity

This section will look at the effects of relative humidity on fatigue behavior of corroded specimens. Specifically, the effect of relative humidity on the fatigue crack initiation location, fatigue initiation life, total fatigue life and MSC growth rates will be analyzed to recognize the extent to which the conclusions in Chapter 2 Section 2 can be generalized when the environmental conditions during fatigue testing change. The results of fatigue tests done at lower relative humidity (< 5%) are compared to DP1 specimens tested at high relative humidity (> 90%) as reported in Chapter 2 Section 2. The summary of fatigue initiation life, total fatigue life, the number of initiation points on the main fracture plane and the depth of corrosion feature that initiate the crack for DP1 specimens tested at low RH (< 5%) and high RH (> 90%) are reported in **Table 2.3.5**.

Figure 2.3.9 shows that the corrosion depth and the pit density do not dictate the location of fatigue initiation site for specimens tested under low relative humidity (< 5%). The location of the fatigue crack initiation occurs at either low or high values of pit depth, and at either low or medium values of pit density. This agrees with the previous findings for specimens tested under high relative humidity (> 90%) that the fatigue crack initiates not on the deepest corrosion damage.

Table 2.3.5 Summary of fatigue initiation life, total fatigue life, number of initiation points on the main fracture plane and depth of corrosion feature that initiate the crack for DP1 specimens tested at low RH (< 5%) and high RH (> 90%). Fatigue tests are done with σ_{max} of 200 MPa, R of 0.5 and a frequency of 20 Hz.

Specimen	Fatigue initiation life (N_i) to create a 10 μm crack	Total fatigue life	$N_i/N_{total} \times 100$	Number of initiation points	Corrosion feature depth that initiate the crack, μm
Low RH R1	25250	1019960	2.48	3	112
Low RH R2	51382	866753	5.93	5	45
High RH R1	45000	457328	9.84	2	66
High RH R2	381076	852103	44.7	1	61
High RH R3	5000	355268	1.41	1	44

The total fatigue life of specimens tested under low RH (< 5%) are greater than the specimens tested under higher RH (> 90%). This trend can be explained by looking at (1) fatigue initiation life, (2) the number of initiation points on the fracture plane (3) depth of corrosion feature that initiate fatigue crack and, (4) crack growth rates. The fatigue initiation life of specimens tested under low RH (< 5%) is still low (< 10% of the total fatigue life), and is comparable to the specimens tested under high RH (> 90%), except for one replicate (High RH R2). Thus, the fatigue initiation life of the low RH (< 5%) specimens are not controlling the high total fatigue life. The number of initiation points for specimens tested at low RH (< 5%) is higher than the number of initiation point for specimens tested at high RH (> 90%). Some authors indicated that higher number of initiation points tend decrease the number of total fatigue life because the crack initiating from different locations can grow and coalesce [17,32,33]. However, the increased number of initiation points in low RH (< 5%) specimens does not lead to a decrease in the total fatigue life. Looking at the depth of the corrosion damage that initiate the fatigue crack, the deepest corrosion feature listed in **Table 2.3.5** even lead to the longest total fatigue life. Thus the damage depth is not controlling the increase in the total fatigue life for specimens that are tested under low RH (< 5%). **Figure 2.3.13** shows the plot of the crack growth rates for specimens tested in low RH (< 5%) and high RH (> 90%). The specimens tested under high RH (> 90%) have generally higher crack growth rates than those of the specimens tested in low RH (< 5%), especially at the long crack regime. Crack growth rate fluctuations are evident at the microstructurally small crack (MSC) regime (< 400 µm on the x-axis) especially for the specimen tested at high RH (> 90%). The fluctuations on the crack growth rates at MSC regime for specimens tested in high RH (> 90%) do not lead to a huge decrease in crack growth rates which can lead to increase in total fatigue life. On the other hand, the fluctuations on the crack growth rates for specimens tested in low RH (< 5%) are evident even at long crack regimes (> 400 µm on the x-axis). The lower crack growth rates for the specimens tested in low RH (< 5%) specimens lead to higher total fatigue life.

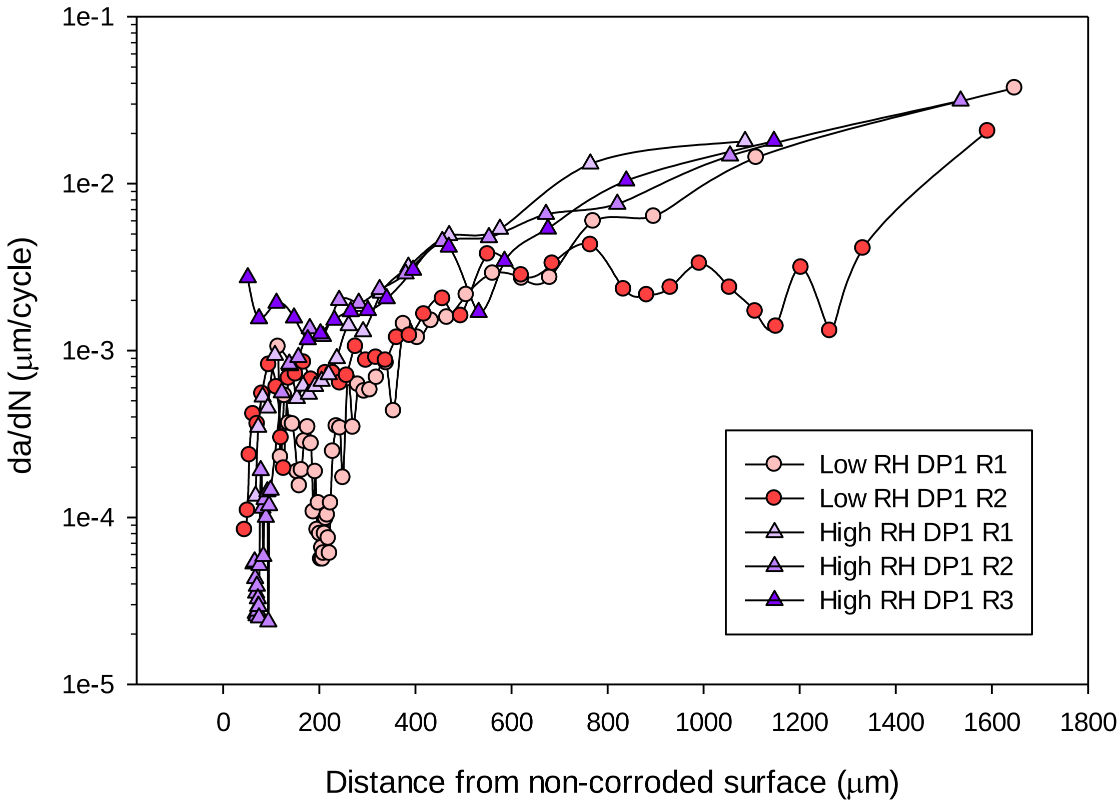

Figure 2.3.13 Crack growth rates (da/dN) for DP1 specimens tested at low RH (< 5%) plotted against the distance measured from the non-corroded edge of the specimen. Plot includes values for DP1 specimens tested at high RH (> 90%) as reported in Chapter 2 Section 2. Specimens are tested with σ_{max} of 200 MPa, R of 0.5 and frequency of 20 Hz.

The findings in this study agree with previous work by Hordon et al and Bray et al [5,34]. Hordon et al. reported that faster crack propagation instead of faster initiation is the main cause for shorter fatigue life as water vapor pressure increases for aluminum specimens tested in air and under vacuum [34]. Bray et al. studied the deleterious effects of moist air environment on fatigue crack growth resistance and fatigue life [5]. The initiation life of DP1 Low RH (< 5%) specimens are comparable to the initiation life of DP1 High RH (> 90%) specimens, < 10%, except for one replicate High RH R2. The crack growth rate of DP1 Low RH (< 5%) is lower than the crack growth rate of DP1 High RH (> 90%) specimens. Specimens tested in high relative humidity environment can have higher crack tip water vapor pressures. This can promote hydrogen penetration into the plastic zone which can reduce the ability of the microstructure to sustain fatigue crack damage thereby increases the crack growth rate [5–7].

2.3.4.3 Effects of σ_{max}

This section will provide knowledge if the prior generalizations in Chapter 2 Section 2 are applicable when the loading conditions (σ_{max}) change. For the purpose of understanding the effect of σ_{max} on the fatigue initiation location, fatigue initiation life, total fatigue life and crack growth rates of corroded AA 7050-T7451, the DP1 High σ_{max} (300 MPa) specimens are compared to DP1 Low σ_{max} (200 MPa) reported in Chapter 2 Section 2. The high σ_{max} specimens are fatigue loaded using σ_{max} equivalent to 300 MPa, while low σ_{max} specimens are cyclically loaded using σ_{max} of 200 MPa. All the tests are performed at 23°C in moist environment (> 90% relative humidity) with an R ratio of 0.5 and loading frequency of 20 Hz. **Table 2.3.6** summarizes the results of the specimen testing.

The fatigue initiation points in specimens subjected to high σ_{max} (300 MPa) occur at medium to high corrosion damage depth and at the areas having low pit density as shown in **Figure 2.3.8**. This agrees with previous findings that the macro-scale corrosion feature do not solely influence the location of fatigue crack initiation.

Table 2.3.6 Summary of fatigue initiation life, total fatigue life, number of initiation points on the main fracture plane and depth of corrosion feature that initiate the crack for DP1 specimens tested at low σ_{max} (200 MPa) and high σ_{max} (300 MPa). Fatigue tests are done in moist air (> 90% RH) , R of 0.5 and frequency of 20 Hz.

Specimen	Fatigue initiation life (N_i) to create a 10 µm crack	Total fatigue life	$N_i/N_{total} \times 100$	Number of initiation points	Corrosion feature depth that initiate the crack, µm
300 MPa R1	5000	101881	4.91	4	45
300 MPa R2	4328	104966	4.12	4	103
200 MPa R1	45000	457328	9.84	2	66
200 MPa R2	381076	852103	44.7	1	61
200 MPa R3	5000	355268	1.41	1	44

The total fatigue life of specimens tested under high σ_{max} (300 MPa) are very low compared to the total fatigue life of specimens tested under low σ_{max} (200 MPa). The initiation life of the specimens tested in high σ_{max} (300 MPa) is very low when compared to the specimens tested in low σ_{max} (200 MPa) except for one replicate, R3. The initiation life of the low σ_{max} (200 MPa) specimens are < 5% of the total fatigue life. This low initiation life can be brought about by the increase in the amount of driving force due to the increase in applied stress, assuming that the corrosion geometry for the specimens is similar [12,35]. The relatively low initiation life can contribute to the low total fatigue life of the specimens tested at σ_{max} of 300 MPa. The number of initiation points are higher for specimens tested at high σ_{max} (300 MPa). The increase in the amount of driving force due to the increase in applied stress can also cause the increase in the number of initiation sites. Some authors reported that higher applied stress cause fatigue to initiate at multiple locations [12]. The amount of applied stress can cause faster coalescence of the cracks initiating from multiple locations, which may contribute to a decrease in the total fatigue life. The depth of the corrosion feature do not contribute to the decrease in the total fatigue life. The specimen that has the largest corrosion damage depth tested in high σ_{max} (R2) still has a shorter total fatigue life as compared to specimens tested at low σ_{max} (200 MPa). **Figure 2.3.14** shows a comparison of crack growth rates for specimens tested at different levels of σ_{max}. There are some overlaps on the da/dN values below the 400 μm distance mark. Most of the specimens start at high crack growth rates but the fluctuations on the crack growth rate are also seen on the graphs. The da/dN values for DP1 High σ_{max} (300 MPa) are relatively higher than the da/dN values for the specimens tested using low σ_{max} (200 MPa). The crack growth rates of the specimen is due to the larger amount of driving forces available to make the crack front move forward. Since the driving forces accounts for the crack geometry and the local stress concentration gradient due to the corrosion pit [12,35], assuming that the crack geometry is similar for the specimens considered, the amount of local stress concentration gradient brought by larger stress applied can then be assumed responsible for the higher crack growth rate of DP1 High σ_{max} (300 MPa) specimens. The higher crack growth rates for specimens tested at high σ_{max} (300 MPa) also accounts for a decrease in the total fatigue life.

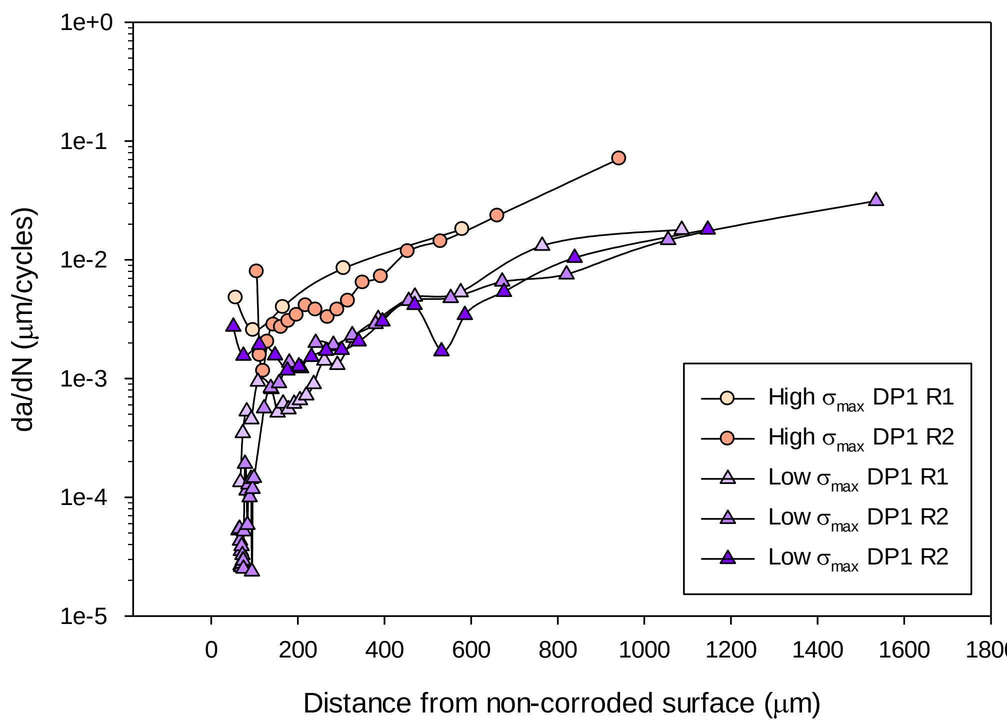

Figure 2.3.14 Crack growth rates (da/dN) for DP1 specimens tested at high σ_{max} (300 MPa) plotted against the distance measured from the non-corroded edge of the specimen. Plot includes values for DP1 specimens tested at low σ_{max} (200 MPa) as reported in Chapter 2 Section 2. Specimens are tested at room temperature with moist air (> 90% RH).

In toto, this section demonstrates that the macro-scale corrosion features do not solely influence the location of fatigue crack formation for specimens with relevant and more severe corrosion morphologies. The macro-scale corrosion damage also do not affect the location of fatigue crack initiation even for specimens tested under different environmental condition and different loading conditions. Some of the macro-scale corrosion metrics, especially pit depth, are commonly considered to predict the total fatigue life or the remaining life of corroded specimens [2,8,20,24–32]. While not fully rigorous, the results of the current study suggest that assuming an initiation life of nil and predicting the remaining life of corroded specimen using the value of the deepest pit is conservative. Moreover, the analysis of micro-scale corrosion damage feature and underlying alloy microstructure is necessary to understand the factor that greatly influence fatigue crack formation location.

2.3.5 Conclusions

The fatigue initiation, fatigue behavior and crack growth rates of AA 7050-T7451 with different corrosion damage morphologies tested under different loading and environmental conditions are evaluated. The macro-scale corrosion metrics are measured and correlated to the fatigue crack formation location. The fatigue life to form a 10 μm crack from the initiation point is estimated and reported together with the total fatigue life of the specimens tested. The following conclusions are established:

- The presence of relevant and more severe corrosion damage (cigar-shape pit and intergranular corrosion) does not lead to extreme reduction in the total fatigue life of specimen tested in moist environment. The fatigue crack initiation lives of the specimens with relevant corrosion damage and regular discrete pits are comparable and are almost negligible. The macro-scale corrosion metrics evaluated in this study do not fully/uniquely dictate the location of the fatigue crack formation. There are other factors that needs to be considered such as the underlying microstructure of the alloy and its interaction with the corrosion morphology.
- Relative humidity decreases the total fatigue life of specimens by increasing the crack growth rate but it does not greatly influence the fatigue initiation life of AA

7050-T451. The fatigue crack formation location for specimens tested at different levels of relative humidity is not solely dictated by the macro-scale corrosion features.

- The increase in σ_{max} for cyclic loading in moist environment caused the decrease in the total fatigue life. Specimens cyclically loaded with high σ_{max} (300 MPa) in moist environment have lower initiation life, higher number of fatigue initiation points and higher crack growth rate leading to great decrease in the total fatigue life. The location of the fatigue crack initiation is not mainly influenced by the macro-scale corrosion feature even when the level of applied maximum stress is varied.

2.3.6 References

[1] Co NEC, Burns JT. Effects of macro-scale corrosion damage feature on fatigue crack initiation and fatigue behavior. Int J Fatigue 2017;103:234–47. doi:10.1016/j.ijfatigue.2017.05.028.

[2] Rafla VN. Unpublished Works. University of Virginia, 2018.

[3] Burns JT, Kim S, Gangloff RP. Effect of corrosion severity on fatigue evolution in Al-Zn-Mg-Cu. Corros Sci 2010;52:498–508. doi:10.1016/j.corsci.2009.10.006.

[4] van der Walde K, Hillberry BM. Initiation and shape development of corrosion-nucleated fatigue cracking. Int J Fatigue 2007;29:1269–81. doi:10.1016/j.ijfatigue.2006.10.010.

[5] Bray GH, Bucci RJ, Brazil RL, Brazill RL. Lessons neglected: effects of moist air on fatigue and fatigue crack growth in aluminum alloys. Mat Sci Forum 2000;331–337:1143–56. doi:10.4028/www.scientific.net/MSF.331-337.1413.

[6] Bradshaw F. The effect of gaseous environment of fatigue crack propagation. Scr Metall 1967;1:41–3. doi:10.1016/0036-9748(67)90011-7.

[7] Bradshaw F, Wheeler C. The influence of gaseous environment and fatigue frequency on the growth of fatigue cracks in some aluminum alloys. Int J Fract Mech 1969;5:255–68. doi:10.1007/BF00190956.

[8] Gao M, Wei RP, Pao PS. Chemical and metallurgical aspects of environmentally assisted fatigue crack growth in 7075-T651 aluminum alloy. Metall Trans A 1988;19:1739–50. doi:10.1007/BF02645142.

[9] Chen GS, Wan K-C, Gao M, Wei RP, Flournoy TH. Transition from pitting to

fatigue crack growth—modeling of corrosion fatigue crack nucleation in a 2024-T3 aluminum alloy. Mater Sci Eng A 1996;219:126–32. doi:10.1016/S0921-5093(96)10414-7.

[10] Kim S, Burns JT, Gangloff RP. Fatigue crack formation and growth from localized corrosion in Al-Zn-Mg-Cu. Eng Fract Mech 2009;76:651–67. doi:10.1016/j.engfracmech.2008.11.005.

[11] Burns JT, Larsen JM, Gangloff RP. Effect of initiation feature on microstructure-scale fatigue crack propagation in Al-Zn-Mg-Cu. Int J Fatigue 2012;42:104–21. doi:10.1016/j.ijfatigue.2011.08.001.

[12] Burns JT, Larsen JM, Gangloff RP. Driving forces for localized corrosion-to-fatigue crack transition in Al-Zn-Mg-Cu. Fatigue Fract Eng Mater Struct 2011;34:745–73. doi:10.1111/j.1460-2695.2011.01568.x.

[13] Ruiz J, Elices M. Environmental fatigue in a 7000 series aluminium alloy. Corros Sci 1996;38:1815–37. doi:10.1016/S0010-938X(96)00096-0.

[14] Ruiz J, Elices M. The role of environmental exposure in the fatigue behaviour of an aluminium alloy. Corros Sci 1997;39:2117–41. doi:10.1016/S0010-938X(97)00095-4.

[15] Burns JT, Bush RW, Ai JH, Jones JL, Lee Y, Gangloff RP. Effect of water vapor pressure on fatigue crack growth in Al-Zn-Cu-Mg over wide-range stress intensity factor loading. Eng Fract Mech 2014;137:34–55. doi:10.1016/j.engfracmech.2014.11.009.

[16] van der Walde K. Corrosion-nucleated fatigue crack growth. Purdue University, 2005.

[17] van der Walde K, Brockenbrough JR, Craig BA, Hillberry BM. Multiple fatigue crack growth in pre-corroded 2024-T3 aluminum. Int J Fatigue 2005;27:1509–18. doi:10.1016/j.ijfatigue.2005.06.026.

[18] McMurtrey MD, Burns JT. Corrosion effects on the initiation life and crack growth rate of 7075-T6511 aluminum. Proceeding DoD Allied Nations Corros. Conf., 2015.

[19] ASTM International. ASTM G1 Standard Practice for Preparing , Cleaning , and Evaluating Corrosion Test. 1999.

[20] Barter SA, Molent L, Wanhill RJH. Marker loads for quantitative fractography of fatigue cracks in aerospace alloys. Bridg. Gap between Theory Oper. Pract. 25th ICAF Symp., Rotterdam, The Netherlands: 2009, p. 14–54.

[21] Spear AD, Li SF, Lind JF, Suter RM, Ingraffea AR. Three-dimensional characterization of microstructurally small fatigue-crack evolution using quantitative fractography combined with post-mortem X-ray tomography and high-energy X-ray diffraction microscopy. Acta Mater 2014;76:413–24. doi:10.1016/j.actamat.2014.05.021.

[22] Ranganathan N, Aldroe H, Lacroix F, Chalon F, Leroy R, Tougui a. Fatigue crack initiation at a notch. Int J Fatigue 2011;33:492–9. doi:10.1016/j.ijfatigue.2010.09.007.

[23] Barter SA, Sharp PK, Holden G, Clark G. Initiation and early growth of fatigue cracks in an aerospace aluminium alloy. Fatigue Fract Eng Mater Struct 2002;25:111–25. doi:10.1046/j.1460-2695.2002.00482.x.

[24] Hu W, Liu Q, Barter SA. A study of interaction and coalescence of microsurface fatigue cracks in aluminium 7050. 25th ICAF Symp., 2009, p. 643–59.

[25] Socha G. Experimental investigations of fatigue cracks nucleation, growth and coalescence in structural steel. Int J Fatigue 2003;25:139–47. doi:10.1016/S0142-1123(02)00068-3.

[26] Medved JJ, Breton M, Irving PE. Corrosion pit size distributions and fatigue lives - A study of the EIFS technique for fatigue design in the presence of corrosion. Int J Fatigue 2004;26:71–80. doi:10.1016/S0142-1123(03)00069-0.

[27] Pidaparti RM, Patel RR. Correlation between corrosion pits and stresses in Al alloys. Mater Lett 2008;62:4497–9. doi:10.1016/j.matlet.2008.08.013.

[28] Turnbull A. The environmentally small/short crack growth effect: current understanding. Corros Rev 2012;30:1–17. doi:10.1515/corrrev-2012-0003.

[29] Cerit M, Genel K, Eksi S. Numerical investigation on stress concentration of corrosion pit. Eng Fail Anal 2009;16:2467–72. doi:10.1016/j.engfailanal.2009.04.004.

[30] Zhang X, Li S, Liang R, Akid R. Effect of corrosion pits on fatigue life and crack initiation. 13th Int. Conf. Fract., 2013.

[31] Mu ZT, Chen DH, Zhu ZT, Ye B, Tao Mu Z, Hai Chen D, et al. The Stress Concentration Factor of Different Corrosion Pits Shape. Adv Mater Res 2010;152–153:1115–9. doi:10.4028/www.scientific.net/AMR.152-153.1115.

[32] McDowell DL, Dunne FPE. Microstructure-sensitive computational modeling of fatigue crack formation. Int J Fatigue 2010;32:1521–42. doi:10.1016/j.ijfatigue.2010.01.003.

[33] McDowell DL. Simulation-based strategies for microstructure-sensitive fatigue modeling. Mater Sci Eng A 2007;468–470:4–14. doi:10.1016/j.msea.2006.08.129.

[34] Hordon MJ, Wright MA. NASA CR 1165 Mechanism of the atmospheric interaction with the fatigue of metals. Washington, D.C.: 1968.

[35] Burns JT, Gangloff RP. Scientific advances enabling next generation management of corrosion induced fatigue. Procedia Eng 2011;10:362–9. doi:10.1016/j.proeng.2011.04.062.

3. Effect of Micro-scale Corrosion Feature and Alloy Microstructure

3.1 Introduction

Corrosion damage is a common culprit for the degradation of fatigue resistance of aluminum alloys generally used in aerospace applications [1–5]. There has been significant investigation of fatigue crack initiation in aluminum alloys commonly used in aerospace structures [2–4,6–11]. Fatigue cracks are usually reported to initiate from discontinuities present in the alloy such as pits, porosities, and cracked constituent particles [6]. Previous chapter focused on macro-scale corrosion damage taking into account parameters such as the corrosion damage depth, and pit density among others. These parameters are commonly used to model fatigue life and these parameters are normally characterized and correlated with fatigue crack initiation [1,3,5,9,10,12,13]. Results show that these parameters are not sufficient to fully predict the location of fatigue crack initiation [1,5,9,10]. According to Burns et al., aside from the corrosion damage feature, the underlying microstructure of the alloy needs to be considered in order to understand the fatigue crack initiation mechanism for corroded aluminum alloy [5]. There has been limited study of the interaction of the corrosion damage features and the underlying microstructural features of the alloy in relation to fatigue crack initiation. Most of the studies either focus on the corrosion damage as fatigue crack initiator, or on the alloy microstructural features as fatigue crack initiator [14–16]. Research on fatigue crack initiation in relation to alloy microstructure are often concentrated on constituent particles [14–16] whereas the alloy microstructural features (such as the grain character) is often neglected. Few research on grain character involves the study of the amount of deformation present in the grain, as well as grain orientation in relation to fatigue cracking [16,17]. However, these studies are done on aluminum alloys that do not have corrosion damage on the fatigue specimen surface.

The objectives of this chapter are to determine how the corrosion micro-scale features affect the location of the fatigue crack initiation, to characterize the underlying microstructure near the vicinity of the fatigue crack initiation and to understand the effects of these microstructural features on fatigue crack initiation of corroded AA 7050-T7451. The micro-scale features considered in this study are the jut-ins, micro pits, and the remaining metallic ligaments. The microstructural features characterized in this study are the constituent particles and the grains of the AA 7050-T7451.

It is hypothesized that the fatigue crack initiation occurs on specific micro-scale corrosion damage feature. It is also hypothesized that the fatigue crack initiation site is at the area having high number of constituent particle and in the grain with higher accumulated damage/deformation.

3.2 Methodology

3.2.1 Materials

The specimens that were corroded and previously fatigue tested as reported in Chapter 2 Section 2 are referred to as the samples used for this study, namely the DP1, DP2, FIS and GCSR specimens. These specimens were characterized and studied in order to determine the contribution of the corrosion micro-feature and alloy microstructure. Details of the characterizations done are described in the following sections.

3.2.2 2D and 3D Characterization of Corrosion Micro-features

SEM imaging of the fracture surfaces was conducted using a FEI Quanta 650 FE-SEM with 250×, 500× and 1000× magnification, an accelerating voltage of 10 kV, spot size of 4, and working distance of 10-15 mm. The initiation points on the fracture surfaces were identified and were classified according to the shape of the micro-feature. There were four general classifications of 2D corrosion micro-feature considered: micro-pit (< 50 μm), jut-in (< 50 μm), ligament (> 50 μm) with high aspect ratio, and ligament (> 50 μm) with high aspect ratio. The aspect ratio is equal to the width of the ligament divided by the length (AR=W/L).

The 3D corrosion micro-features were characterized using white light interferometry and X-ray computed tomography (XCT). Prior to fatigue loading, the specimens were subjected to white light interferometry characterization to capture the corrosion damage shape; the WLI technique was most effective for specimens with discrete pits and general corrosion with surface recession. The post processing software MountainsMap was used to digitally reconstruct the 3D image of the specimens from the white light interferometry characterization.

After fatigue testing, fractured specimens (bottom and top part) were subjected to XCT (via Xradia MicroXCT-200). The source voltage was set to 80 KV, and source power of 8 rendering a 100 μA current during XCT imaging. The source-sample distance was kept in between 25 to 30 mm, and the detector-sample distance was kept in between 17 to 25 mm. The specimen was rotated 180^{o} with the L-direction taken as the axis of rotation. The sample exposure was set to 20-30 sec per image and at least a total of 500 images were taken per fracture specimen. The XCT imaging was done using 2× with a 2 μm resolution and 10× magnification with a 0.7 μm resolution. The XCT images were then post processed using the micro-XCT reconstruction software to correct for the center shift and beam hardening. This procedure was used to remove unnecessary noise on the XCT images. The 2D projections were then reconstructed in 3D. Additional post processing was done using the Avizo program. Thresholding rendered the metal matrix volume of the fractured specimen; by only registering the remaining metal volume the morphology of the corrosion damage was obtained. The bottom and top part of the rendered volume were aligned.

3.2.3 Determination of 2D and 3D Constituent Particle Distribution

Back scatter electron images of the fracture surface were taken using FEI Quanta 650 FE-SEM with 100× magnification, an accelerating voltage of 10 kV, spot size of 4, and working distance of 10-15 mm. The constituent particles on the fractographs appeared as bright white spots. Further image thresholding was done to reveal and isolate the constituent particles using imageJ software. The reference scale in imageJ was set based on the micron bar of the fractographs. A 500 μm-1 mm long region of the fracture surface along the corroded edge, was divided into 250 μm × 250 μm small areas. The constituent particles were analyzed per 62500 μm^2 area division. The number of constituent particles and the area of each constituent particle were measured and recorded per division.

In order to determine the 3D constituent particle distribution around the fatigue crack initiation point, thresholding was done on the XCT images to reveal the constituent particle location within the volume rendered. The thresholding was optimized for each specimen to reveal the location of the constituent particles and the smallest constituent particle captured has a volume of 70 μm^3. The rendered volume of the alloy was divided into smaller cubes of (1) 250 μm × 250 μm × 250 μm, and (2) 100 μm × 100 μm × 50 μm. The number and location of each constituent particles were recorded per volume. This procedure was done on both sides of the fractured specimen. The features of the top and bottom part of the fractured specimens were matched and aligned. The sum of the number of constituent particles were obtained by the matching top and bottom parts. The number of constituent particles reported from this analysis is based on two total volumes: (1) 250 μm × 250 μm × 500 μm, and (2) 100 μm × 100 μm × 100 μm corresponding to S × T × L directions respectively.

3.2.4 Determination of Grain Character through EBSD

A subset of fatigue specimens were chosen for crystallographic orientation characterization. The subset included specimens with the lowest total fatigue life and the highest total fatigue life from each type of corrosion morphology (DP1, DP2, FIS, and GCSR). The fracture surface (TS plane) of the identified specimens was sequentially polished using 600, 800, then 1200 grit SiC paper, followed by 3, 1, 0.5, and 0.25 μm diamond suspensions. The material removed from the fracture surface during polishing did not exceed a total of 100 μm. The specimens were subjected to ultra-sonic bath cleaning in acetone and then methanol. Prior to EBSD characterization, the specimens were subjected to flat milling using the Hitachi IM4000Plus ion polisher with accelerating voltage of 4kV and discharge current of 440 μA while the sample was tilted at 80° and rotated within ±60° for 15 minutes.

Crystallographic orientation of grains were obtained using FEI Quanta 650 FE-SEM with Oxford HKL Channel 5 system. The initiation point of the specimens were verified using the SEM fractographs, and diffraction patterns and EBSD maps were obtained within the vicinity of the initiation point. EBSD maps were collected from 70°

tilted specimens using 100x and 250x magnifications with step-size of 1-3μm, accelerating voltage of 20 kV and working distance of 10-15mm. The EBSD maps collected were reconstructed and analyzed using HKL Channel 5 Tango software. The zero solutions from the orientation map are reduced using the iterative noise-reduction function of the software. Grain size, grain orientation spread, and misorientation angles were obtained from the EBSD orientation maps through the software.

3.3 Results

3.3.1 Corrosion Micro-feature

The fractographs of the specimens revealed the location of the fatigue initiation point and provide a means to determine its 2D shape. The general macro-scale shape of the corrosion damage for the specimens are previously described in [9]. A total of 36 initiation sites are identified on the main fracture plane of the specimens previously studied [9]. The corrosion features, where the initiation points are located, are classified as micro-pit, jut-in or ligaments with low or high aspect ratio. The micro-pits (protruding into the volume of the metal) are small pits along the corrosion damage that are smaller than 50 μm size in depth. Jut-ins (protruding out of the metal volume) are small metal protrusion along the corroded surface that has a length less than 50 μm. Ligaments are classified as remaining metal that have lengths greater than 50 μm. Ligaments with aspect ratio (W/L) > 1 are short and stout with high aspect ratio, while ligaments with aspect ratio (W/L) < 1 are long and skinny with low aspect ratio. These micro-scale features might have formed due to the coalescence of pits and/or metal fall-out. **Figure 3.1** shows the difference between these micro-feature on the fracture surface of the specimens. The results of the analysis are summarized in the **Figure 3.2**. Protruding ligaments are very common on the FIS, DP1 and DP2 specimens, while micro-pit, and jut-ins are common for DP1, DP2 and GCSR specimens. Features on the fractographs that cannot be classified under the four general features described are binned under others, see **Figure 3.3**. The fatigue initiation points corresponding to second phase particle or a grain boundary that is intersected with corrosion damage are binned under others. Based on the results, most of the fatigue crack initiation sites occur at jut-in features for DP1, DP2 and GCSR specimens. On the other hand the fatigue crack initiation sites for FIS specimens are found on ligaments with high aspect ratio. Most of the fatigue crack initiation sites corresponds to jut-ins (55% of the total number of readings) and only a few on micro-pits (11% of the total number of readings). Considering the FIS specimens, 5 out of 6 fatigue crack initiation points occur at ligaments with high aspect ratio. Both jut-ins and ligaments are excess metal protruding out of the metal volume. Although the fatigue crack initiation mostly occur on these excess metal protrusion along the corrosion damage, there are several jut-ins and ligaments present on the corroded surface that do not initiate fatigue. Results of the analysis align with the observed results of Burns et al. where most of the fatigue initiation for corroded AA 7075 occur at jut-ins [5].

In order to fully characterize the 3D feature of the corrosion damage, the data from white light interferometry are analyzed using the Mountainsmap program. The surface roughness of DP1, DP2 and GCSR specimens are obtained through the program. The surface roughness metrics reported in this study are root mean square (Sq), arithmetic mean height (Sa), arithmetic mean peak curvature (Spc), peak density (Spd), maximum valley depth (Sv). Sq is calculated by taking the root mean square of the individual height measurements of peaks and valleys within the selected area of analysis [18]. It is a measure of the standard deviation of heights. Sa is calculated by taking the average of individual absolute height measurements of the surface peaks and valleys with respect to the mean plane [18]. Spc is a measure of the principal curvature of peaks on the surface [18]. A smaller Spc value indicates that the peak have rounded shape, while large Spc value indicates that peak has pointed shape. Spd is a measure of the number of peaks per unit area being characterized [18]. Sv represents the deepest valley in the selected area [18]. It is very important that the target area for analysis be identified in order to obtain the values for the indicated roughness metrics, thus, specific sizes of area is used for the analyses performed. The broad corroded LS surface are divided into areas of 250 μm x 250 μm, and the roughness metrics are recorded for each area of 250 μm x 250 μm. **Figure 3.4** shows the histogram of the surface roughness metrics for DP1, **Figure 3.5** shows the surface roughness metrics for DP2 and **Figure 3.6** shows the roughness metrics for GCSR. The points on the histogram corresponds to the area that has the fatigue crack initiation site. The filled markers on the histograms (**Figure 3.4 - Figure 3.6**) indicate the location of the primary fatigue initiation point, while the hollow markers indicate the location of the secondary fatigue initiation sites. **Figure 3.4** shows that initiation points for DP1 can be found on areas having low Sq, medium Sv, low Sa, medium Spc, and medium Spd. **Figure 3.5** shows that initiation points for DP2 can be found on areas having medium Sq, medium Sv, medium Sa, low to medium Spc, and low to medium Spd. **Figure 3.6** shows that initiation points for GCSR specimens occur at areas having low to high Sq, Sv, Sa, Spc and Spd. There is no specific trend observed on the location of the fatigue crack initiation sites for DP1, DP2, and GCSR specimens for the specific surface roughness metrics analyzed.

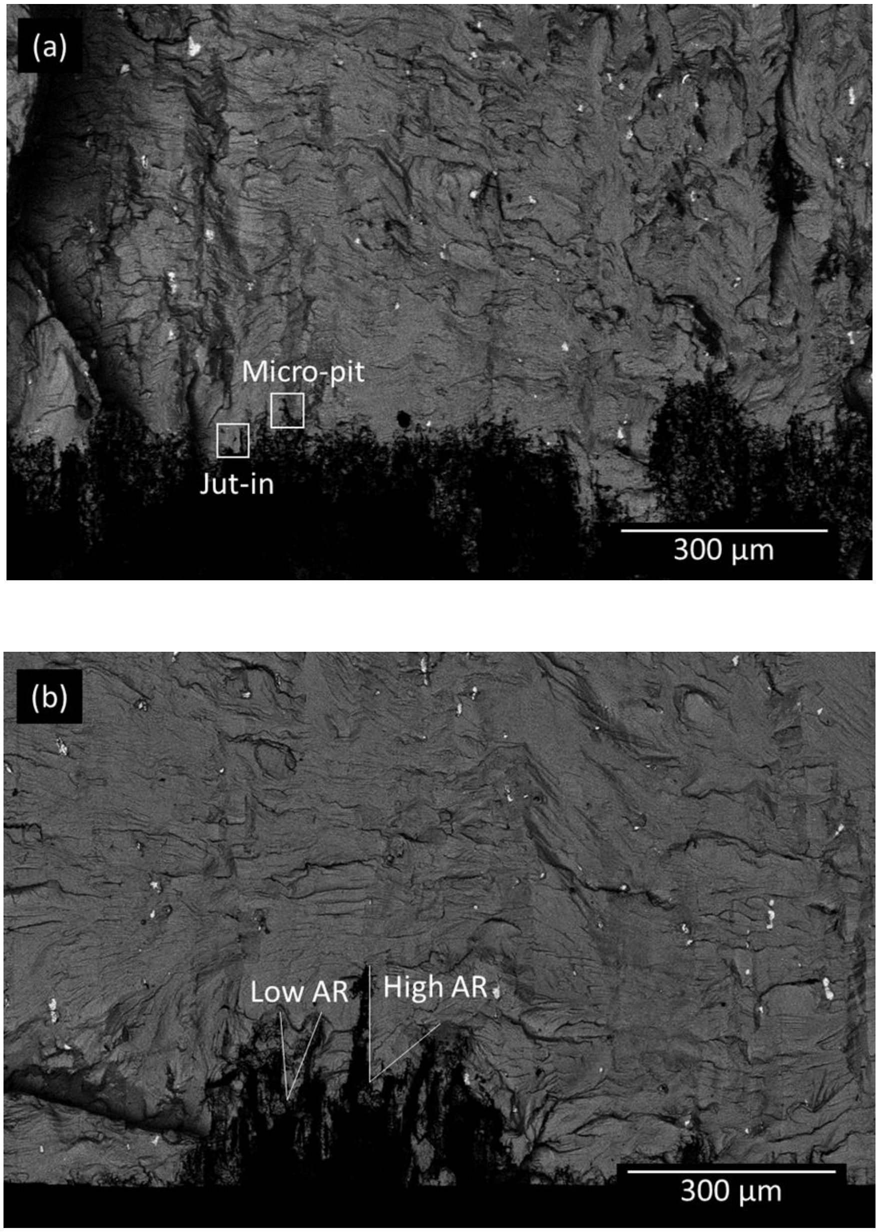

Figure 3.1 Fractographs of fatigue specimens showing (a) micro-features (< 50 µm) such as jut-ins and micro-pit enclosed on the boxes, (b) ligament (> 50 µm) with low aspect ratio (low AR) and high aspect ratio (high AR)

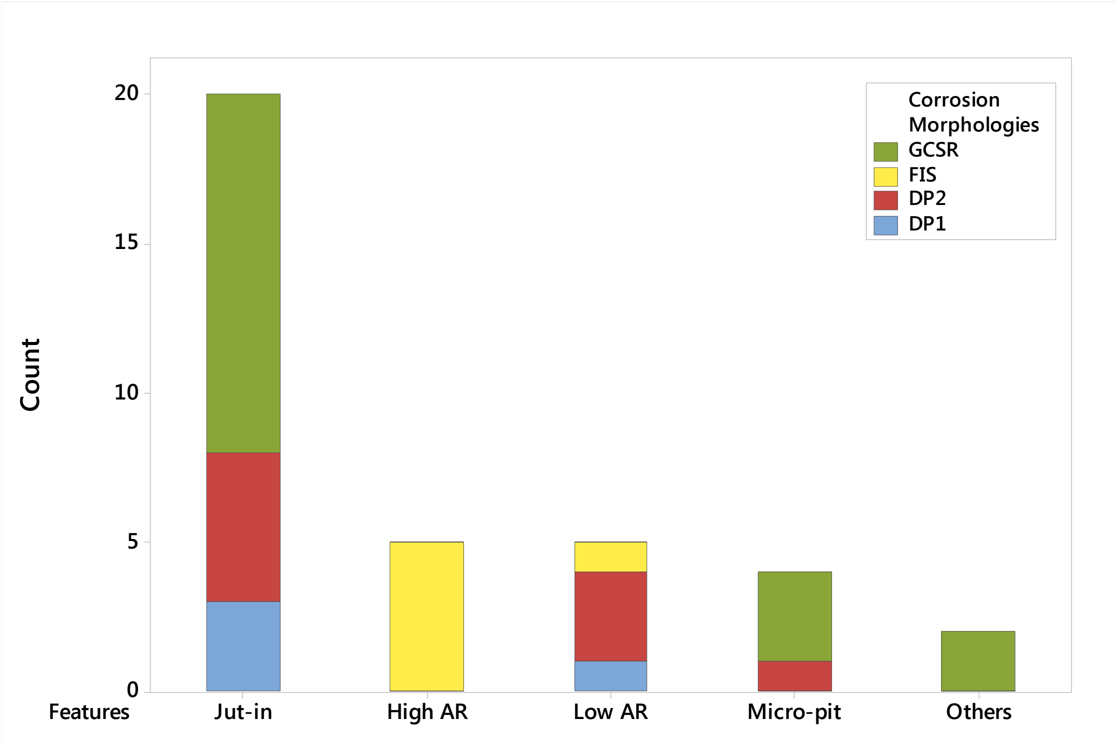

Figure 3.2 Histogram of the micro-scale corrosion features (binned based on the types such as jut-in, micro-pit, ligament with high aspect ratio, ligament with low aspect ratio) within the vicinity of the fatigue initiation site. Micro-scale features on the corrosion surface that do not fit in the classification are binned as others. Different colors in the histogram represent the corrosion morphology of the specimens.

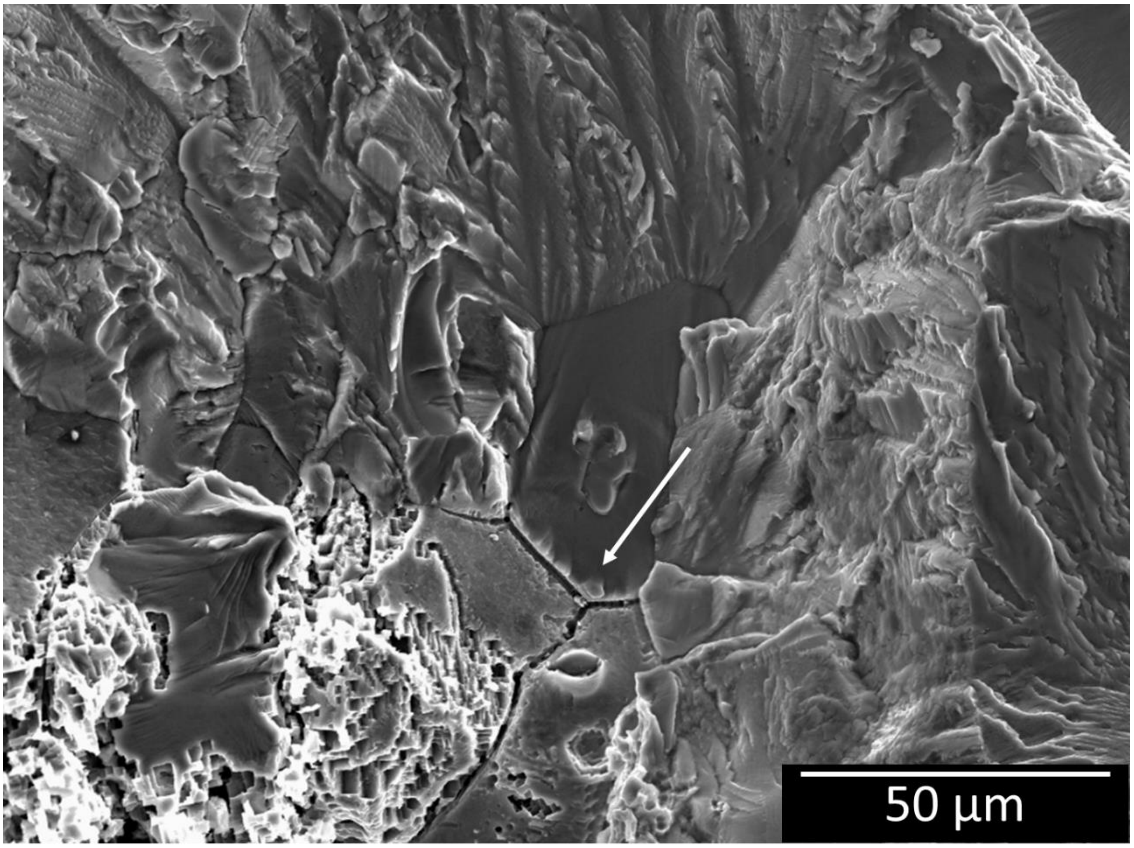

Figure 3.3 SEM image of fatigue initiation point at the grain or phase boundary that is intersected by the corrosion damage. The arrow points to the fatigue initiation location.

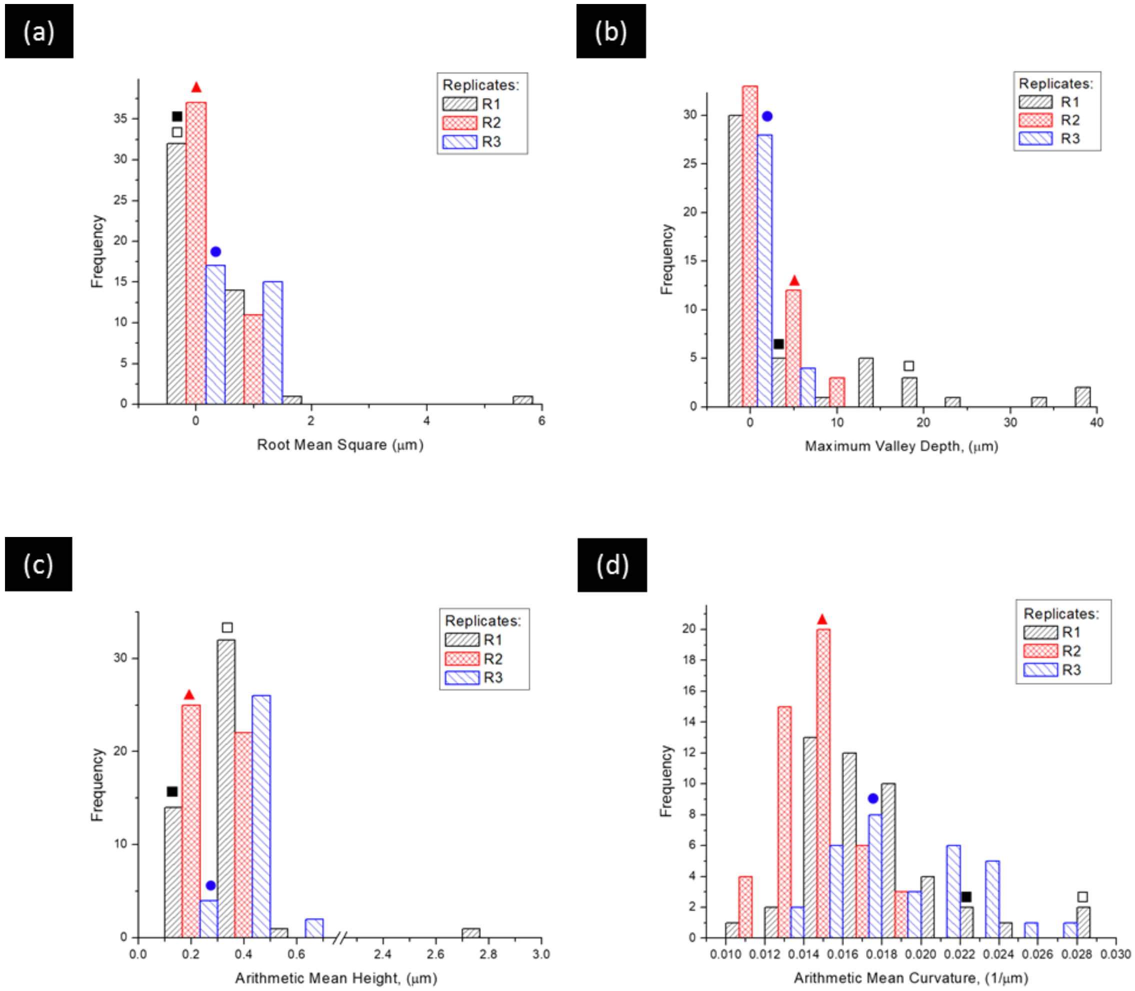

(a)
Replicates:
R1
R2
R3
Frequency
Root Mean Square (μm)
(b)
Replicates:
R1
R2
R3
Frequency
Maximum Valley Depth, (μm)
(c)
Replicates:
R1
R2
R3
Frequency
Arithmetic Mean Height, (μm)
(d)
Replicates:
R1
R2
R3
Frequency
Arithmetic Mean Curvature, (1/μm)

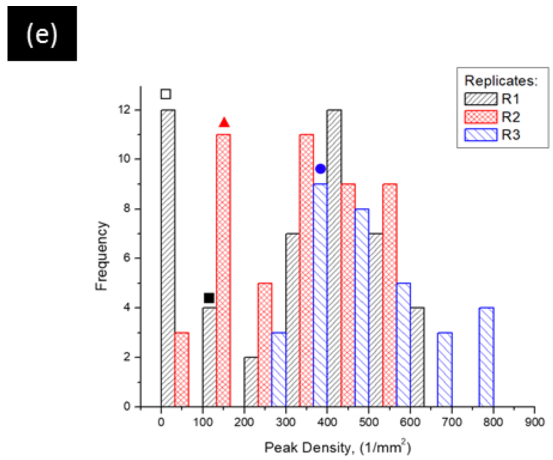

Figure 3.4 Histogram of corrosion surface roughness metrics for DP1 with a defined area size of 250 µm x 250 µm (a) Root Mean Square, (b) Maximum Valley Depth, (c) Arithmetic Mean Height, (d) Arithmetic Mean Curvature (e) Peak Density. Filled markers indicate location of primary fatigue crack initiation, while hollow markers indicate secondary fatigue crack initiation. The color of the markers correspond to the replicate number.

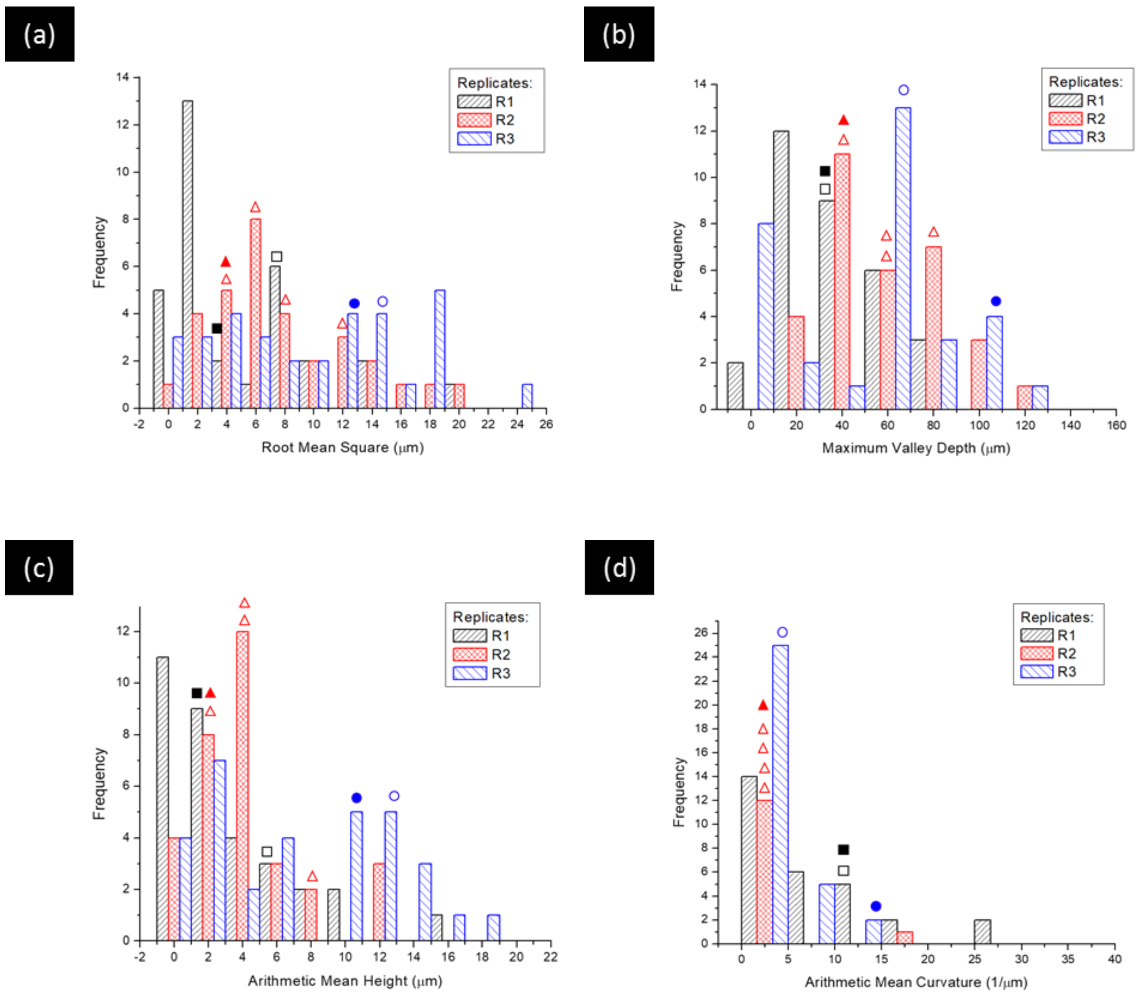

(a)
Replicates:
R1
R2
R3
Frequency
Root Mean Square (µm)
(b)
Replicates:
R1
R2
R3
Frequency
Maximum Valley Depth (µm)
(c)
Replicates:
R1
R2
R3
Frequency
Arithmetic Mean Height (µm)
(d)
Replicates:
R1
R2
R3
Frequency
Arithmetic Mean Curvature (1/µm)

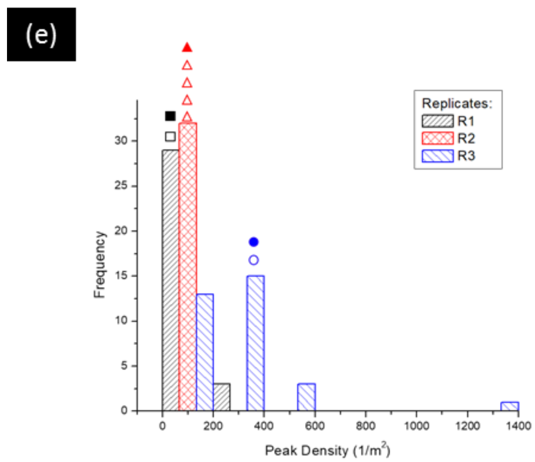

Figure 3.5 Histogram of corrosion surface roughness metrics for DP2 with a defined area size of 250 µm x 250 µm (a) Root Mean Square, (b) Maximum Valley Depth, (c) Arithmetic Mean Height, (d) Arithmetic Mean Curvature (e) Peak Density. Filled markers indicate location of primary fatigue crack initiation, while hollow markers indicate secondary fatigue crack initiation. The color of the markers correspond to the replicate number.

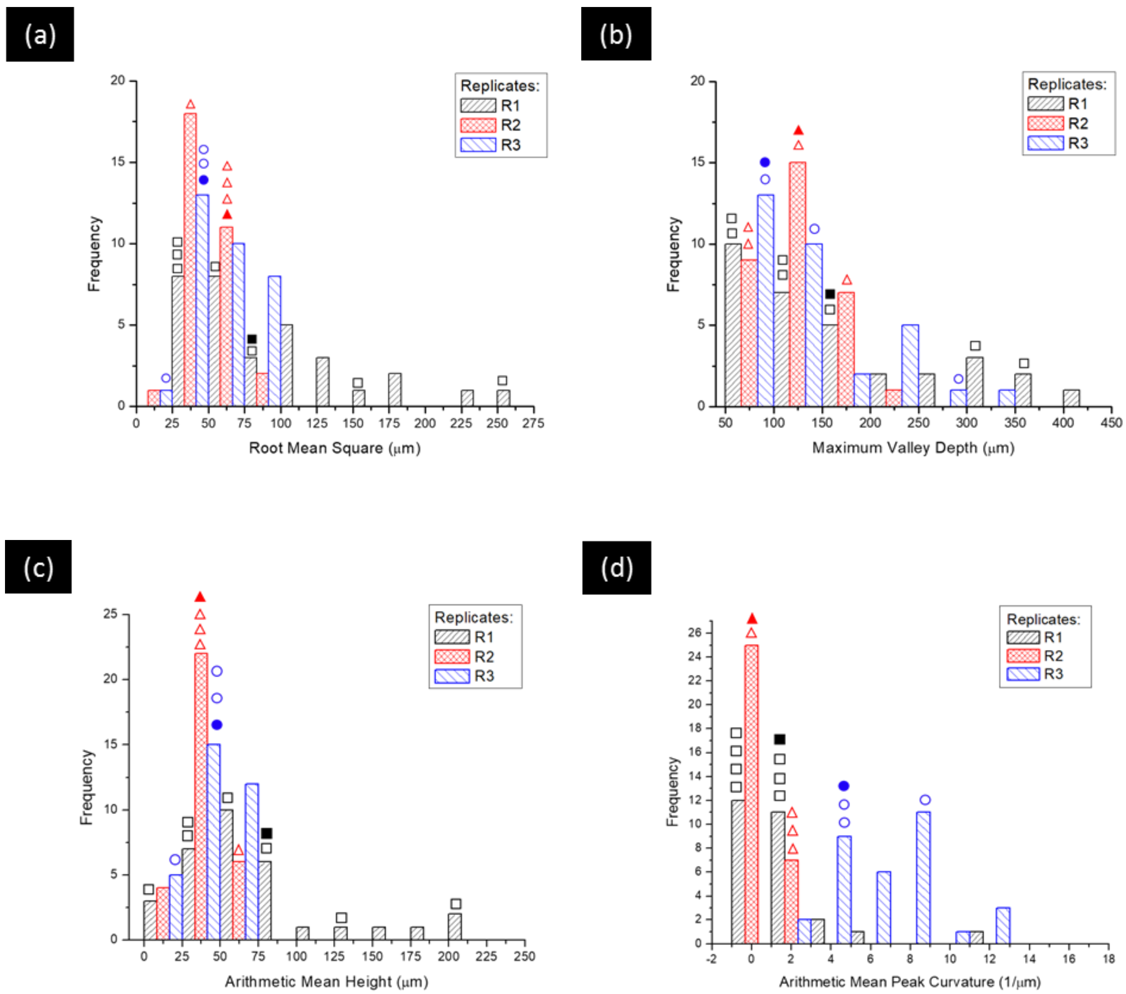

(a)
Replicates:
R1
R2
R3
Frequency
Root Mean Square (μm)
(b)
Replicates:
R1
R2
R3
Frequency
Maximum Valley Depth (μm)
(c)
Replicates:
R1
R2
R3
Frequency
Arithmetic Mean Height (μm)
(d)
Replicates:
R1
R2
R3
Frequency
Arithmetic Mean Peak Curvature (1/μm)

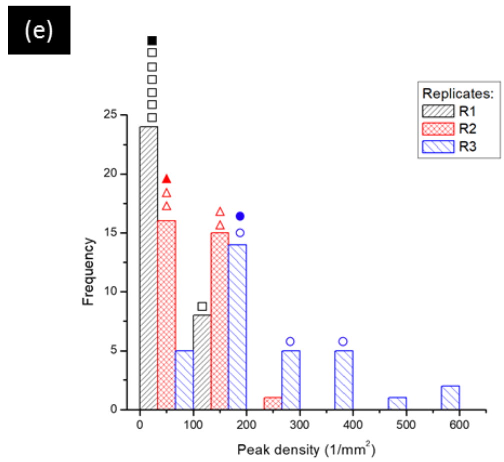

Figure 3.6 Histogram of corrosion surface roughness metrics for GCSR with a defined area size of 250 µm x 250 µm (a) Root Mean Square, (b) Maximum Valley Depth, (c) Arithmetic Mean Height, (d) Arithmetic Mean Curvature (e) Peak Density. Filled markers indicate location of primary fatigue crack initiation, while hollow markers indicate secondary fatigue crack initiation. The color of the markers correspond to the replicate number.

To further isolate the characteristics of the micro-feature of the fatigue crack initiation point, the surface roughness analysis is done locally at the initiation point with a defined area division of 100 µm × 100 µm. **Figure 3.7** shows the histogram of the surface roughness metrics for DP1, **Figure 3.8** shows the roughness metrics for DP2 and **Figure 3.9** shows the roughness metrics for GCSR. The primary fatigue crack initiation points are represented by filled markers on the histograms while the secondary fatigue crack initiation points are represented by the hollow markers. **Figure 3.7** shows that the fatigue crack initiation for DP1 occurs at medium Sq, Sv and Sa, low to medium Spc and Spd. **Figure 3.8** shows that the fatigue crack initiation for DP2 occurs at low to medium Sq, medium Sv, low to medium Sa, Spc and Spd. GCSR histograms in **Figure 3.9** shows that the fatigue crack initiation occurs at low to high Sq, Sa, Sv, Spc and Spd. Despite the locality of the defined areas with respect to the fatigue initiation site, results show that there is no specific trend on the location of the fatigue initiation sites for DP1, DP2 and GCSR specimens in terms of the metrics being analyzed (Sq, Sa, Sv, Spc and Spd).

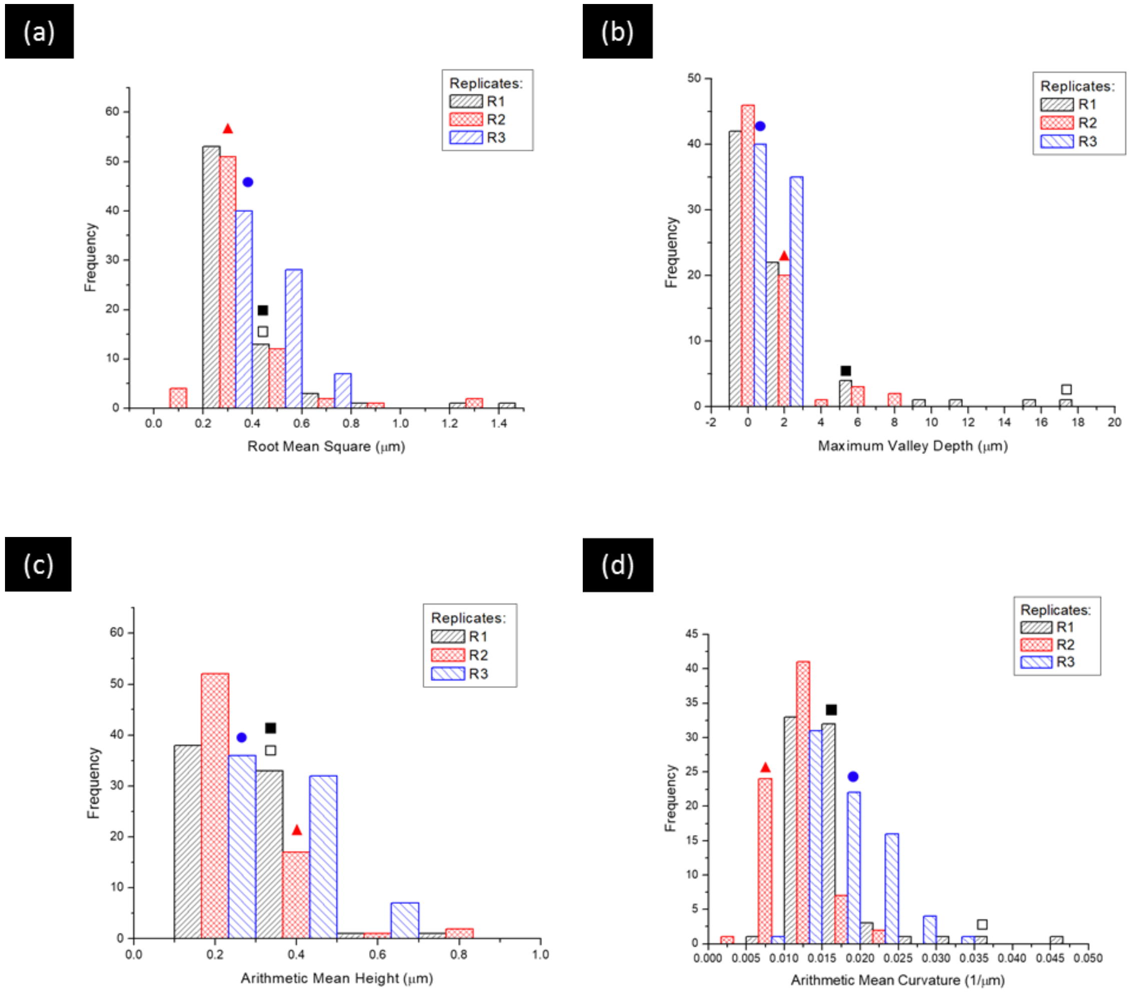

(a)
Replicates:
R1
R2
R3
Frequency
Root Mean Square (μm)
(b)
Maximum Valley Depth (μm)
(c)
Arithmetic Mean Height (μm)
(d)
Arithmetic Mean Curvature (1/μm)

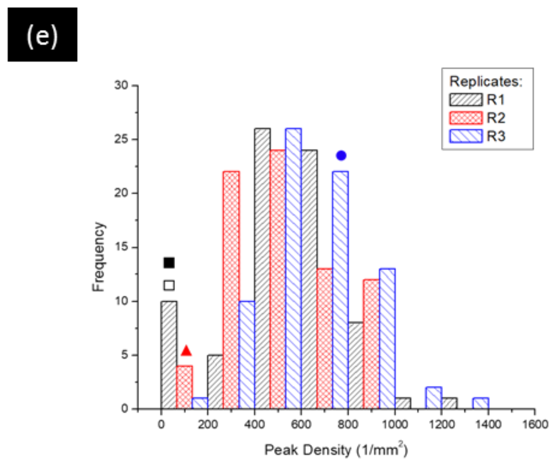

Figure 3.7 Histogram of corrosion surface roughness metrics for DP1 with a defined area size of 100 µm x 100 µm (a) Root Mean Square, (b) Maximum Valley Depth, (c) Arithmetic Mean Height, (d) Arithmetic Mean Curvature (e) Peak Density. Filled markers indicate location of primary fatigue crack initiation, while hollow markers indicate secondary fatigue crack initiation. The color of the markers correspond to the replicate number.

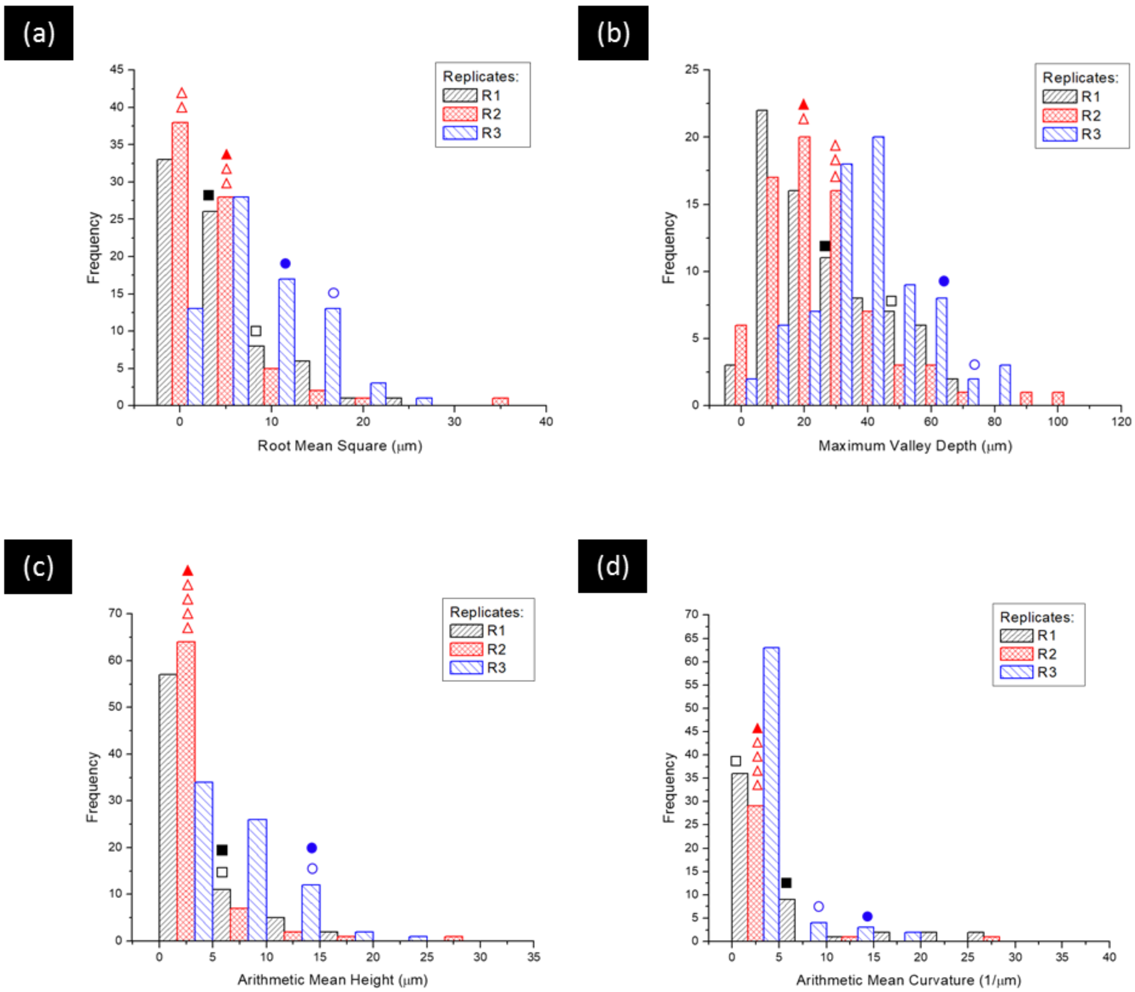
(a)
Replicates:
R1
R2
R3
Frequency
Root Mean Square (μm)
(b)
Replicates:
R1
R2
R3
Frequency
Maximum Valley Depth (μm)
(c)
Replicates:
R1
R2
R3
Frequency
Arithmetic Mean Height (μm)
(d)
Replicates:
R1
R2
R3
Frequency
Arithmetic Mean Curvature (1/μm)

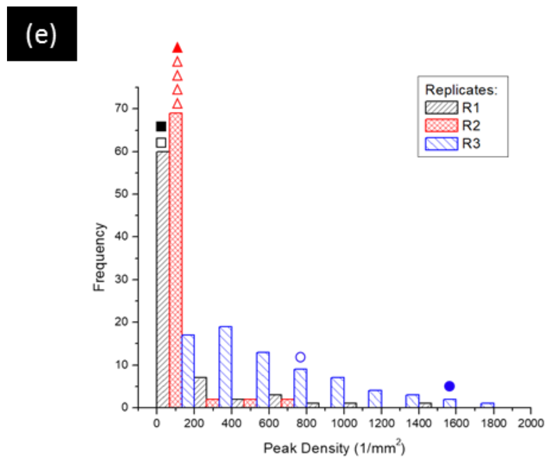

Figure 3.8 Histogram of corrosion surface roughness metrics for DP2 with a defined area size of 100 µm x 100 µm (a) Root Mean Square, (b) Maximum Valley Depth, (c) Arithmetic Mean Height, (d) Arithmetic Mean Curvature (e) Peak Density. Filled markers indicate location of primary fatigue crack initiation, while hollow markers indicate secondary fatigue crack initiation. The color of the markers correspond to the replicate number.

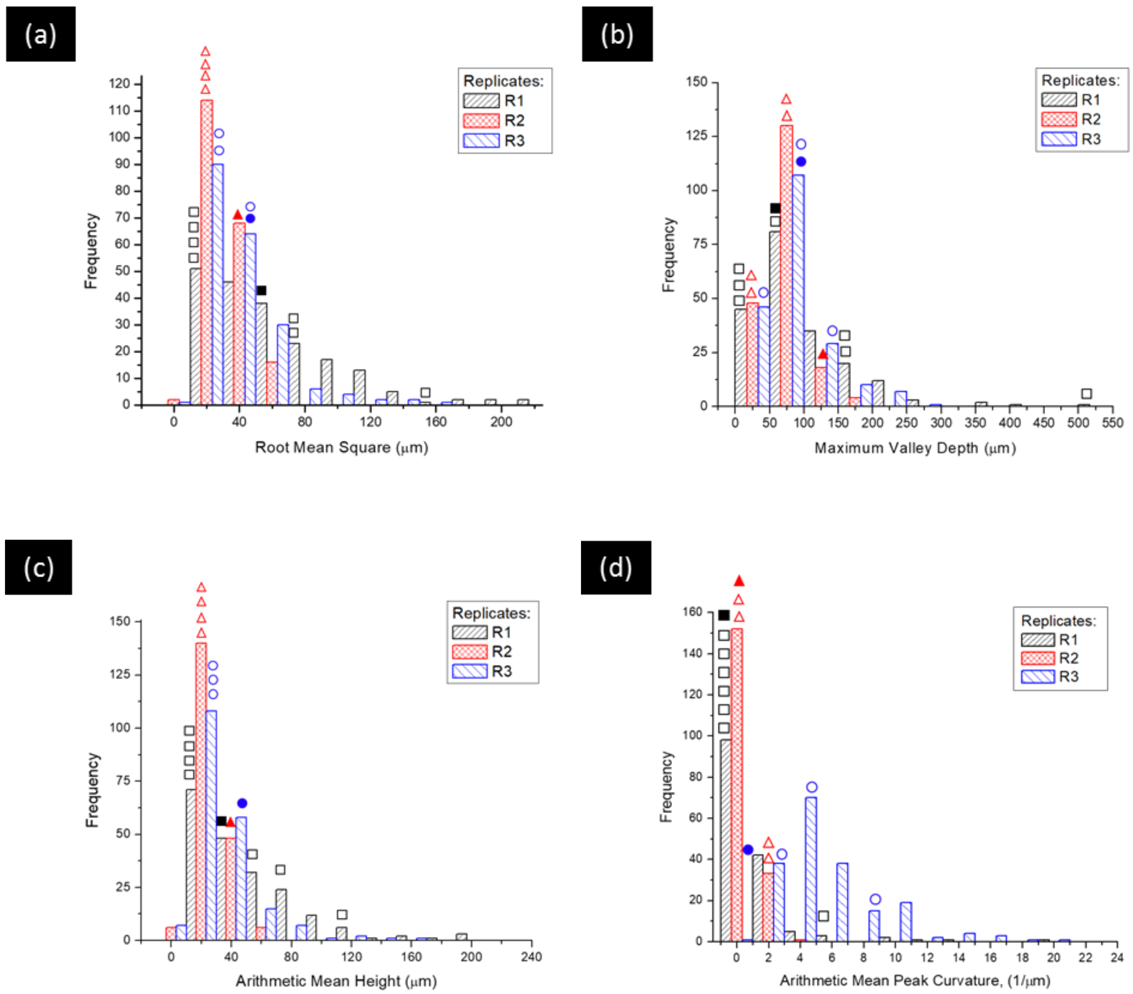
(a)
Replicates:
R1
R2
R3
Frequency
Root Mean Square (μm)
(b)
Replicates:
R1
R2
R3
Frequency
Maximum Valley Depth (μm)
(c)
Replicates:
R1
R2
R3
Frequency
Arithmetic Mean Height (μm)
(d)
Replicates:
R1
R2
R3
Frequency
Arithmetic Mean Peak Curvature, (1/μm)

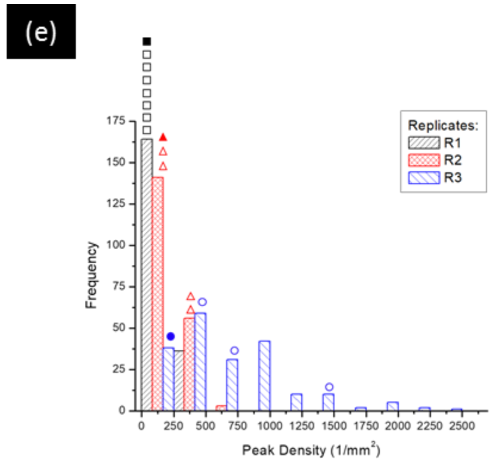

Figure 3.9 Histogram of corrosion surface roughness metrics for GCSR with a defined area size of 100 µm x 100 µm (a) Root Mean Square, (b) Maximum Valley Depth, (c) Arithmetic Mean Height, (d) Arithmetic Mean Curvature (e) Peak Density. Filled markers indicate location of primary fatigue crack initiation, while hollow markers indicate secondary fatigue crack initiation. The color of the markers correspond to the replicate number.

3.3.2 Constituent Particles in the alloy matrix

A wealth of literature establishes that for pristine aluminum alloys that constituent particles tend to initiate fatigue crack [15,16,19–22]. These large constituent particles are typically more brittle than the aluminum matrix; thus, decohesion between the constituent and the matrix or cracking of the particle itself will lead to transition and propagation in the matrix. As such, it is reasonable that underlying constituents proximate to the corroded surface may play an important role in the determining the crack formation location. The location and distribution of the constituent particles with respect to fatigue crack initiation sites are studied. **Figure 3.10** shows the size distribution of constituent particles based on the 2D fracture surface images taken using the back scatter electron technique. The values plotted on the y-axis are the average particle size per area division of the analyzed fracture surface, while the values plotted on the x-axis are the normalized size of the constituent particles with respect to the area of the actual metal matrix. Some of the defined area divisions (250 µm × 250 µm) contained 2D projections of corrosion damage, the actual area of the corrosion damage are subtracted from 62500 µm^2 to obtain the actual metal surface area. The normalized constituent particle size is computed using equation 3.1, these values are used for the subsequent analyses. The constituent particles present in the aluminum alloy considered in this study ranges from 1 to 85 μm^2, similar to other studies for AA 7xxx series [15,23]. Red markers on **Figure 3.10** correspond to the constituent particles present at the area division where the primary fatigue crack initiation occurs. The fatigue crack initiation occurs at the area division that has small to medium size constituent particles.

$$Normalized\ particle\ size = \frac{average\ constituent\ particle}{metal\ surface\ area} x\ 100\ \% \qquad \text{Equation 3.1}$$

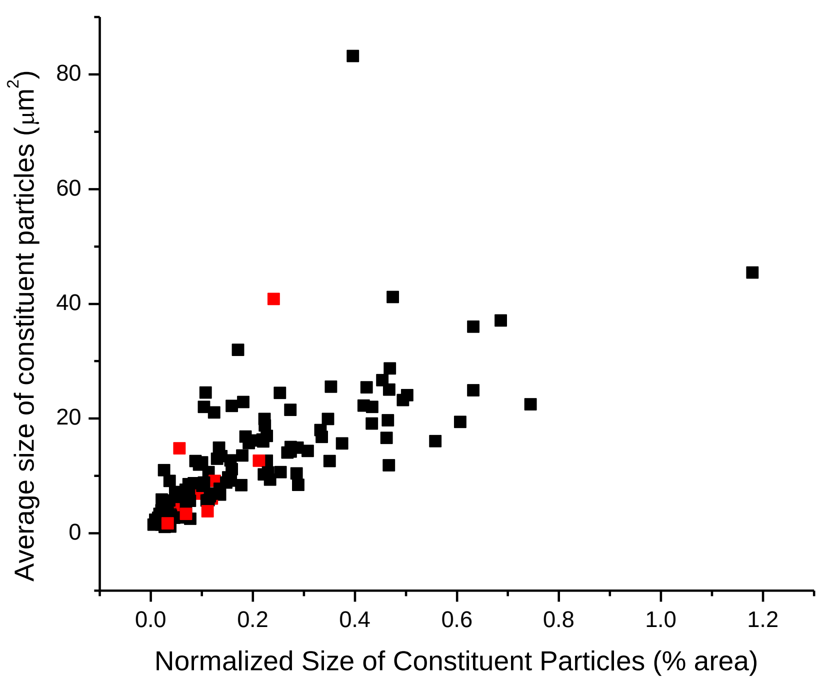

Figure 3.10 Plot of the constituent particle size per area division of 250 μm x 250 μm of the fracture surface. Each dot on the graph corresponds to a value that represents the individual area division of 250 μm x 250 μm. The red marks on the plot represent the area division that has the primary fatigue crack initiation site.

Aside from the size of constituent particles, the number or distribution of constituent particles per area division is considered in this study. A higher number of constituent particles per area division can indicate more hot spots contributing to fatigue crack initiation. **Figure 3.11** shows the plot of the number density of constituent particles. Each number density is calculated for each area division of the fracture surface. This number density is calculated by taking the number of the constituent particles per area division normalized by the actual area of the metal surface. The red markers on the plot indicate the area division where the primary fatigue crack initiation occurs. The constituent particles are clustered in between 50-300 No./mm^2 (number density) and 0.05-0.8 % area (size of constituent particles). Most of the initiation points correspond to the area divisions having few (below 300 No./mm^2) small sized constituent particles (below 0.25%). The four quadrants in **Figure 3.11** represent the combination of the number of constituent particles and the size of constituent particles as noted on the diagram.

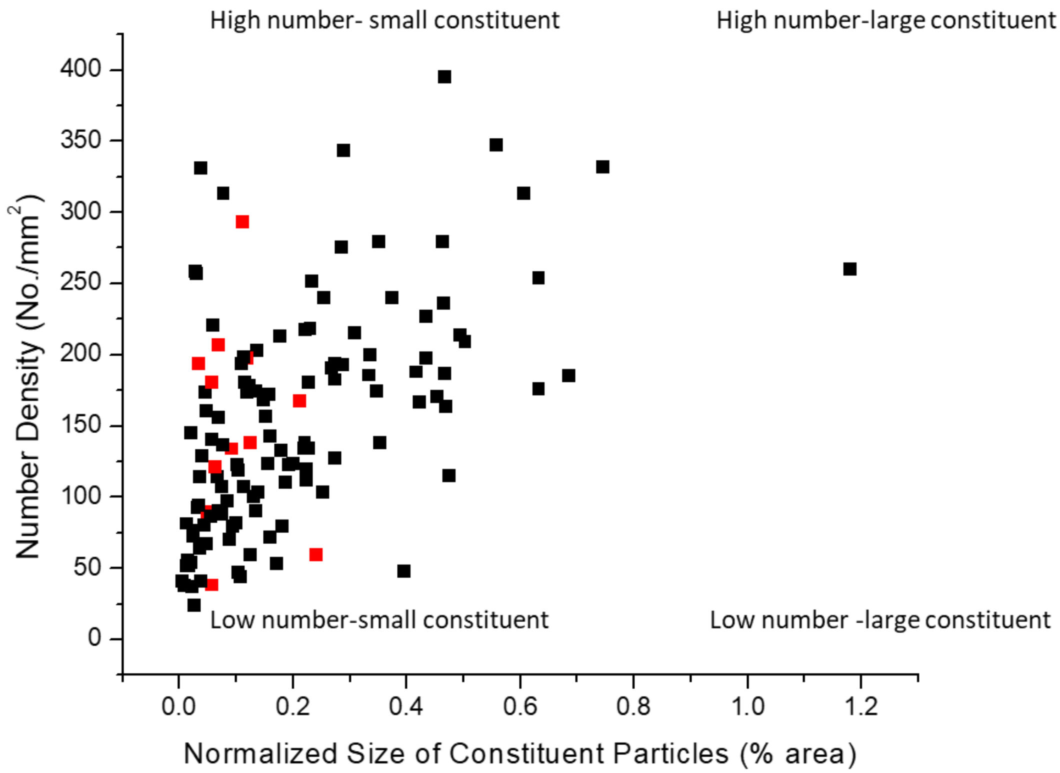

Figure 3.11 Plot of constituent particle number density vs the normalized size of constituent particles per area division. Each dot on the graph corresponds to a value that represents the individual area division of 250 µm x 250 µm. The red marks on the plot represent the area division that has the primary fatigue crack initiation site.

Some constituent particles in aluminum alloys are clustered and some are located far apart. The Average nearest neighbor ratio is a parameter that measures the clustering of particles within a defined area. **Figure 3.12** is a plot of the mean spacing between particles within the defined region of analysis and its relationship to the average nearest neighbor ratio (ANN ratio) per area analyzed. Both the mean spacing between the particles and the average nearest neighbor ratio are measures of particle clustering. Mean spacing reported in **Figure 3.12** represents the average distance between constituent particle centers within the defined area of analysis. ANN ratio is calculated based on equation 2, where the denominator corresponds to mean random distance in a given area. ANN ratio values near zero (0) indicates clustering, ANN ratio values near one (1) indicates random dispersion, while ANN ratio values near 2.15 indicates regular dispersion. **Figure 3.12** shows that as the mean spacing increases, the ANN ratio also increases, and most of the constituent particles have ANN ratio values falling in between 0.5 to 1.5 (randomly dispersed). Red marks in **Figure 3.12** represents the mean spacing and ANN ratio for the area where the fatigue crack initiates. 2 out of 12 fatigue crack initiation sites fall on areas where constituent particles are nearly clustered (less than 0.5 ANN ratio), while 10 out of 12 fatigue crack initiation sites fall on the areas where the constituent particles are dispersed (> 0.5). ANN ratio is used for subsequent analysis in this study.

$$ANN\ Ratio = \frac{Average\ nearest\ particle\ distance}{0.5 \times \sqrt{\left(\frac{no.of\ particles}{Metal\ area}\right)}} \quad \text{Equation 3.2}$$

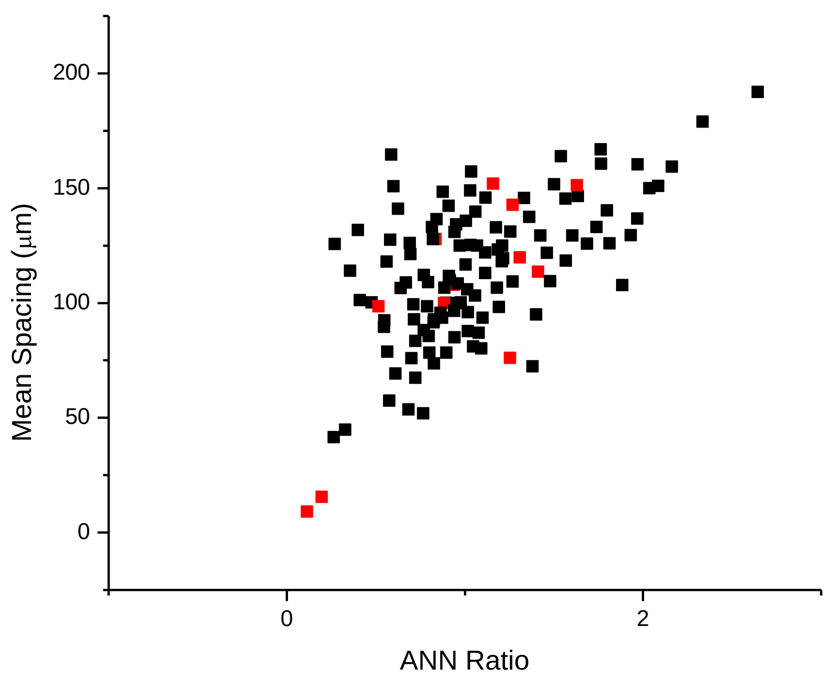

Figure 3.12 Mean spacing between constituent particles within the defined area of analysis plotted against the average nearest neighbor (ANN) ratio. Each dot on the graph corresponds to a value that represents the individual area division of 250 µm x 250 µm. The red marks on the plot represent the area division that has the primary fatigue crack initiation site.

Figure 3.13 (a) shows the relationship of ANN ratio with the normalized size of the constituent particles and **Figure 3.13** (b) shows the relationship of ANN ratio with number density. There is no direct relationship with the ANN ratio and the size of the constituent particles. There is also no direct correlation with ANN ratio and the distribution of the constituent particles. The red markers indicate the primary fatigue crack initiation site. Most of the constituent particles near the fatigue crack initiation sites are small and are dispersed based on **Figure 3.13** (a). The constituent particles near the fatigue crack initiation sites are dispersed with low to high number of constituent particles as seen in **Figure 3.13** (b).

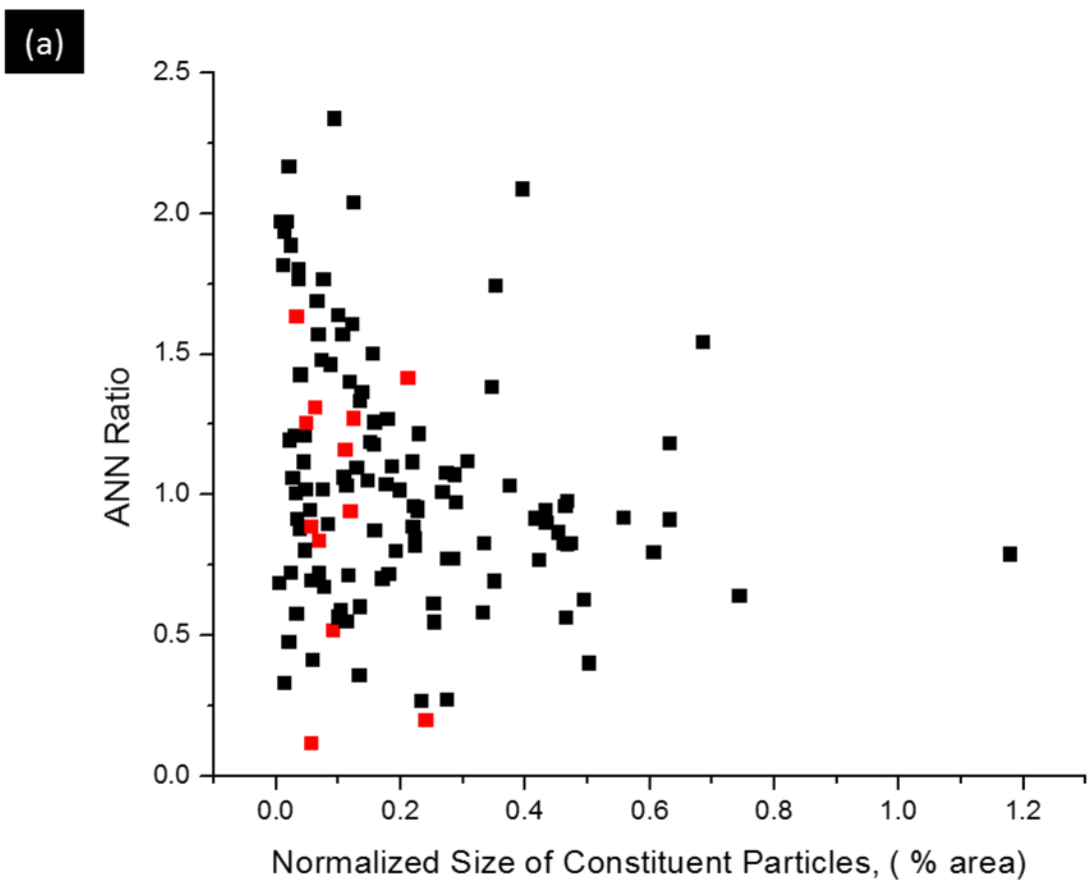

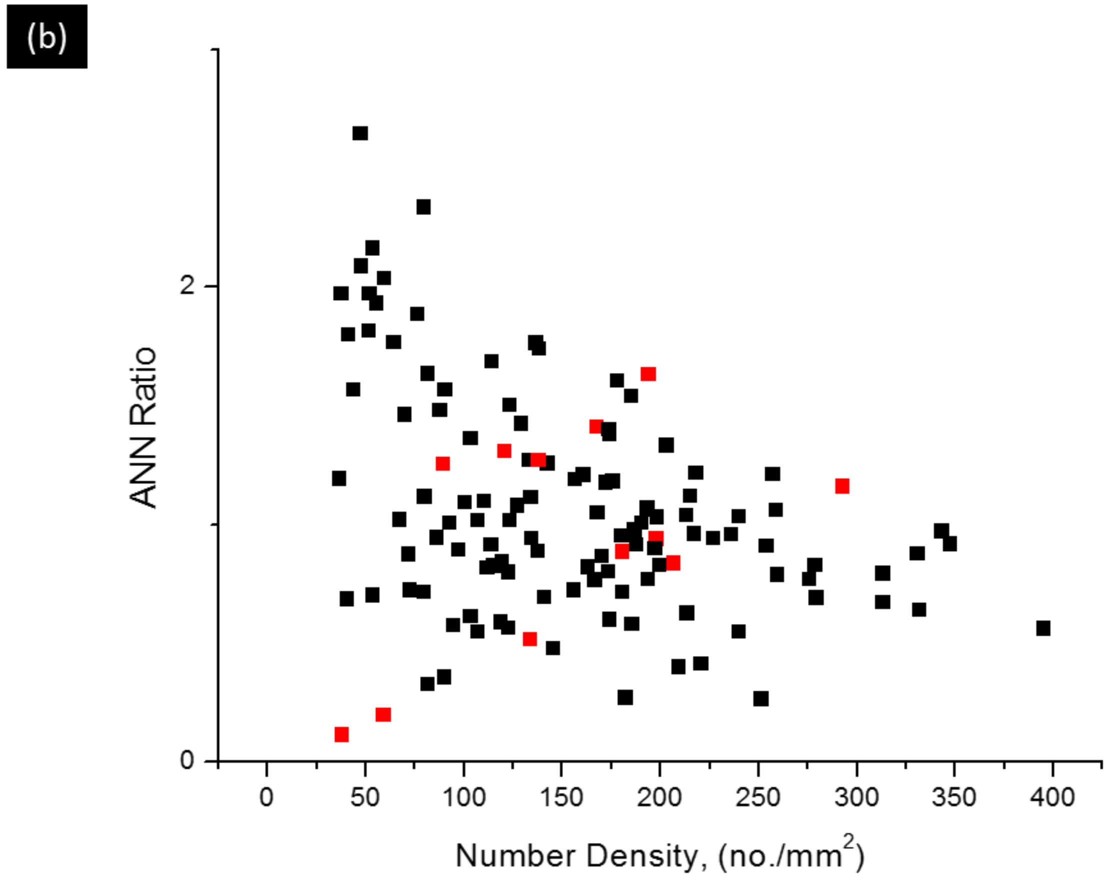

Figure 3.13 Plot of ANN Ratio vs (a) normalized size of constituent particles and (b) number density of constituent particles measured per area division. Each dot on the graph corresponds to a value that represents the individual area division of 250 µm x 250 µm. The red marks on the plot represent the area division that has the primary fatigue crack initiation site.

Further analyses are done on the size of the constituent particles within the 250 µm × 250 µm area enclosing the fatigue initiation, and on distance of large constituent particles from the fatigue crack formation location. The average size of constituent particles that occur at the 250 µm × 250 µm area enclosing the fatigue initiation is 7 µm^2. The particles above 7 µm^2 are considered large constituent particles for these analyses. **Figure 3.14** (a) shows the histogram of the average size of large constituent particles near the fatigue crack initiation site. **Figure 3.14** (b) shows a histogram of the nearest distance of these large constituent particles from the fatigue crack initiation. Labels on the x-axis represent the classification of total fatigue cycles (low, medium or high) for different corrosion morphologies (DP1, DP2, FIS, GCSR). Some specimens (2 out of 12) are not reported in the histogram since there is no large particle found on the 250 μm × 250 μm area enclosing the fatigue initiation site. From **Figure 3.14** (a), considering the High-FIS bar, it can be seen that even if a large particle is present near the fatigue initiation site, it did not cause the fatigue crack to initiate faster and have the total fatigue life to be lower. The size of the constituent particles near the fatigue initiation site do not specifically correlate to the total fatigue life of the specimens. Considering High-GCSR bar on **Figure 3.14** (b), even though there is a large constituent particle near the fatigue initiation site, the presence of this large constituent particle did not cause the fatigue crack to initiate faster which can result low total fatigue life. Low fatigue life specimens have large constituent particles that have distance of 130-240 μm away from the initiation point. The distance of these large constituent particles from the fatigue crack initiation site does not specifically affect the total fatigue life of the specimens.

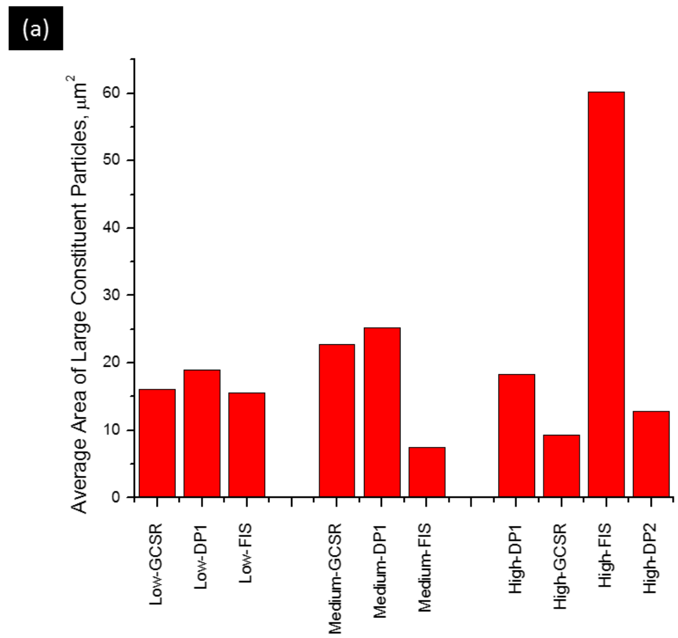

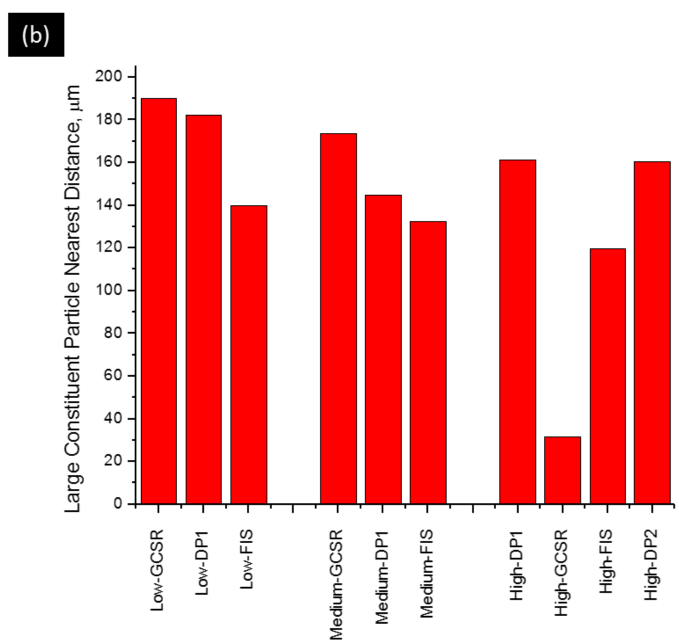

Figure 3.14 (a) Histogram of average size of large constituent particles near the fatigue crack initiation site, and (b) nearest distance between the large constituent particle and the primary fatigue initiation site.

The analysis of number density of constituent particles around the fatigue initiation site is extended to 3D. The number density is calculated by taking the quotient of the number of constituent particles present in the metal and the actual volume of the aluminum matrix. Note that corrosion damage is enclosed within the 250 μm × 250 μm × 500 μm cube, thus the volume of the actual corrosion damage is subtracted from 31,250,000 μm^3 to obtain the actual metal volume. The number density of constituent particles per 250 μm × 250 μm × 500 μm division are plotted in **Figure 3.15** as histogram. The number density of the corresponding cube that enclosed the fatigue initiation site is marked on the plot. Hollow markers represent the number density for the specimens with low total fatigue life, while filled markers represent the number density for the specimens with high total fatigue life. **Figure 3.15** shows that the number density that initiates fatigue crack fall between the medium and high values. There is no specific trend on the effect of number density on the total fatigue life, since high number density can also lead to high total fatigue life as reflected by the filled marker on the 3000-3500 No./mm^3 bar. In order to characterize the distribution of the constituent particle local to the fatigue initiation site, the analysis of number density of constituent particles is repeated considering a smaller volume of 100 μm × 100 μm × 100 μm division. Results of the analysis is plotted in **Figure 3.16**. The number density of the volume enclosing the fatigue initiation site is marked in the histogram. The fatigue initiation location falls within low to medium values of number density (0-12500 No./mm^3) for the 100 μm × 100 μm × 100 μm division analysis. No specific trend can be generalized on the effect of constituent particle number density since low number density can lead to both low and high total fatigue life.

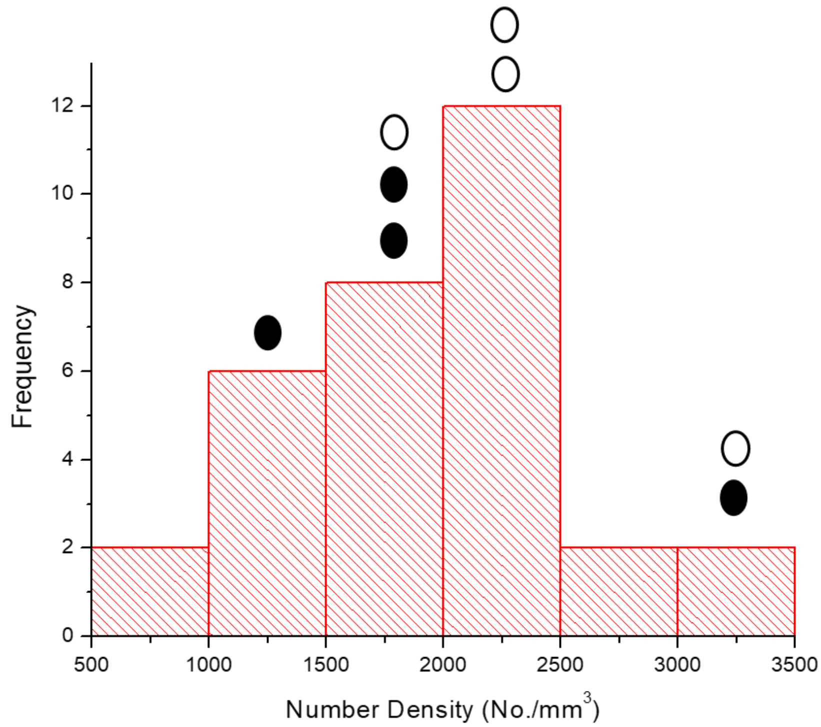

Figure 3.15 Histogram of constituent particles number density within the 250 µm × 250 µm × 500 µm defined cube from XCT analysis. Markers indicate the number density of the cube that enclosed the fatigue crack initiation. Hollow markers indicate specimens with low fatigue life, filled markers indicate specimens with high fatigue life.

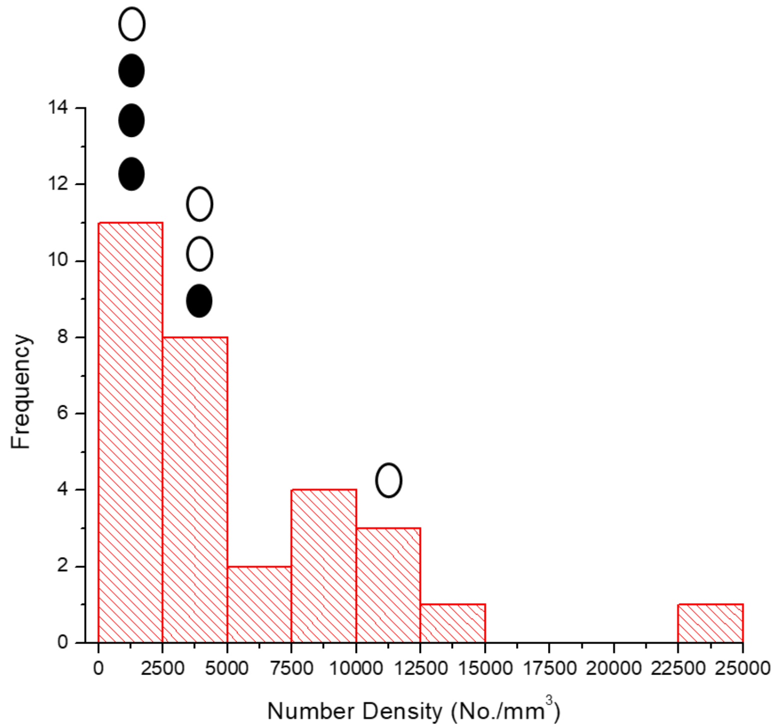

Figure 3.16 Histogram of constituent particles number density within the 100 µm × 100 µm × 100 µm defined cube from XCT analysis. Markers indicate the number density of the cube that enclosed the fatigue crack initiation. Hollow markers indicate specimens with low fatigue life, filled markers indicate specimens with high fatigue life.

3.3.3 Grain Character

In order to understand the effects of the underlying microstructure of the aluminum matrix on the fatigue crack initiation, selected specimens are subjected to EBSD characterization which reveals the characteristics of the grain. The grains along the rolling direction (L-direction) are ≈1500 µm [9]. The fracture surface (TS surface) are polished off perpendicular to the L-direction, thus it is assumed that the grains captured in the EBSD characterization are the same grains on the fracture plane. The primary weakness of this analysis is the assumption that the grains captured in the EBSD characterization represent the actual grains on the fracture plane, however such an approach is reasonable considering the aim to remove < 100 µm during polishing and the 1500 µm average dimension of the grain in the L-direction. Grain size, grain orientation spread, and misorientation angles are obtained from post processing of the EBSD data. These values are obtained through HKL Channel 5 Tango software.

The grain size determination on the TS surface is done through an automatic function in the software and a critical angle of 15° is set as the reference for grain size determination [16,24–26]. The grain size values for ~50 grains enclosed in 500 μm horizontal field width of the SEM are plotted as boxplots and grouped by specimen in **Figure 3.17**. The 50th percentile or median of the grain size values are represented by the middle line on the boxplots, while the average grain size values are represented by the square marks inside the boxplots. The top end of line in the boxplots represents the 95th percentile and the bottom end of line on the other hand represent the 5th percentile. The maximum reading for each specimens are noted on top of the boxplots. Based on **Figure 3.17**, the average size (equivalent diameter) of the grains on the TS surface analyzed is within the range of 35-50 µm, while the median ranges from 20-35 µm. Stars on the boxplots represent the size of the grains where fatigue crack initiation is located. The grains where fatigue cracks initiated are greater than the 50th percentile (median). Some fatigue cracks initiated at very large gains (> 75 µm) such as 1DP1, 2DP1, 1DP2 and 2FIS, while the rest initiated at grains with size falling in between 30 to 75 µm. The fatigue cracks do not initiate on the largest grains.

Aside from grain size, the grain orientation spread is obtained using the HKL Channel 5 Tango software. The grain orientation spread is a measure of the degree of recrystallization of the specimens. It takes into account the change of orientation between every pixel in the grain taking the average orientation of the grain as a reference. It is commonly used as a strain analysis tool to establish the extent of deformation in a grain. Grain orientation spread values near zero indicates highly recrystallized grains (less deformed) while high grain orientation spread (> 3°) values indicate that grains are unrecrystallized or more plastically deformed [27–29]. Based on **Figure 3.18**, the average and the 50th percentile (median) grain orientation spread for each specimen are less than 5°. The boxplots show that a huge portion of the grain orientation spread values are below 5°, however there are values well beyond 5°, thus the specimens can be generalized as partially recrystallized alloy. The stars on the boxplots mark the values of grain orientation spread of grains where fatigue crack initiation are located. Two out of eight specimens have fatigue initiation grains that have grain orientation spread (2DP2 and 1GCSR,) lower than 3°. These two specimens have fatigue initiation site on highly recrystallized grain. Four out of eight specimens have fatigue initiation grains that have grain orientation spread higher than 5°. The remaining two specimens have fatigue initiation grains that have grain orientation spread values between 3-4°.

Researchers have also suggested that the misorientation of a given grain relative to the surrounding grains may potentially impact the crack formation behavior [30]. As such, the misorientation angles are obtained for a 500µm (SEM horizontal field width) region surrounding the fatigue initiation site for eight specimens. Using the HKL Channel 5 Tango software, a horizontal line is drawn across these grains in order to capture the misorientation angle data. The maximum misorientation angle are noted on top of the boxplots. The average misorientation angles for all specimens are below 15°. The misorientation angles in between the fatigue initiating grains and the two neighboring grains (left and right) are marked on the box plots in **Figure 3.19**. Six (6) out of sixteen (16) misorientation angles are less than 15°, while seven (7) out of sixteen (16) misorientation angles are in between 15-40°, and the remaining three (3) out of sixteen (16) are greater than 50°.

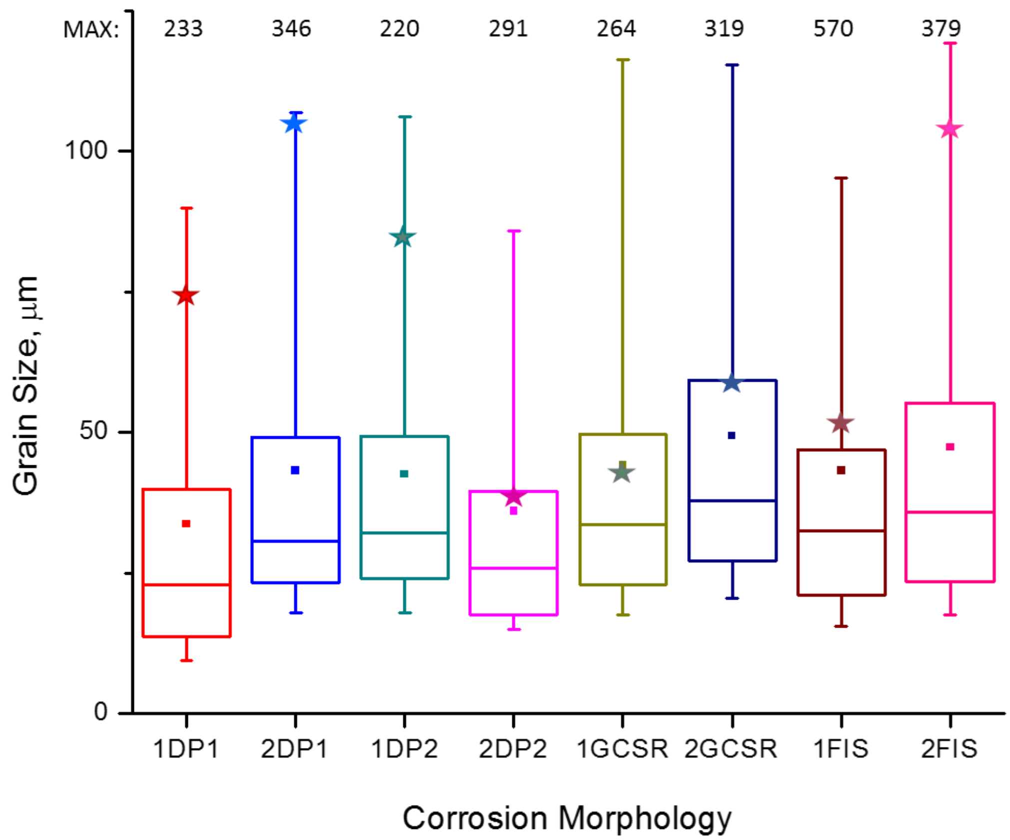

Figure 3.17 Graph of grain size per specimen. Stars indicate the size of the grain that corresponds to the location of fatigue crack initiation. Maximum values of grain size for each specimen are noted on the top of the graph.

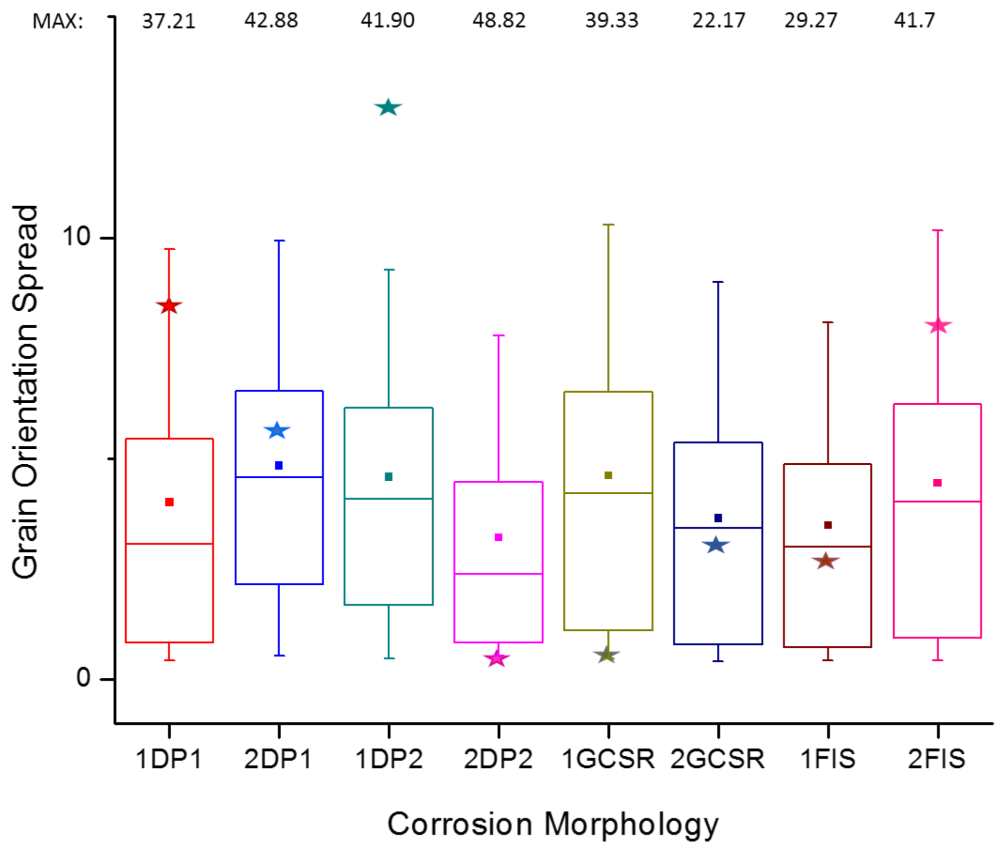

Figure 3.18 Graph of grain orientation spread per specimen. Stars indicate the size of the grain that corresponds to the location of fatigue crack initiation. Maximum values of grain size for each specimen are noted on the top of the graph.

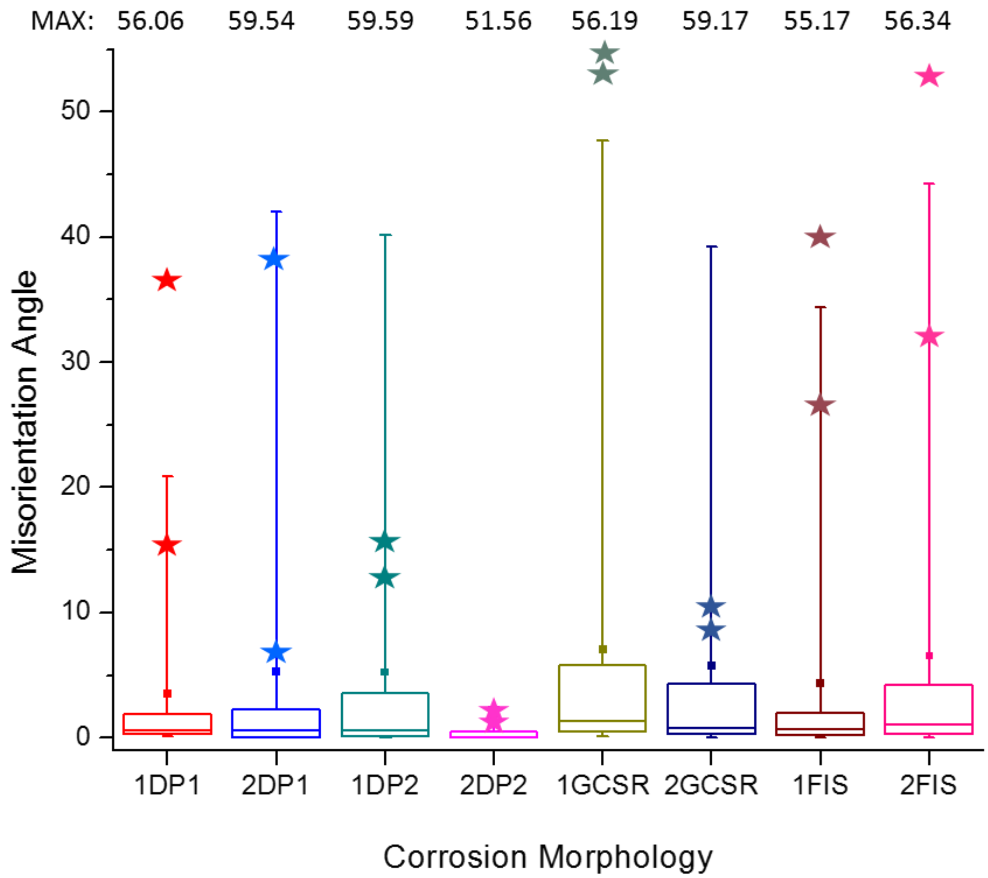

Figure 3.19 Boxplots of misorientation angles of grains near the location of fatigue crack initiation. Stars indicate the size of the grain that corresponds to the location of fatigue crack initiation. Maximum values of grain size for each specimen are noted on the top of the graph.

The inverse pole figures (IPF) are used to determine the orientation of the grains that are parallel to the projection of the IPF [31]. For the case of aluminum (cubic phase) considered in this study, the color of the IPF red, blue and green corresponds respectively to grains with <100>, <110> and <111> axes that are parallel to the projection of the IPF in the loading direction (L direction). **Figure 3.20** (a) shows the fatigue initiation site on the fractograph of the fatigue specimens. The fractograph is used in order to identify the location of the fatigue initiation site on the EBSD image. The EBSD image are overlaid on the fractograph to identify the grain where the fatigue crack initiates as shown in **Figure**

3.20 (b). Since the EBSD image reveals the orientation of the grains parallel to the IPF projection along the loading axis (L-direction), the orientation of the grain in which the fatigue initiation occurs can be determined. **Figure 3.20**(c) shows the IPF representation of the 8 fatigue specimens with the fatigue initiating grain orientation marked as black dots. The grains where fatigue crack initiates have an intermediate grain orientation as revealed by the colors in between red, green and blue (the intermediate color on the IPF shows high index orientations).

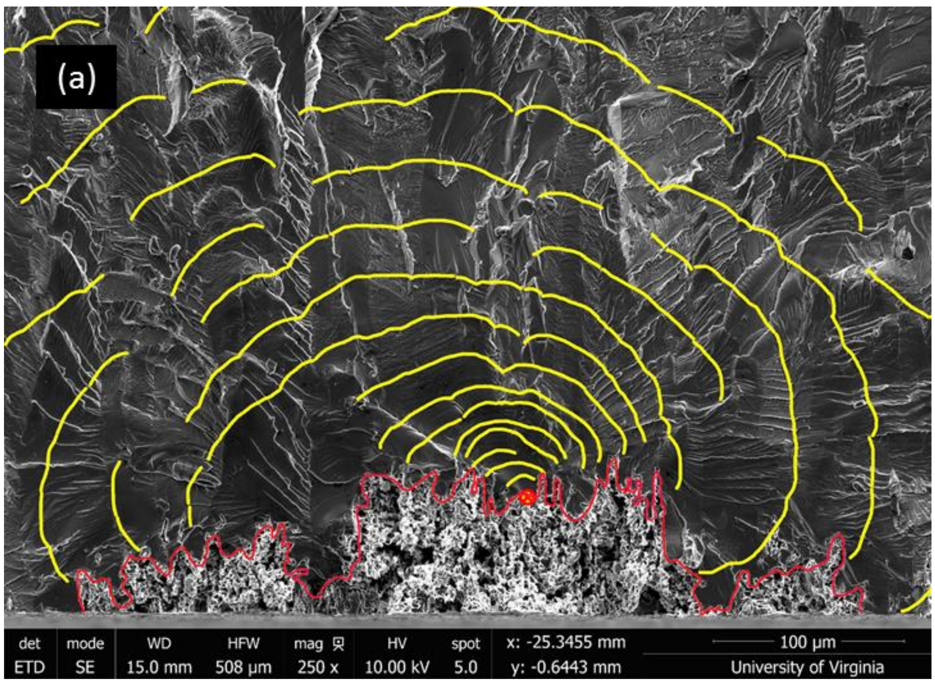

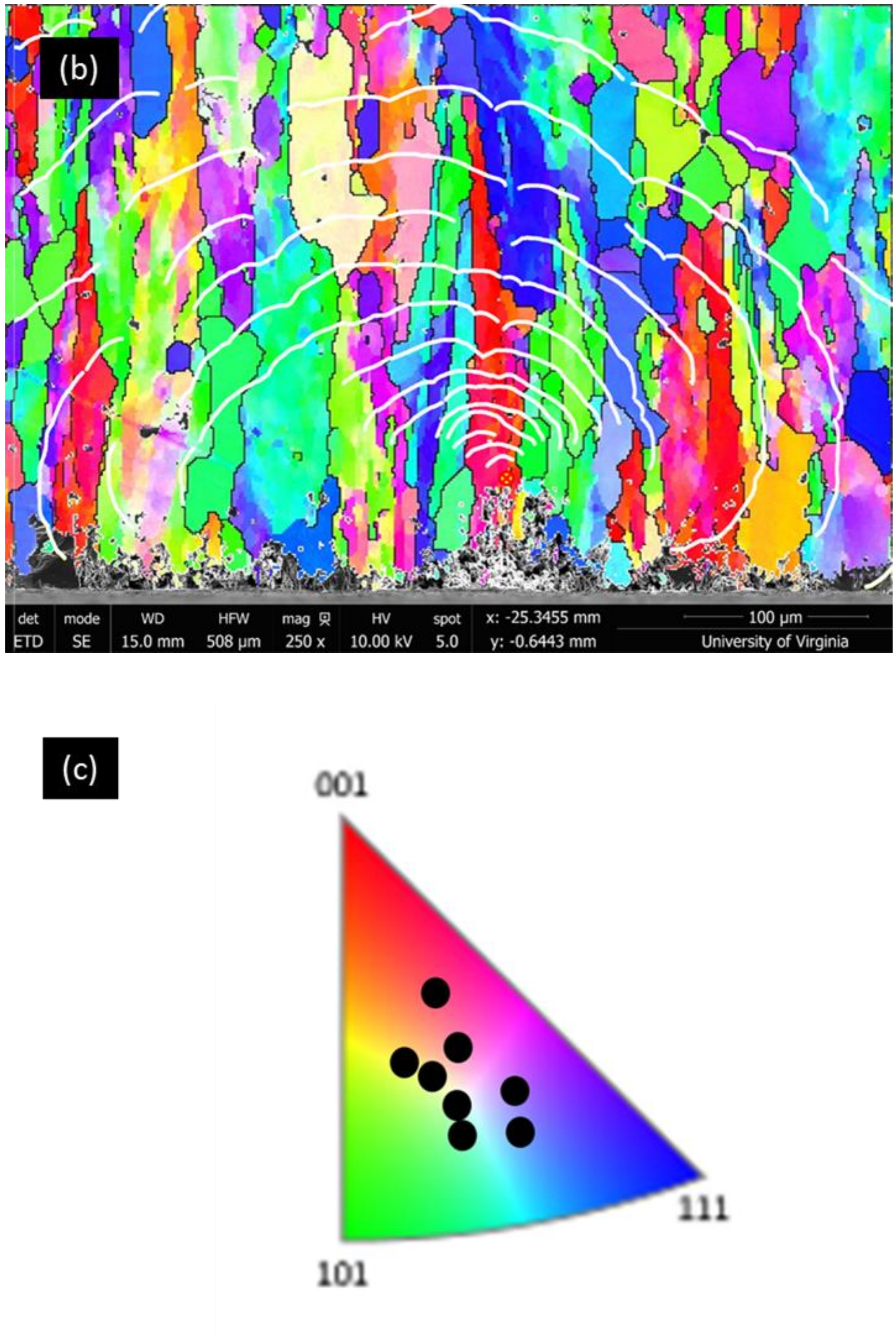

Figure 3.20 (a) Fractograph of the fatigue specimen with initiation point identified (b) EBSD image overlaid on the fracture surface (c) inverse pole figure of AA 7050-T7451 with respect to the loading direction (L-direction), black markers on IPF corresponds to orientation of the primary fatigue crack initiating grain.

3.4 Discussion

3.4.1 Effects of Corrosion Microfeatures

Barter et al. listed the common features that initiate fatigue in metallic aircraft structures [6], and among the list are the different types of corrosion damage pits which have corrosion morphological features that are commonly less than 250 μm in size. In the paper of Burns et al., the authors mentioned that even though the corrosion damage in AA 7075 are seemingly smooth, there are corrosion micro-features such as micro-pits and jut-ins that are found on the corroded metal volume [5]. Previous research indicated that these micro-pits and jut-ins are common location of fatigue crack initiation, with fatigue initiation site having higher percentage of occurrence on jut-ins than micro-pits [1,5]. This is despite the finite element analysis which suggested that, micro-pits generally have higher strains than jut-ins [5]. The current analysis reported in **Figure 3.2** shows that even though micro-pits have higher strains in general, most of the fatigue crack initiation points are located on protruding metal features such as jut-ins and ligaments. This shows that the higher residual strains that develop due to the micro-pit on the corrosion surface are not enough to govern or dictate the location of the fatigue crack initiation.

The 3D micro-feature characteristics of the corrosion damage are considered by looking at various surface roughness metrics reported in **Figure 3.4-Figure 3.9**, it can be seen that the contribution of the neighboring corrosion feature also do not have high influence on the location of the fatigue crack initiation site. If the areal features of the corrosion damage are highly significant, the fatigue crack initiation should have been found on the areas where the Sq (root mean square), Sv (maximum valley depth), Sa (arithmetic mean height), Spc (arithmetic mean curvature) and Spd (peak density) are very high. The markers on the histograms should have been found consistently towards the higher end of the histogram, instead the markers are dispersedly distributed on the histograms of the 250 μm × 250 μm and 100 μm × 100 μm analyses. This also demonstrates that there is a parameter beyond the corrosion damage shape that influence the location of the fatigue crack initiation.

3.4.2 Effects of Microstructure

Aluminum 7xxxx series has a lot of second phase particles that can influence the fatigue cracking properties of the alloy [15,16,19–22,32]. These second phase particles commonly exhibit a different character than the aluminum matrix. The Mg_2Si are softer than the aluminum matrix, and the Al_7Cu_2Fe constituent particles are more brittle than the aluminum matrix [15]. These particles are reported to be detrimental to fatigue [15,16,19–22,32]. These second phase constituent particles are generally larger than the other phase particles such as the dispersoids and the age hardening precipitates. These constituent particles can typically range from 5-30 µm in diameter [33]. Although such large constituent particles at the surface of the material are well known to initiate fatigue cracks in pristine samples [17], fractography reveals that all the fatigue cracks initiated at the corrosion feature, or at the features intersected by the corrosion damage. This shows that when corrosion damage is present, the fatigue initiation site will have a higher probability of occurring at the corrosion damage than in the cracked constituent particles. However, these constituent particles also play an important role on corrosion damage mechanisms in AA 7050-T7451. Some of the second phase particles are anodic with respect to the matrix and some are cathodic with respect to the matrix [34–36]. Rafla et al. also showed that the second phase particles may have anodic or cathodic property with respect to the alloy that is galvanically coupled with the aluminum matrix [35]. Even though the fatigue crack does not commonly initiate from the constituent particles or at the vicinity of the constituent particles when a corrosion damage is present on the aluminum matrix, it is important to acknowledge the influence of these second phases on the corrosion mechanisms of the system. However, this is outside the scope of the current study.

The distribution of constituent particles on the aluminum matrix is also believed to influence the fatigue behavior of the aluminum alloy. These constituent particles can impart residual strains on the aluminum matrix, thus it can influence the fatigue cracking behavior of the alloy. If each constituent particle is to be taken as hot spot [37], it can be assumed that there will be higher probability of fatigue cracking to initiate at these clustered constituent particles. However, the results shown in **Figure 3.13** indicates that most of the fatigue crack initiation have nearby constituent particles that are dispersed (>

0.5 ANN ratio); this is consistent with the findings of Harlow, et al. [22]. Aside from the clustering of the constituent particles, the number of constituent per area (number density) also shows no strong effect on the fatigue crack initiation location. **Figure 3.13** also shows the possible combined effects of constituent particle clustering (ANN ratio) with the normalized size of the constituent particles, and the combined effects of constituent particle clustering (ANN ratio) with the normalized number of constituent particle (number density) on the location of the fatigue crack initiation. Both graphs (**Figure 3.13** (a) and (b)) show no strong correlation. When constituent particles are considered as hot spots, it may seem logical to find the fatigue initiation at the areas having the highest number of constituent particles that are clustered or at the areas having the large constituent particles that are clustered. However, this is not the case for both alloys with (current study) or without (Harlow, et al. [22]) the presence of corrosion damage. The change in the trend on the 3D analysis of number density using 250 μm × 250 μm and 100 μm × 100 μm in **Figure 3.15** (markers are located towards high number density in the histogram) and **Figure 3.16** (markers are located towards low number density in the histogram) respectively, further demonstrates that the 3D number density values are not mainly affecting the location of the fatigue crack initiation.

In considering the nearest distance of the large constituent particles to the fatigue initiation point, results show that the shortest distance of the constituent particle to the fatigue initiation point is roughly around 20 μm as shown in **Figure 3.14** (b). The other values of the shortest distance of large constituent particles from the initiation point are greater than 100 μm. These large constituent particles can be deemed relatively far from the initiation point to influence the fatigue crack initiation mechanism.

Aside from constituent particles, one of the microstructural features commonly associated with fatigue cracking is the amount of deformation present in the grains. The deformation is normally measured by the presence of dislocations. Highly deformed grains requires a high dislocation density. The dislocation density of a material is normally studied using transmission electron microscopy (TEM). Due to the limitation of precise determination of fatigue initiation site on thin and properly polished TEM specimens, EBSD analysis is employed instead. The grain orientation spread is taken as the parameter to measure the amount of deformation present in the grain. Since the fatigue crack initiated both on a grain with high and low grain orientation spread values (see **Figure 3.18**), the amount of deformation is not considered a dominant parameter that mainly influences the location where the fatigue crack can initiate. The analysis of grain orientation spread is done after fatigue testing and it is recognized that loading can affect the values of grain orientation spread. However, a conservative estimate of the plastic zone size for corroded specimens (~ 0.36 μm for a ΔK of 1 MPa$\sqrt{m}$ [8]) indicates that the area analyzed for EBSD (after polishing ~50 μm from the fracture surface) is outside the plastic zone size. Thus, the regions of the EBSD and the grain orientation spread values can reasonably be assumed to not be influenced the crack wake.

There are other parameters that can be analyzed from the EBSD characterization aside from the grain orientation spread. The parameters that may affect the fatigue behavior such as the grain orientation parallel to projection of the IPF on the loading direction (L-direction), grain size, and misorientation angles of the neighboring grains beside the fatigue initiating grain are reported in results section. Both the grain size and grain orientation are commonly used in modeling fatigue cracking [37–39]. The fatigue initiating grains are not on the small or large tails of the distribution based on the distribution of grains obtained from the EBSD scans. According to Sanders and Starke, the reduction in grain size improved the fatigue cracked initiation resistance of AA 7050 [40]. It is more likely to find fatigue initiation sites at relatively larger grains than at smaller grains due to the higher possibility of forming persistent slip bands resulting to slip-band decohesion or grain boundary cracking [41]. Results show that most of the fatigue initiating grains are larger than the mean and median sizes of the grains but not on the largest grain (see **Figure 3.18**). The fatigue initiating sites characterized in this study generally occur at grains with high index orientation. The grain where fatigue cracks can initiate cannot exactly be pre-determined by just considering the grain orientation. There can be other factors such as damage accumulation or hydrogen trapping on defect sites that needs to be considered, such as hypothesized by Gupta et al. [16,17]. However, further analysis of the fatigue crack initiation needs to be done in order to determine the damage accumulation effects and hydrogen trapping effects.

The misorientation angles between these fatigue initiating grains and the neighboring grains are generally greater than 15°. The misorientation angle greater than 15° are commonly classified as high angle grain boundaries[17]. Fatigue initiation is commonly expected to occur at the grain with a high misorientation angle with the adjacent grain. Accumulated dislocations on fatigue initiating grains may have lower possibility of being transmitted on the adjacent grain if the misorientation angle between the fatigue initiating grain and the adjacent grain are high [13,42]. This high misorientation angle provides high mismatch between the fatigue initiating grain and the neighboring grain. Once the accumulated dislocation due to fatigue cycling exceeded a critical value, the fatigue crack can initiate on the grain. Other factors, or a combination there of, might need to be considered in order to explain the occurrence of fatigue crack initiation on grains that have lower misorientation angles with respect to the adjacent grains. The combination of the contribution of each individual microstructural features are not considered in this study.

The individual contribution of alloy microstructural features such as grain size, grain orientation with respect to the loading direction, grain orientation spread, grain misorientation, constituent particle size, constituent particle distribution, constituent particle distance from the fatigue crack formation point does not uniquely dictate the location of fatigue crack formation. Aside from these microstructural features, the individual contribution of the corrosion macro-scale features (pit/fisuure depth, pit/fissure density, number of pits per line or fissures per plane, corrosion damage roughness) and the individual contribution of the corrosion micro-scale features (jut-in, micro-pits, ligaments with high aspect ratio, ligaments with low aspect ratio and areal surface roughness) also do not uniquely and strongly correlate to the location of the fatigue crack formation. No single parameter prominently correlates to the fatigue crack initiation location. Even though these parameters do not particularly dictate the location of fatigue crack initiation, these parameters are important and should not be neglected in further analysis of fatigue crack formation. The coupled effects of these parameters can be studied using two different approach: (1) data science and (2) analytical methods via crystal plasticity modeling. Chapter 4 Section 1 provides a summary of analysis done on corrosion macro scale feature using data science approach and Chapter 4 Section 2 provides an overview of the crystal plasticity modeling done by determining the fatigue indicator parameters on corroded specimens.

3.5 Conclusions

The location of fatigue crack initiation for a corroded AA 7050-T7451 are characterized in terms of the adjacent micro-scale corrosion damage feature and underlying alloy microstructures. The micro-scale features present on the corrosion damage surface are micro-pits, jut-ins, and remaining metallic ligaments. The surface roughness of the corrosion damage are characterized and the values of surface roughness parameters are reported. The alloy microstructural features analyzed in this study are the constituent particle distribution, constituent particle size, constituent particle distance, grain orientation, grain size, grain orientation spread and misorientation angle between the fatigue initiating grain and the neighboring grains. These micro-scale and microstructural features are correlated with the fatigue initiation location. The following conclusions are made:

- Most of the fatigue cracks initiate at jut-in and remaining metallic ligaments, however, not all jut-in and ligament features on the surface of the corrosion damage initiate fatigue crack. The areal corrosion features do not highly dictate the location of the fatigue initiation site. There are other factors aside from the corrosion damage shape that need to be considered in predicting the location of fatigue crack initiation.
- The distribution of constituent particles, constituent particle distance as well as the size of constituent particles have limited contribution to the fatigue crack initiation of corroded AA 7050-T7451.
- There are other parameters aside from the amount of deformation (as measured by the grain orientation spread) present in the grain that can influence fatigue crack initiation.

- Most of the fatigue initiating grains are larger than the median or mean value of the grain size. It is important to note that it is not always the biggest grain that initiates fatigue cracks.
- The fatigue crack initiation generally occurred on grains with high index orientation, and on grains with high misorientation angle with respect to the neighboring grains.

3.6 References

[1] Burns JT, Kim S, Gangloff RP. Effect of corrosion severity on fatigue evolution in Al-Zn-Mg-Cu. Corros Sci 2010;52:498–508. doi:10.1016/j.corsci.2009.10.006.

[2] Pao PS, Gill SJ, Feng CR. On fatigue crack initiation from corrosion pits in 7075-T7351 aluminum alloy. Scr Mater 2000;43:391–6. doi:10.1016/S1359-6462(00)00434-6.

[3] Medved JJ, Breton M, Irving PE. Corrosion pit size distributions and fatigue lives - A study of the EIFS technique for fatigue design in the presence of corrosion. Int J Fatigue 2004;26:71–80. doi:10.1016/S0142-1123(03)00069-0.

[4] Sabelkin V, Perel VY, Misak HE, Hunt EM, Mall S. Investigation into crack initiation from corrosion pit in 7075-T6 under ambient laboratory and saltwater environments. Eng Fract Mech 2015;134:111–23. doi:10.1016/j.engfracmech.2014.12.016.

[5] Burns JT, Larsen JM, Gangloff RP. Driving forces for localized corrosion-to-fatigue crack transition in Al-Zn-Mg-Cu. Fatigue Fract Eng Mater Struct 2011;34:745–73. doi:10.1111/j.1460-2695.2011.01568.x.

[6] Barter SA, Molent L, Wanhill RJH. Typical fatigue-initiating discontinuities in metallic aircraft structures. Int J Fatigue 2012;41:11–22. doi:10.1016/j.ijfatigue.2011.10.017.

[7] Pearson S. Initiation of fatigue cracks in commercial aluminium alloys and the subsequent propagation of very short cracks. Eng Fract Mech 1975;7:235–47. doi:10.1016/0013-7944(75)90004-1.

[8] Burns JT, Larsen JM, Gangloff RP. Effect of initiation feature on microstructure-scale fatigue crack propagation in Al-Zn-Mg-Cu. Int J Fatigue 2012;42:104–21. doi:10.1016/j.ijfatigue.2011.08.001.

[9] Co NEC, Burns JT. Effects of macro-scale corrosion damage feature on fatigue crack initiation and fatigue behavior. Int J Fatigue 2017;103:234–47. doi:10.1016/j.ijfatigue.2017.05.028.

[10] Co NEC, Burns JT. Galvanic Corrosion-Induced Fatigue Crack Initiation and Propagation Behavior in AA7050-T7451. CORROSION 2016;72:1215–9. doi:10.5006/2132.

[11] Barter SA, Sharp PK, Holden G, Clark G. Initiation and early growth of fatigue cracks in an aerospace aluminium alloy. Fatigue Fract Eng Mater Struct 2002;25:111–25. doi:10.1046/j.1460-2695.2002.00482.x.

[12] Huang Y, Ye X, Hu B, Chen L. Equivalent crack size model for pre-corrosion fatigue life prediction of aluminum alloy 7075-T6. Int J Fatigue 2016;88:217–26. doi:10.1016/j.ijfatigue.2016.03.035.

[13] Cheong KS, Smillie MJ, Knowles DM. Predicting fatigue crack initiation through image-based micromechanical modeling. Acta Mater 2007;55:1757–68. doi:10.1016/j.actamat.2006.10.038.

[14] Laz P., Hillberry B. Fatigue life prediction from inclusion initiated cracks. Int J Fatigue 1998;20:263–70. doi:10.1016/S0142-1123(97)00136-9.

[15] Payne J, Welsh G, Christ RJ, Nardiello J, Papazian JM. Observations of fatigue crack initiation in 7075-T651. Int J Fatigue 2010;32:247–55. doi:10.1016/j.ijfatigue.2009.06.003.

[16] Gupta VK, Gangloff RP, Agnew SR. Diffraction characterization of microstructure scale fatigue crack growth in a modern Al-Zn-Mg-Cu alloy. Int J Fatigue 2012;42:131–46. doi:10.1016/j.ijfatigue.2011.08.003.

[17] Gupta VK, Agnew SR. Fatigue crack surface crystallography near crack initiating particle clusters in precipitation hardened legacy and modern Al–Zn–Mg–Cu alloys. Int J Fatigue 2011;33:1159–74. doi:10.1016/j.ijfatigue.2011.01.018.

[18] ISO 25178-2:2012 Geometrical product specifications (GPS) — Surface texture: Areal — Part 2: Terms, definitions and surface texture parameters. International Organization for Standardization; 2012.

[19] Telesman J. Review of the Effects of Micro structure on Fatigue in Aluminum Alloys. 1984.

[20] Cvijović Z, Rakin M, Vratnica M, Cvijović I. Microstructural dependence of fracture toughness in high-strength 7000 forging alloys. Eng Fract Mech 2008;75:2115–29. doi:10.1016/j.engfracmech.2007.10.010.

[21] Papazian JM, Anagnostou EL, Engel SJ, Hoitsma D, Madsen J, Silberstein RP, et al. A structural integrity prognosis system. Eng Fract Mech 2009;76:620–32. doi:10.1016/j.engfracmech.2008.09.007.

[22] Harlow DG, Nardiello J, Payne J. The effect of constituent particles in aluminum alloys on fatigue damage evolution: Statistical observations. Int J Fatigue 2010;32:505–11. doi:10.1016/j.ijfatigue.2009.02.036.

[23] Zhang J, Przystupa MA, Luévano AJ. Characterizations of pore and constituent particle populations in 7050-T7451 aluminum plate alloys. Metall Mater Trans A 1998;29:727–37. doi:10.1007/s11661-998-0263-2.

[24] Humphreys FJ. Grain and subgrain characterisation by electron backscatter diffraction. J Mater Sci 2001;36:3833–54. doi:10.1023/A:1017973432592.

[25] Humphreys FJ. Quantitative metallography by electron backscattered diffraction. J Microsc 1999;195:170–85. doi:10.1046/j.1365-2818.1999.00578.x.

[26] Humphreys FJ. Reconstruction of grains and subgrains from electron backscatter diffraction maps. J Microsc 2004;213:247–56. doi:10.1111/j.0022-2720.2004.01297.x.

[27] Polkowski W, Jóźwik P, Bojar Z. Electron Backscatter Diffraction Study on Microstructure, Texture, and Strain Evolution in Armco Iron Severely Deformed by the Differential Speed Rolling Method. Metall Mater Trans A Phys Metall Mater Sci 2015;46:2216–26. doi:10.1007/s11661-015-2760-4.

[28] Alvi M, Wuk Cheong S, Weiland H, Rollett AD. Recrystallization and Texture Development in Hot Rolled 1050 Aluminum. Mater Sci Forum - MATER SCI FORUM 2004;467:357–62.

[29] Cheong SW, Weiland H. Understanding a Microstructure Using GOS (Grain Orientation Spread) and Its Application to Recrystallization Study of Hot Deformed Al-Cu-Mg Alloys. Mater Sci Forum 2007;558–559:153–8. doi:10.4028/www.scientific.net/MSF.558-559.153.

[30] Wang L, Daniewicz SR, Horstemeyer MF, Sintay S, Rollett a. D. Three-dimensional finite element analysis using crystal plasticity for a parameter study of microstructurally small fatigue crack growth in a AA7075 aluminum alloy. Int J Fatigue 2009;31:651–8. doi:10.1016/j.ijfatigue.2008.03.027.

[31] Maitland T, Sitzman S. Electron Backscatter Diffraction (EBSD) Technique and Materials Characterization Examples. In: Zhou W, Wang ZL, editors. Scanning Microsc. Nanotechnol. Tech. Appl., Springer; 2007, p. 41–75.

[32] Campbell F. Manufacturing Technology for Aerospace Structural Materials. Manuf. Technol. Aerosp. Struct. Mater., Elsevier; 2006, p. 15–92. doi:10.1016/B978-185617495-4/50002-0.

[33] Dixit M, Mishra RS, Sankaran KK. Structure–property correlations in Al 7050 and

Al 7055 high-strength aluminum alloys. Mater Sci Eng A 2008;478:163–72. doi:10.1016/j.msea.2007.05.116.

[34] Birbilis N, Buchheit RG. Electrochemical characteristics of intermetallic phases in aluminum alloys. J Electrochem Soc 2005;152:B140–51. doi:10.1149/1.1869984.

[35] Rafla VN, Davenport A, Scully JR. Determination of Cathodic and Anodic Charge from Operando X-Ray Tomography Observation of Galvanic Corrosion of Aluminum Alloy 7050-T7451 and 304 Stainless Steel in a Simulated Fastener. CORROSION 2015;71:1300–3. doi:10.5006/1871.

[36] Rafla VN, King AD, Glanvill S, Parsons A, Davenport A, Scully JR. Operando Observation of Galvanic Corrosion Between Aluminum Alloy 7050-T7451 and 304 Stainless Steel in a Simulated Fastener Arrangement Using X-Ray Tomography. CORROSION 2015;71:1171–6. doi:10.5006/1813.

[37] Mello AW, Nicolas A, Lebensohn RA, Sangid MD. Effect of microstructure on strain localization in a 7050 aluminum alloy: Comparison of experiments and modeling for various textures. Mater Sci Eng A 2016;661:187–97. doi:10.1016/j.msea.2016.03.012.

[38] Tryon RG, Dey A, Krishnan G, Zhao Y. Microstructural-Based Physics of Failure Models to Predict Fatigue Reliability 2006;0:520–5.

[39] Rovinelli A, Lebensohn RA, Sangid MD. Influence of microstructure variability on short crack behavior through postulated micromechanical short crack driving force metrics. Eng Fract Mech 2015;138:265–88. doi:10.1016/j.engfracmech.2015.03.001.

[40] Sanders RE, Starke EA. The effect of intermediate thermomechanical treatments on the fatigue properties of a 7050 aluminum alloy. Metall Trans A 1978;9:1087–100. doi:10.1007/BF02652213.

[41] Chan KS. Roles of microstructure in fatigue crack initiation. Int J Fatigue 2010;32:1428–47. doi:10.1016/j.ijfatigue.2009.10.005.

[42] Tanaka K, Mura T. Fatigue crack growth along planar slip bands. Acta Metall 1984;32:1731–40. doi:10.1016/0001-6160(84)90229-3.

4. Combined Effects

4.1 Overview

The individual macro-scale corrosion metrics are previously correlated to the location of the fatigue crack initiation as discussed in Chapter 2. Results of this analysis show that individual macro-scale corrosion metrics are not dictating the location of the fatigue crack initiation. Crude analysis of the macro-scale corrosion metrics by plotting one parameter versus the other parameter is done. This crude analysis also leads to the generalization that the combined effects of macro-scale corrosion metrics are not completely governing the fatigue crack initiation location. However, this rudimentary analysis of the combined effects of macro-scale corrosion metrics are not enough to prove the non-existent relationship between the corrosion features and the fatigue crack formation location.

Data science is the first technique employed in this chapter to determine the relationship of the macro-scale corrosion metrics analyzed in Chapter 2. This is done in collaboration with Dr. Donald Brown of UVa Data Science Institute, and the Department of Systems and Information Engineering. The paper published in the Journal of Minerals, Metals and Materials is included in this dissertation as Chapter 4 Section 2. The author performed the experiments to obtain the data, as well as the data binning. Dr. Brown contributed on the modeling and the combined metrics analyses.

Data science analysis can be employed to determine if the extent to which the crack formation location can be predicted by the characterized corrosion damage and microstructure metrics. The current work takes the first step in this process by evaluating possible coupled effects of the macro-scale corrosion metrics to determine if the crack formation location can be predicted by taking into account interactions between these features. It is hypothesized that the data science technique will identify the best macro-scale parameter that can be used to predict the fatigue crack initiation location.

These input parameters are used in logistic regression modeling and random forest modeling to predict the probabilities of fatigue crack formation. In order to assess the significance of the resulting models, a permutation test is employed. The probabilities that exceed the threshold value based on the permutation test are considered significant. Only a few points exceeded the threshold for the relationship between the predictor variables (macro-scale corrosion morphology metrics) and the fatigue crack initiation to be considered significant. Thus, the results of the data science analyses show that even when considering interactions between the macro-scale corrosion metrics for DP1, FIS, GCSR, the fatigue crack initiation site cannot be described solely by the macro-scale metrics. This is consistent with the previous analysis for the individual contribution of macro-scale corrosion features. It is important to note that even though the results of these analyses indicate that the macro-scale corrosion morphologies alone have minimal significance in predicting the crack formation location, this does not mean that they are not potentially important. Rather this analysis suggests that it is necessary to account for other parameters such as micro-scale corrosion feature and underlying microstructure to obtain a more informed prediction of fatigue crack initiation. If the incorporation of such additional parameters results in predictive models it will be possible to identify the relative significance of each features. Such work to incorporate these additional micro-scale and microstructure metrics into these data science methods is ongoing.

Crystal plasticity modeling is the second method used to analyze the combined effects of the macro-scale and micro-scale corrosion damage features as well as the underlying alloy microstructure. This is done in collaboration with Andrea Nicolas and Dr. Michael Sangid of Purdue University. The results obtained from Chapters 2 and 3 are used as inputs to the crystal plasticity modeling. The author performed all the experimentation and initial thresholding of data, while the final thresholding and crystal plasticity modeling is performed by Purdue University. The inputs in the model include information on the corrosion damage shape and constituent particle distribution from XCT, and the grain information from EBSD. Fatigue indicator parameters (FIPs) are calculated and analyzed for a specific corrosion morphology. The calculated distribution of FIPs on the fracture plane is compared to the actual location of the experimental fatigue initiation site. It is hypothesized that the fatigue crack initiation site corresponds to the area having the highest FIP value. Chapter 4 Section 3 provides details of this collaboration with the initial findings using FIS specimen.

4.2 Data Science Analysis of the Macro-scale Features Governing the Corrosion to Crack Transition in AA7050-T7451

4.2.1 Introduction

Aluminum 7xxx-series alloys used in aerospace applications [1] have high-strength-to-weight ratios and high toughness values, but are prone to corrosion damage that serves to preferentially initiate fatigue cracking [2–9]. Literature has established that different aspects of the corrosion damage will govern the crack formation behavior depending upon the morphology and extent of the damage [6–16]. Recent efforts [6] systematically explored the effect of varying corrosion morphologies on the mechanisms that govern crack formation [7–13]. This was done by evaluating a variety of different corrosion morphologies in 7050-T7451 produced under different electrochemical conditions relevant to those induced by galvanic coupling of an Al-structure and stainless steel fastener. Macro-scale corrosion metrics (depth, area, volume, diameter, density, etc.) of the fatigue initiating sites were quantified and compared to the overall distribution of these metrics on the broadly corroded surface. Critically, this effort found that when evaluating each metric individually, none uniquely correlated to the location of the fatigue crack initiation [6]. For example, while the fatigue damage generally initiated at one of the deeper pits on the sample, it did not occur on the deepest pit. These findings suggest that either (1) the macro-scale metrics are not the features that dominantly govern the crack formation behavior (i.e. micro-scale features or microstructure interactions play a more prominent role), and/or (2) that there is an interacting effect between the macro-scale metrics that governs the behavior. Companion efforts are underway to perform analysis on potentially relevant micro-feature and microstructure features (addressing (1)) and analytically describe the sensitivity of the local material stress/strain response to the macro-scale, micro-scale corrosion morphology and microstructure features via crystal plasticity modeling (addressing (1) and (2)). However, the current study aims to determine if a more robust correlation between the macro-scale metrics and the crack formation location can be achieved (e.g. addressing (2)) by applying data-science techniques to account for the interactions between the different macro-scale metrics.

Data science provides techniques and methods to discover relationships in data from observations and experiments [17]. While using data to uncover relationships has been at the foundation of the scientific method since its inception, data science now joins modern computational resources with newer analytical approaches to allow researchers to more quickly discover relationships with larger or more complicated data sets [18,19]. The objective of this paper is to apply data science techniques to the experimental data reported in prior work [6] to determine if the crack initiation behavior can be rigorously described by accounting for interactions between relevant macro-scale corrosion metrics. If this can be done, then such data science techniques could be used to provide a sensitivity analysis of the crack formation behavior to each of the individual metrics, which could inform inspection protocols for engineering applications.

4.2.2 Methodology

Full details of the material, corrosion protocols, characterization methods, and fatigue testing were previously reported [6]; however it is appropriate to present an abbreviated description of these parameters and discuss how the data were organized for the current analysis.

4.2.2.1 Corrosion Protocol and Fatigue Testing

The fatigue experiments were performed using 7.60 mm thick AA 7050-T7451 dog bone specimens, with a reduced gage section width of 7.60 mm and length of 20.96 mm. Microstructure and mechanical properties are reported elsewhere [6]. Prior to testing, a ~4-7 mm^2 region of the L-S surface of the fatigue specimens were subjected to various electrochemical exposures [6,20] to impart either: (1) shallow discrete pits (DP1), (2) fissure-like corrosion damage (FIS), or (3) surface recession (GCSR). A 3D representation of the damage was obtained via white light interferometry or X-ray computed tomography (XCT). **Figure 4.2.1** shows the image representation for DP1 specimen obtained using MountainsMap post processing software to visualize white light interferometry data. The metrics for DP1 specimens analyzed and reported were depth, surface area of the pit mouth, volume, diameter, and pit density. Line scan based metrics were also used for DP1; specifically, the number of pits per line, total depth of pits per line, and average depth of pits per line. The line scan analysis was done in order to determine the influence of coplanar damage on fatigue crack initiation [6]. The line scan (corresponding to a specific plane) analysis was done perpendicular to the axis of the loading direction, and line profile was taken at every 50 μm interval for the entire corroded area of the specimen. Details of the analysis was reported in [6]. The metrics analyzed and reported for FIS were fissure depths, number of fissures per plane, and total fissure depth per plane. For GCSR specimens, surface roughness metrics were reported such as average roughness or root mean square (RMS), peak density, maximum valley depth, maximum height, texture aspect ratio, auto correlation length, kurtosis, and arithmetic mean height. For this paper, all the metrics listed above are considered as predictor variables in the data science analysis; detailed descriptions of these metrics can be found elsewhere [6].

Specimens were subjected to fatigue testing with a σ_{max} of 200 MPa, R = 0.5 and frequency of 20 Hz. Specimens were loaded along the L-direction and specimens were kept in sealed acrylic chamber to keep the humidity >90% RH during the entire duration of fatigue test. Special fatigue loading protocol was used to create identifiable marks on the fracture surface. Fractography using the scanning electron microscope was performed on the failed specimens in order to track the location of the marker bands, and determine the fatigue crack initiation location. The optical microscope and white light interferometry or XCT characterization of the corrosion damage were coupled with the SEM fractrographs to identify the location of the fatigue initiation point in the optical microscope image and in the 3D representation [6].

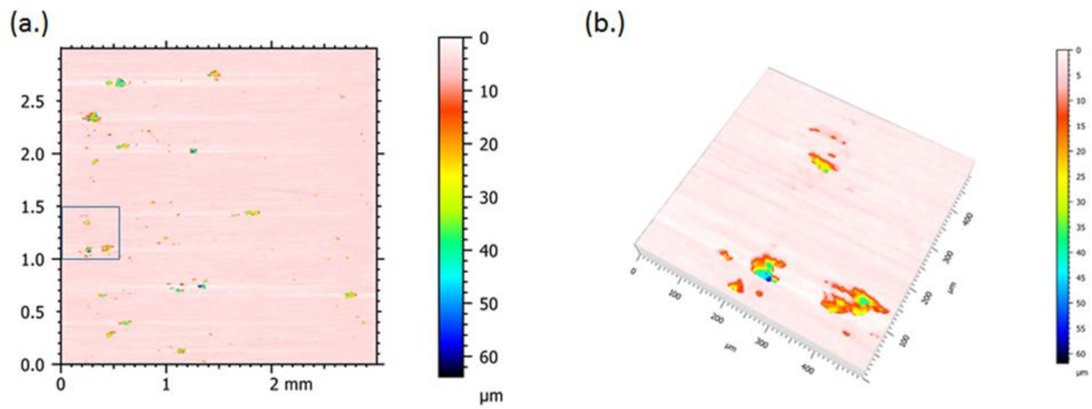

Figure 4.2.1 (a.) Image representation of white light interferometry data obtained for DP1 specimen with corrosion pits on the surface. (b.) 3D rendering of pits within the 500 µm x 500 µm area. The depth of pits corresponds to the value denoted by the color map.

Specimens were subjected to fatigue testing with a σ_{max} of 200 MPa, R = 0.5 and frequency of 20 Hz. Specimens were loaded along the L-direction and specimens were kept in sealed acrylic chamber to keep the humidity >90% RH during the entire duration of fatigue test. Special fatigue loading protocol was used to create identifiable marks on the fracture surface. Fractography using the scanning electron microscope was performed on the failed specimens in order to track the location of the marker bands, and determine the fatigue crack initiation location. The optical microscope and white light interferometry or XCT characterization of the corrosion damage were coupled with the SEM fractrographs to identify the location of the fatigue initiation point on the optical microscope image and in the 3D representation [6].

4.2.2.2 Data Binning

It is necessary to segregate the quantitative metrics obtained from white light interferometry or XCT characterization into distinct bins to enable the application of the data science approach. Specifically, the damage metrics described above were quantified for each feature on the corroded surface. The data corresponding to the primary initiation point that lead to failure in each sample was assigned a value of 2, while secondary crack initiation points were assigned a value of 1. (Details on how the primary crack was determined can be found in [6]). All other data points not corresponding to a particular fatigue crack initiation location were assigned a value of 0. These inputs serve as the raw data used in the data science analysis that aims to determine if there is a correlation (either individual or coupled) between these macro-scale damage descriptors and the crack formation location.

4.2.2.3 Data Science Approach

The goals of this paper represent a small but complicated data problem. The complications arise due to the potential for non-linear relationships between variables, such as, depth, surface area, volume and diameter of corrosion, and the response (the initiation location). Data science uses techniques from machine learning to address these types of problems. Several useful machine learning techniques for discovering nonlinear relationships include random forests, extreme gradient boosting, support vector machines, and neural networks. All of these techniques do well at uncovering complex, nonlinear relationships, but support vector machines and neural networks do not provide easily interpretable models of their results. In that sense, they are considered black boxes that provide accurate but opaque versions of the phenomena they are modeling. As such, random forests and extreme gradient boosting were used. The results provided by both techniques were similar, so only random forests results were reported.

Random forest modeling is an ensemble technique that combines the outputs from a group of classifiers to produce an overall classification. The individual classifiers in random forests use a recursive algorithm to partition the space defined by the predictor variables into separate regions. **Figure 4.2.2** shows an example of a partitioning of two variables X_1 and X_2 by a single tree in order to classify green crosses and blue triangles. The recursive algorithm in random forest creates many of these partitions (or trees) across all dimensions. For the data in this study, the variables were morphology metrics such as pit depth and number of pits. The random forest model combines a large number of these partitions or trees and takes votes among them to produce probabilities of initiation points. As a result of this combined partitioning, the random forest technique can find nonlinear and perhaps disjoint relationships between the predictor variables and response or classification values.

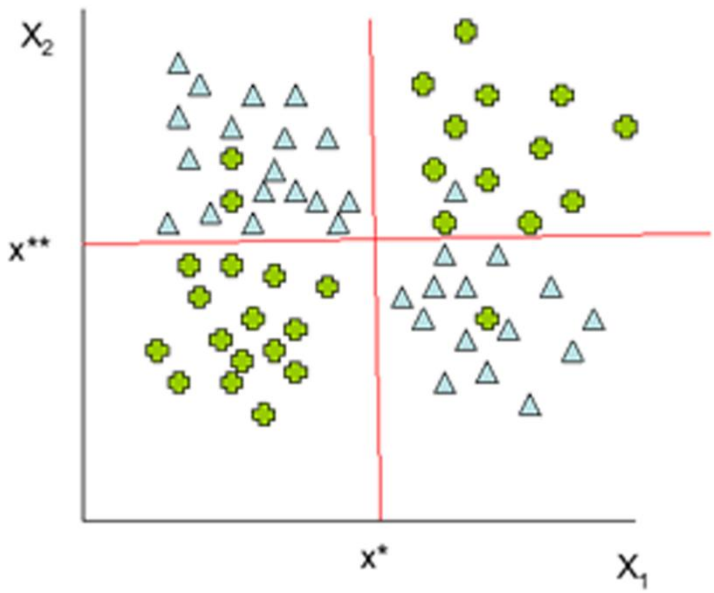

Figure 4.2.2 Example of random forest single tree partitioning of two variables X_1 and X_2 in order to classify green crosses and blue triangles

Logistic regression, which finds linear separators for classification, was employed to judge whether any nonlinearity found by the random forest is real. Logistic regression extends ordinary least squares regression to problems where the response or dependent variable is binary. The method finds a linear relationship between the predictor or independent variables and the log odds of the binary response. The log odds can be easily transformed into probabilities. Further details on the use of both random forest models and logistic regression in data science can be found in [21,22]. To implement the modeling approach, the randomForest package [23] in R for random forest modeling and the base statistics in R for the logistic regression were used. In the random forest models, the authors built 500 trees after initial experimentation with this parameter and local grid search. All other parameters were set at their default values. *In toto*, these techniques were used to determine the probability that the various macro-scale corrosion metrics (and their interactions) are sufficiently descriptive to predict the crack initiation location.

4.2.3 Results

In this study, data from DP1, FIS, and GCSR testing were considered, each with their own metrics that describe the shape of the corrosion damage and were being evaluated as predictor variables. Each morphology has three experimental replicates that provide the basis for building the data science models. This means that for each morphology, three random forest and three logistic regression models were constructed using two of the replicates for parameter estimation and the third for performance evaluation. This allows fair assessment of the performance of each of the models. To judge performance, the authors focused on false negatives; that is, incorrectly classifying an initiation site.

To develop both the logistic regression and the random forest models, the initiation sites were oversampled for two of the three morphologies (DP1 and FIS). Oversampling allows the methods to build classification models when one of the two classification values is extremely under-represented in the data. In this case, there are very few initiation sites. For example, in DP1, there are only 4 initiation sites out of a total of 2384 sites evaluated. So, oversampling forces the models to more fairly consider the correct classification of the initiation sites. For this study, the authors used an oversampling rate of $2^k m$ where m is the number of initiation sites in the data and k is the oversampling parameter. Experimentation showed that $k = 6$ produced predictions of initiation points by the models. Oversampling was only used to train or build the models, and testing was only performed with actual data from the appropriate replicate. For the GCSR morphology, oversampling was not used since the data set is smaller and has a comparatively large number of initiation sites.

To judge if an initiation site prediction by a model is significant, a permutation test was used. This means that the values of the morphology metrics were permuted and the predicted probabilities for the initiation sites were evaluated. Random permutation destroys any structural relationship between the morphology metrics and the initiation sites; hence, simulations of a random process using the metrics to predict initiation sites were obtained. With these simulations, we can test the hypothesis that the observed predictions are not significantly different from a random process. Values that lie above the 95th (5%) percentile (a one-sided test) for the distribution of these probabilities are considered significantly different from this random permutation process. Hence, for observations above this threshold, the hypothesis can be rejected at $p<0.05$.

1000 permutations were ran for each replication of each morphology for logistic regression. For random forest, the authors ran 1000 permutations for GCSR and 100 for the other morphologies. Since random forest gives random predictions of initiation sites, 10 different random forest models were produced for each replication and morphology.

The results are shown in **Table 4.2.1**. Where there are multiple initiation sites in the morphology, the prediction column for logistic regression shows the minimum and maximum values observed. For random forest the prediction column shows the maximum and minimum values obtained for the 10 runs for each initiation point. Highlighted predicted values show significance ($p < 0.05$).

Table 4.2.1 Hypothesis test thresholds ($p < 0.05$) for each morphology, each test replicate, and each model, and model predicted probabilities for the presence of an initiation point. Parenthetical predictions show minimum and maximum predicted probabilities for multiple initiation points in a morphology for logistic regression and for the 10 separate runs of random forest for each initiation point in the morphology. Highlighted predicted values show significance ($p < 0.05$).

Morphology	**Replicate**	**Random Forest**		**Logistic Regression**	
		Thresholds	Predictions	Thresholds	Predictions
DP1 Grid	1	0.31	(0.00, 0.10)	0.11	(0.01, 0.06)
	2	0.40	(0.00, 0.00)	0.13	**0.65**
	3	0.35	(0.03, 0.05)	0.11	0.02
DP1 Line	1	0.49	(0.19, 0.25)	0.35	**0.84**
	2	0.44	(0.00, 0.00)	0.30	0.00
	3	0.45	(**0.82, 0.87**)	0.35	**0.99**
FIS	1	0.22	(0.00, 0.00)	0.11	(0.00, 0.00)
	2	0.36	(0.17, **0.53**)	0.13	**(0.91, 0.96)**
	3	0.26	(0.00, 0.00)	0.13	(0.01, 0.01)
GCSR	1	0.34	(0.04, **0.74**)	0.50	(0.07, 0.45)
	2	0.84	(0.06, 0.23)	0.84	(0.00, 0.02)
	3	0.35	(0.17, **0.40**)	0.40	(0.01, **0.63**)

For DP1, **Table 4.2.1** shows that, with the one exception of replicate 2 with logistic regression, there is no relationship between the morphology metrics (surface area, volume, pit diameter, pit density, and pit depth) and the classification of the initiation points. The lack of similar predictions by the random forest model and by logistic regression for the other replicates imply no relationship.

In the case of the DP1 line profile data (**Table 4.2.1**), the logistic regression model shows significant predictions for the initiation points in two of the replicates (1 and 3), while the random forest model shows significant prediction for only replicate 3. However, the logistic regression models for replicates 1 and 3 are not entirely consistent. The logistic regression model for replicate 1 does not consider the count of pits per line as significant, while the logistic regression model for replicate 3 considers all variables significant in making the prediction. The random forest model for replicate 1 considers pit depths as most important and sum of pit depths as second while the random forest model for replicate 3 reverses that ordering. The results (**Table 4.2.1**) for the FIS case show that both initiation sites for replicate two (2) were well predicted by logistic regression and moderately well predicted by the random forest model. The logistic regression model for this replicate considers all variables, fissure depth, count of the fissures per line, total fissure depth per line, and average fissure depth per line, as significant. For the random forest model, again all variables are important, but fissure depth is the most important in making these predictions. Notice that the tests with the other two replicates provide no confirmation for the results on replicate 2.

Several of the GCSR results (**Table 4.2.1**) show significance for a relationship between the morphology metrics (average roughness (RMS), peak density, maximum area valley depth, maximum height, texture aspect ratio, autocorrelation length, kurtosis, and arithmetic mean height) and the initiation site. Logistic regression shows an accurate prediction for one point in replicate 3, while the random forest model has accurate predictions for one point in replicate 1 and one point in replicate 3. The random forest models that make these predictions are not consistent between replicates or with the logistic regression model for replicate 3. Further, there are four initiation points in each of the GCSR replicates for a total of 12. Of these, only two have correct predictions with the random forest model and only one of the twelve is significant with logistic regression. With this many hypothesis tests, if the Bonferonni correction is applied, only replicate 1 prediction is significant for random forest and the significant prediction for logistic regression corresponds to a different initiation point in a different replicate.

4.2.4 Discussion

Overall, the results from the previous section show that there is little evidence for significance relationships between the morphology metrics and the initiation points. Very few of the results cross the 0.05 (5%) level defined by the permutation test. The predictions that do show significance have issues that raise doubts about the generalizability of the models that produced them.

To understand more fully why at least one initiation point in each morphology is significantly predicted by at least one model, the authors visually explored the data using t-distributed Stochastic Neighborhood Embedding (t-SNE) plots. A t-SNE plot is a nonlinear projection of the variables, in this case, the morphology metrics into two dimensions for viewing [24]. The axes in the t-SNE plot are the two projected dimensions from the original multidimensional space that optimize local proximity or structure. Each axis is a non-linear composite of the original values.

As an example of how the authors used t-SNE plots to better understand the data, **Figure 4.2.3** shows a t-SNE plot of the DP1 line profile data. The DP1 line profile data have only three initiation points and logistic regression accurately predicts two of them while random forests predicts one of them. The t-SNE plot in **Figure 4.2.3** shows the color coded pit depth (the variable identified as most important by random forest). The binning in this plot comes from the statistics in a box plot, roughly the lower extreme (about the 5th percentile for Gaussian data), the 25th percentile, the median, the 75th percentile, and upper extreme (about the 95th percentile in Gaussian data). For the pit depth in the DP1 line profile data, the 25th percentile and the median are the same, so there are only four bins. The local region (colored purple) with high pit depth (30-135 μm) contains the initiation points from replicates 1 and 3 (circled in the figure). They are very close even in the original four dimensional space. However, the initiation point for replicate 2 (square in the figure) is in another local region with pit depths from 5-30 μm. This means that model built with data from replicate 1 can accurately predict replicate 3 and vice versa, but this model cannot generalize to predict replicate 2. t-SNE plots of the other morphologies show similar patterns.

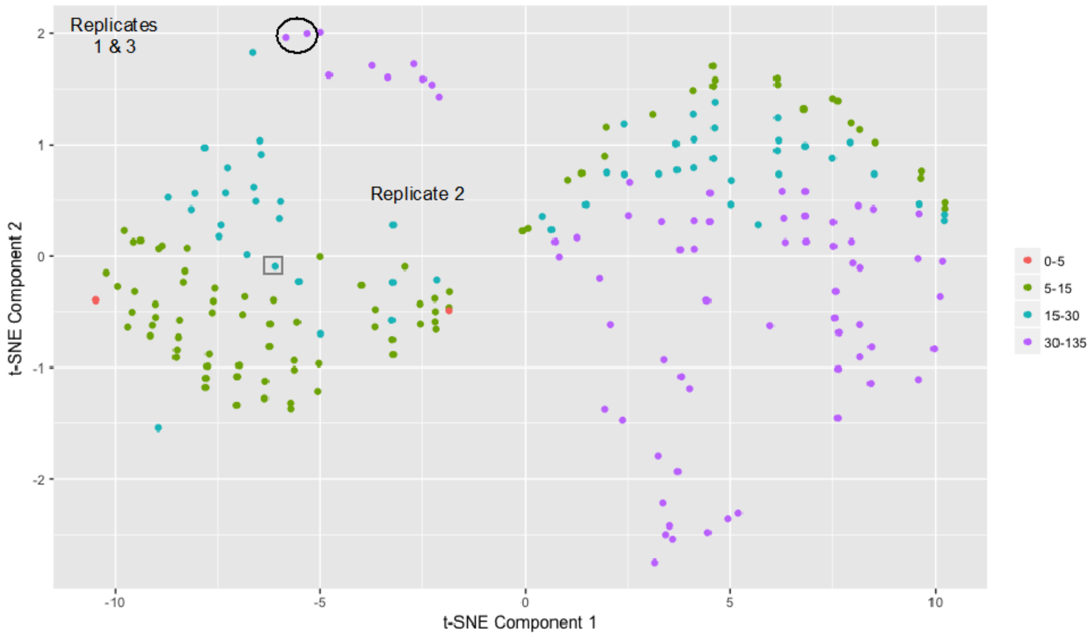

Figure 4.2.3 t-SNE plots of DP1 line profile predictors with color coding for pit depth. The locations of initiation points are marked (circle, square) on the graph. Bin sizes determined by the statistics in a box plot.

In the FIS data, both the random forest model and logistic regression predicted initiation points in the replicate 2 with good accuracy. However, this model does not do well on either of the other replicates. In this data set, the two initiation points for each replicate have exactly the same values for three of the four predictor variables. The major difference with the other replicates is that the number of fissures and total fissure depth is larger than the other fissures. This makes easy segmentation in replicate 2. However, this separation was not evident in the other replicates which means these results are not reproducible.

For GCSR, the data for several points in replicates 1 and 3 are similar and the random forest model exploits this. In particular t-SNE plots (not shown here) reveal that two of the initiation points (in replicates 1 and 3) have average roughness of 87-153 μm. However, this is not true for replicate 2 nor is it consistent among the other initiation points. This results in poor performance for replicate 2 and most of the other initiation points. Again, this means the model is not generalizable.

The results of data science analyses show that the metrics describing the macro-scale corrosion features of AA 7050-T7451 with DP1, FIS and GCSR corrosion morphologies evaluated in this study do not provide a strong prediction of the location of the fatigue crack initiation that can be generalized. The lack of consistency from one replicate to another shows that these parameters (even when accounting for their coupled impact) are not enough to accurately and effectively predict the fatigue crack initiation site. The results of this study support previous findings that there are other parameters (aside from the macro-scale corrosion damage features) that can strongly affect the fatigue crack initiation [6]. While the coupled effect of the macro-scale corrosion damage feature parameters do not strongly predict the location of fatigue crack initiation, it is important to note the analysis above does not imply that these parameters are not significant. Rather, the study suggests it is necessary to take into account additional variables. Ongoing efforts are characterizing other parameters, such as the micro-scale (< 250 μm) corrosion damage features and the underlying alloy microstructure such as grain size, grain character, grain orientation, and local misorientation angles. Such models are being evaluated individually and will be incorporated into similar data science approaches to understand coupled effects.

4.2.5. Conclusion

The macro-scale corrosion damage features of three different corrosion morphologies (DP1, FIS and GCSR) are evaluated in this study using data science methods. The parameters that describe the macro-scale corrosion damage features are taken as predictor variables to determine the probability of the fatigue initiation site using a permutation test. Results from the logistics regression model and random forest models were analyzed and the following conclusions are obtained:

- There is no relation between the morphology metrics and the classification of fatigue initiation point for DP1 grid data. The random forest model for DP1 line profile data shows that the pit depth is most important predictor variable for one replicate, and the sum of pit depth as the most important predictor variable for the another replicate.
- The random forest models and logistics regression model for replicate 2 of FIS show that all the predictor variables are significant but this does not generalize to the other replicates.
- The random forest models for GCSR indicates that the predictor variables such as the average roughness (RMS), maximum peak height and the arithmetic mean height are significant for two replicates.
- The lack of consistency on the analyses of the models between the replicates indicates minimal significance of the relationship between the predictor variables for each corrosion morphology and the fatigue crack initiation points.
- Other parameters such as micro-scale corrosion features and underlying alloy microstructure can be more significant in predicting fatigue crack initiation. Although these macro-scale corrosion feature parameters have minimal significance in predicting the fatigue crack initiation, they should not be neglected.

4.2.6 References

[1] Dursun T, Soutis C. Recent developments in advanced aircraft aluminium alloys. Mater Des 2014;56:862–71. doi:10.1016/j.matdes.2013.12.002.

[2] Shoales GA, Fawaz SA, Walters MR. Compilation of damage findings from multiple recent teardown analysis programs. Bridg. Gap between Theory Oper. Pract. 25th ICAF Symp., Rotterdam, The Netherlands: Springer; 2009, p. 187–207. doi:10.1007/978-90-481-2746-7_11.

[3] Barter SA, Molent L, Wanhill RJH. Typical fatigue-initiating discontinuities in metallic aircraft structures. Int J Fatigue 2012;41:11–22. doi:10.1016/j.ijfatigue.2011.10.017.

[4] Mahadevan S, Shi P. Corrosion fatigue reliability of aging aircraft structures. Prog Struct Eng Mater 2001;3:188–97. doi:10.1002/pse.77.

[5] Rezig E, Irving PE, Robinson MJ. Development and early growth of fatigue cracks from corrosion damage in high strength stainless steel. Procedia Eng 2010;2:387–

96. doi:10.1016/j.proeng.2010.03.043.

[6] Co NEC, Burns JT. Effects of macro-scale corrosion damage feature on fatigue crack initiation and fatigue behavior. Int J Fatigue 2017;103:234–47. doi:10.1016/j.ijfatigue.2017.05.028.

[7] Burns JT, Kim S, Gangloff RP. Effect of corrosion severity on fatigue evolution in Al-Zn-Mg-Cu. Corros Sci 2010;52:498–508. doi:10.1016/j.corsci.2009.10.006.

[8] Burns JT, Larsen JM, Gangloff RP. Driving forces for localized corrosion-to-fatigue crack transition in Al-Zn-Mg-Cu. Fatigue Fract Eng Mater Struct 2011;34:745–73. doi:10.1111/j.1460-2695.2011.01568.x.

[9] Kim S, Burns JT, Gangloff RP. Fatigue crack formation and growth from localized corrosion in Al-Zn-Mg-Cu. Eng Fract Mech 2009;76:651–67. doi:10.1016/j.engfracmech.2008.11.005.

[10] Turnbull A. Characterising the pit to crack transition. Annu. Conf. Australas. Corros. Assoc. 2012, Melbourne, Victoria, Australia: 2012, p. 139–45.

[11] Zhou, Turnbull. Influence of pitting on the fatigue life of a turbine blade steel. Fatigue Fract Eng Mater Struct 1999;22:1083–93. doi:10.1046/j.1460-2695.1999.00226.x.

[12] Turnbull A, Horner DA, Connolly BJ. Challenges in modelling the evolution of stress corrosion cracks from pits. Eng Fract Mech 2009;76:633–40. doi:10.1016/j.engfracmech.2008.09.004.

[13] Burns JT, Larsen JM, Gangloff RP. Effect of initiation feature on microstructure-scale fatigue crack propagation in Al-Zn-Mg-Cu. Int J Fatigue 2012;42:104–21. doi:10.1016/j.ijfatigue.2011.08.001.

[14] Co NEC, Burns JT. Galvanic Corrosion-Induced Fatigue Crack Initiation and Propagation Behavior in AA7050-T7451. CORROSION 2016;72:1215–9. doi:10.5006/2132.

[15] Buxton D., Cottis R., Scarf P., McIntyre P. Life prediction in corrosion fatigue n.d.:901–13.

[16] Medved JJ, Breton M, Irving PE. Corrosion pit size distributions and fatigue lives - A study of the EIFS technique for fatigue design in the presence of corrosion. Int J Fatigue 2004;26:71–80. doi:10.1016/S0142-1123(03)00069-0.

[17] Dichev C, Dicheva D. Towards Data Science Literacy. Procedia Comput Sci 2017;108:2151–60. doi:10.1016/j.procs.2017.05.240.

[18] Kamath C, Fan YJ. Data Mining in Materials Science and Engineering. Informatics Mater. Sci. Eng., Elsevier; 2013, p. 17–36. doi:10.1016/B978-0-12-

394399-6.00002-3.

[19] Brence JR, Brown DE. Data mining corrosion from eddy current non-destructive tests. Comput Ind Eng 2002;43:821–40. doi:10.1016/S0360-8352(02)00142-0.

[20] Khullar P, Badilla JV, Lim MLC, Hahn SC, Ellis DW, Kelly RG. Critical factors affecting intergranular corrosion of AA5083 under atmospheric axposures. ECS Meet. Abstr., vol. MA2015-02, 2015, p. 689.

[21] Brown DE. Introduction to Data Mining for Medical Informatics. Clin Lab Med 2008;28:9–35. doi:https://doi.org/10.1016/j.cll.2007.10.008.

[22] Breiman L. Random forests. Mach Learn 2001;45:5–32. doi:10.1023/A:1010933404324.

[23] Liaw A. randomForest v.4.6-12, https://www.rdocumentation.org/packages/randomForest, October 7, 2015.

[24] van der Maaten L, Hinton G. Visualizing High-Dimensional Data using t-SNE. J Mach Learn Res 2008;9:2579–605.

4.3 Fatigue Indicator Parameters

4.3.1 Introduction

The aims of this section are to evaluate the coupled effect of the corrosion damage morphology and the underlying microstructure using crystal plasticity modeling and calculation of fatigue indicator parameters (FIPs). The current corrosion damage morphology and microstructure characterization in the near crack formation region coupled with the quantitative crack formation life data provides a unique opportunity to inform a micro-mechanical modeling approach that aims to capture the influence of local plasticity and tensile stresses on the crack formation behavior. Specifically, the detailed experimental work and characterization of the corrosion damage and microstructure proximate to the crack formation location provides the exact inputs necessary for a crystal plasticity model to analytically calculate the local stress/strain states and thus local driving forces for crack formation.

Recent studies on the driving force for nucleation and short crack growth involve the determination of a so-called fatigue indicator parameter (FIP) for nucleation of cracks [1]. FIP is used to define the crack nucleation driving forces and to evaluate the effects of microstructure in the short crack growth and fatigue crack initiation life [2–5]. Several FIPs based on energy dissipation, plastic accumulation or maximum stress have been proposed and studied by different authors [2,3,6–10]. In this work, we will adopt the parameters and nomenclature summarized and published by Hochhalter et al. [7,8] Five FIPs have been proposed and exercised to describe for cracks extending from secondary phase particles in AA 7075, three of which are based on the accumulated local cyclic plastic slip at a cracked particle (D_1, D_2, D_3), one is based on the maximum value of energy dissipated due to plastic slip (D_4) and one is based on the normal stress on the critical plane of maximum shear (D_5) which takes into account the well-known Fatemi-Socie parameter [7,8,11]. Accumulated slip Γ^α for slip system α is given in Equation 4.1, where $\dot{\gamma}^{\alpha}$is the rate of slip in slip system α integrated throughout the loading cycle, *t* [7,8,11]. D_1 is the nucleation metrics that represents the maximum value of accumulated total slip, Γ, over each of the slip systems α, while D_2 is the maximum value of total accumulated slip over each plane, *p* and D_3 represents the total accumulated slip over all slip systems [7,8,11]. $D_{4,}$ on the other hand, assumes that crack nucleation is related to the maximum value of energy dissipation due to slip on the plane during plastic deformation, where τ^α is the resolved shear stress along slip system α and N_d is the total number of slip systems on a given slip plane [7,8,11]. Finally, D_5 which considers the combined effect of crystallographic slip and tensile stress on the slip plane, is a modification of the Fatemi-Socie parameter [7,8,11]. $\langle \sigma_n^p \rangle$ is the tensile stress on slip plane *p*, $g_o$represents the initial hardness on the slip systems, and k is set to 0.5 [7,8,11].

Hochhalter et.al. examined the effectiveness of the FIPs using replicated-microstructure modeling and reported that cyclic accumulated rate of slip can be used to model which among the cracks would nucleate but is not sufficient to predict the number of cycles to nucleate the crack [7,8]. Other authors used such FIPs (D_1, D_3, D_5) in studying the effects of the orientation of cracked grain and crack length on crack propagation using elasto-viscoplastic fast Fourier transform model and concluded that energy dissipation on the critical plane as the best candidate for small crack growth driving force [9]. Current models of fatigue initiation considers the effect of microstructure to early fatigue response using statistical framework to cyclic crystal plasticity [3,7]. McDowell et.al. utilized the concept of microplasticity within individual grains as key driving force for fatigue crack nucleation, and related fatigue crack formation to plastic strain accumulation due to grain or phase boundary impingement [2,3,12]. Gupta et.al reported that grain orientation can also contribute to local plasticity effects and govern the fatigue initiation and crack growth mechanisms [13]. These recent studies have demonstrated that FIPs can provide a critical localized representation of the driving force, however validation against high fidelity experimental data is severely lacking.

$$\Gamma^{\alpha} = \int_0^t |\dot{\gamma}^{\alpha}| \, dt \qquad \textit{Equation 4.1}$$

$$D_1 = \max_{\alpha} \Gamma^{\alpha} \qquad \textit{Equation 4.2}$$

$$D_2 = \max_{p} \Gamma^{p} \qquad \textit{Equation 4.3}$$

$$D_3 = \sum_{\alpha=0}^{N_s} \Gamma^{\alpha} \qquad \textit{Equation 4.4}$$

$$D_4 = \max_{p} \int_0^t \sum_{\alpha=0}^{N_d} \left|\dot{\gamma}_p^{\alpha} \, \tau_p^{\alpha}\right| \, dt \qquad \textit{Equation 4.5}$$

$$D_5 = \max_{p} \int_0^t \sum_{\alpha=0}^{N_d} \left|\dot{\gamma}_p^{\alpha}\right| \left(1 + k \frac{\langle \sigma_n^p \rangle}{g_o}\right) dt \qquad \textit{Equation 4.6}$$

Most of the current FIP studies involve computational approach and lack experimental validation. However, validation requires (1) data of exact local geometry, microstructure and loading conditions (2) the local stress/strain state and (3) quantitative metrics for crack formation. Information necessary for items (1) and (3) are obtained from Chapter 2 and Chapter 3 of this dissertation and item (2) can be obtained from a collaborative work with Purdue University. The objective of this section is to assess the viability of using the data from corrosion geometry, secondary particle distribution and grain orientation to the local conditions to predict fatigue initiation.

4.3.2 Methodology

In order to calculate the FIP for the specimens with corrosion damage, the following information are pertinent (1) constituent particle distribution or location, (2) corrosion damage shape. (3) the Euler angles or the grain orientation (grain ID) at the fracture surface. The constituent particle distribution and the corrosion damage shape of the fatigue specimens were obtained using the XCT. While the information about the grains at the fracture surface were obtained using EBSD. The details of the XCT and EBSD characterizations are discussed on the next sections. Fatigue specimens obtained using corrosion protocol described in Chapter 2 Section 2 are used to obtain the data necessary for this analysis.

The long term goal of this effort are to (1) enable a validation of the FIPs using the actual microstructure and stress and compare them to the actual crack formation location on the fatigue specimens, and (2) be able to perform sensitivity analysis (removing different microstructure features) to quantitatively see how will this impact the magnitude and location of the FIP hot spots. This work is unprecedented and provides a very unique opportunity to model actual corrosion morphologies and microstructure features and compare the hot spots to experimental/actual fatigue initiation location. Other studies involve the use of statistical volume elements to model the alloy microstructure and do not consider corrosion morphologies [3,6,12,14–16]. The entire matrix for this work involves 8 specimens (long and short total fatigue life with different corrosion morphologies: DP1, DP2, FIS, GCSR). The purpose of selecting the short and long total fatigue life specimens is to determine if there will be a difference between the distributions of calculated FIPs for specimens with different total fatigue life. For this proof of concept evaluation, one FIS specimen with long total fatigue life is analyzed. The crystal plasticity modeling is on-going for the other specimens. Initial results will be presented in this dissertation.

4.3.2.1 EBSD Characterization

The primary fatigue initiation location were identified on the fracture surface of the fatigue specimens using SEM. The EBSD scans were performed on targeted area that coincided with the primary fatigue initiation site. The topography of the fracture surface obtained by white light interferometry (WLI) is shown in **Figure 4.3.1**. It can be seen that the maximum peak to valley height difference is about 250 μm, with an average height of the fracture surface is at 100 μm. Note that the polishing procedure employed for the sample preparation was carefully done to remove a minimal amount of the material on the fracture surface with the goal of having a flat surface on the fatigue initiation site in order to obtain good diffraction. The grain orientation were obtained from EBSD characterization of the polished surface just below the fracture surface plane indicated in red in the polishing schematic shown in **Figure 4.3.2**. The fracture surface of one side (either top or bottom part) of each specimen was polished using 600, 800, 1200 grit SiC papers, and 3 μm, 1 μm, 0.5 μm and 0.25 μm diamond suspensions successively. The specimens were cleaned using ultrasonic bath of acetone and then methanol. Prior to EBSD characterization, the specimens were subjected to flat milling using the Hitachi IM4000Plus with accelerating voltage of 4 kV and discharge current of 440 μA for 15 minutes with ion beam irradiation angle of 80° and specimen iteration angle of ±60°. The estimated average height removed from the sample was about 100 μm. The EBSD scans were captured from 70° tilted specimens with an accelerating voltage of 20 kV, working distance of 10-15 mm and a step size of 1-3 μm

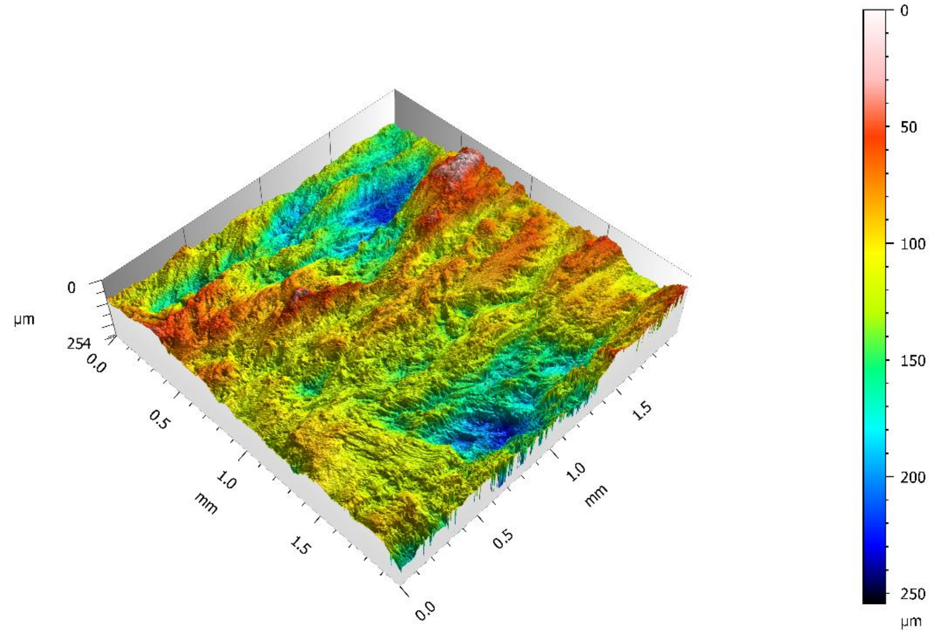

Figure 4.3.1 Topography of the fracture surface after fatigue testing obtained using white light interferometry prior to EBSD sample preparation.

Even though there was a ~100 µm height (along L-direction) removed from the specimen fracture surface, it was assumed that the grains from the EBSD image obtained represent the same grain orientations as those that failed and are visible on the fracture surface. The length of grains along the L-direction is typically longer than field of view of the SEM which is about 1.27 mm (**Figure 4.3.3)** which in part justifies the assumption. It is recognized that the primary weakness of this approach is associated with this assumption but this approach provides a good starting point to approximate grain orientations needed for the calculation of FIPs.

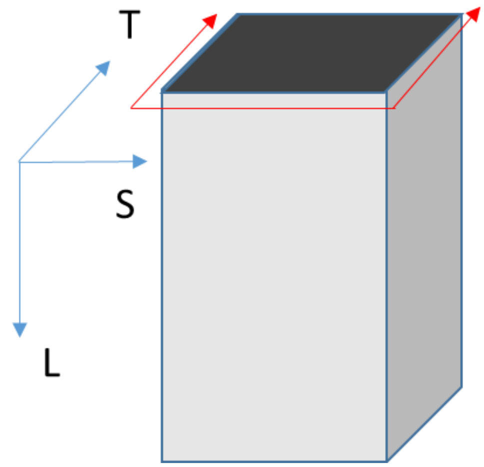

Figure 4.3.2 Schematic of specimen preparation for EBSD. TS surface represents the fracture surface polished down for EBSD characterization. T is the transverse direction, S is the short-transverse direction while L corresponds the longitudinal (rolling) direction.

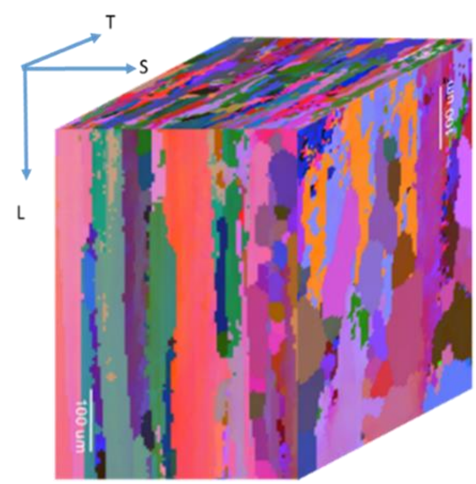

Figure 4.3.3 EBSD cube for AA 7050-T7451. The EBSD cube shows the grains on the LS plane, TS plane and LT planes.

The grain boundary orientation and grain boundary data from pole figure and Euler angle/grain boundary maps were reconstructed using HKL Channel 5 Tango software. An iterative noise-reduction function (grain dilation) of the software was used to reduce the zero solutions from the orientation maps [17,18]. The EBSD maps were overlaid on the fractograph with initially identified fatigue initiation site and traced marker bands. **Figure 4.3.4** shows the (a.) fractograph with traced marker bands and identified initiation point, and (b.) the EBSD image with transposed marker bands and initiation point. The EBSD raw data (obtained by UVa) were post processed (by Purdue University) using the MTEX tool box in Matlab in order to determine the Euler angles and grainID. These Euler angles and grain ID within the fatigue initiation site were fine-tuned and used as input into the crystal plasticity modeling.

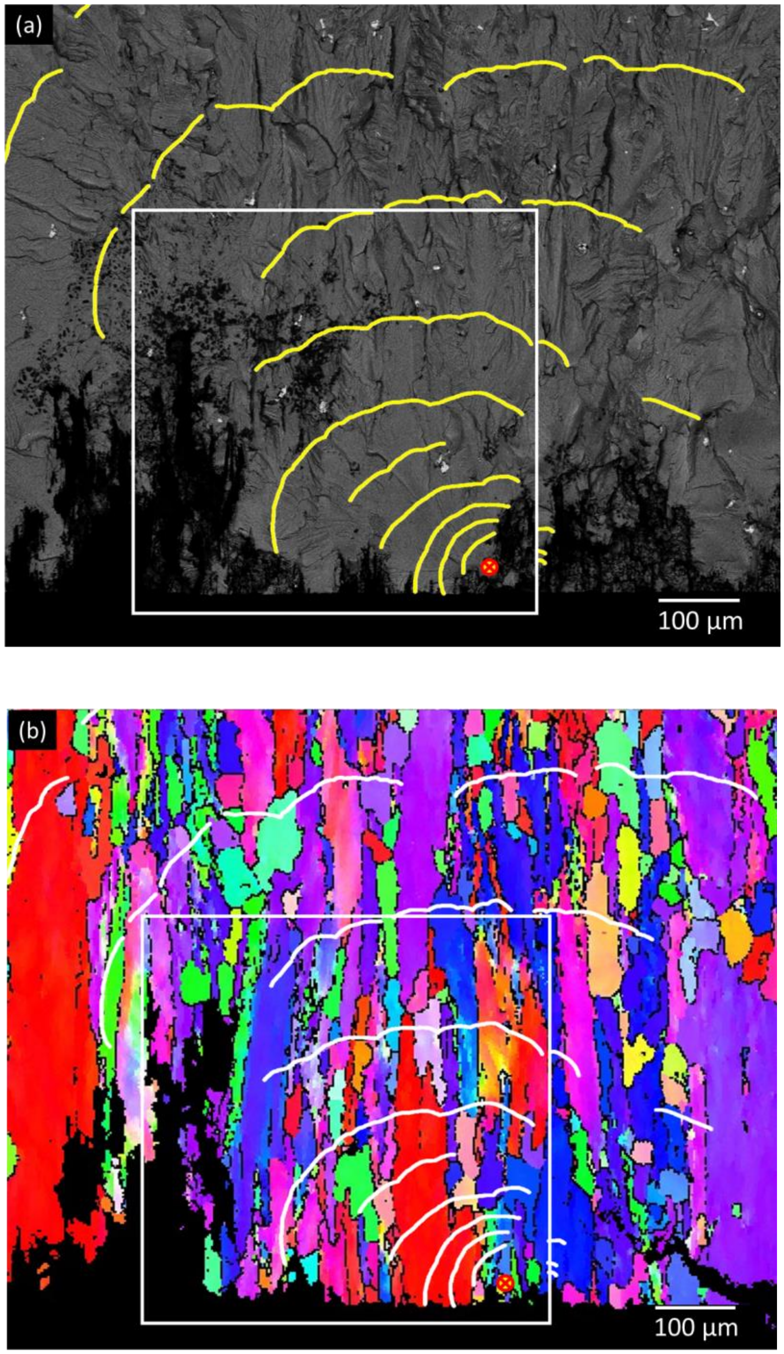

Figure 4.3.4 a. Fractograph of FIS specimen where the yellow lines indicate the location of the marker bands produced by the loading protocol and the primary fatigue crack is indicated by the red cross mark on the image b. EBSD image overlaid on the fracture surface, the white lines indicate the marker bands transposed on the EBSD image, while the primary fatigue crack is indicated by the red cross mark. The boxes on the images correspond to the 500 µm x 500 µm area.

4.3.2.2 XCT Characterization

The XCT (Xradia Micro XCT-200) characterization was done post-fatigue test due to the limitation of the sample holder. In order to obtain the constituent particle distribution and the corrosion damage morphology near the fatigue crack initiation point, it was necessary to obtain XCT images for both the top and bottom parts of the fractured specimen. The bottom and top portion of the fractured FIS specimens were subjected to XCT using a source voltage of 80 kV, and a source power of 8 resulting to a 100 μA current. The source-sample distance was set in between 25 to 30mm while the detector sample distance was kept between 17 to 25mm. Images were taken at an exposure of 20-30 sec per image, and the specimen was rotated 180° in the L-direction. The images were taken using 10x magnification with a 0.7 μm pixel resolution.

The 3D images of the fracture specimens were reconstructed using Avizo volume rendering function to reveal the location of the large constituent particles and the topography of the fracture surface and the corrosion damage. A sub-volume of 500 μm x 500 μm x 500 μm was used for the reconstruction of the bottom fracture specimen and another subvolume of 500 μm x 500 μm x 500 μm for top fracture specimen. **Figure 4.3.3** shows the corresponding volume rendering of the (a) bottom and (b) top portions of the fracture specimen. Subsequent image thresholding and volume rendering were performed to obtain both the corrosion damage morphology and then the constituent particle distribution. Information obtained from XCT used for the spatial location of the second phase particles and the corrosion morphology were passed to collaborators at Purdue University for further fine-tuning then input into the crystal plasticity model.

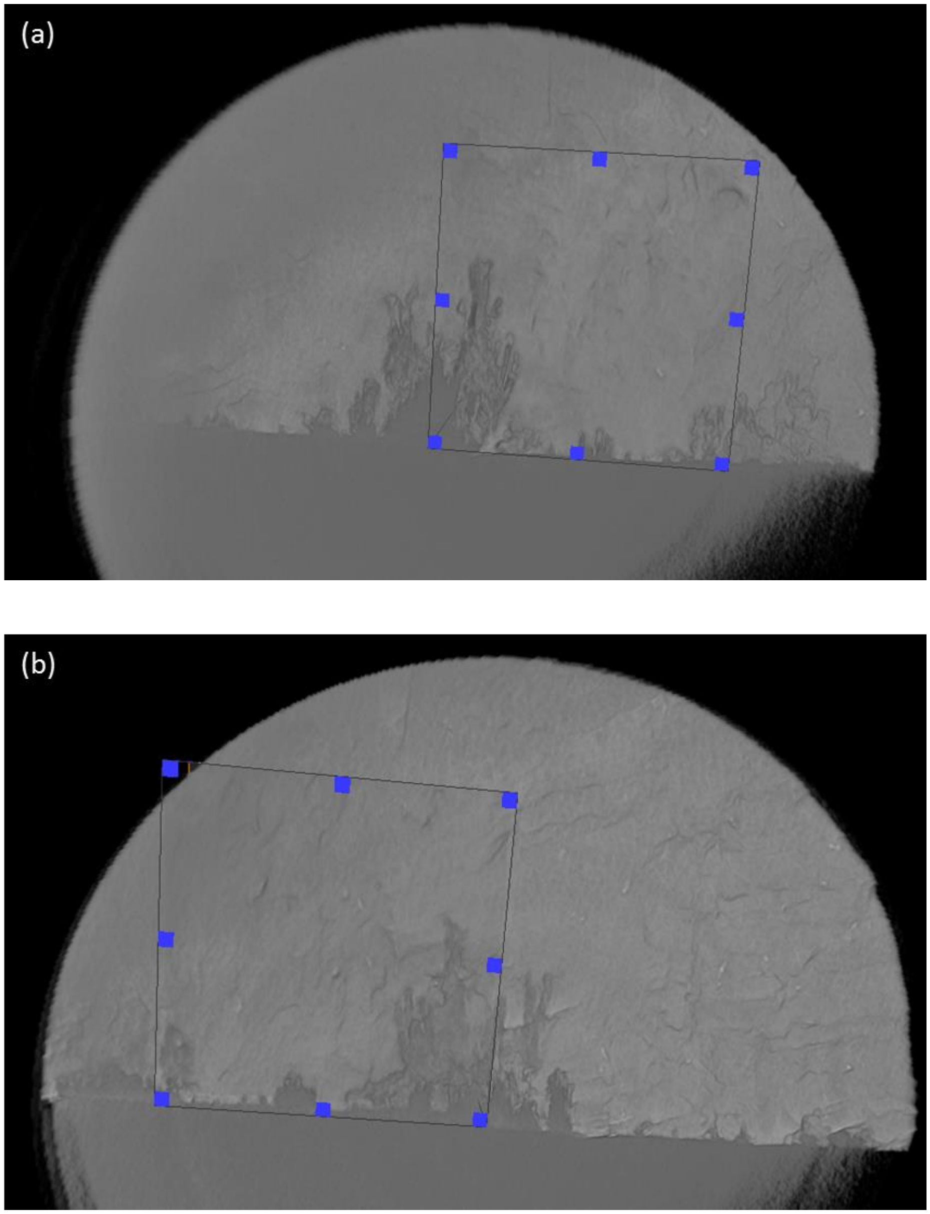

Figure 4.3.5 3D volume rendering of (a) bottom and (b) top portion of the fracture specimens using Avizo software. The boxes indicate the location of 500 μm x 500 μm x 500 μm subvolume. The bottom and top portion are carefully aligned to obtain a bigger volume surrounding the fatigue crack initiation site.

4.3.2.3 Crystal Plasticity Modeling

While the crystal plasticity modeling was done by collaborators at Purdue University, it is useful to outline the general techniques that were employed. Crystal plasticity modeling was done via an elasto-viscoplastic fast Fourier transform (EVP-FFT) formulation that required Euler angles, Grain IDs, spatial location and a material phase identifier, along with material properties as inputs [9,19]. Given these inputs to the EVP-FFT as well as the loading conditions, the corresponding strain state [19] within the vicinity of the corrosion damage were modeled. The unique aspect of this work is that the crystal plasticity computed local stress/strain state was established for the specific corrosion morphology, grain structure, and constituent distribution that were present in the vicinity of the crack formation location. By using these specific inputs, it is possible to calculate different FIP about the perimeter of the corrosion damage. This presents a novel opportunity to compare these values with the actual crack formation location to determine the efficacy of the FIP parameters in predicting the crack formation location using a holistic representation of the actual microstructure. The crystal plasticity modeling used a Generalized Voce Hardening Law given in Equation 4.7 describing the isotropic microscopic slip hardening [9,19]. Γ is the weighted sum of accumulated resolved shear strain of all the slip systems of the material, τ_0 represents the initial CRSS, while θ_0 is the stiffness at the end of microscopic linear elastic zone, θ_1 and τ_1 are parameters used to describe the asymptotic behavior of the material [9,19]. The assumption incorporated in applying the Generalized Voce Hardening Law is that the slip system hardens at the same rate [9,19].

$$\tau(\Gamma) = \tau_0 + (\tau_0 + \theta_1 \Gamma)\left[1 - e^{-\frac{\Gamma\theta_0}{\tau_1}}\right] \qquad \textit{Equation 4.7}$$

The FIPs calculated using Equations 4.2-4.6 are evaluated in this study. Due to the similarity of results, only the FIP calculated based on Equation 4.6 is reported in this study and the material hot spot is compared against the high fidelity experimental data gathered for pre-corroded AA 7050-T7451 specimens.

4.3.2.4 Division of Labor

It is important to delineate the aspects of the work performed at UVa and that performed by collaborators. The experimentation, characterization, selection of specimens on which to perform the matrix of analysis, and conceptual framework for coupling the unique experimental/microstructure characterization results was performed by UVa. Further refinement of the raw characterization data for input into modeling, final volume rendering, all crystal plasticity modeling, and all calculation of the FIP parameters was performed by collaborators at Purdue University. The analysis and interpretation of the data in the context of the crack formation behavior is being performed jointly. The results below are presented as a single result of this collaboration with the division of labor described above.

4.3.3 Results

There are several aspects of this process: (1) final thresholding, (2) final volume rendering to a single volume, (3) crystal plasticity analysis with monotonic loading to yield (4) calculation of the FIP, and (5) comparison to the initiation site.

The initial results presented in this section are for the FIS specimen with long total fatigue life. The final thresholding using the XCT data for both the bottom and top portion of the fatigue specimens are based on the enclosed area on the fracture surface and EBSD image in **Figure 4.3.4**. The box in **Figure 4.3.4** (b) captures about ~40 grains within the 500 μm x 500 μm area. This area represents the vicinity of the fatigue crack initiation location. It is important to capture the constituent particle distribution, the corrosion morphology, the grain orientation (grain ID) within the vicinity of the fatigue crack initiation in order to validate the FIP hot spot prediction with the actual location of the fatigue crack formation.

Figure 4.3.6 shows the resulting rendering of 500 μm x 500 μm x 500 μm sub-volume as identified by the box in **Figure 4.3.5** (a). The volume rendering of the aluminum matrix is shown on **Figure 4.3.6** (a) while the volume rendering of the second phase particles is shown on **Figure 4.3.6** (b). These volume rendering steps are carefully done to match the location of the boxes indicated on the fractograph and EBSD image in **Figure 4.3.4** (a) and (b), respectively. Pertinent corrosion damage features are identified within the location of the fatigue crack initiation and these are matched between the fractograph, EBSD image and the XCT rendered volume. The volume rendering of the aluminum matrix in **Figure 4.3.6** (a) captures both the fracture surface and the corroded surface of the specimen. These results are obtained by UVa.

The constituent particles spatial locations in **Figure 4.3.6** (b) are captured in 3D (x, y, z coordinates). The spatial locations of the constituent particles together with the rendered aluminum matrix volume for the bottom and top portions of the fractured specimen (obtained by UVa), as well as the grain ID obtained from MTEX program in Matlab (obtained by Purdue) are used as inputs to the crystal plasticity modeling.

Figure 4.3.7 shows the resulting volume rendered from the combination of aluminum matrix and second phase particles spatial information both from the top and bottom portion of the fractured specimen. The corroded surface (LS) is also reflected on the resulting image. The fracture plane is represented by the corresponding grain information (based on grainID) as shown in the image.

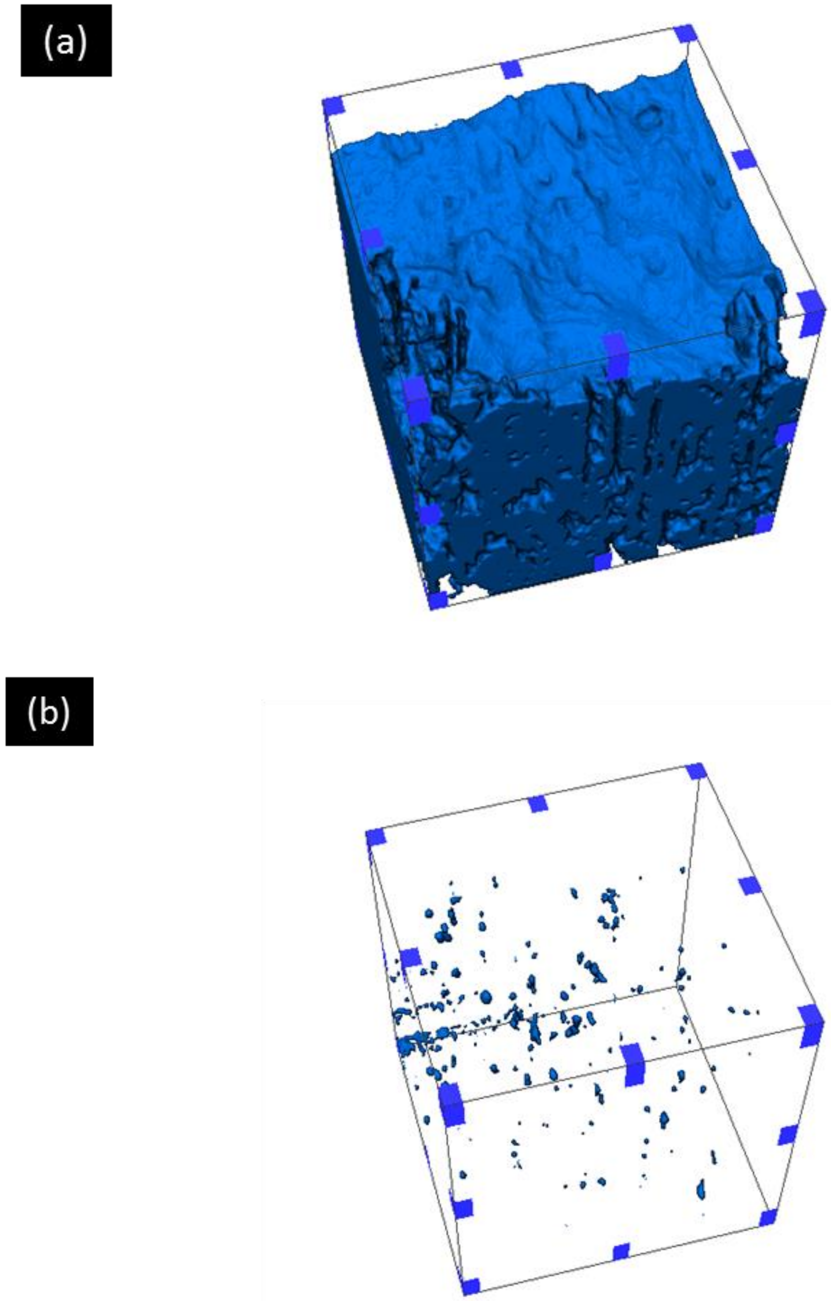

Figure 4.3.6 (a) Volume rendering of the aluminum matrix showing the fracture surface and the corroded surface; (b) volume rendering of the constituent particles for the 500 μm x 500 μm x 500 μm subvolume of the bottom portion of the fractured specimen.

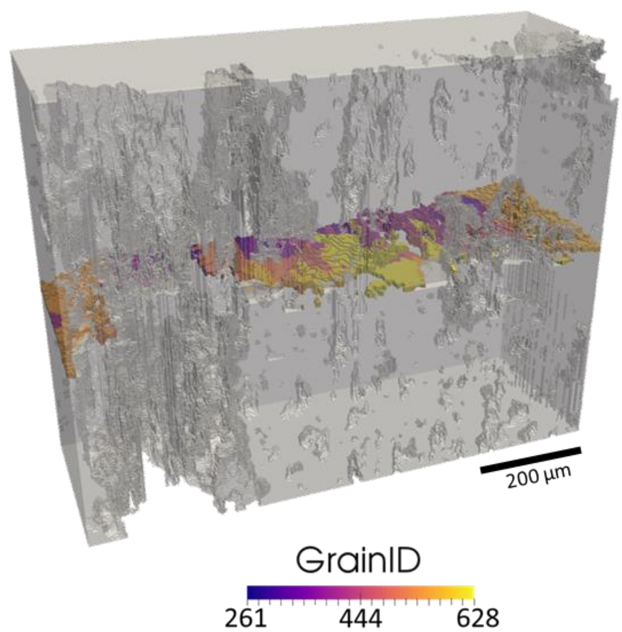

Figure 4.3.7 Combined spatial representation of the aluminum matrix, constituent particles from the top and bottom portions and the grainIDs of FIS specimen. Final volume rendering and GrainID matching are obtained by Purdue.

Figure 4.3.8 shows the calculated FIP representation on the fracture plane for the actual FIS specimen that is cyclically loaded at room temperature with >90% relative humidity using σ_{max} of 200 MPa, R of 0.5 at frequency of 20 Hz. The resulting fatigue initiation life for this specimen is 30,621 cycles [20]. The constituent particles are shown in green while the arrow indicates the location of the actual fatigue crack formation site. Note that for crystal plasticity modeling, the specimen is monotonically loaded to yield stress in order to delineate the FIP hot spots in the material. The values of FIP are determined using Equation 4.6 (modified Fatemi-Socie parameter). The areas with high FIP values are shown in orange to yellow gradient. The actual fatigue crack initiation site lie at the location where the calculated FIP is relatively higher (yellow orange color). The arrow on the figure points to the location of the primary fatigue crack initiation.

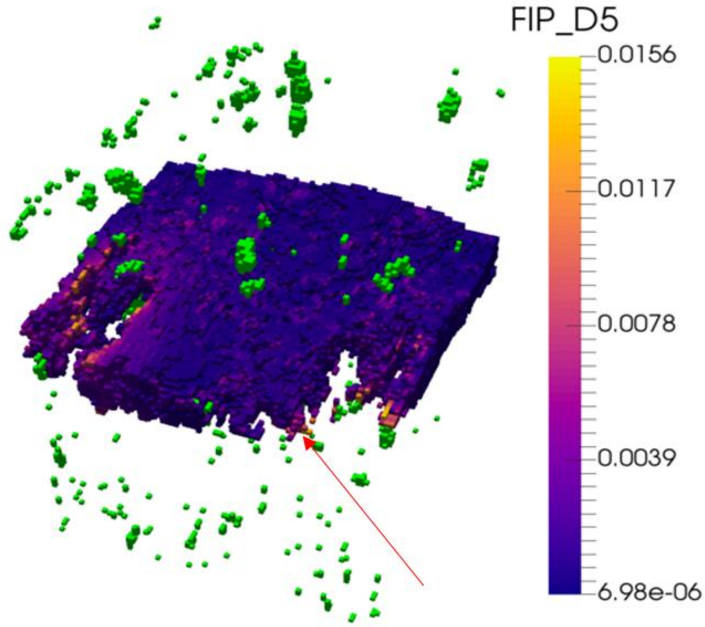

Figure 4.3.8 Calculated FIP for FIS specimen. The secondary phase particles are shown in green. The arrow indicates the location of the primary fatigue crack formation site. The color shows the level of FIP values calculated for the fracture surface. FIP calculation and image rendering are done by Purdue.

4.3.4 Discussion

The calculation of FIPs using Equations 4.2-4.6 resulted to similar distribution of FIPs. Only the results of FIP values calculated using Equation 4.6 (modified Fatemi-Socie parameter) is shown in **Figure 4.3.8**. Literature has proposed several fatigue indicator parameters that are postulated to capture the local conditions that drive crack formation, however, according to Rovinelli et al., FIP calculation based on the modified Fatemi-Socie parameter given in Equation 4.6 is the best candidate for small crack growth driving force as it accounts the energy dissipated on the critical plane [9]. Greater FIP values indicate the hot spots on the material.

The actual fatigue initiation point shown by the arrow in **Figure 4.3.8** lies on the location where the FIP calculated using Equation 4.6 is higher compared to most of the areas in the fracture surface. However, this location is not actually the highest calculated FIP. Some of the areas correspond to higher calculated FIP (yellow color in **Figure 4.3.8**) but these areas do not correspond to any other fatigue initiation sites when compared on the actual result of the fatigue testing. Further analysis needs to be performed to determine the reason for this and more quantitatively evaluate potential subtle differences in the different FIP parameters. The actual fatigue initiation site is near (above) some constituent particles, but the distance of the constituent particles to the initiation site is not analyzed. These constituent particles that are very near the initiation point do not lie on the same plane as the fracture plane, the constituent particle nearest the fatigue initiation location seen in **Figure 4.3.8** is not seen **Figure 4.3.4** (a). Note that the white dots on the back scatter image of the fracture surface (see **Figure 4.3.4** (a)) are the only constituent particles on the fracture surface. The sensitivity analysis of the constituent particle contribution has not been performed. Thus, the contribution of the constituent particle to the FIP values cannot be generalized yet. The initial exercise of using the experimental data as input to crystal plasticity modeling provides a promising approach that enables the determination of the weak spots in the material [21].

4.3.5 Future Work and Analysis

During the course of this PhD effort the UVa aspects of the characterization was performed on a total of 8 samples (2 different life values for 4 different corrosion morphologies namely DP1, DP2, FIS and GCSR) and passed to collaborators at Purdue. The modeling effort is ongoing. The initial exercise done in this study provides a proof of concept that the morphological and microstructural and fatigue cracking data of corroded AA 7050-T7451 can be used as input in the crystal plasticity modeling in order to determine material hot spots on corroded specimens by calculating the FIPs. This initial work leads to additional questions: (1) Will the FIP behave differently without the presence of constituent particles? Or without the different grain orientations? Or without different levels of recrystallization? (2) Will different absolute values of the FIP be able to differentiate the subtlety different values of initiation life **Table 2.2.1**)? (3) Can the FIP values quantitatively capture the slight variations that are observed between the different corrosion morphologies?

Further work is necessary to evaluate the contribution of the constituent particles by performing a sensitivity analysis. FIPs need to be evaluated without the presence of constituent particles. This then needs to be compared to the initial FIP results with the presence of constituent particles. Aside from the sensitivity analysis, the FIP evaluation needs to be extended to other corrosion morphologies (e.g. DP1, DP2 and GCSR) and other specimens with different total fatigue lives (e.g. shorter total fatigue life). This evaluation will provide information about the absolute values of FIPs obtained for different morphologies, or different total fatigue lives. Finally, quantitative analysis of the FIP values on actual fatigue crack formation sites for different specimens will provide information if failure is occurring at specific values, which could inform a "critical" value for crack formation.

4.3.6 Conclusions

Experimental data from fatigue testing of corroded AA 7050-T7451 are used as input in the evaluation of fatigue indicator parameter based on the modified Fatemi-Socie parameter which takes into account the effect of crystallographic slip and tensile stress on the slip plane. The following conclusions are drawn:

- The grainIDs obtained from the EBSD analysis of the TS surface can represent the actual grains on the fracture surface since the grains on the L-direction can extend up to 1000 μm in length.
- The constituent particle distribution from XCT characterization provide important information about the 3D spatial location of the second phase particles with respect to the initiation point. However, the distance of the second phase particles from the initiation point still needs to be evaluated.
- The volume rendering of the aluminum matrix from XCT characterization represents the actual corrosion damage shape that can be incorporated in the strain analysis of the specimen

- Initial exercise of incorporating data obtained from actual experimentation into the crystal plasticity modeling proves that the method can predict the location of fatigue initiation location. This also proves that the method can be applied to other corrosion damage morphologies, provided that the XCT and EBSD characterizations are performed.

4.3.7 References

[1] Peralta P, Laird C. Fatigue of Metals. Phys. Metall. Fifth Edit, Elsevier B.V.; 2014, p. 1765–880. doi:10.1016/B978-0-444-53770-6.00018-6.

[2] Xue Y, McDowell DL, Horstemeyer MF, Dale MH, Jordon JB. Microstructure-based multistage fatigue modeling of aluminum alloy 7075-T651. Eng Fract Mech 2007;74:2810–23. doi:10.1016/j.engfracmech.2006.12.031.

[3] McDowell DL, Dunne FPE. Microstructure-sensitive computational modeling of fatigue crack formation. Int J Fatigue 2010;32:1521–42. doi:10.1016/j.ijfatigue.2010.01.003.

[4] McDowell DL. Simulation-based strategies for microstructure-sensitive fatigue modeling. Mater Sci Eng A 2007;468–470:4–14. doi:10.1016/j.msea.2006.08.129.

[5] Dabiri M, Laukkanen A, Bjork T. Fatigue Microcrack Nucleation Modeling A Survey of the State of the Art. Int Rev Mech Eng 2015;9:368–76.

[6] Shenoy M, Zhang J, McDowell DL. Estimating fatigue sensitivity to polycrystalline Ni-base superalloy microstructures using a computational approach. Fatigue Fract Eng Mater Struct 2007;30:889–904. doi:10.1111/j.1460-2695.2007.01159.x.

[7] Hochhalter JD, Littlewood DJ, Christ RJ, Veilleux MG, Bozek JE, Ingraffea a R, et al. A geometric approach to modeling microstructurally small fatigue crack formation: II. Physically based modeling of microstructure-dependent slip localization and actuation of the crack nucleation mechanism in AA 7075-T651. Model Simul Mater Sci Eng 2010;18:45004. doi:10.1088/0965-0393/18/4/045004.

[8] Hochhalter JD, Littlewood DJ, Veilleux MG, Bozek JE, Maniatty AM, Rollett AD, et al. A geometric approach to modeling microstructurally small fatigue crack formation: III. Development of a semi-empirical model for nucleation. Model Simul Mater Sci Eng 2011;19:35008. doi:10.1088/0965-0393/19/3/035008.

[9] Rovinelli A, Lebensohn RA, Sangid MD. Influence of microstructure variability on short crack behavior through postulated micromechanical short crack driving

force metrics. Eng Fract Mech 2015;138:265–88. doi:10.1016/j.engfracmech.2015.03.001.

[10] Sangid MD, Maier HJ, Sehitoglu H. An energy-based microstructure model to account for fatigue scatter in polycrystals. J Mech Phys Solids 2011;59:595–609. doi:10.1016/j.jmps.2010.12.014.

[11] Fatemi A, Socie D. A critical plane approach to multiaxial fatigue damage including out of phase loading. Fatigue Fract Eng Mater Struct 1988;11:149–65.

[12] Bennett V, McDowell DL. Polycrystal orientation distribution effects on microslip in high cycle fatigue. Int J Fatigue 2003;25:27–39. doi:10.1016/S0142-1123(02)00057-9.

[13] Gupta VK, Gangloff RP, Agnew SR. Diffraction characterization of microstructure scale fatigue crack growth in a modern Al-Zn-Mg-Cu alloy. Int J Fatigue 2012;42:131–46. doi:10.1016/j.ijfatigue.2011.08.003.

[14] Przybyla C, Prasannavenkatesan R, Salajegheh N, McDowell DL. Microstructure-sensitive modeling of high cycle fatigue. Int J Fatigue 2010;32:512–25. doi:10.1016/j.ijfatigue.2009.03.021.

[15] Pineau A, McDowell DL, Busso EP, Antolovich SD. Failure of metals II: Fatigue. Acta Mater 2016;107:484–507. doi:10.1016/j.actamat.2015.05.050.

[16] Farukh F, Zhao LG, Jiang R, Reed P, Proprentner D, Shollock BA. Realistic microstructure-based modelling of cyclic deformation and crack growth using crystal plasticity. Comput Mater Sci 2016;111:395–405. doi:10.1016/j.commatsci.2015.09.054.

[17] Wright SI, Nowell MM, Lindeman SP, Camus PP, De Graef M, Jackson MA. Introduction and comparison of new EBSD post-processing methodologies. Ultramicroscopy 2015;159:81–94. doi:10.1016/j.ultramic.2015.08.001.

[18] Randle V. Electron backscatter diffraction: Strategies for reliable data acquisition and processing. Mater Charact 2009;60:913–22. doi:10.1016/j.matchar.2009.05.011.

[19] Mello AW, Nicolas A, Lebensohn RA, Sangid MD. Effect of microstructure on strain localization in a 7050 aluminum alloy: Comparison of experiments and modeling for various textures. Mater Sci Eng A 2016;661:187–97. doi:10.1016/j.msea.2016.03.012.

[20] Co NEC, Burns JT. Effects of macro-scale corrosion damage feature on fatigue crack initiation and fatigue behavior. Int J Fatigue 2017;103:234–47. doi:10.1016/j.ijfatigue.2017.05.028.

[21] Co NEC, Burns JT, Nicolas A, Sangid MD. Effect of corrosion micro-scale features and alloy microstructure on the fatigue initiation and crack growth of AA7050-T7451 Paper No. 2017-845990. 2017 Dep. Def. Allied Nations Tech. Conf., 2017.

5. Conclusions

5.1 Macro-scale Corrosion Features

The fatigue behavior and crack growth rates of specimens with different damage morphologies representative of Al-stainless steel galvanic coupling are evaluated in moist air at 23^{o}C. Different stages of fatigue life are quantified for each specimen. Several corrosion macro-scale metrics are correlated to the location of the fatigue initiation sites. This systematic investigation of the effects of macro-scale corrosion feature on the fatigue initiation and fatigue behavior of AA 7050-T7451 established the following conclusions:

- Presence of corrosion damage on the surface of the aluminum greatly reduced the total fatigue life of AA 7050-T7451. The fatigue crack initiation life for vastly different corrosion morphologies is relatively constant and can be assumed negligible at this relatively high maximum stress level (200 MPa).
- The metrics analyzed for the macro-scale corrosion damage feature and the combination effects of these metrics do not fully dictate the location of fatigue crack formation sites. The complex interaction of corrosion micro-scale features as well as the presence of nearby constituent particles needs to be further investigated.
- The crack growth rates for specimens having different corrosion damage morphologies converge to comparable values as the crack extends away from the corrosion damage feature.
- The slight decrease in total fatigue life as the corrosion damage increases in severity (despite constant initiation lives) is attributed to an increase in the number of crack formation sites and larger crack formation features that decrease the crack propagation length necessary to reach the critical crack size for failure.

The fatigue initiation, fatigue behavior and crack growth rates of AA 7050-T7451 with different corrosion damage morphologies tested under different loading and environmental conditions are evaluated. The macro-scale corrosion metrics are measured and correlated to the fatigue crack formation location. The fatigue life to form a 10 μm crack from the initiation point is estimated and reported together with the total fatigue life of the specimens tested. The following conclusions are established:

- The presence of relevant and more severe corrosion damage (cigar-shape pit and intergranular corrosion) does not lead to extreme reduction in the total fatigue life of specimen tested in moist environment. The fatigue crack initiation lives of the specimens with relevant corrosion damage and regular discrete pits are comparable and are almost negligible. The macro-scale corrosion metrics evaluated in this study do not fully/uniquely dictate the location of the fatigue crack formation. There are other factors that needs to be considered such as the underlying microstructure of the alloy and its interaction with the corrosion morphology.
- Relative humidity decreases the total fatigue life of specimens by increasing the crack growth rate but it does not greatly influence the fatigue initiation life of AA 7050-T451. The fatigue crack formation location for specimens tested at different levels of relative humidity is not solely dictated by the macro-scale corrosion features.
- The increase in σ_{max} for cyclic loading in moist environment caused the decrease in the total fatigue life. Specimens cyclically loaded with high σ_{max} in moist environment have lower initiation life, higher number of fatigue initiation points and higher crack growth rate leading to great decrease in the total fatigue life. The location of the fatigue crack initiation is not mainly influenced by the macro-scale corrosion feature even when the level of applied maximum stress is varied.

5.2 Micro-scale Corrosion Features and Alloy Microstructure

The location of fatigue crack initiation for a corroded AA 7050-T7451 are characterized in terms of the adjacent micro-scale corrosion damage feature and underlying alloy microstructures. The micro-scale features present on the corrosion damage surface are micro-pits, jut-ins, and remaining metallic ligaments. The surface roughness of the corrosion damage are characterized and the values of surface roughness parameters are reported. The alloy microstructural features analyzed in this study are the constituent particle distribution, constituent particle size, constituent particle distance, grain orientation, grain size, grain orientation spread and misorientation angle between the fatigue initiating grain and the neighboring grains. These micro-scale and microstructural features are correlated with the fatigue initiation location. The following conclusions are made:

- Most of the fatigue cracks initiate at jut-in and remaining metallic ligaments, however, not all jut-in and ligament features on the surface of the corrosion damage initiate fatigue crack. The areal corrosion features do not highly dictate the location of the fatigue initiation site. There are other factors aside from the corrosion damage shape that need to be considered in predicting the location of fatigue crack initiation.
- The distribution of constituent particles, constituent particle distance as well as the size of constituent particles have limited contribution to the fatigue crack initiation of corroded AA 7050-T7451.
- There are other parameters aside from the amount of deformation (as measured by the grain orientation spread) present in the grain that can influence fatigue crack initiation.
- Most of the fatigue initiating grains are larger than the median or mean value of the grain size. It is important to note that it is not always the biggest grain that initiates fatigue cracks.
- The fatigue crack initiation generally occurred on grains with high index orientation, and on grains with high misorientation angle with respect to the neighboring grains.

5.3 Combined Effects

The macro-scale corrosion damage features of three different corrosion morphologies (DP1, FIS and GCSR) are evaluated in this study using data science methods. The parameters that describe the macro-scale corrosion damage features are taken as predictor variables to determine the probability of the fatigue initiation site using a permutation test. Results from the logistics regression model and random forest models were analyzed and the following conclusions are obtained:

- There is no relation between the morphology metrics and the classification of fatigue initiation point for DP1 grid data. The random forest model for DP1 line profile data shows that the pit depth is most important predictor variable for one replicate, and the sum of pit depth as the most important predictor variable for the another replicate.
- The random forest models and logistics regression model for replicate 2 of FIS show that all the predictor variables are significant but this does not generalize to the other replicates.
- The random forest models for GCSR indicates that the predictor variables such as the average roughness (RMS), maximum peak height and the arithmetic mean height are significant for two replicates.
- The lack of consistency on the analyses of the models between the replicates indicates minimal significance of the relationship between the predictor variables for each corrosion morphology and the fatigue crack initiation points.

Experimental data from fatigue testing of corroded AA 7050-T7451 are used as input in the evaluation of fatigue indicator parameter based on the modified Fatemi-Socie parameter which takes into account the effect of crystallographic slip and tensile stress on the slip plane. The following conclusions are drawn:

- The grainIDs obtained from the EBSD analysis of the TS surface can represent the actual grains on the fracture surface since the grains on the L-direction can extend up to 1000 μm in length.
- The constituent particle distribution from XCT characterization provide important information about the 3D spatial location of the second phase particles with respect to the initiation point. However, the distance of the second phase particles from the initiation point still needs to be evaluated.

- The volume rendering of the aluminum matrix from XCT characterization represents the actual corrosion damage shape that can be incorporated in the strain analysis of the specimen
- Initial exercise of incorporating data obtained from actual experimentation into the crystal plasticity modeling proves that the method can predict the location of fatigue initiation location. This also proves that the method can be applied to other corrosion damage morphologies, provided that the XCT and EBSD characterizations are performed.

6. Future Works

One of the current limitations of this project is the assumption that the grains revealed by the EBSD are similar to the grains in the actual fracture plane. While the current assumption is reasonable, ideally improved correlations and modeling would come from a more comprehensive characterization of this area. Such a characterization could be performed by next generation "3D EBSD" techniques such as reported by Spear et al., lab-based diffraction contrast tomography (Lab-DCT), or focused ion beam (FIB)-based serial sectioning techniques[1–4].

Furthermore, while this work developed an understanding of the features that impact the fatigue behavior form a galvanic couple, extending to unique moprhologies that may arise in the presence of corrosion inhibitors can also be interesting to look at. Particularly, if the micro-scale corrosion features are very different from corrosion pits or IGC. Currently, the collaborators are systematically collecting an encyclopedia of corrosion damage morphologies [5]. This can be used to determine the other corrosion morphologies that can further be tested and analyzed.

The parameter that has not been investigated in this dissertation is the effect of hydrogen. The amount of hydrogen after electrochemical exposure and during the fatigue testing can be estimated through different hydrogen modeling available. Targeted fatigue experiments with different hydrogen concentration (which can be varied during pre-charging, up-take, or environmental exposure) can be performed to see how the amount of hydrogen impacts the fatigue initiation location. Further analysis of hydrogen concentration can also help in understanding why fatigue crack initiation site occur mostly on jut-in features.

Focused analysis on the grain orientation spread difference between the initiating grain and the neighboring grains within the corroded surface can bring more insight on the nature of fatigue crack initiation.

The micro-scale corrosion damage features and alloy microstructure effects can further be analyzed using data science techniques. This will involve individual data binning to incorporate the effects of the micro-scale corrosion damage metrics and then another data binning with the information about the constituent particle distribution, constituent particle size, grain size and grain orientation. The data binning can be extended to include both the micro-scale features and the microstructure.

Future works on crystal plasticity modeling were detailed in the prior section. Specifically, ongoing work will build upon the successful proof of concept to performing modeling on the other corrosion morphologies and life combinations that were characterized in this study and passed to our collaborators. Furthermore more quantitative and comparative analysis of the resulting FIP calculation is needed. Once there is confidence in the calculations and specific FIP parameter then a sensitivity analysis of the microstructure and corrosion morphology features can be performed. Furthermore, since these models already include all of the microstructure information and the MSC growth rates are known via the marker bands, it is useful to determine if the growth rates map to calculated FIP values as the crack progresses.

6.1 References

[1] Spear AD, Li SF, Lind JF, Suter RM, Ingraffea AR. Three-dimensional characterization of microstructurally small fatigue-crack evolution using quantitative fractography combined with post-mortem X-ray tomography and high-energy X-ray diffraction microscopy. Acta Mater 2014;76:413–24. doi:10.1016/j.actamat.2014.05.021.

[2] Spear AD. Numerical and Experimental Studies of Three-Dimensional Crack Evolution in Aluminum Alloys: Macroscale To Microscale. Cornell University, 2014.

[3] Lienert U, Li SF, Hefferan CM, Lind J, Suter RM, Bernier J V., et al. High-energy diffraction microscopy at the advanced photon source. Jom 2011;63:70–7. doi:10.1007/s11837-011-0116-0.

[4] Uchic MD, Groeber MA, Dimiduk DM, Simmons JP. Viewpoint Paper. Scr Mater 2006;55:23–8. doi:10.1016/j.scriptamat.2006.02.039.

[5] Rafla VN. Unpublished Works. University of Virginia, 2018.